Ore Genesis and Fluid Evolution of the Goat Hill Orebody, Questa Climax-type Porphyry-Mo System, NM and Its Comparison to the Climax-type Deposits of the Colorado Mineral Belt

By

Amanda Rowe

DISSERTATION

Submitted in Partial Fulfillment
of the Requirements for

Doctor of Philosophy in Earth & Environmental Science (Geology)

Department of Earth & Environmental Science
New Mexico Institute of Mining & Technology

Socorro, New Mexico

May 2012

To my best friend, Amber Alice Woodyatt – never forgotten, always there.
February 18, 1975 – May 18, 2007

and

To my Grama, Marion Andrews, who once told me that trying to understand God is like trying to empty the ocean with a tea cup.

ABSTRACT

The world class Questa porphyry molybdenum deposit occurs in northern New Mexico and belongs to a unique Climax-type class of ore deposit. Several deposits of the same genre (Climax, Henderson, Silver Creek, and Mount Emmons) occur in Colorado along the Colorado Mineral Belt (COMB). The genetic origin of Climax-type deposits has been debated throughout the economic geology community in terms of source of mineralizing fluids, temperature of mineralization, and fluid evolution. A detailed geochemical study of the Goat Hill orebody of the Questa Climax-type porphyry molybdenum deposit provided evidence from three complimentary analyses (fluid inclusion microthermometry, stable isotope analyses, and fluid inclusion gas analyses) for the genetic origin and fluid evolution of the Questa system.

The Goat Hill orebody at Questa is comprised of a stratified magmatic-hydrothermal breccia (MHBX) and later quartz-molybdenite (qtz-mo) stockwork veinlets. The MHBX consists of five facies (A-E) based upon a distinct mineralogic and alteration evolution within the breccia. It was revealed by fluid inclusion microthermometry, stable isotope analyses, and fluid inclusion gas analyses that no fluid evolution based upon MHBX facies was evident in quartz to correlate with the mineralogic/alteration evolution. Fluid inclusion microthermometry resulted in similar wide ranges of homogenization temperatures (Tlv = 81-520°C) and salinities (0-64 eq. wt.% NaCl+KCl+$CaCl_2$) for quartz from all of the MHBX facies. The later qtz-mo veinlet data was essentially analytically indistinguishable from the MHBX quartz (Tlv range of 62-560°C and salinity range of 0-63 eq. wt.% NaCl+KCl+$CaCl_2$) with only minor differences, demonstrating that the veinlets experienced a similar evolutionary

history as the MHBX. The minor differences between the veinlets and the MHBX (fluid inclusion size, abundance, and type) may indicate that the veinlets began as a slightly more evolved magmatic-hydrothermal fluid. Even though no evidence of fluid evolution based upon facies was revealed in the quartz fluid inclusion data, four stages (1-4) of fluid evolution independent of facies were identified in the MHBX and veinlet fluid inclusion data. The earliest, most pristine fluid (Stage 1) with a mode temperature of 460°C evolved to the later stages (2-4) by phase separation, simple cooling, and meteoric mixing. The main stage of molybdenite mineralization occurred in Stage 2 (mode Tlv of 380°C) and a secondary mineralization phase in Stage 3 (mode Tlv of 280°C), both due to temperature decrease from simple cooling and meteoric mixing. Meteoric influx and fluorite/calcite precipitation occurred in Stage 4 (mode Tlv of 200°C).

Despite the lack of evolutionary pattern based upon facies in the quartz stable isotope data, a fluid evolution was evident, however, in the $\delta^{18}O_{H2O}$ and δD_{H2O} values between the different mineral phases of the MHBX matrix paragenetic sequence (fluorophlogopite →quartz →fluorite→calcite) with the fluid evolving from a marginally magmatic to magmatic-dominant mixed magmatic-meteoric to meteoric-dominant mixed magmatic-meteoric source. Water isotope values for molybdenite-associated fluorophlogopite ($\delta^{18}O_{H2O}$ and δD_{H2O} values of 3.8-7.4‰ and -89 to -63‰) and quartz ($\delta^{18}O_{H2O}$ range of 1.5-3.7‰) were calculated at the main mineralization mode temperature of 380°C. Fluid inclusion δD_{H2O} values from quartz ranged from -101 to -71‰. Post-mineralization fluorite yielded fluid inclusion $\delta^{18}O_{H2O}$ and δD_{H2O} values of -4.0 to -1.7‰ and -109 to -106‰, respectively. $\delta^{18}O_{H2O}$ values for calcite (-4.3 to -1.3‰) were calculated utilizing the associated Stage 4 mode temperature of 200°C. Similar to

the fluid inclusion microthermetry data, the veinlet quartz was essentially analytically indistinguishable from the MHBX for calculated $\delta^{18}O_{H2O}$ values (1.6-3.9‰ at 380°C), further supporting that the veinlets underwent the same evolutionary history as the MHBX. The veinlets exhibited widespread fluid inclusion δD_{H2O} values (-143 to -52‰) compared to the MHBX matrix, possibly due to an interstitial water contribution or analytical error associated with smaller, less abundant fluid inclusions and associated small sample peaks.

Sulfur stable isotope analyses on molybdenite, pyrite, and anhydrite and carbon stable isotope analysis on calcite revealed a magmatic source for Questa sulfur and carbon with $\delta^{34}S$ ranges of 0.4-2.3‰, 1.6-2.5‰, and 6.6-10.0‰, respectfully, and calculated $\delta^{13}C_{CO2}$ values of -6.0 to -4.9‰ at 200°C. Despite a meteoric component of varying degrees to the fluid associated with these minerals, a magmatic source is possible for these two species due to the fact that meteoric water is low in sulfur or carbon, hence allowing the magmatic signature to remain with the fluid.

Similar to the fluid inclusion microthermometry and stable isotope data, the fluid inclusion gas analyses showed a similar evolution on the fluid source diagrams of Norman and Moore (1999) and Blamey and Norman (2002) with N_2/Ar vs. CO_2/CH_4 and N_2/Ar vs. Ar/He ratios that plotted in near magmatic to meteoric source fields for MHBX quartz and meteoric to evolved (crustal) source fields for later MHBX fluorite. The veinlet fluid inclusion gas analysis data was also essentially analytically indistinguishable from MHBX quartz, with only a minor difference that suggests that the veinlets began from a slightly more evolved magmatic-hydrothermal fluid.

A comparison of the geochemical data of Questa with the Climax-type deposits of the COMB revealed that these deposits not only possess common physical characteristics, but also similar genetic fluid evolution histories, that render them members of this unique deposit class. Similar to Questa, the Climax-type deposits of the COMB possess common fluid inclusion types, non-magmatic raw homogenization temperature modes ranging from 320-400°C, and magmatic to mixed magmatic-meteoric $\delta^{18}O_{H2O}$ and δD_{H2O} ranges of 2-9.7‰ and -140 to -83‰ associated with molybdenite mineralization. Another similarity between the deposits is a magmatic source for sulfur with a $\delta^{34}S_{molybdenite}$ range of 0.4-5.3‰ for all of the deposits. In comparison of the different deposits, it was also found that the difference in reported fluid origins (magmatic vs. a meteoric component) between the deposits was not necessarily due to data differences, but often the interpretation of Tshl>>Tlv fluid inclusions or the lack of complimentary data sets.

Keywords: Climax-type porphyry molybdenum deposit; fluid inclusion analysis; stable isotope analysis; fluid inclusion gas analysis; Questa, New Mexico; ore genesis.

ACKNOWLEDGEMENTS

First and foremost, I would like to thank the Lord for all that He has given me. Thanks so much to my committee, Andy Campbell (Advisor), Nigel Blamey, and Kent Condie of NMT, Bruce Walker of Chevron Mining (Questa Mine), and Ginger McLemore of the NMBGMR, for their faith in me and this project, their support, and their valuable contributions to this project. Additional thanks to Andy Campbell for his amazing knack and gift in teaching people to think in an entirely different manner – my brain will never be the same and definitely for the better! Also additional thanks to my dear friend, mentor, and spiritual advisor Bruce Walker, for his incredible mentoring, friendship, and support through this entire process, including my great contemporaneous life experiences. Also additional thanks to my South African friend, Nigel Blamey, for always lending a helping hand and an idea. A special acknowledgement to the late Dave Norman - you left big shoes to fill, on my committee, in the department, and in life. Thanks to Chevron Mining (formerly Molycorp, Inc.) for granting permission to perform this study. Thanks to Pierre-Simon Ross for setting the fantastic and very interesting groundwork for this project, and giving me a very concentrated MHBX 101 in such a short period of time. A special thanks to my former boss and mentor Cal Callaghan of the Climax Molybdenum Company Henderson Mine for his extreme support and encouragement in the latter end of this process, it was invaluable. A huge thank you to my supervisors at Freeport-McMoRan Copper & Gold Sierrita Operations - Greg Baugh, John Hawley, Derek Cooke, Annette Gelfi, and Kent Cramer - for their major support in my finishing this process. I would like to thank my Aunt Kathy for moving to Phoenix, Arizona, so that I could come to the Southwest, fall in love with rocks and geology, and

later follow my dream of become a geologist. Thanks to my invaluable undergraduate helpers, Joel Bensing and Penny Ortiz, for sample prep and running analyses. I would like to thank all of my dear friends who have helped see me through it, and are STILL my friends, you know who you are! Special thanks to Andy Graves and Jess Lynch for taking me to the emergency room at 4 a.m. after my accident in the stable isotopes lab…I will never forget them for all that they did for me during that time. A special thanks to Shane Clarkson for his eternal patience, tolerance, support, unconditional love, and encouragement. Over peaks and valleys, you were my best friend and biggest supporter at many points on this journey. I would like to thank my sister Heather for her love and support, and for keeping Aunt Amanda a vital and important part of Cameron and Ryan's lives, despite 2000 miles and the lack of time I had to give. A special heart-felt thank you to the most incredible human being I know, Lee Fronapfel – you are amazing! Your undying support got me through the bitter torturous end of this thing. I adore you and am forever grateful that you are in my life. Most of all, an extra special thanks to my parents Larry and Jeannie Rowe, for without their undying love, support, guidance, and encouragement from birth, this would not have been possible. I love you both. Thank you. This project was funded in part by the New Mexico Bureau of Geology & Mineral Resources, the New Mexico Geological Society, the Geological Society of America, the New Mexico Tech Graduate Student Association Matuszeski Research Grant, Rocky Mountain Freedom of Mineralogical Societies for the ARMS Scholarship Foundation, The Women's Auxiliary to the AIME, and the Society of Economic Geologists.

TABLE OF CONTENTS

LIST OF TABLES

LIST OF FIGURES

CHAPTER I.

CHAPTER II.

CHAPTER III.

PREFACE

This dissertation is separated into three chapters (I-III), with each chapter consisting of a paper written in scientific journal format for publication. Chapter I involves the fluid inclusion microthermometry of Questa, Chapter II involves stable isotope and gas analyses on Questa, and Chapter III integrates the findings of the first two papers on Questa with a comparison of those findings to the Climax-type deposits of the Colorado Mineral Belt. Please note that due to the scientific paper format of this dissertation where each chapter was composed to be a stand-alone paper, some redundancy will be encountered between the chapters.

CHAPTER I.

Genetic Fluid Evolution of the Magmatic-hydrothermal Breccia and Stockwork Veinlets of the Goat Hill Orebody, Questa Climax-type Porphyry-Mo System, New Mexico – A Fluid Inclusion Study

ABSTRACT

The Goat Hill orebody of the Questa Climax-type porphyry molybdenum system is composed of a magmatic-hydrothermal breccia (MHBX) and later quartz-molybdenite (qtz-mo) stockwork veinlets. Ross (2002) defined five distinct stratified facies (A-E) within the Goat Hill MHBX based upon matrix mineralogy, and clast alteration and texture. Higher temperature mineralogic and alteration assemblages occur in the facies closest to the source intrusion (facies A and B), and lower temperature mineralogic and alteration assemblages occur in the facies most distal to the source (facies D and E). It was proposed by Ross (2002) that evolution of the magmatic-hydrothermal fluid away from its source is a plausible mechanism for these differences in the breccia facies.

A spatially and temporally constrained fluid inclusion study was performed on MHBX matrix and veinlet quartz in order to delineate the source of the ore-bearing fluids, the mechanism for molybdenite mineralization, and if there was a fluid evolution that occurred in association with the mineralogic/alteration evolution of the Goat Hill MHBX. Two MHBX matrix fluorite samples were also analyzed. Four major fluid inclusion types were identified in both the MHBX matrix and veinlets of the Goat Hill: liquid-vapor type I inclusions, halite-bearing type II inclusions, halite+sylvite-bearing type III inclusions, and CO_2-rich type IV inclusions. A large number of the halite-bearing fluid inclusions homogenized by halite dissolution at temperatures much greater

than the homogenization temperatures of the liquid-vapor phase. Based upon phase equilibria constraints and various evidence reported in this study, it is concluded that these inclusions are a result of entrapment of a halite crystal during heterogeneous trapping rather than in-situ precipitation. Consequently, fluid inclusion temperature data is reported in terms of homogenization of the liquid-vapor phase (Tlv) rather than the final temperature of homogenization.

No fluid evolutionary pattern based upon MHBX facies in quartz was evident, with similar wide ranges in temperatures and salinities in all facies. However, an evolution was evident between MHBX matrix quartz (paragenetically early) and fluorite (paragenetically late), with fluorite reflecting meteoric influx into the system with low temperatures and salinities. This evidence suggests that sampling and analysis of different mineral phases of the MHBX paragenetic sequence would most likely reflect the mineralogic/alteration of the MHBX.

The MHBX matrix and qtz-mo veinlet data was essentially analytically indistinguishable, and most likely followed a similar fluid evolution history. The MHBX matrix (quartz and fluorite) exhibited a wide Tlv range of 81-520°C, with modes at 180°C, 280°C, 380°C, and 460°C and a salinity range of a salinity range of 0-64 eq. wt.% NaCl+KCl+$CaCl_2$. The qtz-mo veinlets exhibited a wide Tlv range of 62-560°C, with modes at 200°C, 280°C, and 380°C and a salinity range of 0-63 eq. wt.% NaCl+KCl+$CaCl_2$. Four stages (1-4) of fluid evolution were identified to explain the broad ranges in temperature and salinity (T-X) data for the MHBX matrix and qtz-mo stockwork veinlets, and are associated with the Tlv modes in the fluid inclusion data. The earliest, most pristine fluid (Stage 1) evolved to the later stages (2-4) by phase

separation, simple cooling, and meteoric mixing. In addition, meteoric influx occurred in Stage 4. Molybdenite deposition occurred in Stages 2 and 3 as a result of temperature decrease.

INTRODUCTION

The genetic origin of Climax-type porphyry molybdenum deposits (i.e. Questa, NM and Mt. Emmons, Silver Creek, Climax, and Henderson/Urad, CO) has been debated throughout the economic geology community. Various previous fluid inclusion studies on Climax-type deposits have concluded magmatic (Kamilli, 1978; White et al., 1981; Cline and Bodnar, 1994; Cline and Vanko, 1995; Seedorff and Einaudi, 2004), magmatic and meteoric mixing (Hall 1974; Smith, 1983), or evolution from magmatic to meteoric (Bloom, 1981), as the origin of the molybdenum-bearing fluids and associated molybdenite mineralization. Fluid inclusion analyses yielding different types, temperatures of homogenization, and salinities, have been utilized to determine the genetic origin of Climax-type deposits. High salinity fluid inclusions with a temperature of halite dissolution much greater than the temperature of liquid-vapor homogenization have been identified and are common in this type of deposit (Hall, 1974; Kamilli, 1978; Bloom, 1981; White et al., 1981; Smith, 1983; Carten 1987; Cline and Bodnar, 1994; Cline and Vanko, 1995; Ross, 2002; Ross et al., 2002; Seedorff and Einaudi, 2004; Klemm et al., 2004; Klemm et al., 2008). Several authors have used these high salinity brines as a justification for a magmatic origin for the ore fluids, in that the fluids exsolved from the silicic melt (Kamilli, 1978; White et al., 1981; Cline and Bodnar, 1994; Cline and Vanko, 1995). Other authors debate that this type of fluid inclusion is a result of the captured halite phenomenon and is not representative of a real fluid (Eastoe, 1978; Wilson, 1978; Erwood et al., 1979; Bloom, 1981; Campbell et al., 1995; and Kodera et al., 2004). Lastly, some authors have attributed this phenomenon to post-entrapment modification of fluid inclusions (Klemm et al., 2004; Klemm et al., 2008).

At the Questa Climax-type porphyry molybdenum system, the Goat Hill orebody consists of a magmatic-hydrothermal breccia (MHBX) and cross-cutting quartz-molybdenite stockwork veinlets. The Goat Hill MHBX is composed of five distinct stratified facies (A-E), which are defined by matrix mineralogy, and clast alteration and textures. Higher temperature mineralogic and alteration assemblages occur at the base of the breccia and closest to the source intrusion (facies A), and lower temperature mineralogic and alteration assemblages occur at the upper and distal edges of the MHBX (facies D and E). The facies closest to the source intrusion (A) contains recognizable magmatic textures, in addition to higher temperature assemblages (Ross, 2002; Ross et al., 2002).

The purpose of this study was to perform a spatially and temporally constrained fluid inclusion microthermometric analysis of the Questa Goat Hill orebody to determine the genetic origin of the MHBX and veinlet ore fluids, the mechanism for molybdenite mineralization, and if there was a fluid evolution for the Goat Hill MHBX that coincided with the mineralogic/alteration zonation of the MHBX facies. The spatial and temporal constraint of this study proves significant, in that previous studies did not constrain samples in terms of space and time (Bloom, 1981; Cline and Bodnar, 1994; Cline and Vanko, 1995; Klemm et al., 2004; Klemm et al., 2008). In addition, this study focuses on the origin of the much debated high salinity fluid inclusions, where the temperature of halite dissolution is much greater than the temperature of liquid-vapor homogenization.

BACKGROUND

Climax-type vs. Quartz Monzonite Type Porphyry-Mo Deposits

Porphyry molybdenum deposits are the a significant source of the world's molybdenum. These deposits are genetically related to porphyritic intrusions ranging from quartz-monzonite to granite in composition. Based upon the composition of the source intrusion and their fluorine content, porphyry molybdenum deposits are divided into two subclasses, the low-fluorine quartz monzonite-type (which has a quartz-monzonite source intrusion) and the high-fluorine Climax-type (name originating from Climax, CO, a world-class porphyry Mo deposit which has a high-silica, alkali-rich granite source intrusion). In addition to having different source intrusion whole-rock compositions and fluorine content, quartz monzonite-type and Climax-type porphyry-Mo deposits vary in other characteristics as well, such as average deposit grade (0.1-0.2% MoS_2 and 0.3-0.45% MoS_2, respectively), Cu: Mo ratio (1:30 to 1:1 and 1:100 to 1:50, respectively), tectonic setting (subduction zones/orogenic belts and rift zones, respectively), age (most commonly Mesozoic and Tertiary and mainly Mid-Tertiary, respectively), mineralogy, geochemical signature, ore controls, etc. Questa is classified as a Climax-type porphyry Mo deposit (White et al., 1981; Cox and Singer, 1986; Guilbert and Park, 1986; White et al., 1990; Carten et al., 1993; Donahue, 2002).

Location

The Questa Climax-type porphyry molybdenum system (Questa system) is located in north-central New Mexico in the Taos Range of the Sangre de Cristo Mountains (Figure 1). The Questa system is sited on the southern flank of the Tertiary

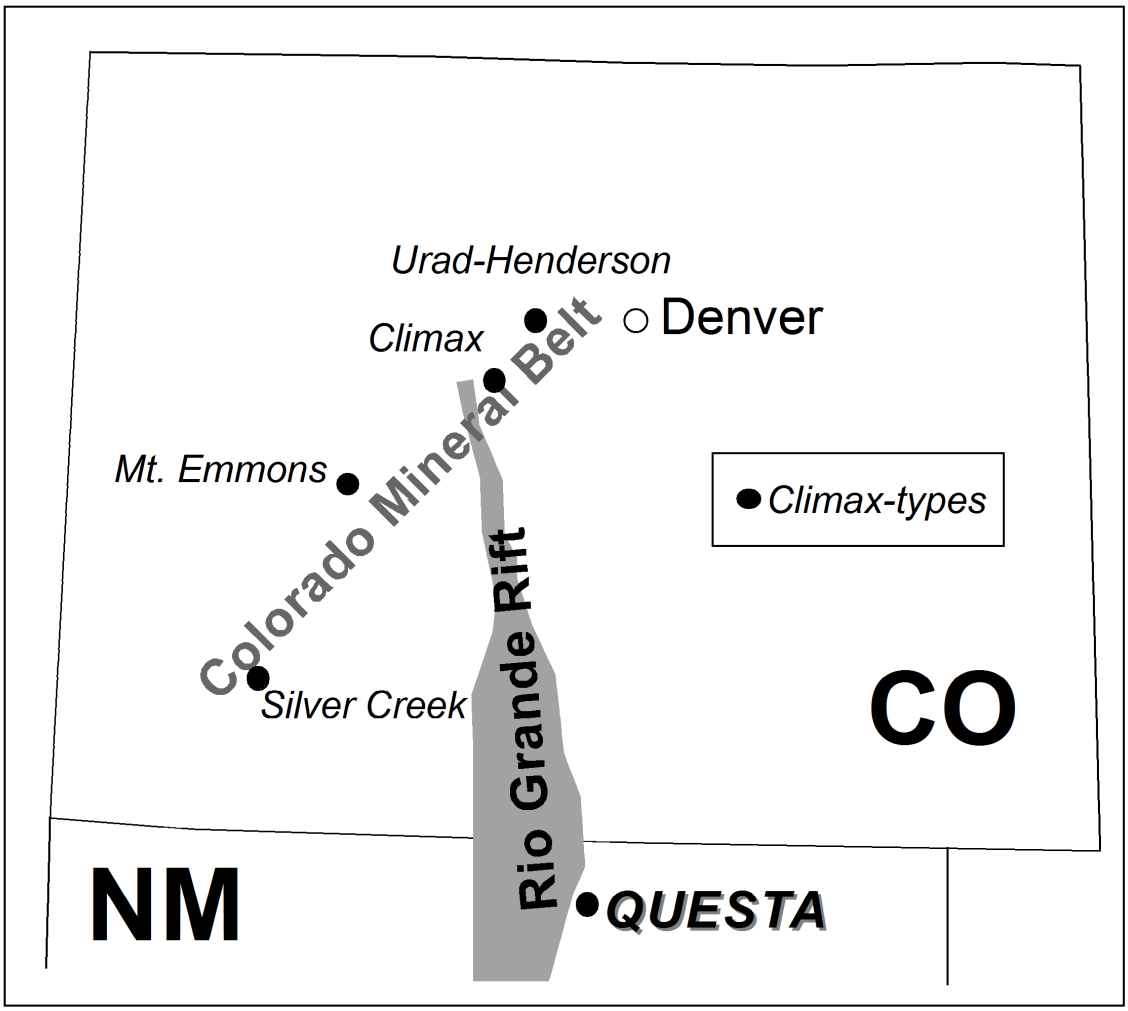

Figure 1. Mine location map showing the relative location of the Climax-type deposits of NM and CO that occur along the Rio Grande Rift. Not to scale.

Questa Caldera in the Latir volcanic field. Mineralization of the Questa system follows a structural trend along the southern flank of the caldera, referred to as the Red River Trench, with a N70^{o}E to N75^{o}E orientation (Figure 2) (Lipman, 1992; Ross, 2002; Ross et al., 2002). Mineralization occurs as three distinct Mo deposits from west to east – the Log Cabin, Central, and Spring Gulch deposits. The Central deposit is the only site of molybdenum mining in the district. It is horseshoe-shaped and consists of two distinct ore zones, the Northeast and Southwest. Several distinct orebodies exist within these ore zones and are defined by a 0.2% MoS_2 grade cutoff (Figure 3) (Ross, 2002; Ross et al., 2002).

Mining History

The Questa and Red River mining districts were mined for gold, silver, copper, and molybdenum since the late 1800s (Carpenter, 1968; Schilling, 1956; Ross, 2002; McLemore and Mullen, 2004). Molybdenum is the only commodity being mined in the Questa and Red River mining districts at the present time (New Mexico Energy, Minerals, and Natural Resources, 2010).

Ferrimolybdite ($Fe_2(MoO_4)_3 \cdot nH_2O$) and molybdenite were discovered along the Sulphur Gulch drainage of the Red River in 1916-1917 (Martineau et al., 1977; Schilling, 1956). Underground lode mining commenced in 1923 on the Old Underground Mine, with a production of 50 tons/day at >4% MoS_2 (Carpenter, 1968; Ross, 2002; Ross et al., 2002). Production ceased due to the exhaustion of veins in the Old Underground Mine by 1958, with a total production of 0.375 million tons (Mt) of ore at >4% MoS_2 (Carpenter, 1968; Schilling, 1956; Ross et al., 2001; Ross, 2002; Ross et al., 2002).

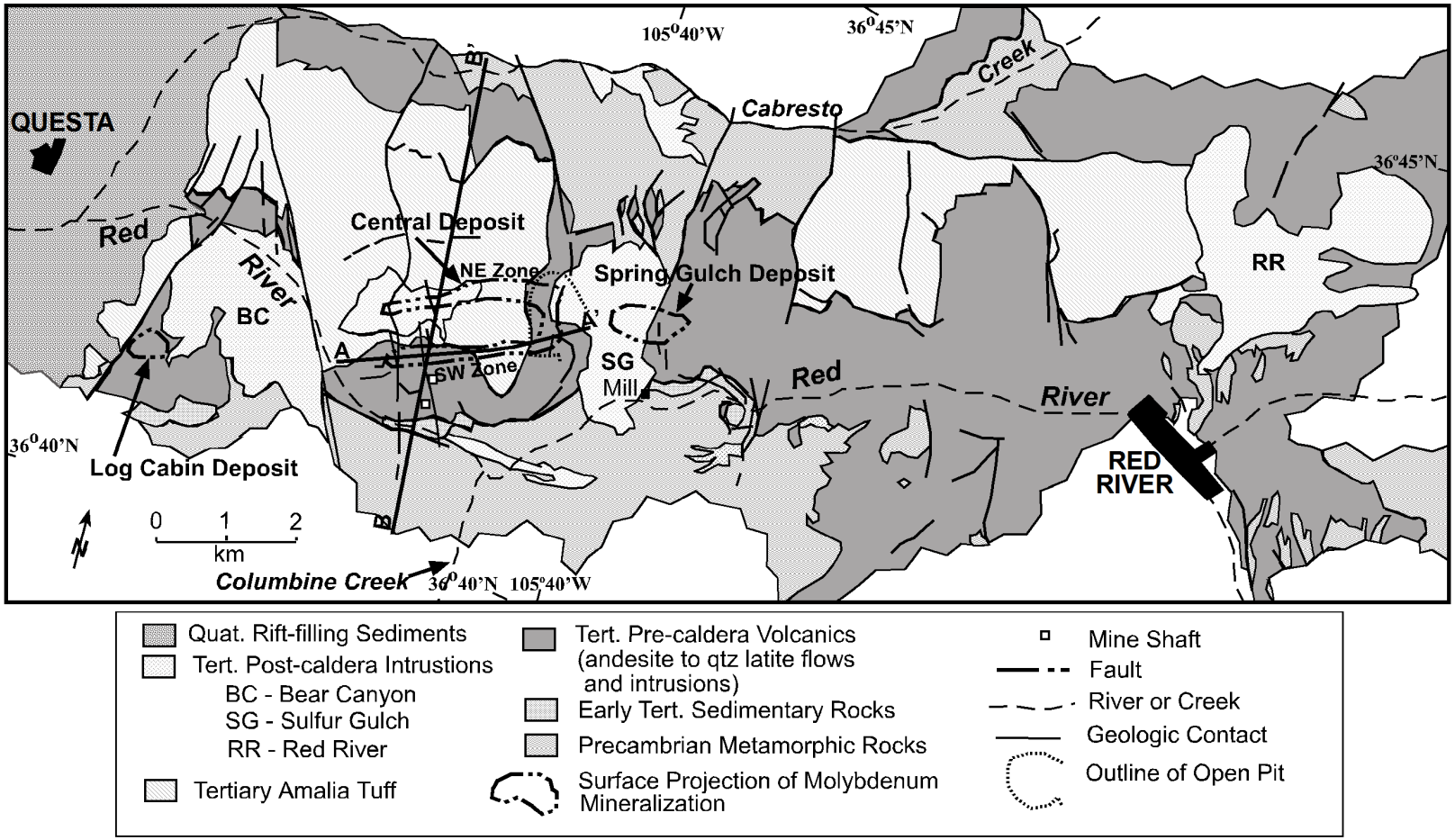

Figure 2. Geologic map of the Questa-Red River area. A-A' and B-B' are cross-section lines for Figure 3. Modified from Meyer and Foland (1991).

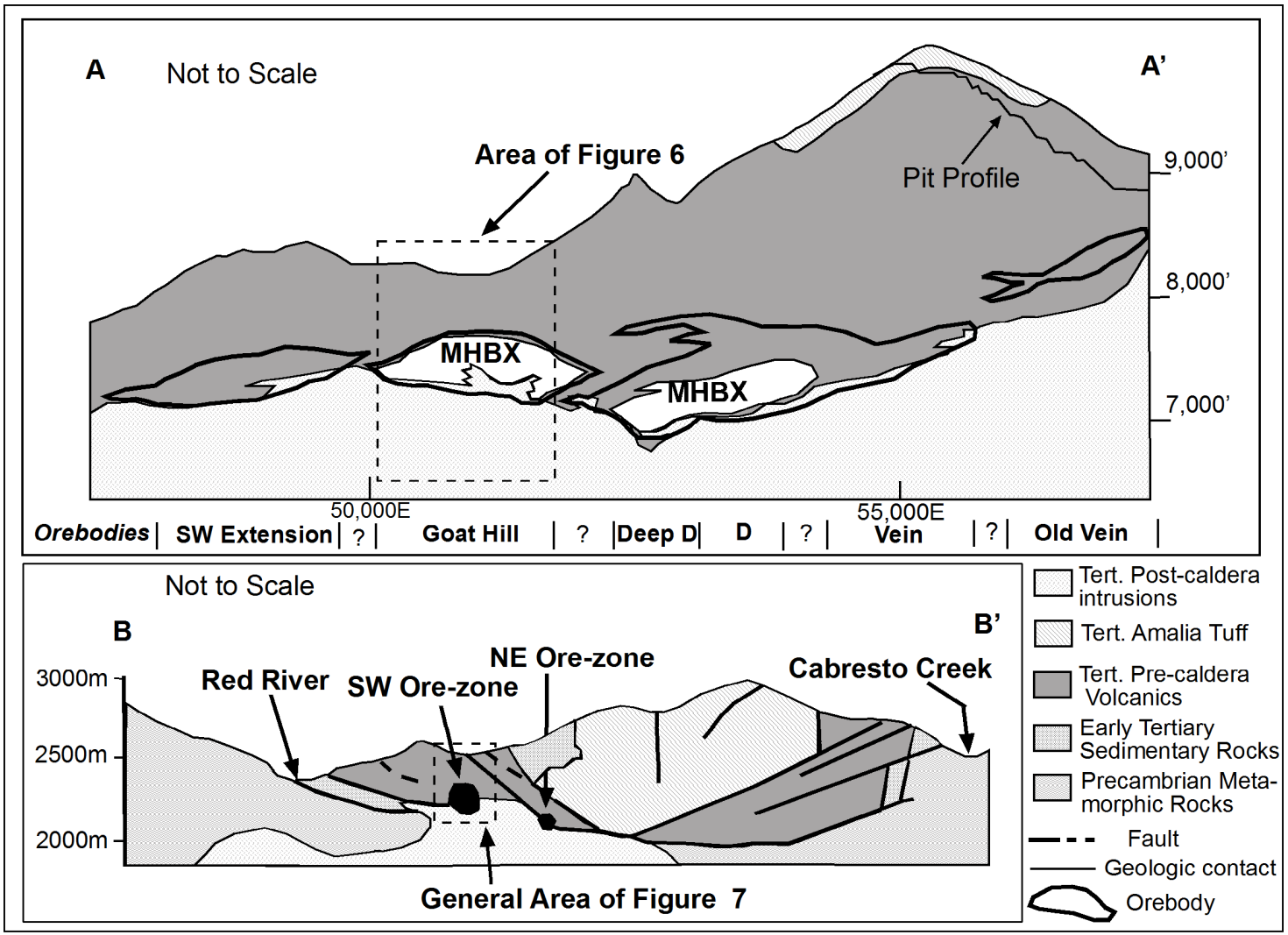

Figure 3. Respective cross-sections A-A' and B-B' from Figure 2. General areas for Figures 6 and 7 in dashed boxes. Modified from Ross et al. (2002) and Walker (1997).

Exploration efforts soared by 1956, which led to the 1957 discovery and delineation of a low-grade, large tonnage molybdenite orebody, mineable by the open-pit method (Carpenter, 1968; Schilling, 1956). Open-pit mining of stockwork veins of the Central deposit commenced in 1965 and ceased in 1982 (Schilling, 1956; Bloom, 1981; Walker, pers. comm., 2004). Between 1965 and 1982, the open pit produced 81 Mt of molybdenum ore at 0.191% MoS_2 (Ross, 2002; Ross et al., 2002; Walker, pers. comm., 2004).

In 1975, exploration efforts led to the discovery and delineation of several, deeper mineable orebodies in the Southwest ore zone and Northeast ore zone (Schilling, 1956; Martineau et al., 1977; Bloom 1981). Development of a large underground mine below the Goat Hill Gulch in the Southwest ore zone was initiated, leading to the commencement of underground mining of the Goat Hill orebody by the blockcaving method in 1983. Mining ceased in 1986 due to a dip in the market prices for molybdenum, but by 1989, production recommenced in the underground mine. Mining of a magmatic-hydrothermal breccia (MHBX), and cross-cutting stockwork veinlets, of the Goat Hill orebody ceased in 2000 with a total production of 21.11 Mt of ore at 0.318% MoS_2. The Goat Hill orebody has not been exhausted (Ross, 2002; Ross et al., 2002).

Presently, underground mining is in the D-orebody of the Southwest ore zone, which is adjacent to and east of the Goat Hill orebody. Blockcaving mining commenced in 2001 on the D-orebody, producing an average ore grade of 0.338% MoS_2, and consisting of MHBX and crosscutting stockwork veinlets (Ross, 2002; Ross et al., 2002).

Future mining may consist of proven and probable reserves, including the currently mined D-orebody, of 63.54 Mt of ore at 0.338% MoS_2 with a 0.25% MoS_2 cutoff grade (Ross, 2002; Ross et al., 2002).

Geologic History of the Questa Area

Precambrian felsic intrusions and amphibolite grade metamorphic rocks (1750-1610 Ma) comprise the basement complex of the Questa area (Figure 4) (Carpenter, 1968; Smith, 1983; Meyer, 1991; Ross, 2002; Ross et al., 2002). A steeply dipping Precambrian shear zone along the present day Red River valley separates two Precambrian terranes - the Taos terrane metaigneous suite to the south (mafic schists and gneisses, amphibolite, and felsic schist) and the younger metasediments of the Questa terrane to the north (Meyer, 1991; Ross, 2002; Ross et al., 2002). Precambrian quartz-monzonite to granite plutons that intruded the accreted package also occur in the area (Meyer, 1991).

Shallow subduction of the Farallon oceanic plate underneath the North American continental plate during the late Cretaceous-early Eocene prompted uplift in northern New Mexico and southern Colorado forming the Sangre de Cristo Mountains (Meyer, 1991; Kelley et al., 1992). Erosion of the Laramide highlands during the Paleocene and Eocene produced the locally derived sandstones and conglomerates of the Sangre de Cristo formation in the Questa area (Meyer, 1991). The Sangre de Cristo formation only occurs in a few locations in the mine area.

During the mid-Oligocene to early Miocene, subduction of the Farallon plate provided a source for the calc-alkaline intermediate volcanism of the Latir volcanic field (28-26 Ma) (Leonardson et al., 1983; Johnson and Lipman, 1988; Meyer, 1991). The

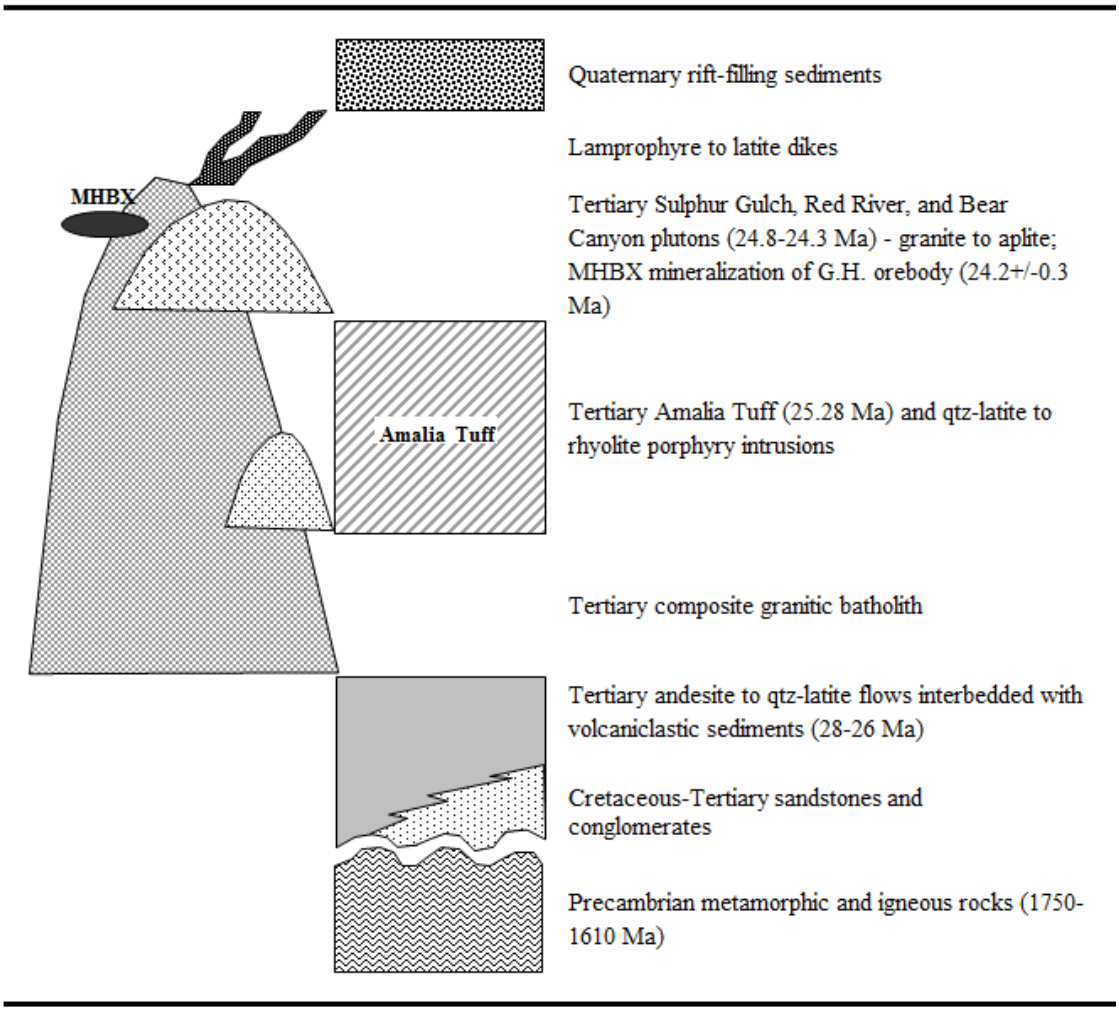

Figure 4. General stratigraphic column of the Questa-Red River area. Thicknesses not to scale. In part modified from Ross, 2002. Thicknesses and dates from Leonardson et al. (1983), Johnson et al. (1989), Czamanske et al. (1990), Meyer (1991), and Zimmerer (2008).

volcanic rocks of the Latir field are andesite to quartz-latite and are interbedded with volcanically derived sedimentary rocks. In the Questa area, the andesite volcanic package (both flows and volcaniclastics) that overlies the Precambrian basement is approximately 1 to 2 km thick (Martineau et al., 1977; Meyer, 1991; Ross, 2002; Ross et al., 2002).

Thermal weakening of the crust by Oligocene volcanism caused the late Oligocene onset of a NE-SW trend of regional crustal extension from the Southern Rocky Mountains to Mexico - the Rio Grande Rift (Leonardson et al., 1983; Meyer, 1991). The onset of peralkaline magmatism (26 Ma) in the Questa area coincided with the initiation of the Rio Grande Rift (32 Ma) (Johnson and Lipman, 1988; Johnson et al., 1990; Meyer, 1991). Extensional rift-related fractures aided in localizing the emplacement of a 20x35 km composite batholith that underlies the entire mining district (Leonardson et al., 1983; Meyer, 1991). Following emplacement of the batholith, eruption of the >500 km^3 high silica rhyolite ashflow Amalia Tuff (25.28 Ma) initiated collapse of the Questa caldera (Leonardson et al., 1983; Johnson and Lipman, 1988; Meyer, 1991; Ross, 2002; Ross et al., 2002; Zimmerer, 2008). Penecontemporaneous with eruption of Amalia Tuff, a genetically related intrusive suite consisting of quartz latite to rhyolite in composition intruded the margins and floor of the caldera (Meyer and Foland, 1991; Meyer, 1991).

Approximately one million years following the eruption of the Amalia Tuff, three syn-mineralization, high silica granite plutons (24.8-24.3 Ma; Zimmerer, 2008) intruded the southern margin of the Questa caldera – the Bear Canyon, Sulphur Gulch and Red River plutons, respectively from west to east (Leonardson et al., 1983; Czamanske et al., 1990; Ross, 2002; Ross et al., 2002). These plutons are cupolas of the massive batholith

underlying the mining district (Czamanske et al., 1990). The intrusions consist of distinct granitic to aplitic phases (Czamanske et al., 1990). The aplitic phase of the Sulphur Gulch pluton is believed to be the source intrusion for the molybdenum mineralization of the Central deposit (24.2+/-0.3 Ma) (Czamanske et al., 1990; Meyer and Foland, 1991).

Following mineralization, rhyolite porphyry intruded the mine area. In addition, lamprophyre to latite dikes intruded the area, post-dating all rocks, mineralization, and alteration in the area. The western margin of the Questa caldera was normal-faulted into the rift by a rift-front fault (Meyer, 1991). Quaternary rift-filling sediments are the youngest in the area (Meyer and Foland, 1991).

The Goat Hill Orebody

The Goat Hill orebody, located in the Southwest ore zone of the Central deposit at the Questa Mine, occurs between the western-most orebody (Southwest Extension) and the D-orebody of the Southwest ore zone (Figure 3). The Goat Hill orebody is hosted in Tertiary andesite (Tan) and partially in an aplitic source intrusion. Molybdenite mineralization within the Goat Hill orebody occurs within a magmatic-hydrothermal breccia (MHBX) and later quartz-molybdenite (qtz-mo) stockwork veinlets that exceed the confines of the MHBX (Figure 5). MHBX-related molybdenite mineralization contributed approximately 40% of grade (0.2% MoS_2 cutoff) to the orebody, whereas the later stockwork veinlets contributed the remaining 60% of the molybdenite mineralization (Ross, 2002; Ross et al., 2002). The Goat Hill orebody exhibits typical Climax-type porphyry alteration with that is centered on the orebody and evolves above and outward of the source intrusion. The earliest alteration occurs farthest from the source intrusion and is a regional pre-mineralization/pre-brecciation propylitization of the

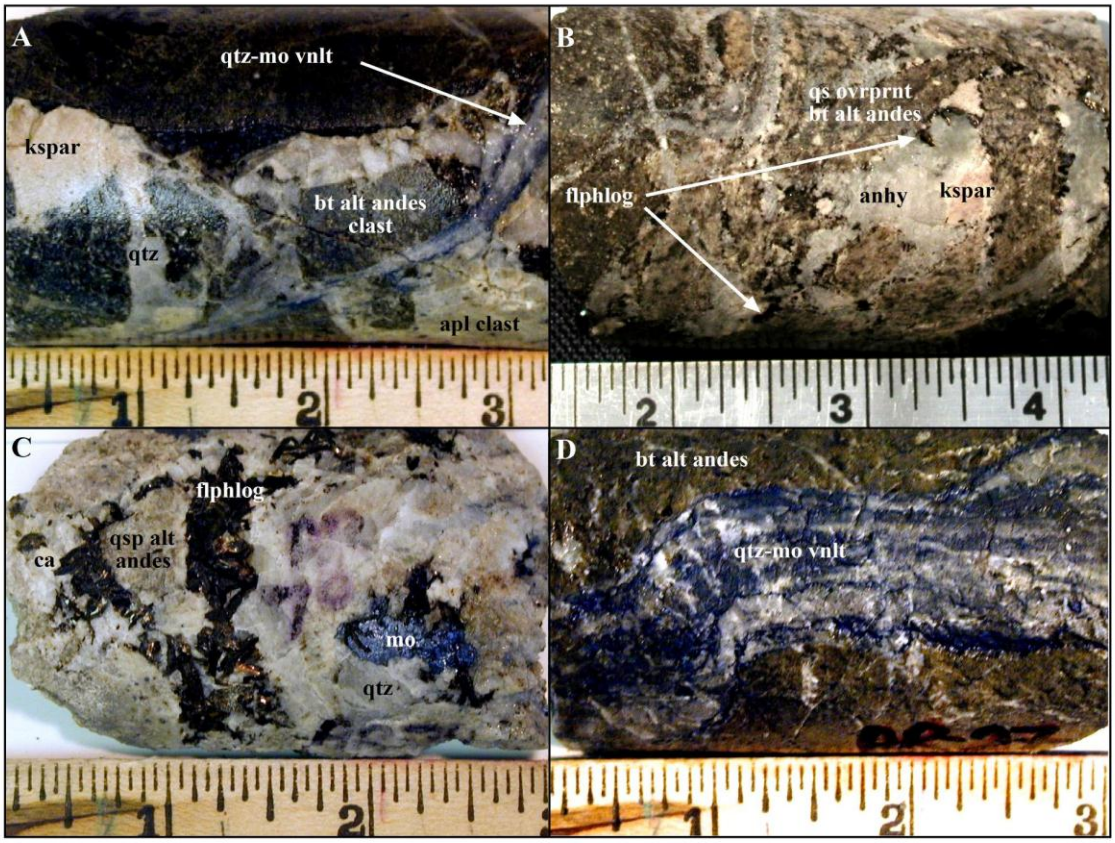

Figure 5. Hand sample photographs showing the two different types of ore and the difference between the MHBX facies. Scale in inches. Note the differences in the two end-members of the MHBX (A and E facies) and the C-facies that is intermediate between the two. (A) MHBX from A3-facies with quartz(qtz)-potassium feldspar(kspar)-trace molybdenite(mo) matrix and aplite and biotite altered andesite clasts. A qtz-mo veinlet crosscuts the MHBX. (B) MHBX from the C-facies with fluorophlogopite(flphlog)-kspar-qtz-mo-trace calcite(ca)-anydrite(anhy) matrix and biotite altered and quartz-sericite-pyrite(qsp) overprinting biotite altered andesite clasts. (C) MHBX from the E-facies with qtz-flphlog-mo-ca matrix and corroded qsp altered andesite clasts. (D) qtz-mo veinlet from unbrecciated andesite from within the orebody but outside of the MHBX.

Tertiary andesite, associated with interaction of the country rock with meteoric water. The first alteration type associated with the intrusion of the source aplite and release of magmatic hydrothermal fluids is a poorly defined high silica zone closest to the source intrusion. Moving outward from the source intrusion in spatial and temporal order are potassic and phyllic alteration. Lastly, local argillic alteration occurred in fracture zones (Leonardson et al., 1983; Meyer, 1991).

The Magmatic-hydrothermal Breccia (MHBX)

The Goat Hill MHBX was formed by hydraulic fracturing of andesite and premineral dikes by ore-bearing fluids that evolved from a crystallizing water-saturated granitic magma which was emplaced at depths of 3 to 5 km (lithostatic pressures of 0.8-1.4 kbars) below surface (Ross, 2002; Ross et al., 2002; Molling, 1989; Cline and Bodnar, 1994). Volumetrically, the breccia body is $>6x10^6$ m^3. It is located above and southward of the apex of an aplitic stock, which is believed to be the source for the mineralizing fluids (Figures 6 and 7). The upper contact of the breccia dips 18° to the north and is thought to follow a pre-breccia fabric, either representing a fracture zone or volcanic bedding, in which the magmatic-hydrothermal fluids were focused (Ross, 2002; Ross et al., 2002).

Ross (2002) defined 5 distinct stratified facies (A-E) within the MHBX based upon matrix mineralogy, clast alteration, and breccia textures (Table 1; Figure 5). Facies A occurs at the bottom of the MHBX, adjacent to the source aplite intrusion, and is divided into 3 subfacies (A_1, A_2, and A_3). Facies D and E occur at the top of the MHBX, most distal to the source intrusion. The MHBX matrix evolves mineralogically from the bottom of the breccia and closest to the source intrusion to the top and distal edges of the

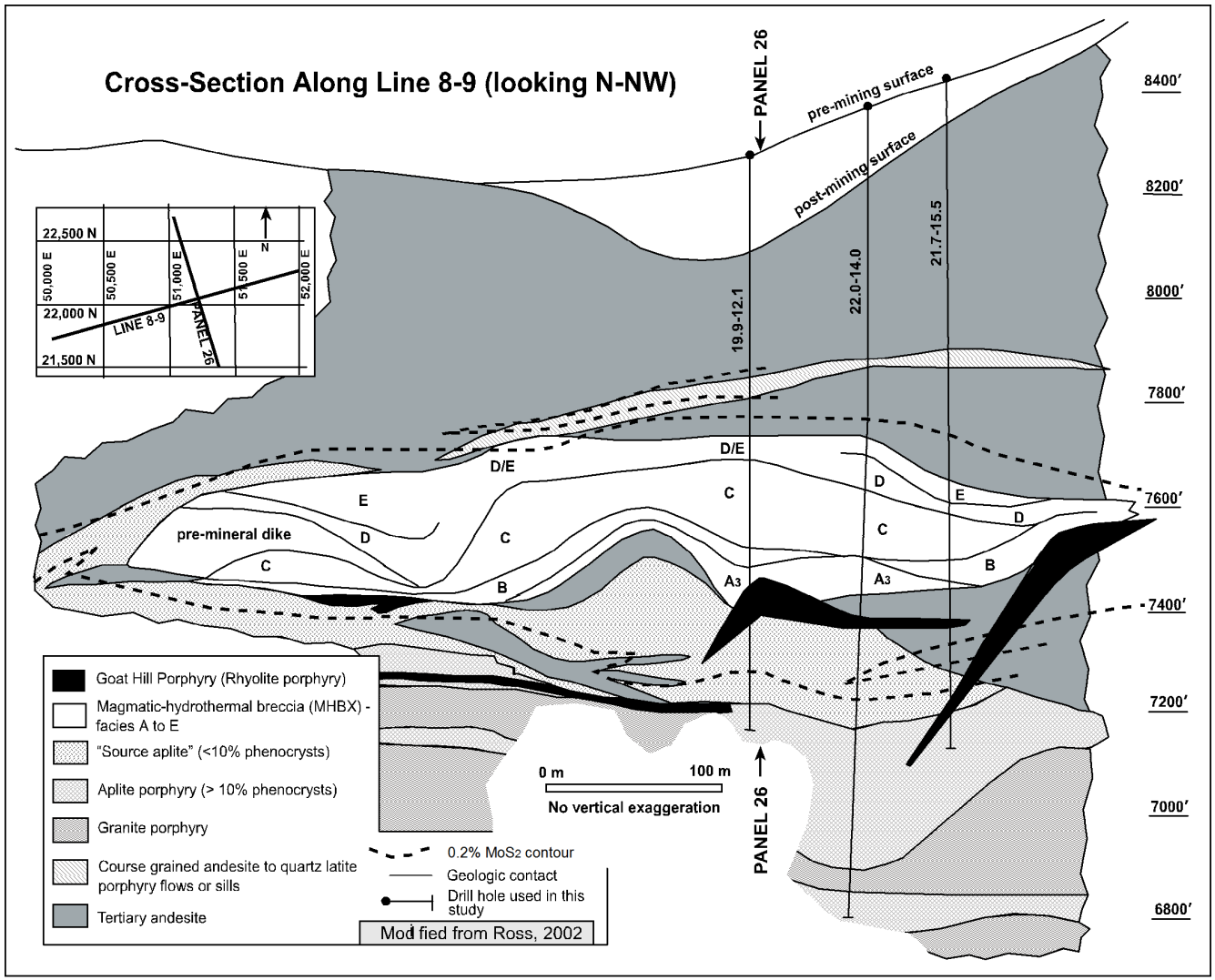

Figure 6. Long-section of the Goat Hill orebody along Line 8-9. Drillholes 19.9-12.1, 22.0-14.0 and 21.7-15.5 used in this study.

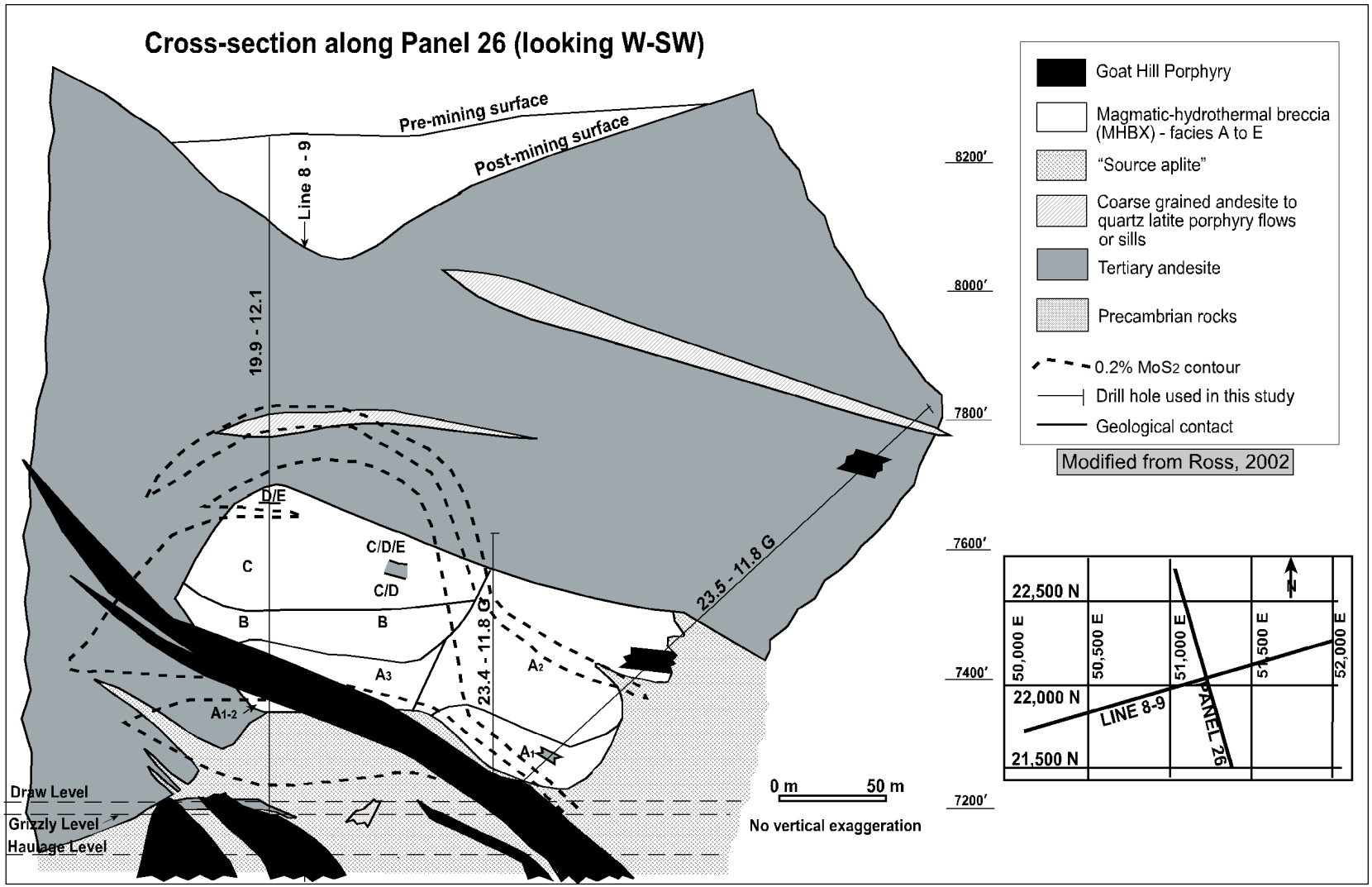

Figure 7. Short-section of the Goat Hill orebody along Panel 26. Drillholes 19.9-12.1, 23.4-22.8G and 23.5-11.8G used in this study.

Table 1. MHBX Classification by Ross et al. (2002).

MATRIX			ANDESITE FRAGMENTS				
Facies	***%***	***Composition***	***Alteration***	***Shape***	***Corrosion***	***Size (cm)***	***Fabric***
E	5 - 30	qtz, flphlog, ca, mo, +/-fl	qsp	rounded to angular	present	0.1 - 10	none
D	?	qtz, flphlog, ca, mo, +/-fl, vugs	qsp ovrprnt bt	rounded to angular	present	0.1 - 10	shingle BX
C	5 - 50	qtz, flphlog, kf, ca, mo, +/-fl	bt, qsp ovrprnt bt	rounded to angular	present	0.1 - 10	shingle BX
B	5 - 30	qtz, kf, tr mo	bt	angular	none	<1 - >10	mosaic
A_3	5 - 40	qtz-kf, tr mo, minor aplite	bt	angular	none	<1 - >10	mosaic
A_2	10 - 95	qtz-kf+/-mo>aplite	bt core, kfp margin	angular	none	2 - 20	mosaic
A_1	50 - 95	aplite, minor qtz+/-kf +/-mo	bt core, kfp margin	irregular to angular	none	3 - 30	inclusion BX

Abbreviations: BX = breccia, bt = biotite, ca = calcite, fl = fluorite, flphlog = fluorophlogpite, kf = K-feldspar, mo = molybdenite, qtz = quartz, ovrprnt = overprinting, qsp = quartz-sericite-pyrite, tr = trace

breccia. The major matrix constituents of the MHBX consist of aplite, quartz, potassium feldspar and trace molybdenite in the A facies; quartz, potassium feldspar and trace molybdenite in the B facies; quartz, potassium feldspar, fluorophlogopite, calcite, molybdenite and fluorite in the C facies; quartz, fluorophlogopite, calcite, molybdenite and fluorite D and E facies. The MHBX clast alteration also evolves from the base of the breccia to the upper and distal edges. The major alteration types in the MHBX consist of biotite and potassium feldspar alteration in the A facies; biotite alteration in the B facies; biotite alteration and quartz-sericite-pyrite (QSP) alteration in the C facies; QSP alteration overprinting biotite alteration in the D facies; and QSP alteration in the E facies. It was proposed that the differences in the breccia facies is due to evolution of the magmatic-hydrothermal fluid away from its source, differing intensities of water/rock interaction, and/or differing breccia forming processes (Ross, 2002; Ross et al., 2002).

Previous Fluid Inclusion Studies on Questa

Bloom (1981) performed a fluid inclusion reconnaissance study on samples related to mineralization and associated alteration at Questa, and Hudson Bay Mountain and Endako in British Columbia. The samples collected and analyzed at Questa were from the open pit. Bloom identified five distinct fluid inclusion types at Questa: [liquid(l)>vapor(v)+/-hematite(hm)] type A, [l<v+/-hm+/-halite(hl)] type B, [l>v+hl+/-hm] type C, [l>v+hl+sylvite(sylv)+/-hm+/-molybdenite (mo)+/-unknowns] type D, and [l_{H2O}+l_{CO2}+v_{CO2}] type E. Hypersaline (33.5-51 eq. wt.% NaCl; 10-19% eq. wt. % KCl; 40-70% NaCl+KCl) Type D fluid inclusions are suggested to be associated with early, fluorine-rich biotite-stable potassic alteration. Type D inclusions predominantly exhibited final homogenization (T_h) by halite dissolution with a range of 320°C to

>600°C and a mode at 390°C. Bloom suggests that the bulk of molybdenite mineralization coincided with quartz-sericite-pyrite, or phyllic, alteration and with the moderately saline (30-60 eq. wt.% NaCl) type C fluid inclusions or the low to moderately saline (5-15 eq. wt.% NaCl) type A fluid inclusions. Type C fluid inclusions homogenized by the dissolution of halite (Tshl) or vapor bubble disappearance (vbd) with a range from 300 to >600°C and a mode at 390°C. Type A inclusions homogenized by vapor bubble disappearance and also exhibited a final T_h of 300 to >600°C with a mode at 390°C. Pressures varied during mineralization from lithostatic to hydrostatic load with intermittent overpressures. Hence, a universal pressure correction could not be applied. Local or intermittent boiling was evident, however Bloom (1981) concluded that significant boiling was not probable due to low abundance of co-existing vapor-rich inclusions.

Bloom (1981) suggested that the various fluid inclusion data are evidence for evolution from magmatic to meteoric conditions. The hypersaline type D solution was a precursor to the bulk of mineralization and evolved directly from the granitic source magma. Fluids re-equilibrated with the granitic source intrusion, or the dissolution of halite precipitated by earlier hypersaline type D solutions along the halite trend, are possible origins of saline type C inclusion fluids. Fracturing events causing adiabatic cooling may be a possible mechanism of cooling the hydrothermal solutions from near magmatic temperatures (390°C mode). Further fracturing in the system permitted the influx of meteoric water, a source for the low salinity type A fluid inclusions.

Smith (1983) performed a reconnaissance fluid inclusion study and a study on the solution geochemistry of molybdenum at Questa. Four types of primary fluid inclusions

were observed: two-phase l>v that homogenize by vapor bubble disappearance, two-phase l<v that homogenize by liquid disappearance, three-phase l>v+hl±hm±mo that homogenize by vapor disappearance or dissolution of halite, and multiphase l>v+hl+sylv±hm±mo±anhydrite±opaques(op). A wide range of homogenization temperatures were measured (300-600°C) with three distinct histogram populations of 300-500°C, 520-555°C, and 580-600°C. Salinities demonstrated broad distribution of 5-20 eq. wt.% NaCl and 25-65 eq. wt.% NaCl. Liquid-rich secondary inclusions were observed in almost every sample with a T_h range of 200-370°C.

Smith (1983) found that the hypersaline inclusions containing halite and sylvite only occurred in quartz-biotite veins which predate molybdenite mineralization and therefore represent the earliest fluids. Smith concluded that halite-bearing saline inclusions found in quartz veins associated with potassic and sericitic alteration may represent fluids generated from earlier hypersaline fluids by the exchange of K for Na during potassic alteration. The halite-bearing saline inclusions and the liquid-rich two-phase inclusions are believed to be associated with molybdenite mineralization. Smith could not establish the paragenesis of the vapor-rich inclusions due to their coexistence with all other inclusion types. Co-existence of liquid-rich and vapor-rich fluid inclusions was interpreted to represent boiling. In the case of boiling fluids, Th=Tt (temperature of trapping) and no pressure correction was necessary. The pressure of the boiling fluids was approximately 180 bars for this case. Smith states that local or sporadic boiling is evident, however most inclusions were not trapped at P-T-V conditions that allowed boiling. For the inclusions that represented non-boiling fluids, pressures were calculated to range from less than 100 bars to 500 bars. Temperatures of halite dissolution occurred

within 40°C of vapor bubble disappearance in fluid inclusions which homogenized by halite dissolution. Smith calculated a pressure of approximately 330 bars for these inclusions.

Smith (1983) delineated the following geochemical factors that would favor molybdenite mineralization. Molybdenite is transported in saline, high temperature fluids. A decrease in the temperature of the fluid from 350 ^{o}C-250°C would result in a 98% decrease in molybdenite solubility. A decrease in pressure from 500 bars to 65 bars at 350°C would decrease molybdenite solubility by 60%. An increase in pH and decrease in oxygen fugacity would aid in molybdenite deposition. Dilution of saline hydrothermal fluids by meteoric water would decrease molybdenite solubility. Molybdenite deposition would occur in response to wall-rock interaction with the fluids associated with potassic alteration, i.e. the formation of fluorine-rich micas, or the alteration of igneous biotite to magnesium-rich hydrothermal biotite.

Cline and Bodnar (1994) performed a fluid inclusion study on samples collected from andesite in the MHBX footwall at the 7120 ft haulage level of the Deep "D"-orebody. Cline and Bodnar chose these samples because they were thought to be representative of system sealing following brecciation and aqueous fluid exsolution that prohibited fluid influx following ore deposition. These samples were also chosen due to the high fluorine content of the MHBX matrix phlogopite, which is interpreted by Cline and Bodnar to be an indicator that no alteration by post magmatic, fluorine-poor fluids has occurred. Cline and Bodnar only analyzed inclusions in the quartz-biotite-molybdenite matrix zone with silica- and potassium feldspar-flooded clasts (Ross et al., 2002 - C, D or E zones), which excludes other zones of the MHBX. In addition,

predominantly only large inclusions in clear quartz adjacent to the fluorophlogopite were analyzed.

Three fluid inclusion types representing three distinct fluids were identified in this study at Questa: liquid-rich low salinity type I inclusions that homogenize by vapor bubble disappearance, vapor-rich type II that homogenize to liquid, vapor, or by critical behavior, and high salinity liquid-rich type III fluid inclusions in which approximately 80% homogenize by halite dissolution and the remainder homogenize by vapor bubble disappearance. Type I fluid inclusions exhibited a final T_h range of 150-370°C and a salinity range of 0-12 eq. wt.% NaCl. Near critical type II fluid inclusions exhibited a wide range of homogenization temperatures and salinities of 360-500°C and 2-26 eq. wt.% NaCl, respectively. Saline type III fluid inclusions homogenized between 200° and 500°C with a mode at 360° to 400°C. Type III salinities varied from 31 to 57 eq. wt. % NaCl.

Based upon phase equilibria constraints (inclusions that homogenize by halite dissolution are required to have been trapped in the liquid-stable, vapor-absent field) and lack of low-density inclusions co-existing with liquid-rich brine inclusions, Cline and Bodnar concluded that these fluids were not boiling and the different fluid inclusion types were not formed by aqueous fluid immiscibility. Instead, Cline and Bodnar suggest that the fluids originated by exsolution directly from the crystallizing silicic melt and different pressure regimes yielded the three different fluid types with their respective homogenization temperatures and salinities. The system consisted of an increasing pressure regime with MHBX formation which yielded the moderate salinity fluids and moderate pressures, system sealing causing a high pressure setting and high salinity

inclusions, overpressures yielding high salinity inclusions where Tlv<<Tshl, and a low pressure post-brecciation setting which yielded the low salinity fluids and/or the low salinity. Lower temperature fluids may have exsolved directly from the silicic melt prior to MHBX formation. Based upon all of these criteria, Cline and Bodnar suggest that the system at Questa was purely magmatic, with no meteoric input.

Klemm et al. (2004) and Klemm et al. (2008) performed a preliminary fluid inclusion study on "deep" and "upper" MHBX and stockwork veinlets from one drillhole in the Goat Hill orebody and also from the D-orebody stockpile. Klemm et al. (2008) observed only very small liquid-vapor fluid inclusions in the "deep" portion of the Goat Hill MHBX and no thermometric data was reported for these inclusions. Observed fluid inclusions were divided into 3 groups: i) l=v, variable CO_2, low to moderate salinity, opaque daughters present; ii) high salinity brine with several daughters (both opaques and other translucent daughters); and iii) vapor-rich inclusions (Klemm et al. 2004 and 2008). Klemm et al. (2004) identified two distinct brine fluids: an early brine with a salinity of 38-46 eq. wt.% NaCl and Th>450°C, and a late brine with a salinity of 32-40 eq. wt.% NaCl with a Th range of 270-350°C. The early brine co-exists with the vapor-rich fluid inclusions, evidence of boiling. Klemm et al. (2004) analyzed individual fluid inclusions with an LA-ICPMS for Mo. The early brines contained up to 1000 ppm of Mo (Klemm et al., 2004). Mo was below detection limits in the late brines. Early single-phase low salinity inclusions (group i) were concluded to represent fluid that exsolved directly from the crystallizing magma. In addition, it was concluded that Mo precipitated from the brine by temperature decrease, since Mo concentrations decrease dramatically by over an order of magnitude with decreasing T_h (Klemm et al., 2004; Klemm et al., 2008).

METHODS

Two matrix and two veinlet samples from each of the MHBX facies (A_1, A_2, A_3, B-E), were collected from among 5 different drillholes (19.9-12.1, 21.7-15.5, 22.0-14.0, 23.4-11.8G, 23.5-11.8G) in the eastern portion of the Goat Hill MHBX for petrographic and fluid inclusion microthermometric analysis (Figure 6 and Figure 7). The presence of quartz was the primary criteria for sample selection. Quartz was the main mineral of interest due to its abundance in the orebody, known association/cogenesis with molybdenite, general transparency, abundant preservation of fluid inclusions in all the facies in quartz, and low susceptibility to leakage and necking-down of the fluid inclusions. Two fluorite samples were collected from facies C and D for petrographic and fluid inclusion analysis as well. In addition, three background samples from the source intrusion (one qtz-mo veinlet [SAV] and two barren magmatic-hydrothermal quartz [SABQ]) were collected for petrographic and fluid inclusion analysis.

Petrographic Analysis

Prior to fluid inclusion analysis, a detailed petrographic analysis was performed on each of the samples for mineralogy, alteration, and paragenetic relationships. The petrographic thin sections were analyzed under both reflected and transmitted light with a petrographic microscope.

Fluid Inclusion Microthermometry Analysis

After analyzing the samples petrographically, fluid inclusion microthermometry analyses were performed on a mirror slice thick section of the corresponding petrographic section. The fluid inclusion samples were also analyzed petrographically for fluid

inclusion paragenetic relationships, distribution, content or phases present, size and shape prior to microthermometric measurements.

Microthermometric measurements were made using a Linkam THMS-600 heating/freezing stage that was mounted on a petrographic microscope and associated automatic temperature controller. The calibration of the heating/freezing stage was checked in the beginning of each session on the fluid inclusion stage utilizing a pure water standard. In addition, each week the instrument calibration was checked using a pure water standard (mid temperature, Tm_{ice}= 0°C), CO_2-water standard (low temperature, Tm_{CO2} =-56.6^{o}C), and potassium chromate standard (high temperature, Ts_{K2CrO4} = 398°C). The analytical error of the instrument is +/-0.1^{o}C for temperatures at or below 25°C and +/-2.0^{o}C for temperatures around 400°C.

Microthermometric measurements were performed on 434 fluid inclusions (FIs) (194 FIs from veinlets, 239 FIs from matrix). Due to the possibility of stretching of the fluid inclusions during the heating process, freezing measurements were taken first. Freezing measurements were performed on fluid inclusions that did not contain a halite or sylvite daughter mineral, and any inclusion suspected or known to contain a CO_2 phase. Inclusions were cooled rapidly to -110°C and warmed at a 20-0.1^{o}C/min ramp speed, depending on the proximity to the target temperatures. The slowest ramp speed was used when approaching the target temperature. After freezing measurements were obtained, the fluid inclusions were heated until the final phase change (final Th) or decrepitation occurred. The inclusions were heated at a ramp speed of 2-0.5^{o}C/min. Salinity was calculated from either the temperature of final ice melting (Tm_{ice}) or the

temperature of halite dissolution (Tshl) utilizing the MacFlinCor computer program of Brown and Hagemann (1994).

RESULTS

Petrography

MHBX

The MHBX clast alteration and matrix were found to evolve from the base of the breccia (A-facies) to the upper and distal edges (E-facies) as similarly noted by Ross et al. (2002) with a few minor differences noted below in matrix composition (Table 2). Trace biotite is found in the B-facies matrix. Anhydrite is a major matrix constituent in facies C, D, and E and occurs late paragenetically (Figure 8). Trace matrix potassium feldspar occurs in facies D and E. Gypsum noted as a matrix constituent in facies C and D could be a primary matrix constituent or a result of post-mineralization alteration of anhydrite. Both of these cases have been observed. Pyrite was noted as a minor late matrix constituent in facies C, D, and E. Minor late hypogene kaolinite occurs as a vug filling in facies C, D, and E. Microscopic fluorite is almost always associated with molybdenite. Other matrix minerals that were observed in thin section are rutile, sericite (as an alteration product of potassium feldspar and fluorophlogopite), topaz and apatite.

Veins

The major constituents of the later stockwork veinets are quartz, molybdenite, pyrite and calcite (Figure 9). The veinlets are often composite in nature. Microscopic fluorite is almost always associated with vein molybdenite as well. Other vein minerals

	Matrix Mineralogy								Clast Alteration			
Facies	**aplite**	**kspar**	**qtz**	**mo**	**bt**	**fl**	**ca**	**anhy**	**bt with kspar selvages**	**bt**	**qsp ovrprnt bt**	**qsp**
A	x	x	x	x					x	x		
B		x	x	x	x					x		
C		x	x	x	x	x	x	x		x	x	
D		x	x	x	x	x	x	x			x	
E		x	x	x	x	x	x	x				x

Table 2. Facies distribution of clast alteration and major matrix minerals in the MHBX. Note the systematic change/evolution in mineralogy and alteration from the bottom (A) to the top (E) of the breccia. Table incorporates data of Ross et al. (2002) and this study.

- trace to minor amount

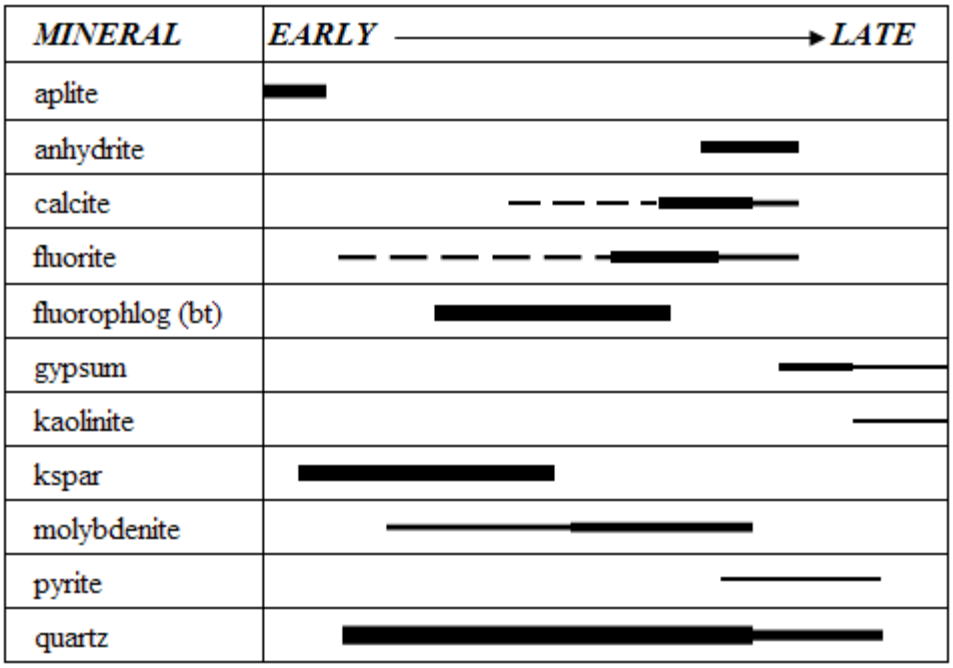

Figure 8. MHBX matrix paragenesis. Thickness of line represents abundance of mineral.

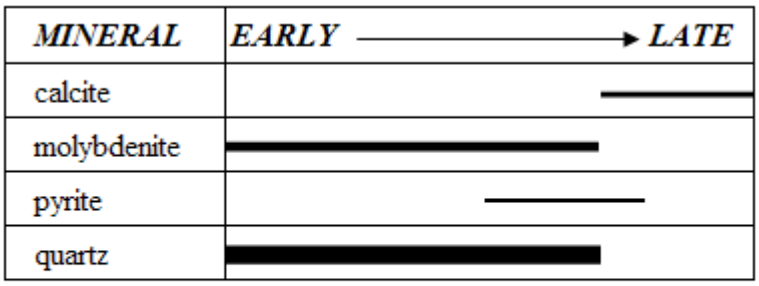

Figure 9. Veinlet paragenesis. Thickness of line represents abundance of mineral.

that were observed in thin section are apatite, fluorophlogopite, potassium feldspar, rutile, sericite, topaz and zircon.

Fluid Inclusions

Paragenesis

Due to the ambiguity of superimposed fluid inclusion populations, classifying individual fluid inclusions as primary, pseudosecondary, or secondary proved to be difficult, leading to an indeterminable paragenetic origin for most inclusions. However, fluid inclusion paragenetic origin was identified whenever possible based upon criteria summarized by Roedder (1979, 1984).

Microthermometric measurements on MHBX primary, pseudosecondary, and inclusions of indeterminate origin revealed a broad range of Tlvs and salinities of 68-520°C and 0-64 eq. wt.% NaCl+KCl+$CaCl_2$, respectively. MHBX secondaries demonstrated a Tlv and salinity range of 88-241°C and 0-6 eq. wt.% NaCl+KCl+$CaCl_2$, respectively.

Microthermometric measurements on veinlet primary, pseudosecondary and inclusions of indeterminate origin also revealed a broad range of Tlvs and salinities of 62-560°C and 0-63 eq. wt.% NaCl+KCl+$CaCl_2$, respectively. Secondary fluid inclusions from the veinlets demonstrated a Tlv and salinity range of 183-277°C and 1-5 eq. wt.% NaCl+KCl+$CaCl_2$, respectively.

Types

Based upon visible phases at room temperature, four major fluid inclusion types (I-IV) were identified at Questa (Figure 10). Type I inclusions contain liquid and vapor, and are divided into three subtypes (a, b, and c) (Table 3). Type Ia fluid inclusions are

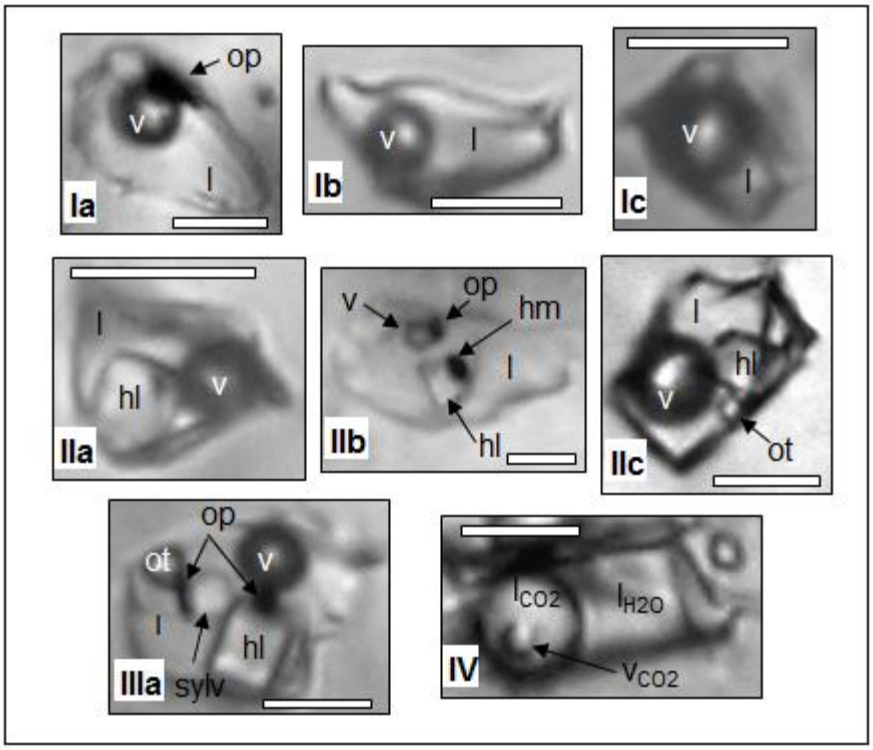

Figure 10. Microphotographs of fluid inclusion types. A) Type Ia B) Type Ib C) Type Ic D) Type IIa E) Type IIb F) Type IIc G) Type IIIa H) Type IV. White bar is approximately 5 μm. No pictures are available for types IId and IIIb.

Table 3. Fluid inclusion types and their microthermometric data.

FI Type	# of FIs	Phases	Tlv Range in °C	Salinity Range in eq. wt.% $NaCl+KCl+CaCl_2$	Mode of Final Th	Occurrence
Ia	31	l+v+s; l>v; s=hm,op, ot	88-520	0-25	vbd	All MHBX facies, qtz-mo vnlts, SAV
Ib	114	l+v; l>v	105-540	0-25	vbd	All MHBX facies, SABQ, qtz-mo vnlts, SAV
Ic	87	l+v±s; v≥l; s=op, hm, ot	240-560	0-25	ld or cb	All MHBX facies, SABQ, qtz-mo vnlts, SAV
IIa	41	l+v+s; l>v; s=hl	145-520	30-59	hd or vbd	A1, A2, A3, C, D, E, SABQ, qtz-mo vnlts, SAV
IIb	76	l+v+s; l>v; s=hl±op±hm	62-480	24-64	hd or vbd	All MHBX facies, qtz-mo vnlts, SAV
IIc	67	l+v+s; l>v; s=hl+ots±hm±op	68-560	32-64	hd, vbd, or otd	All MHBX facies, qtz-mo vnlts, SAV
IId*	min.	l+v+s; v>>l; s=hl±hm±op±ot	-------	-------	-------	A1, A2, C, D
IIIa	14	l+v+s; l>v; s=hl+sylv±hm±op±ot	178-325	39-63	hd or otd	A2, A3, B, C, D
IIIb*	min.	l+v+s; v>>l; s=hl+sylv±hm±op±ot	-------	-------	-------	A2 and C
IV	4	$l_{H2O}+l_{CO2}+v_{CO2}$; $l_{H2O}>l_{CO2}+v_{CO2}$	130-260	0-9	l_{H2O}	A2, B, C

l=liquid v=vapor s=solid hm=hematite op=opaque(s) hl=halite ot=other translucent daughter(s) sylv=sylvite vbd=vapor bubble disappearance hd=halite dissolution ld=liquid disappearance cb=critical behavior otd=other translucent daughter dissolution SABQ=source aplite barren qtz SAV=source aplite veinlet min.=minimal # observed

* IId and IIIb were observed in some samples, but were not used in this study due to the difficulty in observing phase changes with this type of inclusion.

liquid-rich and contain either opaque (op) and/or hematite (hm) and/or unknown other translucent (ot) daughter minerals (Figure 10). The opaque daughter minerals may be molybdenite, fluorophlogopite or rutile. Pyrite was identified as an opaque daughter mineral species as well. The unknown ot daughter minerals could be anhydrite, nahcolite, fluorite, or calcite. Type Ib inclusions, the most abundant of the fluid inclusion types, are liquid-rich with no daughter minerals present. Type Ic inclusions are vapor-rich and may contain one or more op, ot, or hm daughter minerals. Type II fluid inclusions contain liquid, vapor and halite, and are subdivided into four subtypes (a, b, c, and d). Type IIa, IIb, and IIc inclusions are liquid-rich and contain no additional daughters, contain op and/or hm daughters, and contain ot±hm±op daughters, respectively. Type IId are vapor-rich inclusions containing halite and possible op, hm, and ot daughter minerals. Type III fluid inclusions are divided into two subtypes (a and b). Type IIIa and IIIb are liquid-rich and vapor-rich aqueous inclusions, respectively and contain a halite crystal and sylvite±hm±op±ot daughter minerals. Types IId and IIIb were not used in this study due to the difficulty in observing any phase changes with these inclusions and the minimal number of these inclusions observed in the samples. Type IV fluid inclusions, the least abundant of the fluid inclusion types, are carbonic-bearing inclusions that contain liquid water, liquid CO_2, and vapor CO_2 (double bubble). The water phase is greater than the carbonic phases in Type IV inclusions.

Type Ia and Ib inclusions homogenize by vapor bubble disappearance (vbd) with a Tlv range of 88-520°C, and 105-540°C, respectively. Type Ic fluid inclusions homogenize by liquid disappearance (ld) or critical behavior (cb) with a Tlv range of 240-560°C. All type I inclusions demonstrated a salinity range of 0-25 eq. wt.%

$NaCl+KCl+CaCl_2$. Due to the minute amount of liquid that exists in type Ic fluid inclusions, difficulty in observing the final ice melting temperatures (Tm_{ice}) resulted in minimal salinity data for this type inclusion. Five type I inclusions (two Ia and three Ib) from the MHBX exhibited a Tm_{ice} (-24.1 to -21.7^{o}C) that was below the eutectic temperature of -20.8^{o}C for a pure H_2O-NaCl system, suggesting $CaCl_2$ content. The two criteria needed to report the salinity in terms of wt.% NaCl and $CaCl_2$ (melting temperatures of hydrohalite and ice) were only observed in two of the five inclusions, resulting in salinities of 6% NaCl and 19% $CaCl_2$ and 12% NaCl and 13% $CaCl_2$, with a bulk salinity of 25 wt.% $NaCl+CaCl_2$ equivalent for both inclusions. The $NaCl/CaCl_2$ ratios for the two inclusions are both 0.79 (Shepherd et al., 1985).

Type IIa and IIb fluid inclusions homogenized by halite dissolution (hd) or vbd with a Tlv range of 145-520°C and 62-480°C and salinity range of 30-59 and 24-64 eq. wt.% $NaCl+KCl+CaCl_2$, respectively. Type IIc inclusions homogenized by vbd, hd, or other translucent daughter dissolution (otd) with a Tlv range of 68-560°C and a salinity range of 32-64 eq. wt.% $NaCl+KCl+CaCl_2$.

Sylvite-bearing type IIIa fluid inclusions homogenized by halite dissolution or other translucent daughter dissolution with a Tlv range of 178-325°C. The salinity for sylvite-bearing type IIIa inclusions ranged from 21-47% NaCl and 14-21% KCl, with bulk salinities of 39-63 wt.% $NaCl+KCl(+CaCl_2)$ equivalent. The K/Na ratios for type IIIa inclusions range from 0.35-0.82 (Roedder, 1984). Carbonic type IV fluid inclusions homogenized to liquid water with a Tlv and salinity range of 130-260°C and 0-9 eq. wt.% $NaCl+KCl+CaCl_2$, respectively.

All four fluid inclusion types were observed in the MHBX matrix and only types I and II were observed in the qtz-mo veinlets, source aplite veinlets (SAV) and source aplite barren quartz (SABQ). Types Ia, Ib, and Ic were observed in the qtz-mo veinlets and all of the MHBX facies (Table 3). Types Ib and Ic were also observed in the SABQ. The $CaCl_2$-bearing inclusions of types Ia and Ib occurred in facies A_1, A_2, B, and E. Type IIa inclusions were observed in the qtz-mo veinlets, SABQ and all MHBX facies except facies B. Types IIb and IIc occurred in the qtz-mo veinlets, SABQ and all of the MHBX facies. Type IId was noted in facies A_1, A_2, C, and D. This inclusion type may have occurred in other MHBX facies, SABQ or qtz-mo veinlets, but since this type was not to be analyzed, minor attention was applied to this type. Sylvite-bearing Type IIIa occurred in facies A_2, A_3, B, C, and D. Type IIIb was noted in A_2 and C, but similarly to IId, was only given minor attention and may have occurred in other MHBX facies or SABQ as well. Carbonic type IV inclusions occurred in facies A_3, B, and C only.

MHBX Facies and Qtz-Mo Veinlets

The MHBX matrix (qtz and fl) exhibited a wide Tlv range of 81-520°C, with the largest mode at 380°C, the second largest mode at 180°C, the smallest mode at 460°C, and the second smallest mode at 280°C (Figure 11). The MHBX matrix (qtz and fl) exhibited a salinity range of 0-64 eq. wt.% NaCl+KCl+$CaCl_2$ (Figure 12). Similarly, the qtz-mo veinlets exhibited a wide Tlv range of 62-560°C, with the largest mode at 380°C, the second largest mode at 200°C, and the smallest mode at 280°C (Figures 11 and 12; Table 4). The qtz-mo veinlets exhibited a salinity range of 0-63 eq. wt.% NaCl+KCl+$CaCl_2$ (Figure 12).

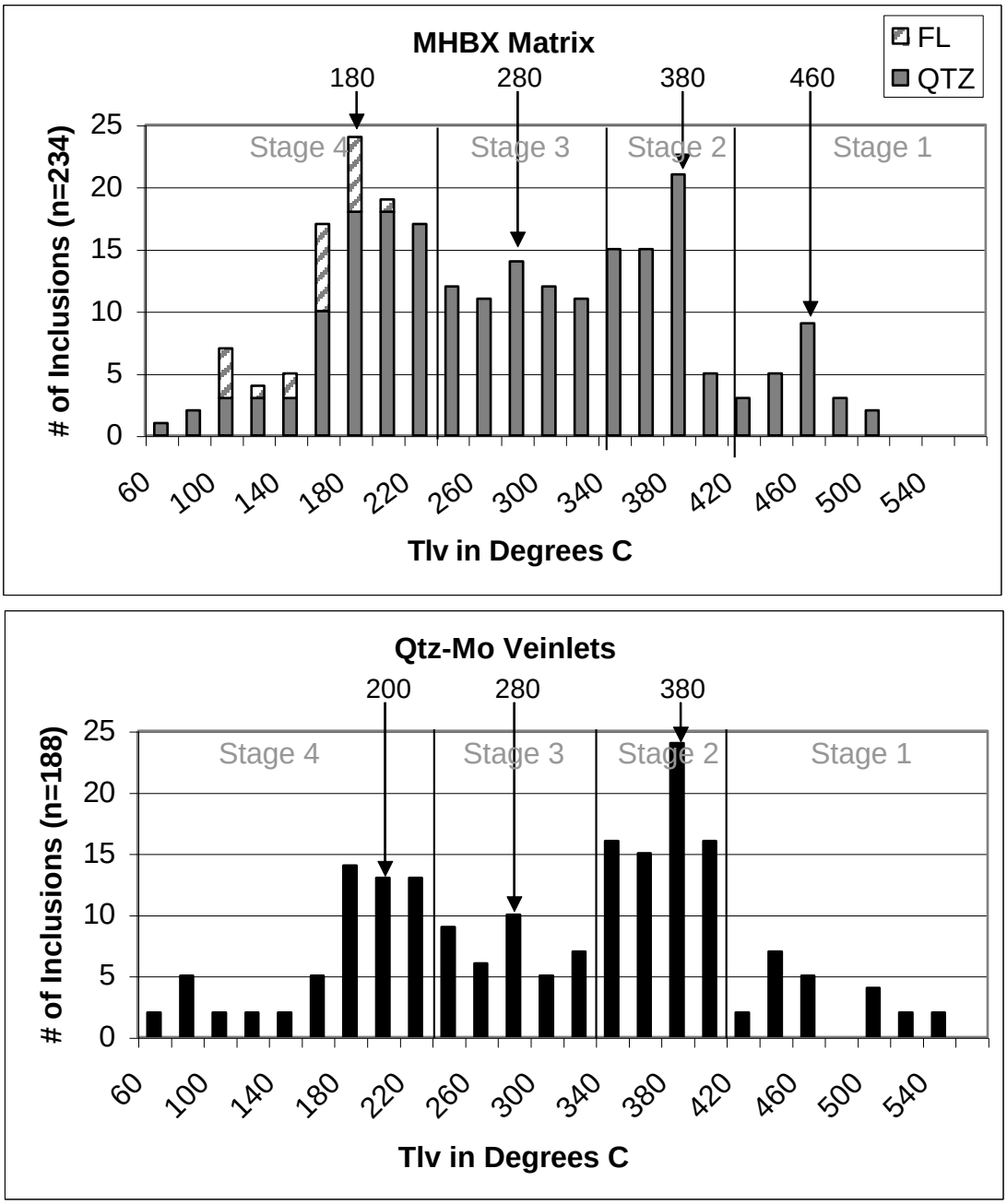

Figure 11. Tlv histograms comparing MHBX matrix and qtz-mo veinlet data. Arrows point to the modes in each suite. Temperature ranges for Stages 1-4 and respective modes are indicated.

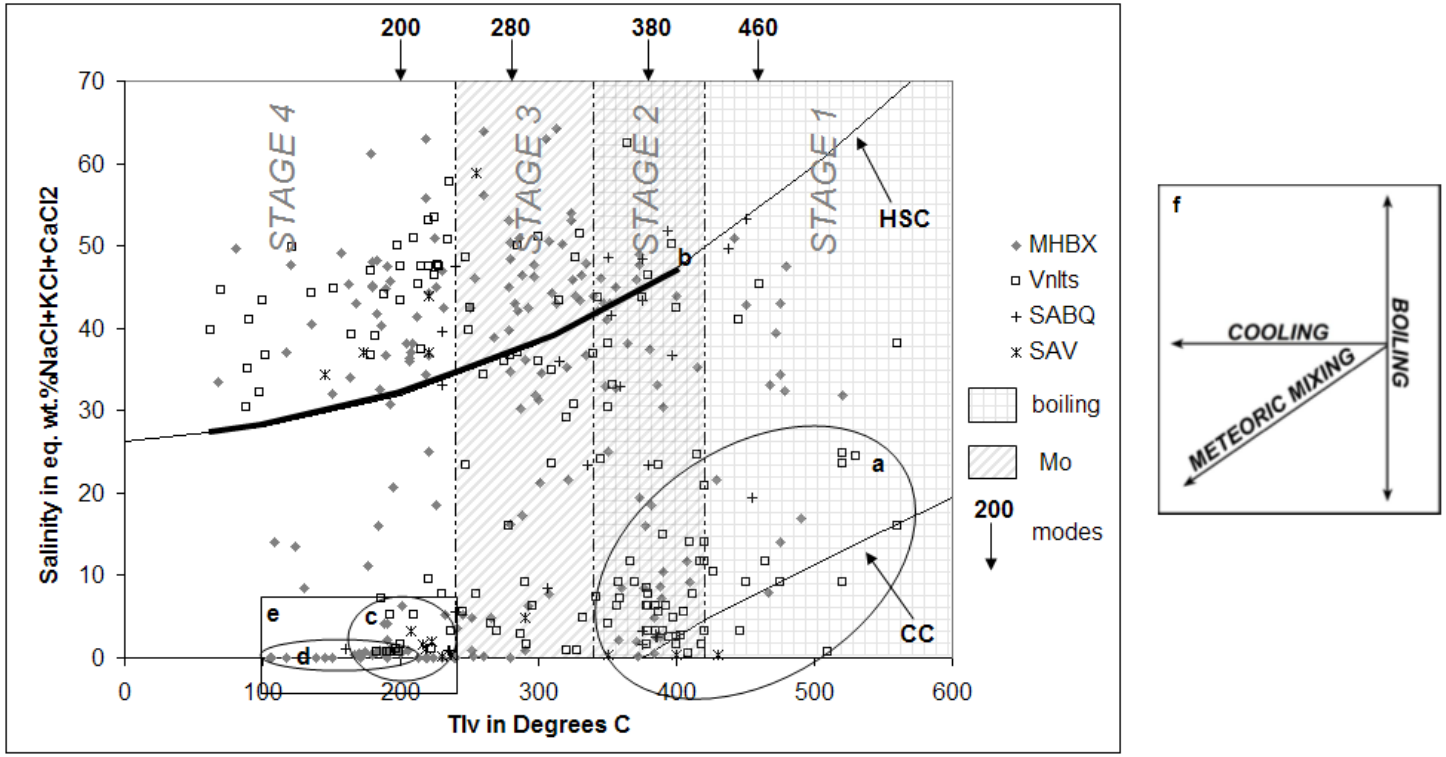

Figure 12. Tlv versus salinity diagram for MHBX matrix, qtz-mo veinlets and background samples Source Aplite Barren Quartz (SABQ) and Source Aplite Veinlet (SAV). Inclusions above the halite saturation curve (HSC) homogenized (final Th) by halite dissolution. The critical curve (CC) shows the minimum temperature at which a fluid of given salinity can separate into two phases, for unsaturated H_2O-NaCl solutions. Inclusions on or near this curve represent critical or near-critical fluids (Bodnar, 2003 and Roedder, 1984). Temperature ranges for Stages 1-4, with modes are indicated here. Temperature ranges for boiling and for molybdenite mineralization are also indicated. a) T-X range containing all vapor, critical, and near critical inclusions. b) Temperature where fluid became oversaturated with respect to halite (FIs above the HSC) due to simple cooling and/or boiling down. To the left of this point and above the HSC is where halite crystals are floating in the fluid and become captured in inclusions. Hence, the fluid inclusions above the HSC do not represent a real fluid and can be brought down to HSC at the same temperature (as represented by the dark line on the HSC) in order to represent the real fluid from with these inclusions originated. c) T-X range containing known secondaries and carbonic inclusions, representative of meteoric influx. d) T-X range for FIs in fluorite, also representative of meteoric influx onto the system. e) c and d are representative of stage 4b as described in text. f) Fluid evolution paths and associated mechanisms.

Table 4. MHBX and qtz-mo veinlet microthermometry data.

Phase	Facies*	Tlv in °C	Salinity**
MHBX	A1	109-475	0-51
	A2	88-472	0-52
	A3	81-520	0-53
	B	188-429	2-64
	C	130-372	0-63
	C fl	139-211	0-1
	D	68-468	0-51
	D fl	105-180	0
	E	117-490	0-61
Veinlets	All	62-560	0-63

* All data is for quartz, except C fl and D fl are fluorite.

** Salinity is in eq. wt.% $NaCl+KCl+CaCl_2$.

The A facies exhibited a wide range of Tlvs of 109-475°C, 88-472°C, and 81-520°C for A_1, A_2, and A_3, respectively (Figure 13 and Table 4). Facies A exhibited a salinity range of 0-51, 0-52, and 0-53 eq. wt.% NaCl+KCl+$CaCl_2$ for A_1, A_2, and A_3, respectively. The B facies exhibited a tighter Tlv range of 188-429°C and a salinity range of 2-64 eq. wt. % NaCl+KCl+$CaCl_2$. Facies C also exhibited a tighter Tlv range of 130-372°C and a salinity range of 0-63 eq. wt.% NaCl+KCl+$CaCl_2$. Facies D and E exhibited Tlv ranges of 68-468°C and 117-490°C and salinity ranges of 0-51 and 0-61 eq. wt.% NaCl+KCl+$CaCl_2$, respectively. The C and D facies fluorite exhibited Tlv ranges of 139-211 and 105-180°C, and a salinity of 0-1 and 0 eq. wt.% NaCl+KCl+$CaCl_2$, respectively.

DATA ANALYSIS AND INTERPRETATION

Heterogeneous Trapping - Captured Halite

The majority of the fluid inclusions that contained halite daughter minerals (types II and III) demonstrated final Th by halite dissolution (Figure 14). There are several instances where the dissolution of halite occurred well above (over 50°C) that of vapor bubble disappearance. According to the phase relations in the NaCl-H_2O system (Roedder, 1984; Bodnar, 2003; Shephard et al., 1985), homogeneous trapping of these fluids would require pressures of 2 kbars and above (Bodnar, 1994; Bodnar & Vityk, 1994; Cline & Bodnar, 1994; Gunter et al., 1983; Bodnar, 2003; Kamilli, 1978; Becker et al., 2008), which are “much greater than any reasonable lithostatic load” (Kamilli, 1978). Such pressures would place the Goat Hill orebody at an unreasonable depth of emplacement of > 7 km depth, an unreasonable depth given other geologic constraints. Based upon stratigraphic reconstruction, Molling (1989) determined that the source

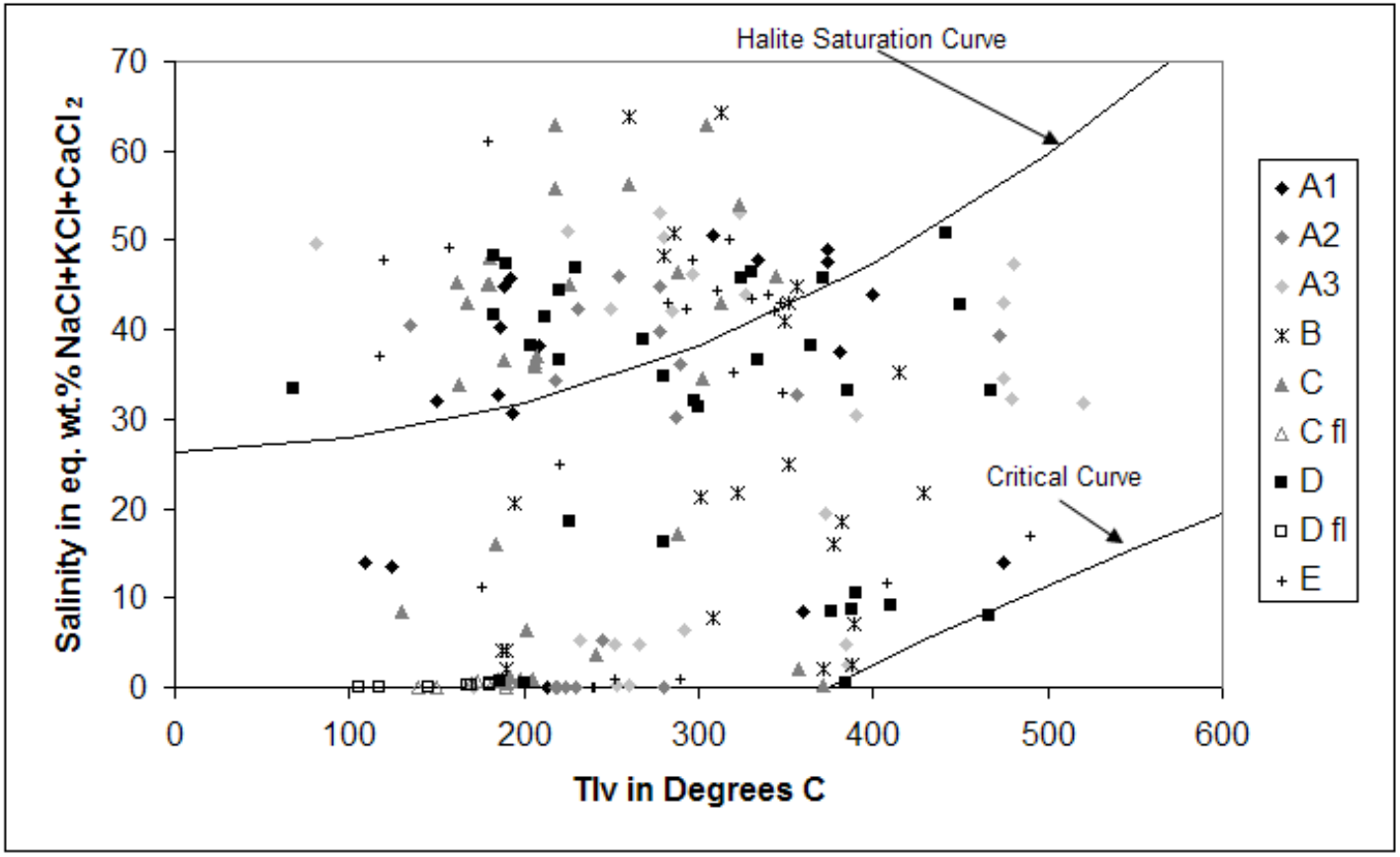

Figure 13. Tlv versus salinity diagram demonstrating MHBX facies distributions. All phases are quartz, except for the noted C and D fluorites (C fl and D fl).

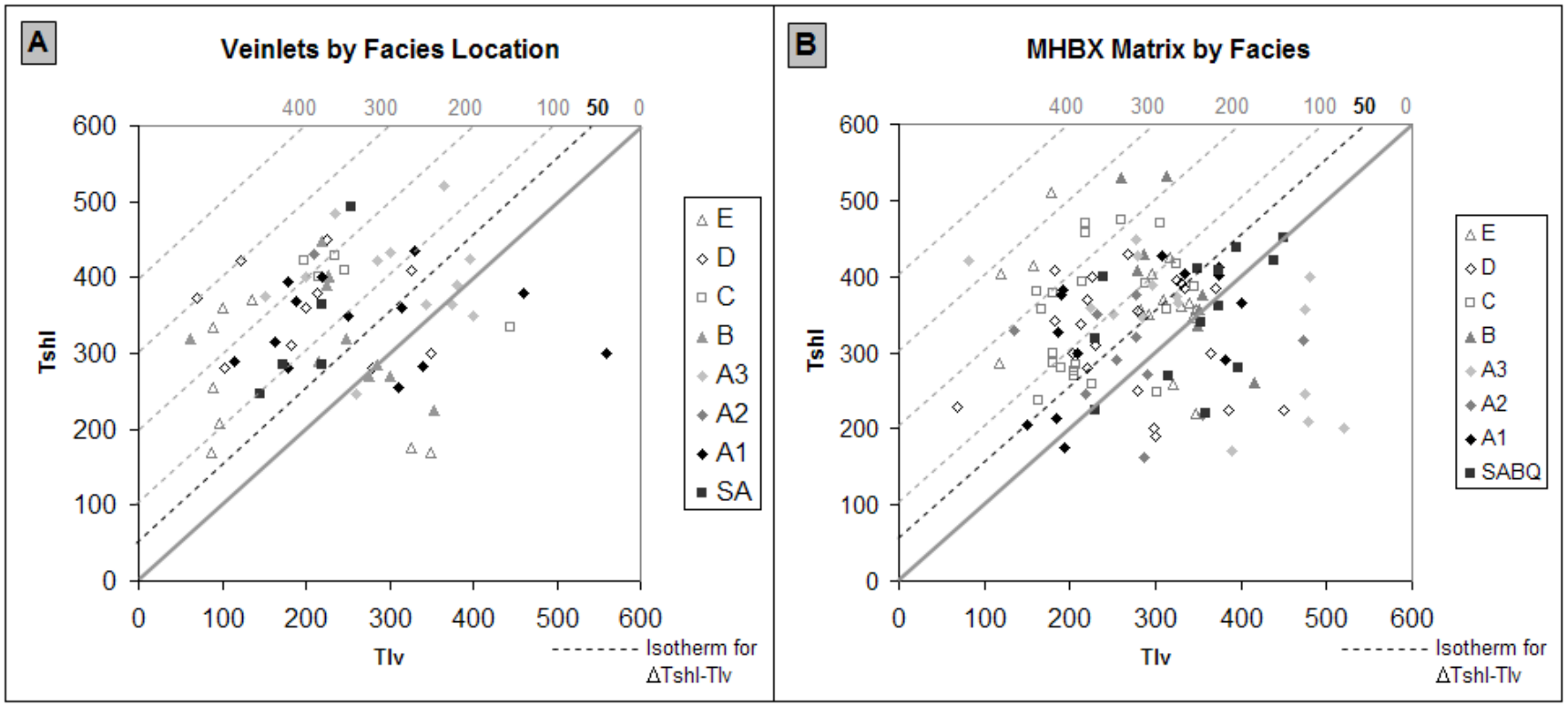

Figure 14. Tlv vs. Tshl diagram for: (A) veinlets by facies location and source aplite (SA) and (B) MHBX matrix by facies and source aplite barren quartz (SABQ). Inclusions above the thick gray line (0) homogenized by halite dissolution or other translucent daughter dissolution. Those below the line homogenized by vapor bubble disappearance. Those inclusions above the black dotted line (50°C isotherm for DTshl-Tlv) have a Tshl>>Tlv and are most likely a representation of inclusions that have captured halite crystals, a result of heterogeneous trapping.

granitic magma was emplaced at depths of 3 to 5 km, corresponding to lithostatic pressures of 0.8-1.4 kbars. Based upon fluid inclusion analyses, Smith (1983) determined a lithostatic pressure of 180-550 bars for the Goat Hill orebody, with a corresponding depth of 0.7-2 km, assuming lithostatic load.

Previous studies on Climax-type deposits have suggested three possibilities for the origin of the inclusions that exhibited a final homogenization by Tshl>>Tlv – overpressures, caused by exsolution and evolution of the hydrothermal fluid (Kamilli, 1978) or by system sealing (Cline & Bodnar, 1994), post-entrapment modification of fluid inclusions (Klemm et al., 2004; Klemm et al., 2008), or captured halite crystals (Bloom, 1981). The generation of overpressure is unreasonable given the host lithologies of the Goat Hill orebody at Questa. The tensile strength of the altered andesite and volcaniclastic country rock is very low (average of 35 bars) (Calle & Nicholas, Inc., 2008), therefore fracturing likely occurred before overpressures could develop. If exsolution and hydrothermal fluid evolution were the mechanism for overpressures, and accounted for the Tshl>>Tlv inclusions, it would be reasonable to expect an evolutionary pattern would be evident from the quartz fluid inclusion data in terms of MHBX facies and veins from the bottom of the orebody to the top. This is not the case. Inclusions that have a final Th by Tshl>>Tlv occur in all of the MHBX facies and all the veins from the bottom of the breccia to the top, with no evident pattern (Figure 14), hence ruling out exsolution as a control on fluid inclusion P-T-X. Post-entrapment modification of fluid inclusions is ruled out in this study due to the significant number of Tshl>>Tlv fluid inclusions, a number too high to be solely from post-entrapment modification, and the

fact that only fluid inclusions that appeared to be intact and have no evidence of necking down were analyzed.

Entrapment or capture of halite crystals from a heterogeneous fluid that is saturated with respect to halite is the favored mechanism for producing the Tshl>>Tlv inclusions in this study. Entrapment of a halite crystal in an inclusion would provide an over-estimate in salinity and final Th, hence giving way to unrealistic PTX conditions. Several previous studies on other ore deposits such as Naica (Erwood et al., 1979), Capitan Mountains (Campbell et al., 1995), Panguna (Eastoe, 1978), Granisle-Bell (Wilson, 1978), and the Banska Stiavnica district (Kodera et al., 2004), concluded that heterogeneous trapping, or entrapment of halite crystals, is the mechanism for producing this fluid inclusion type. Evidence for the trapped halite phenomenon would be solid inclusions of halite in quartz. This feature is hard to recognize due to a close index of refraction (*n*) for both quartz (1.55) and halite (1.54) (Ford, 1966). There were several instances in this study where solid inclusions in quartz were observed and suspected to be halite (Figure 15). However, unless the suspected solid inclusions are analyzed for chemistry their composition cannot truly be known. Campbell et al. (2001) documented several solid inclusions of halite in quartz from the Capitan Mountains, NM with electron microprobe analyses. Daughter minerals that did not dissolve upon heating (other translucent daughters, hematite, and opaques) can also be an indication of capture rather than in-situ precipitation (Kodera et al., 2004). Only 14 of 75 other translucent daughter bearing inclusions contained other translucent daughter minerals that dissolved. In addition, no opaque or hematite daughter minerals were observed to dissolve. Both of these facts further support heterogeneous trapping.

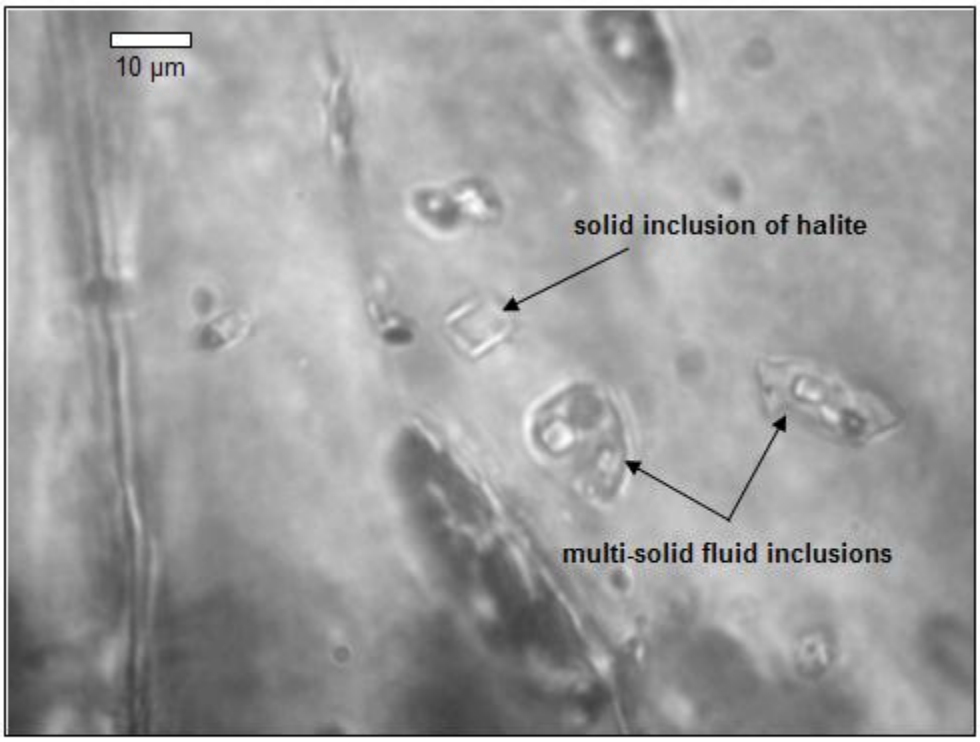

Figure 15. Photograph of suspected solid inclusion of halite in quartz that occurs adjacent to multi-solid fluid inclusions, evidence of heterogeneous trapping. Photo taken at 25°C prior to heating.

A fluid saturated with respect to NaCl is not an unlikely occurrence in a magmatic-hydrothermal system. This is a result of direct exsolution of a two-phase fluid from the magma and/or boiling in the system. Pervasive boiling and/or simple cooling of a high salinity fluid can result in these fluids becoming oversaturated with respect to halite. Drillcore filled with halite crystals from pervasive boiling of geothermal fluids have been observed in geothermal systems (Norman, D.I. – NMT E&ES, pers. comm., 2004). Coexisting vapor-rich and hl-bearing liquid-rich fluid inclusions (Ic, IId, and IIIb) were found in several instances in the Goat Hill, evidence of boiling. Based upon phase equilibria constraints, if an inclusion homogenizes by halite dissolution, it had to have formed in the vapor absent field (Figure 16). Therefore, the presence of co-genetic liquid-rich brines and vapor-rich inclusions indicate that the liquid-rich brine inclusions could not have precipitated halite in-situ, but rather are a result of heterogeneous trapping. Types IId and IIIb inclusions (vapor-rich, but contain halite and/or other minerals) can be a result of boiling and trapping of minerals (heterogeneous trapping) or leakage of fluid inclusions. The latter does not seem likely considering that Type IId and IIIb inclusions were identified in several instances in this study. Bloom (1981) also found vapor-rich halite-bearing fluid inclusions, equivalent to type IId of this study. Additional evidence of captured halite in this system is variable halite to liquid phase ratios and an inclusion containing three suspected halite crystals, rather than one (Figure 17). If the halite was precipitated from the fluid after trapping of the inclusion, the inclusion would contain only one halite crystal based upon surface free energy constraints (White et al., 1981). In the instance of an over-saturated fluid containing halite crystals, it is possible to trap more than one halite crystal in an inclusion.

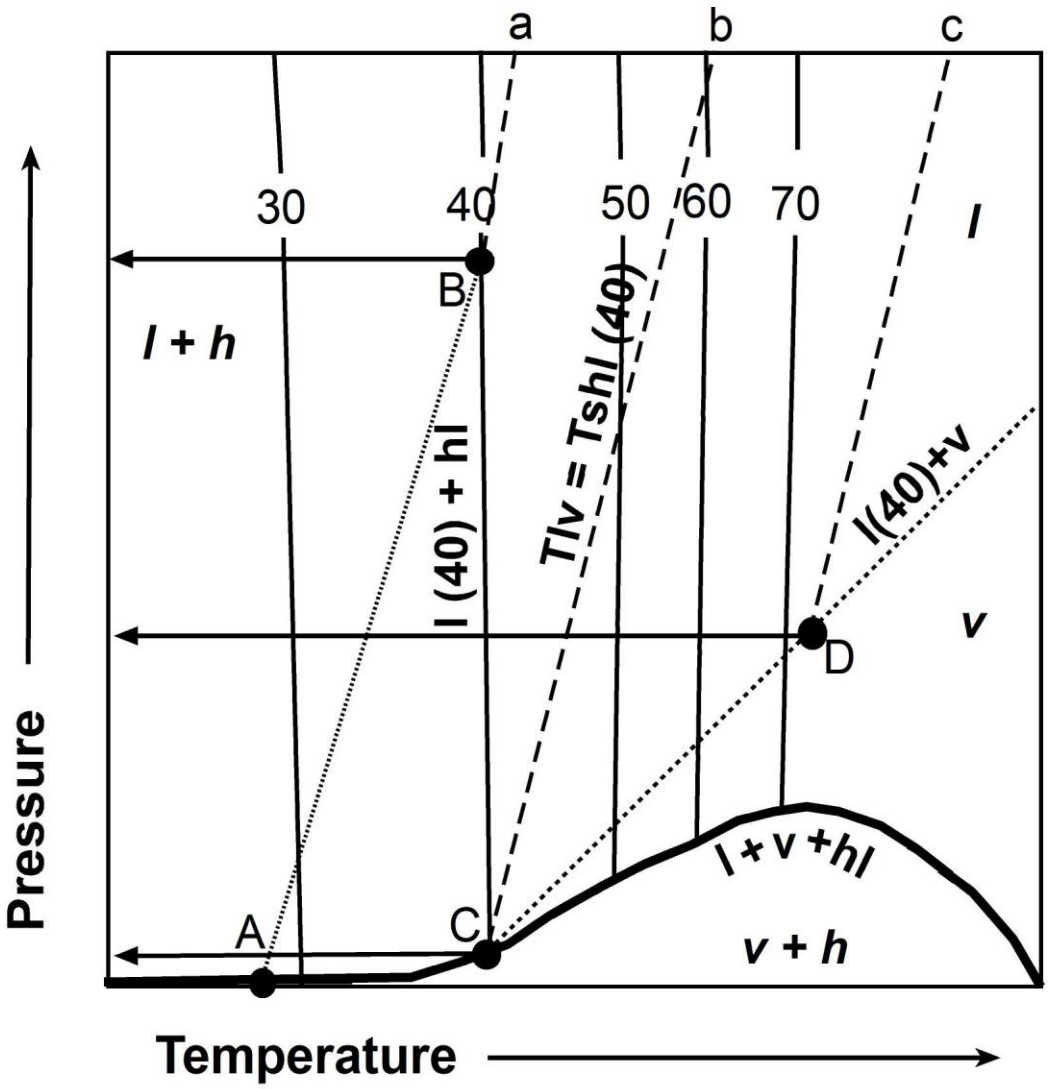

Figure 16. Schematic P-T diagram for the water-NaCl system demonstrating the steepness of the liquidus (l+hl) for 30-70 wt.% NaCl and the three different modes of halite dissolution for a 40 wt.% NaCl solution. Upon heating, a fluid inclusion with Tshl>>Tlv will follow the path A (Tlv) - B (Tshl) - a (isochoric path after final Th). Note the high pressure associated with point B that when to scale can demonstrate unrealistic pressures. A fluid inclusion with Tshl=Tlv will homogenize at C and follow the isochoric path b after homogenization. Note the low pressures associated with point C. An inclusion with Tshl<Tlv will follow the path C (Tshl) - D (Tlv) - c (isochoric path after final Th). Note the moderate pressure for D relative to the pressures of B and C. Modified from Bodnar, 1994 and Shephard et al., 1985.

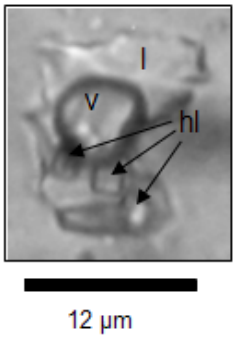

Figure 17. Microphotograph of liquid-rich fluid inclusion containing three suspected halite crystals, suggestive of heterogeneous trapping. The three daughter minerals labeled hl were suspected to be halite crystals due to shape, birefringence, and they did not dissolve at $T_s$sylvite temperatures. Inclusion was heated with intention of homogenizing and allowing to go back to room temperature. If the three suspected halite crystals became one upon cooling, this would be supportive that they were indeed halite. However, the sample decrepitated before the suspected crystals homogenized.

Due to the plausibility of heterogeneous trapping and the entrapment of halite, the fluid inclusion data is reported in terms of the homogenization of the liquid-vapor phase (Tlv) rather than in terms of the final homogenization temperature. Reporting in terms of Tlv is more representative of the fluid temperature at the time of trapping. The fluid inclusions above the halite saturation curve (HSC) are not representative of a real fluid, due to the captured halite phenomenon (Figure 12). The inclusions above the HSC are the result of a halite saturated fluid along the HSC at the same homogenization temperature, and a captured halite crystal. The salinities of the inclusions above the HSC are a function of the size of the halite crystal that was entrained. The fluid inclusions above the HSC can be projected down to the HSC at their same temperature of homogenization, represented by the dark line on the HSC in Figure 12, in order to denote the real fluid in which they originated.

Fluid Evolution

MHBX Facies

There is a pronounced mineralogic/alteration evolution that occurred in this system, on which the facies classifications are based (Ross, 2002). It was hypothesized that the fluid inclusions in quartz from each facies would reflect the mineralogic/alteration zonation in terms of an evolutionary pattern in the temperature and salinity data, i.e. facies closest to the source intrusion would have higher temperatures and salinities and facies distal to the source intrusion would have lower temperatures and salinities. This is not the case, however. There is no distinct evolutionary pattern based upon facies in the quartz data (Figure 13). All facies quartz reflect similar wide ranges in temperatures and salinities. A Pearson's correlation was used in an attempt to identify a

	Facies	
Type	0.0618 153 0.22395	Correlation coefficient valid cases one-tailed significance
Tlv	-0.06347 153 0.21784	Correlation coefficient valid cases one-tailed significance
Final Th	0.05721 153 0.24117	Correlation coefficient valid cases one-tailed significance
Salinity	0.05653 153 0.24378	Correlation coefficient valid cases one-tailed significance

Table 5. Pearson's correlation data between facies and type, Tlv, final Th, and salinity. Pearsons correlations were obtained utilizing the WinSTAT Statistics for Windows Version 3.1 computer program distributed by Kalmia Co. Inc., 1991-1996.

correlation between facies and type, Tlv, final Th, and salinity, or the lack thereof (Table 5). If the absolute value of a correlation coefficient (|cc|) is 0.5 and greater, then it is considered to represent a correlation between the variables. All |cc|s between facies and other variables were well below 0.5, with values of 0.056-0.063, demonstrating that there is no facies correlation with type, Tlv, final Th, and salinity.

An evolution is evident between the different mineral phases of the MHBX matrix paragenetic sequence, however, as reflected by early quartz and later fluorite (Figure 8). The two fluorite samples from the C and D facies did not exhibit the wide ranges of temperatures and salinities, nor the high temperatures and salinities, that were exhibited by quartz (Figure 13). Fluorite fluid inclusion data indicates that the fluorite was precipitated at low temperatures (105-211°C) and salinities (0-1 eq. wt.% $NaCl+KCl+CaCl_2$). These temperatures and salinities most likely reflect an evolution from magmatic-hydrothermal to meteoric waters entering the system. This is further supported by known secondary fluid inclusions in quartz with similar T-X (88-241°C, 0-6 eq. wt.% $NaCl+KCl+CaCl_2$), most likely a result of meteoric influx into the system that is associated with fluorite precipitation.

When looking at the data in terms of different mineral phases, the evolution does correspond to matrix facies, as fluorite only occurs in the C, D, and E facies and quartz occurs in all facies. Based upon the differences in fluorite and quartz, it appears that performing fluid inclusion microthermometry on all of the different mineral phases (quartz, fluorophlogopite, fluorite, calcite, and anhydrite) in each of the facies, rather than just quartz, would most likely reflect the mineralogic/alteration evolution of the MHBX. Similar to the quartz and fluorite data, it is likely that the data from the earlier mineral

phases (quartz and fluorophlogopite) would exhibit higher temperatures and salinities associated with potassic alteration and the later mineral phases (fluorite, calcite, and anhydrite), which only occur in the C, D, and E facies, would exhibit lower temperatures and salinities associated with retrograde collapse of isotherms onto the system, influx of meteoric water, and the onset of QSP alteration.

MHBX Matrix and Veinlets

MHBX matrix and veinlet quartz data, including the background Source Aplite Veinlet and Source Aplite Barren Quartz, is essentially indistinguishable, with a few minor differences. Fluid inclusions in the veinlets were less abundant and, on average, smaller than the fluid inclusions in the MHBX matrix. This is most likely due to the smaller sized quartz grains in the veinlets compared to the MHBX matrix, a possible result of extensive boiling. In addition, the pre-vein mineralization fractures allotted much less space for veinlet precipitation, producing smaller grains, and hence smaller inclusions, then the much more voluminous MHBX. The veinlets contain less halite-bearing fluid inclusions than the matrix. This is most likely related to the smaller inclusion size in the veinlets, where it would be harder to entrain a halite crystal or nucleate a halite daughter. Lastly, the veinlets did not contain any sylvite-bearing type III, carbonic type IV, or $CaCl_2$ fluid inclusions. The lack of K, Ca, and CO_2-bearing inclusions may be an indicator that the veinlets are from a slightly more evolved or fractionated magmatic-hydrothermal fluid than the MHBX matrix. This is not unlikely since the veinlets are later than the MHBX and they do not contain the coarse-grained K-feldspar, biotite, anhydrite, fluorite, and calcite mineral phases that occur in the MHBX.

As previously discussed, an evolutionary pattern is not evident from facies quartz data, whereas an evolution is evident by the different mineral phases quartz and fluorite. No major evolutionary difference is reflected by the MHBX matrix and veinlet quartz, since their data are essentially indistinguishable. However, since there is such a broad range in the quartz T-X data, there must be an evolutionary history of the fluid contributing to such broad ranges in data. Since the MHBX and the veinlets have data that is essentially indistinguishable from one another, each phase most likely followed similar fluid evolution history. This history has been broken up into four main stages (1-4) (Figures 11 and 12).

The first stage in fluid evolution is Stage 1 at 540-420°C, with a mode at 460°C (Figures 11 and 12). This stage represents the parent fluid that exsolved directly from the magma. Three types of fluids are represented in Stage 1, and are the precursors to all other fluids in the later stages. The first is a single phase critical fluid of low to moderate salinity that exsolved directly from the magma at the hydrofracturing phase (Williams-Jones and Heinrich, 2005). These fluids are represented by those inclusions on or below the critical curve (CC) (Figure 12). Secondly, a near-critical transition period between critical and non-critical conditions occurs, causing phase separation of the exsolving fluid, with only a moderate difference in total salinity between the two phases (Williams-Jones and Heinrich, 2005). This is represented by inclusions with low salinities (0-10 eq. wt.% NaCl) and moderate salinities (11-25 eq. wt.% NaCl) (within (a) of Figure 12). These moderate salinity inclusions may also be due to the introduction of meteoric fluid into the system. Lastly, a two-phase fluid consisting of a brine and low salinity vapor separated simultaneously from the magma and/or were produced by phase separation of

the exsolving fluid. Since boiling, or phase separation, is indicated in Stage 1, no pressure correction is necessary. Based upon fluid inclusion temperatures, it is concluded that early potassic alteration with little to no molybdenite mineralization is associated with this stage in the system. Molybdenum is soluble at these high temperatures, and hence would remain in the fluid rather than precipitate out (Smith, 1983). This is supported by Klemm et al. (2004), in which LA-ICPMS results on early, high T brines were up to 1000 ppm Mo, indicating that molybdenite remained in the fluid.

Stage 2 is represented by fluid inclusions with temperatures from 420-340°C, with a mode at 380°C (Figures 11 and 12). This stage is a result of heat loss from initial boiling (Stage 1), but also continued boiling or phase separation. At 400°C, fluid became oversaturated with respect to halite due to boiling and cooling, resulting in halite capture (Figure 12, above the HSC). This stage is considered to be representative of potassic alteration associated with molybdenite mineralization due to the temperature range. Based upon FI petrography, molybdenite mineralization commenced at $\leq$420°C due to temperature decrease. In addition, molybdenite mineralization is associated with inclusions of all salinities – low, moderate, and brine. Boiling ceased at 350°C as indicated by the lack of vapor inclusions below 350°C. Due to boiling in Stage 2, no pressure corrections are necessary. The moderate salinity inclusions may also be a result of meteoric mixing with the parent fluids in this stage.

Stage 3 occurred at 340-240°C, with a mode at 280°C (Figures 11 and 12). This stage is representative of simple cooling of the phase separated fluids in Stage 2 and possible continued mixing with meteoric fluids. Based upon the fluid inclusion

temperatures, this stage is considered to be representative of isothermal collapse of the system due to magma cooling and retreat. In this stage, QSP alteration is prevalent, overprinting potassic alteration associated with the previous two stages. Molybdenite deposition is prevalent in this stage due to temperature decrease from simple cooling. This is supported by Klemm et al. (2004) LA-ICPMS results, in which Mo in moderate temperature late brines was below detection limits, an indicator that molybdenite is no longer in solution. The last bit of molybdenite came out of solution at 220°C, as indicated by FIs with a known association to molybdenite.

Stage 4 is the last stage of the system, is in two parts (a and b) and occurs at <240°C, with a mode at 200°C (Figures 11 and 12). Stage 4a is considered to be representative of continued simple cooling from the previous stage as a result of continued collapse of the isotherms onto the system. Possible continued meteoric mixing may have occurred in this stage as well. QSP alteration is associated with Stage 4a. Stage 4b (Figure 12 – e) is representative of a meteoric influx being the dominant fluid in the system, as indicated by secondary and carbonic inclusions (Figure 12 – c). Carbonic inclusions also occur in Stage 4b (Figure 12 – c), which correlates with the precipitation of the lower temperature late-stage mineral calcite. An additional lower temperature late-stage mineral phase that is associated with Stage 4b (Figure 12 – d) is fluorite. QSP and minor argillic alteration are also associated with Stage 4b.

COMPARISON WITH PREVIOUS QUESTA FI STUDIES

The data set from this study exhibited similarities and differences to the previous fluid inclusion studies on Questa (Bloom, 1981; Smith, 1983; Cline & Bodnar, 1994;

Cline & Vanko, 1995; Klemm et al., 2004; and Klemm et al., 2008) in terms of fluid inclusion types, temperature of homogenization ranges and modes, and salinity ranges. In addition, there are similarities and differences in the data interpretation between various authors and this study. Comparing previous fluid inclusion study data sets and interpretations with those of this study will aid in deriving an ore genesis model for the Questa system.

Fluid Inclusion Types Comparison

Fluid inclusion types observed in this study are essentially the same as those reported by the previous fluid inclusion studies on Questa, with a few minor differences, despite the fact that this study analyzed from almost two times to six times the number of fluid inclusions of previous studies (Table 6). Carbonic (Type IV) inclusions were not observed by Smith (1983) or either Cline study (1994, 1995), however only four carbonic (Type IV) fluid inclusions were observed in this study. Klemm (2004 and 2008) also observed minimal carbonic (Type IV) fluid inclusions as well. The lack of significant liquid CO_2-bearing inclusions in the Questa fluid inclusion data sets reveals that the system is fairly low in CO_2 (<5%) (Shephard et al., 1985). Another difference is that no vapor-rich halite-bearing Type IId inclusions were observed in any previous study, with the exception of Bloom (1981), as well as no vapor-rich multi-solid Type IIIb fluid inclusions. These inclusions were likely overlooked by previous studies due to the vapor-rich property and the inability to observe phase-changes in this type of inclusion. None the less, this type of inclusion is deemed important in supporting the heterogeneous trapping or trapped halite phenomenon mechanism for the Tshl>>Tlv fluid inclusions.

Fluid Inclusion Temperatures Comparison

When considering all studies at Questa, fluid inclusion homogenization temperatures exhibited a variable range; however, the reported modes are in agreement between the Questa studies at 380-390°C (Figure 18 and Table 6). This study exhibited the widest range of fluid inclusion homogenization temperatures out of the Questa fluid inclusion studies (Figure 18). However, as previously mentioned, the data for this study is reported in terms of Tlv rather than Final Th. Note the temperature and salinity distribution differences when reporting in terms of Tlv versus Final Th (Figure 19). Reporting temperatures in Tlv allowed for more data on the lower temperature end and less data on the higher temperature end when comparing Tlv and Final Th methods. This might be a possible explanation why this study reveals lower temperatures compared to the previous Questa studies that reported their data in terms of Final Th (Figure 18). If the homogenization temperature data is looked at in terms of Tlv rather than the reported Final Th for Cline & Bodnar (1994) and Cline & Vanko (1995), the temperature range is 55-490°C (as opposed to 150-500°C for Final Th), a range that is similar to this study. Again, this reveals that lower temperatures are brought out from reporting Tlv rather than Final Th on the Tshl>>Tlv fluid inclusions.

Other factors that may have contributed to the larger range in fluid inclusion homogenization temperatures for this study compared to previous studies are the number and type of inclusions that were analyzed, as well as temporal-spatial relationships. This study has the highest number of fluid inclusions analyzed, 434 compared to 70 to 251 for the other Questa studies (Figure 18 and Table 6). As discussed previously, the utmost care was taken in choosing primary or pseudosecondary, intact fluid inclusions for

Author [n = # of FIs]	Type Equivalent to This Study	Missing Type Equivalent	Final Th in °C*	Salinity	Boiling	Mo Mineralization	Alteration associated with Mo Mineralization	Origin
Rowe (This Study) [n=434]	**Ia-Ic IIa-IId IIIa, IIIb IV**	**--**	**All Types: MHBX Tlv =68-520 w/ modes (from largest to smallest) at 380, 180, 460, 280; vnlt Tlv = 62-560 w/ modes (from largest to smallest) at 380, 200. 280 All Types: MHBX Final Th = 88-537 w/largest mode at 380; vnlt Final Th = 169-560 w/largest mode at 380**	**All: MHBX 0-64 eq. wt.% NaCl±KCl±$CaCl_2$; vnlts 0-63 eq. wt.% NaCl±KCl±$CaCl_2$**	**Yes**	**≤420-240°C with a 380°C mode and 0-64 eq. wt.% NaCl±KCl±CaCl2**	**Mo associated with potassic (Stage 2: 420-340°C) and phyllic alteration (Stage 3: 340-240°C)**	**Magmatic with meteoric input**
Bloom (1981) [n=98]	Ia, Ib Ic IIa-IId IIIa IV	IIIb	300 to >600, mode at 390 300 to >600, mode at 390 320 to >600, mode at 390	5-15 eq. wt.% NaCl±KCl 30-60 eq. wt.% NaCl±KCl 40-70 eq. wt.% NaCl±KCl	Yes	500-300°C with a mode @390°C and 5-15 and/or 30-60 eq. wt.% NaCl±KCl	Mo associated with phyllic alteration (500-300°C); potassic alteration occurred @ ≥500°C and not associated with Mo	Mixed magmatic and meteoric
Smith (1983) [n=70]	Ib, Ic IIa, IIb IIIa	Ia IIc, IId IIIb IV	All: 300-600 w/a mode at 380, secondaries - 200-370	All: 5-65 eq. wt.% NaCl±KCl	Yes	550-350°C with a mode @380°C and 5-57 eq. wt.% NaCl±KCl	Mo associated with potassic (550-450°C) and phyllic alteration (450-350°C)	Mixed magmatic and meteoric **
Cline & Bodnar (1994) and Cline & Vanko (1995) [n=251]	Ia, Ib Ic IIa, IIb, IIc, IIIa	IId, IIIb IV	150-370 360-500 200-500, mode @ 360-400; Tlv = 55-490	0-12 eq. wt.% NaCl±KCl 2-26 eq. wt.% NaCl±KCl 31-57 eq. wt.% NaCl±KCl	No	500-150°C with a mode @ 380°C and 0-26 and 31-57 eq. wt.% NaCl±KCl	none reported	Magmatic
Klemm et al. (2004) and Klemm et al. (2008) [n=150]	Ia-Ic IIa, IIb IIIa IV	IIc, IId IIIb	Range of 250-500 for all types in MHBX and qtz-mo veinlets	Range of 2-17 and 30-50 eq. wt.% NaCl±KCl for all types in MHBX and qtz-mo veinlets	Yes	420-350°C (no mode reported) and 33-45 eq. wt.% NaCl±KCl	none reported	Magmatic

* All studies reported in Final Th whereas this study was reported in this table as both Tlv homogenization and Final Th.
** Conclusion derived based upon both FI and stable isotope data.
[n=X] - number of analyzed fluid inclusions

Table 6 - Comparison of fluid inclusion data from this study to previous authors.

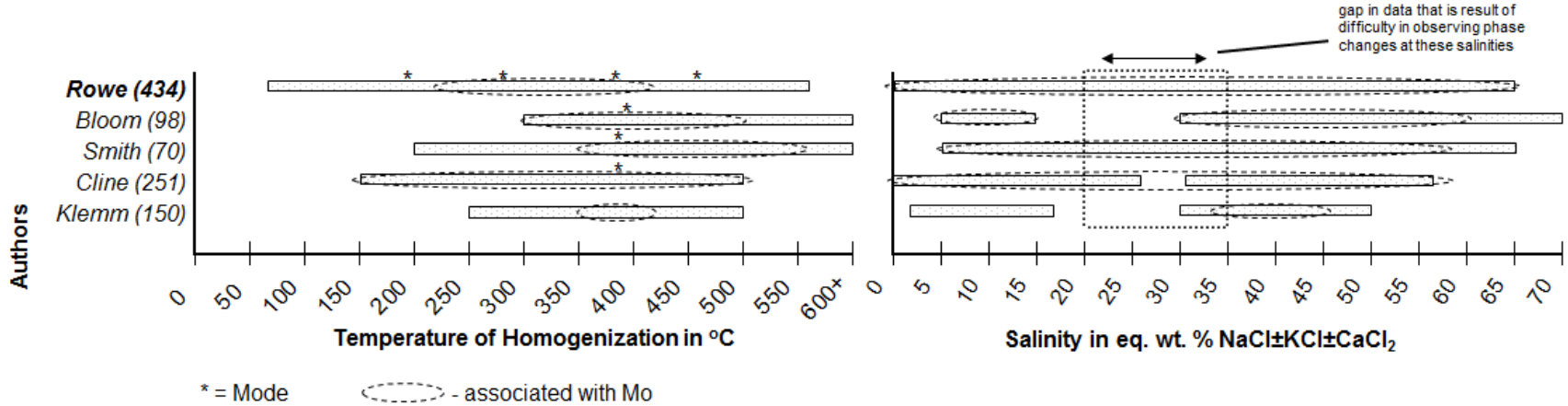

Figure 18. Temperatures of homogenization and salinities for various authors on Questa (Bloom, 1981; Smith, 1983, Cline& Bodnar, 1994; Cline & Vanko, 1995; Klemm et al., 2004; Klemm et al., 2008). The number in paranthesis next to author is the number of fluid inclusions analyzed. All temperatures are Final Th except for Rowe (this study) which are in Tlv.

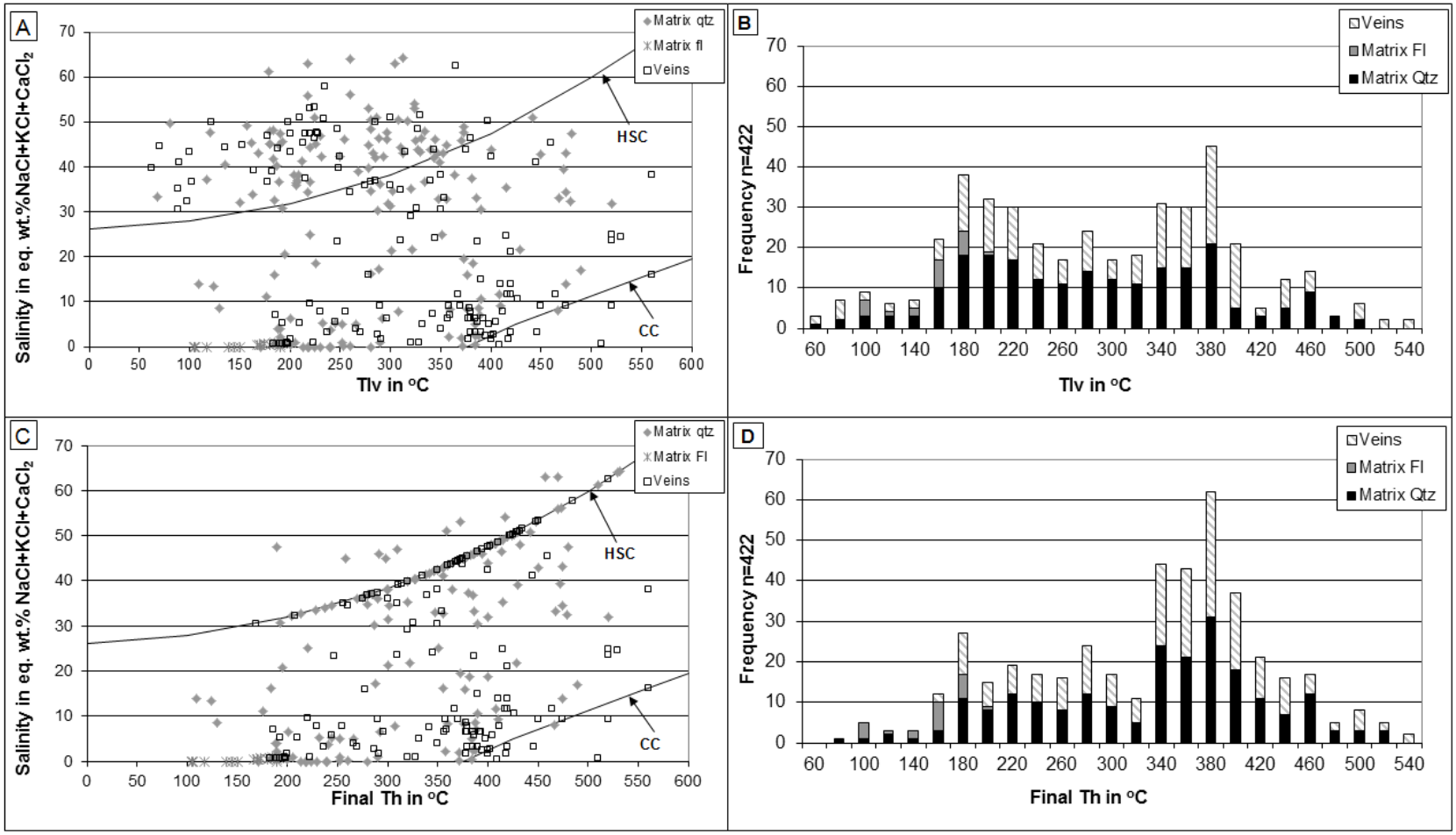

Figure 19. - Temperature vs. salinity diagrams demonstrating differences when reporting in terms of Tlv vs. Final Th. All of the FIs above the Halite Saturation Curve (HSC) homogenized by Tshl and do not represent the true salinity of the fluid due to the Trapped Halite Phenomenon. The real salinity of the fluid is the same temperature, but brought down to the HSC. B) Temperature of homogenization in Tlv. C) Temperature of homogenization in terms of Final Th vs. Salinity. All of the FIs on the HSC homogenized by Tshl. FIs above the HSC contain sylvite. The FIs on or above the HSC represent temperatures and salinities that higher than real fluid due to the Trapped Halite Phenomenon. D) Temperature of homogenization in Final Th. Note the differences between these two reporting types: the Tlv diagrams have more FIs at lower temperatures and less FIs at higher temperatures than the Final Th diagrams. This demonstrates how the data can be skewed depending on how it is reported.

analysis. Hence, the data from this study is considered accurate and real. All types of fluid inclusions that appeared to be primary/pseudosecondary in origin were considered representative of the fluid and not eliminated from this study. Fluid inclusion analysis was not biased to easily measured, large fluid inclusions since they were not always available in all of the MHBX facies and/or veinlets. Also, as previously mentioned, this study was performed with rigorous temporal-spatial constraints. All of the samples were taken from several drillholes in very well defined facies within one orebody, the GoatHill. All of the above (the higher number of fluid inclusions analyzed, all primary fluid inclusions analyzed, and established temporal-spatial constraints from sampling) can give way to a larger temperature range compared to previous studies who have less fluid inclusions that were analyzed at Questa (Bloom, 1981; Smith, 1983; Cline & Bodnar, 1994; Cline & Vanko, 1995; Klemm et al., 2004; and Klemm et al., 2008), limited temporal-spatial constraints (Bloom, 1981; Smith, 1983; Cline & Bodnar, 1994; Cline & Vanko, 1995; Klemm et al., 2004; and Klemm et al., 2008), and sampling bias to only large, easily measured fluid inclusions (Cline & Bodnar, 1994; Cline & Vanko, 1995; Klemm et al., 2004; and Klemm et al., 2008) and/or only fluid inclusions that have Tshl<Tlv (Klemm et al., 2004; and Klemm et al., 2008).

Fluid Inclusion Salinities Comparison

Similarly to the variability in homogenization temperatures between studies, a variety of salinity ranges were reported by the previous Questa studies (Figure 18 and Table 6). Despite the salinity variability between studies, the salinity results from each study reveal that there are low to moderate salinity (≤27 eq. wt.% NaCl±KCl± $CaCl_2$) inclusions and hypersaline (≥30 eq. wt.% NaCl±KCl±$CaCl_2$) inclusions. This study and

the studies of Cline (1994, 1995) are the only studies who reported salinities on the very low end, whereas Klemm (2004, 2008) did not observed any inclusions with less than 2 eq. wt.% NaCl±KCl±$CaCl_2$, and Bloom (1981) and Smith (1983) did not observe any inclusions with a salinity of less than 5 eq. wt.% NaCl±KCl±$CaCl_2$. This study and Smith (1983) reported the same upper limit (65 eq. wt.% NaCl±KCl±CaCl2) for the hypersaline inclusions, whereas Bloom (1981) reported the highest fluid inclusion salinities (70 eq. wt.% NaCl±KCl±$CaCl_2$), Cline (1994, 1995) reported slightly lower upper salinity limit (57 eq. wt.% NaCl±KCl±$CaCl_2$), and Klemm (2004, 2008) reported the lowest upper salinity limit (50 eq. wt.% NaCl±KCl±CaCl2) with the greatest difference from this study. Klemm (2004, 2008) considered fluid inclusions with Tshl>>Tlv to have undergone post-entrapment modification and were not reported. This is the likely reason for the considerable lower upper salinity limit of Klemm (2004, 2008) compared to this and other previous studies.

This study and Smith (1983) are the only Questa studies that reported a large, continuous range of salinities (0-65 and 5-65 eq. wt.% NaCl±KCl±$CaCl_2$, respectively). Cline & Bodnar (1994) and Cline & Vanko (1995) reported a salinity range similar to this study (0-57 eq. wt.% NaCl±KCl±$CaCl_2$), but with a gap from 26-30 eq. wt.% NaCl±KCl±$CaCl_2$. This gap is quite common in fluid inclusion data and often extends from 20 to 35 eq. wt.% NaCl. This gap is not real, but rather a result of the difficulty of recognizing phases and phase changes at these particular salinities. From 20-23.2 eq. wt.% NaCl, the final ice melting is so close to the eutectic temperature and the final melting of hydrohalite (-21.2^{o}C) that it is often missed. From 23.2 to 26.3 eq. wt.% NaCl, it is very hard to recognize phase changes with hydrohalite and it is often misidentified

as ice. From 26.3 to 35 eq. wt.% NaCl, the nucleated halite crystal is often too small to see within the fluid inclusion and/or the halite crystal itself often fails to nucleate. Once at 30 eq. wt.% NaCl, halite daughters are larger and easier to identify. With that being said, the gap from 26-31 eq. wt.% NaCl±KCl±$CaCl_2$ in the data of Cline & Bodnar (1994) and Cline & Vanko (1995) is likely not real and the salinity data sets can be considered to be continuous through these salinities (0-57 eq. wt.% NaCl±KCl±$CaCl_2$).

Data Interpretation Comparison

Boiling, indicated by cogenetic liquid-rich (±halite) and vapor-rich fluid inclusions, was reported in all of the Questa studies with the exception of Cline & Bodnar (1994) and Cline & Vanko (1995) (Table 6). Hence, no pressure corrections were applied to the fluid inclusion temperatures by the studies that reported boiling in the system. Conversely, Cline & Bodnar (1994) and Cline & Vanko (1995) did apply pressure corrections to get the reported homogenization temperatures summarized in the previous section.

The concluded temperature of mineralization by the Questa studies shows some variation (420-240°C for this study; 500-300°C for Bloom, 1981; 550-350°C for Smith, 1983; 500-150°C for Cline & Bodnar, 1994 and Cline & Vanko, 1995; and 420-350°C for Klemm et al., 2004 and 2008), however the mode temperature of mineralization is from 380°C for four of the seven studies (this study; Smith, 1983; Cline & Bodnar, 1994; Cline & Vanko, 1995), 390°C for one of the studies (Bloom, 1981), and for the two studies without a reported mode (Klemm et al., 2004 and 2008), the mid-point of the reported range for mineralization is 385°C (Figure 18 and Table 6). Both this study and Smith (1983) concluded that molybdenite mineralization is associated with both potassic

and phyllic alteration, however the temperatures associated with those alteration types are different (420-340°C and 550-450°C, respectively, for potassic alteration; and 340-240°C and 450-350°C, respectively, for QSP alteration) (Table 6). Bloom (1981) concluded molybdenite mineralization to be associated with phyllic alteration at 500-300°C and that potassic alteration (at ≥500°C) had no association with mineralization. All of the Questa studies, with the exception of Klemm et al. (2004 and 2008), reported a very wide range of salinities (0-64 eq. wt.% NaCl±KCl±$CaCl_2$ for this study; 5-15 and 30-60 eq.wt.% NaCl±KCl for Bloom, 1981; 5-57 eq. wt.% NaCl±KCl for Smith, 1983; 0-26 and 31-57 eq. wt.% NaCl±KCl for Cline & Bodnar, 1994 and Cline & Bodnar, 1995) to be associated with molybdenite mineralization (Figure 18 and Table 6).

The origin of the molydenite-bearing fluids presented by all of the Questa fluid inclusion studies can be categorized into two schools of thought – purely magmatic (Cline & Bodnar, 1994; Cline & Vanko, 1995; Klemm et al., 2004 and 2008) and magmatic with meteoric input (this study; Bloom, 1981; Smith, 1983). The evolutionary history of the mineralizing fluid described by each study is quite variable, despite the fact that all studies reported essentially the same fluid inclusion types and the main mode temperature for molybdenite mineralization , as well as all studies but Klemm et al. (2004 and 2008) concluding that molybdenite mineralization can be attributed to basically all salinities (Table 6) (please see Previous Studies and Fluid Evolution sections of this paper for more details on fluid evolution). Interpreting the origin of the fluids represented by the wide-spread T-X fluid inclusion data sets reported by the Questa fluid inclusion studies is no easy feat. However, based upon the similarities between the Questa FI studies and major interpretations made in this study, it is concluded that the

mineralization model for Questa includes a main mode of mineralization at 380°C, mineralization is associated with a very wide range of salinities (0-64 eq. wt.% NaCl±KCl±$CaCl_2$), and the system is magmatic with a meteoric input.

CONCLUSIONS

Based upon phase equilibria constraints and various evidences reported in this study, it has been concluded that the halite-bearing fluid inclusions demonstrating a Tshl>>Tlv did not precipitate halite in-situ, but rather are a result of the captured halite phenomenon. Hence, it has been suggested that for fluid inclusion studies, reporting fluid inclusion temperatures in terms of the homogenization of the liquid-vapor phase rather than final homogenization temperature is more representative of the fluid temperature at the time of trapping.

Contrary to the hypothesis, no evolutionary pattern based upon facies was evident in the fluid inclusion data from MHBX matrix quartz. An evolution was evident between the mineral phases (early quartz and later fluorite) of the MHBX matrix paragenetic sequence, however, which in turn does reflect the mineralogic evolution of the Goat Hill MHBX. Results indicate that the quartz evolved from a magmatic fluid, whereas an evolution from magmatic to meteoric is the source of the fluorite producing fluids. Consequently, findings suggest that performing fluid inclusion microthermometry on the different mineral phases of the MHBX matrix paragenetic sequence would demonstrate the mineralogic evolution of the Goat Hill MHBX. In other words, the earlier mineral phases (quartz, fluorophlogopite) would most likely exhibit higher T-X associated with potassic alteration, and the later mineral phases (fluorite, calcite, anhydrite) would exhibit

lower T-X associated with retrograde collapse of isotherms, the onset of QSP alteration, and the influx of meteoric water into the system.

An evolutionary pattern based upon facies was not evident in the MHBX quartz, however the MHBX quartz data did reflect an evolutionary history independent of facies. The essentially analytically indistinguishable MHBX and veinlet quartz fluid inclusion data exhibited only minor differences, which suggests that the veinlets are from a slightly more evolved magmatic-hydrothermal fluid, but likely followed a similar fluid evolutionary history as the MHBX – four main stages (1-4). Stage 1 represents the parent fluid that exsolved from the magma and is associated with early potassic alteration with little to no molybdenite mineralization. Stage 2 fluids evolved directly from Stage 1 as a result of heat loss from initial boiling of Stage 1, in addition to continued phase separation. The halite phenomenon first occurs in this stage. Stage 2 is representative of potassic alteration associated with molybdenite mineralization. Stage 3 represents retrograde isothermal collapse of the system resulting in simple cooling from Stage 2, QSP alteration, and high grade molybdenite deposition. Stage 4 of the fluid evolution of the Goat Hill orebody is representative of continued simple cooling from Stage 3, meteoric influx onto the system, and QSP and minor argillic alteration. Meteoric mixing likely occurred in Stages 1-4 as well, until meteoric fluids become dominant in Stage 4. Based upon fluid inclusion petrography and supporting LA-ICMS data of Klemm et al. (2004), molybdenite mineralization commenced at $\leq 420^{o}C$ and ceased at $220^{o}C$, and was a result of temperature decrease caused by boiling, meteoric mixing, and simple cooling in the system.

REFERENCES

Becker, S. P., Fall, A., and Bodnar, R. J., 2008, Synthetic Fluid Inclusions. XVII. PVTX Properties of High Salinity H2O-NaCl Solutions (>30 wt% NaCl): Application to Fluid Inclusions that Homogenize by Halite Disappearance from Porphyry Copper and Other Hydrothermal Ore Deposits: Economic Geology, v. 103, p. 539-554.

Bloom, M. S., 1981, Chemistry of inclusion fluids; stockwork molybdenum deposits from Questa, New Mexico, Hudson Bay Mountain and Endako, British Columbia: Economic Geology v. 76, no. 7, p. 1906-1920.

Bodnar, R. J., 1994, Synthetic fluid inclusions. XII. Experimental determination of the liquidus and isochores for a 40 wt.% H2O-NaCl solution: Geochimica Cosmochimica Acta 58, p. 1053-1063.

Bodnar, R.J., 2003, Introduction to aqueous-electrolyte fluid inclusions, *in* Samson, I. M., Anderson, A. J., and Marshall, D., eds., Fluid Inclusions: Analysis and Interpretation, Volume 32: Vancouver, B.C., Mineralogical Association of Canada, p. 81-100.

Bodnar, R. J., and Vityk, M. O., 1994, Interpretation of Microthermometric data for H2O-NaCl fluid inclusions, *in* B., D. V., and M.L., F., eds., Fluid Inclusions in Minerals: Methods and Applications: Blacksburg, VA, Virginia Tech, p. 117-130.

Brown, P. E., and Hagemann, S. G., 1994, MacFlinCor: A computer program for fluid inclusion data reduction and manipulation, *in* de Vivo, B., and Frezzottie, M. L., eds., Fluid Inclusions in Minerals: Methods and Applications, Volume Short Course IMA, VPI Press, p. 231-250.

Calle & Nicholas, I., 2008, Questa_Aug-08_All_Lab_Testing_CNI: Tucson, AZ.

Campbell, A. R., Banks, D. A., Phillips, R. S., and Yardley, B. W. D., 1995, Geochemistry of Th-U-REE mineralizing magmatic fluids, Capitan Mountains, New Mexico: Economic Geology, v. 90, p. 1271-1287.

Campbell, A. R., Lundberg, S. A. W., and Dunbar, N. W., 2001, Solid inclusions of halite in quartz: evidence for the halite trend: Chemical Geology (including Isotope Geoscience), v. 173, p. 179-191.

Carpenter, R. H., 1968, Geology and ore deposits of the Questa molybdenum mine area, Taos County, New Mexico.

Carten, R. B., 1987, Evolution of immiscible Cl- and F-rich liquids from ore magmas, Henderson porphyry molybdenum deposit, Colorado [abs.]: Geological Society of America Abstracts with Programs, v. 19, no. 613.

Carten, R. B., White, W. H., and Stein, H. J., 1993, High-grade granite-related molybdenum systems; classification and origin: Mineral deposit modeling, v. 40, p. 521-554.

Cline, J. S., and Bodnar, R. J., 1994, Direct evolution of brine from a crystallizing silicic melt at the Questa, New Mexico, molybdenum deposit: Economic Geology, v. 89, no. 8, p. 1780-1802.

Cline, J. S., and Vanko, D. A., 1995, Magmatically generated saline brines related to molybdenum at Questa, New Mexico, USA, *in* Thompson, J. F. H., ed., Magmas, Fluids, and Ore Deposits: Mineralogical Association of Canada Short Course

Series, Victoria, B.C., Canada, Volume 23, p. 153-174.
Cox, D. P., and Singer, D. A., 1986, Mineral deposit models, Reston, VA, U. S. Geological Survey, 379 p.:
Czamanske, G. K., Foland, K. A., Kubacher, F. A., and Allen, J. C., 1990, The (super 40) Ar/ (super 39) Ar chronology of caldera formation, intrusive activity and Mo-ore deposition near Questa, New Mexico, *in* Bauer, P. W., Lucas, S. G., Mawer, C. K., and McIntosh, W. C., eds., New Mexico Geological Society Forty-first annual field conference, Volume 41, New Mexico Geological Society, p. 355-358.
Donahue, K. M., 2002, Geochemistry, geology and geochronology of the Victorio mining district, Luna County, New Mexico: Linking skarn and porphyry systems to carbonate-hosted lead-zinc replacement deposits [Master of Science Thesis]: New Mexico Institute of Mining & Technology, 186 p.
Eastoe, C. J., 1978, A fluid inclusion study of the Panguna porphyry copper deposit, Bougainville, Papua New Guinea: Economic Geology, v. 73, p. 721-748.
Erwood, R. J., Kessler, S. E., and Cloke, P. L., 1979, Compositionally distinct, saline hydrothermal solutions, Naica mine, Chihuahua, Mexico: Economic Geology, v. 74, p. 95-108.
Ford, W. E., 1966, Dana's Textbook of Mineralogy, J. Wiley.
Fournier, R. O., 1981, Application of water geochemistry togeothermal exploration and reservoir engineering, *in* Rybach, L., and Muffler, L. J. P., eds., Geothermal systems: Principles and Case Histories, Volume 109-143: New York, John Wiley & Sons.
Guilbert, J. M., and Park, C. F., Jr., 1986, The Geology of Ore Deposits, New York, NY, W. H. Freeman and Company, 985 p.:
Gunter, W. D., Chou, I.-M., and Girsperger, S., 1983, Phase relations in the system NaCl-KCl-H2O II: Differential thermal analysis of the halite liquidus in the NaCl-H2O binary above 450C: Geochimica Cosmochimica Acta 47, p. 863-873.
Hall, W. E., Friedman, I., and Nash, J. T., 1974, Fluid Inclusion and Light Stable Isotope Study of the Climax Molybdenum Deposits, Colorado: Economic Geology, v. 69, no. 6, p. 884-901.
Johnson, C. M., and Lipman, P. W., 1988, Origin of metaluminous and alkaline volcanic rocks of the Latir volcanic field, northern Rio Grande rift, New Mexico: Contributions to Mineralogy and Petrology, v. 100, p. 107-128.
Johnson, C. M., Lipman, P. W., and Czamanske, G. K., 1990, H, O, Sr, Nd, and Pb isotope geochemistry of the Latir volcanic field and cogenetic intrusions, New Mexico, and relations between evolution of a continental magmatic center and modifications of the lithosphere: Contributions to Mineralogy and Petrology, v. 104, no. 1, p. 99-124.
Kamilli, R. J., 1978, The genesis of stockwork molybdenite deposits; implication from fluid inclusion studies at the Henderson Mine [abs.]: The Geological Society of America (91st annual meeting), v. 10, p. 431.
Kelley, S. A., Chapin, C. E., and Corrigan, J., 1992, Late Mesozoic and Cenozoic cooling histories of the flanks of the northern and central Rio Grande rift, Colorado and New Mexico: New Mexico Bureau Bulletin, v. 145, p. 39.
Klemm, L. M., and Pettke, T. H. C. A., 2004, Early magmatic-hydrothermal evolution of the Questa porphyry Mo deposit, New Mexico, USA, *in* Muhling, J., Goldfarb, R.

J., Vielreicher, N., Bierlein, F. P., Stumpfl, E. F., Groves, D. I., Kenworthy, S., and Knox-Robinson, C. M., eds., Seg 2004, Volume 33, University of Western Australia Geology Department and Extension Service, p. 431.

Klemm, L. M., Pettke, T. H. C. A., and Heinrich, C. A., 2008, Fluid and source magma evolution of the Questa porphyry Mo deposit, New Mexico, USA: Mineralium Deposita, v. 43, no. 5, p. 533-552.

Kodera, P., Lexa, J., Rankin, A. H., and Fallick, A. E., 2004, Fluid evolution in a subvolcanic granodiorite pluton related to Fe and Pb-Zn mineralization, Banska Stiavnica Ore District, Slovakia: Economic Geology, v. 99, p. 1745-1770.

Leonardson, R. W., Dunlop, G., Starquist, V. L., Bratton, G. P., Meyer, J. W., and Osborne, L. W., Jr., 1983, Preliminary geology and molybdenum deposits at Questa, New Mexico, *in* Babcock, J. W., ed., Denver Region Exploration Geologists Society symposium; the genesis of Rocky Mountain ore deposits; changes with time and tectonics: Wheat Ridge, CO, Denver Reg. Explor. Geol. Soc.

Lipman, P. W., 1992, Ash-flow calderas as structural controls of ore deposits; recent work and future problems, *in* Thorman, C. H., ed., Application of structural geology to mineral and energy resources of the Central and Western United States, U. S. Geological Survey, p. L1-L12.

Martineau, M. P., Heinemeyer, G. R., Craig, S. D., and McAndrews, K. P., 1977, Geologic report - Questa Project 1975-1977: Questa Molybdenum Company internal report.

Meyer, J., and Foland, K. A., 1991, Magmatic-tectonic interaction during early Rio Grande Rift extension at Questa, New Mexico: Geological Society of America Bulletin, v. 103, no. 8, p. 993-1006.

Meyer, J. W., 1991, Volcanic, plutonic, tectonic and hydrothermal history of the southern Questa Caldera, New Mexico [Doctor of Philosophy Dissertation]: University of California Santa Barbara, 348 p.

Molling, P. A., 1989, Applications of the reaction progress variable to hydrothermal alteration associated with the deposition of the Questa molybdenite deposit, NM [Doctor of Philosophy Dissertation]: Johns Hopkins Univ., 249 p.

Molling, P. A., and Sverjensky, D. A., 1989, Thermodynamic analysis of ore fluids at the Questa Mo-porphyry deposits, *in* Dymek, R. F., and Shelton, K. L., eds., Geological Society of America, 1989 annual meeting, Volume 21, Geological Society of America (GSA), p. 150.

Norman, D. I., 2004, Personal communication: New Mexico Institute of Mining & Technology, Department of Earth & Environmental Science.

Roedder, E., 1979, Fluid inclusions as samples of ore fluids., *in* Barnes, H. L., ed., Geochemistry of Hydrothermal Ore Deposits. 2nd ed.: Wiley, New York, p. 684-737.

Roedder, E., 1984, Fluid Inclusions: Mineralogical Society of America, Reviews in Mineralogy, v. 12, p. 644.

Ross, P. S., 2002, Magmatic-hydrothermal Breccia Formation in Porphyry Mo Systems: A Horizontal Stratified Body at Questa, New Mexico [Master of Science Thesis]: Earth Sciences Dept. University of Quebec in Montreal.

Ross, P. S., Jebrak, M., and Walker, B. M., 2001, A magmatic-hydrothermal breccia

formed by hydraulic fracturing under a compressive stress regime at the Questa porphyry molybdenum deposit, *in* Anonymous, ed., Geological Society of America, 2001 annual meeting, Volume 33, Geological Society of America (GSA), p. 420.

Ross, P.-S., Jebrak, M., and Walker, B. M., 2002, Discharge of hydrothermal fluids from a magma chamber and concomitant formation of a stratified breccia zone at the Questa porphyry molybdenum deposit, New Mexico: Economic Geology v. 97, no. 8, p. 1679-1699.

Schilling, J. H., 1956, Geology of the Questa molybdenum (Moly) mine area, Taos County, New Mexico: New Mexico Bureau of Mines and Mineral Resources Bulletin 51, p. 87.

Seedorff, E., and Einaudi, M. T., 2004, Henderson Porphyry Molybdenum System, Colorado: II. Decoupling of Introduction and Deposition of Metals during Geochmical Evolution of Hydrothermal Fluids: Economic Geology, v. 99, p. 39-72.

Shephard, T. J., Rankin, A.H., and Alderton, D.H.M., 1985, A Practical Guide to Fluid Inclusion Studies, Glasgow, Blackie & Son Limited, 239 p.

Smith, R. W., 1983, Aqueous chemistry of molybdenum at elevated temperatures and pressures with applications to porphyry molybdenum deposits [PhD Dissertation]: New Mexico Institute of Mining and Technology, 311 p.

Walker, B. M., 2004, Personal communication: Molycorp, Inc.

White, W. H., Bookstrom, A. A., Kamilli, R. J., Ganster, M. W., Smith, R. P., Ranta, D. E., and Steininger, R. C., 1981, Character and origin of climax-type molybdenum deposits: Economic Geology, Seventy-fifth anniversary volume (1905-1980).

White, W. H., Carten, R. B., Bookstrom, A. A., and Stein, H. J., 1990, A Model for Climax-tpe Molybdenum Deposits [abs.], 8th IAGOD Symposium in Conjunction with International Conference in Mineral Deposit Modeling - Program with Abstracts, p. 133-134.

Williams-Jones, A. E., and Heinrich, C. A., 2005, Vapor transport of metals and the formation of magmatic-hydrothermal ore deposits: Economic Geology v. 100, no. 7, p. 1287-1312.

Wilson, J. W. J., 1978, Fluid inclusion geochemistry of the Granisle and Bell Copper porphyry deposits, B.C. [Master of Science Thesis]: University of Toronto, 117 p.

Zimmer, M. J., 2008, The $^{40}Ar/^{39}Ar$ Geochronology and Thermochronology of the Latir Volcanic Field and Associated Intrusions: Implications for Caldera-related Magmatism [Master of Science Thesis], 113 p.

CHAPTER II.

Genetic Fluid Evolution of the Magmatic-hydrothermal Breccia and Stockwork Veinlets of the Goat Hill Orebody, Questa Climax-type Porphyry-Mo System, New Mexico – A Stable Isotope and Fluid Inclusion Gas Analysis Study

ABSTRACT

The Goat Hill orebody of the Questa Climax-type porphyry molybdenum system is composed of a stratified magmatic-hydrothermal breccia (MHBX) and later quartz-molybdenite (qtz-mo) stockwork veinlets. The MHBX consists of five distinct facies (A-E) that display an evolution in matrix mineralogy and clast alteration. Oxygen and hydrogen stable isotope and fluid inclusion gas analysis on MHBX matrix quartz revealed that there is no fluid evolution pattern based upon facies that could be associated with the mineralogic/alteration evolution of the breccia. A fluid evolution was evident, however, between the different mineral phases of the MHBX matrix paragenetic sequence (fluorophlogopite→ quartz→fluorite→calcite). Fluorophlogopite demonstrated the most magmatic signature to magmatic-dominant magmatic-meteoric mixing with calculated $\delta^{18}O_{H2O}$ and δD_{H2O} values of 3.8-7.4‰ and -89 to -63‰, respectively, at 380°C. Paragenetically after fluorophlogopite, quartz exhibited a less magmatic-dominant magmatic-meteoric mixing signature with a calculated $\delta^{18}O_{H2O}$ range of 1.5-3.7‰ at 380°C and fluid inclusion δD_{H2O} range of -101 to -71‰. Fluorophlogopite and quartz are both associated with molybdenite mineralization, hence revealing a meteoric component to the Questa mineralizing fluid. Next in the paragenetic sequence, post-mineralization fluorite revealed a meteoric-dominant magmatic-meteoric mixing signature with fluid inclusion $\delta^{18}O_{H2O}$ and δD_{H2O} values of -4.0 to -1.7‰ and -109 to -

106‰, respectively. Late stage post-mineralization calcite also exhibited a meteoric-dominant fluid with calculated $\delta^{18}O_{H2O}$ values of -4.3 to -1.3‰ at 200°C. Fluid inclusion gas analyses showed a similar evolution on the fluid source diagrams of Norman and Moore (1999) and Blamey and Norman (2002) with N_2/Ar vs. CO_2/CH_4 and N_2/Ar vs. Ar/He ratios that plotted in near magmatic to meteoric source fields for earlier quartz and meteoric to evolved (crustal) source fields for later fluorite.

The data for the later qtz-mo veinlets that crosscut the MHBX was essentially analytically indistinguishable from the MHBX quartz for both the oxygen stable isotopes (calculated $\delta^{18}O_{H2O}$ values of 1.6-3.9‰ at 380°C) and the fluid inclusion gas analyses, therefore the veinlets experienced the same fluid evolution history as the MHBX. The veinlets exhibited widespread fluid inclusion δD_{H2O} values (-143 to -52‰) compared to the MHBX matrix, possibly due to an interstitial water contribution or analytical error associated with smaller, less abundant fluid inclusions and associated small sample peaks.

Sulfur stable isotope analyses on molybdenite, pyrite, and anhydrite revealed a pure magmatic source for Questa sulfur with $\delta^{34}S$ ranges of 0.4-2.3‰, 1.6-2.5‰, and 6.6-10.0‰, respectfully. Similarly, carbon stable isotope analysis on calcite revealed a magmatic source for carbon with calculated $\delta^{13}C_{CO2}$ values of -6.0 to -4.9‰ at 200°C. Despite a meteoric component of varying degrees to the fluid associated with these minerals, a magmatic source is possible for these two species due to the fact that meteoric water is low in sulfur or carbon, hence allowing the magmatic signature to remain with the fluid.

INTRODUCTION

The genetic origin of Climax-type porphyry molybdenum deposits (i.e. Questa, NM and Mt. Emmons, Climax, and Henderson/Urad, CO) has been debated throughout the economic geology community. Various previous fluid inclusion and/or stable isotope studies on Climax-type deposits have concluded magmatic (Kamilli, 1978; White et al., 1981; Stein & Hannah, 1985; Hannah & Stein, 1986; Carten, 1987; Stein, 1988; Carten, 1988; Cline and Bodnar, 1994; Cline and Vanko, 1995; Ross, 2002; Klemm, 2004; Seedorff and Einaudi, 2004; Klemm et al., 2008), magmatic and meteoric mixing (Hall, 1974; Smith, 1983), or evolution from magmatic to meteoric (Bloom, 1981; Rowe, 2011 or Chapter I), as the fluid origin of the system and associated molybdenite mineralization. Often, in these studies, a conclusion is made as to the origin of the system with only one data set, i.e. fluid inclusions only or stable isotopes without corresponding fluid inclusion data.

At the Questa Climax-type porphyry molybdenum system, the Goat Hill orebody consists of a magmatic-hydrothermal breccia (MHBX) and cross-cutting quartz-molybdenite stockwork veinlets. The Goat Hill MHBX is composed of five distinct stratified facies (A-E), which are defined by matrix mineralogy, and clast alteration and textures. A mineralogic and alteration zonation occurs from the bottom of the breccia and closest to the source intrusion (facies A) to the top and distal edges of the MHBX (facies D and E).

The purpose of this study was to perform a spatially and temporally constrained stable isotope and fluid inclusion gas analyses study, in combination with the fluid inclusion microthermometry of Rowe (2011) or Chapter I, of the Questa Goat Hill

orebody to determine the genetic origin of the MHBX and veinlet ore fluids, the mechanism for molybdenite mineralization, and if there was a fluid evolution for the Goat Hill MHBX that coincided with the mineralogic/alteration zonation of the MHBX facies. The spatial and temporal constraint of this study proves significant, in that previous studies did not constrain samples in terms of space and time (Bloom, 1981; Cline and Bodnar, 1994; Cline and Vanko, 1995; Klemm et al., 2004; Klemm et al., 2008). This study has additional significance in that it combines the fluid inclusion microthermometry data of Rowe (2011) or Chapter I with the corresponding stable isotope analyses and an additional data set from the fluid inclusion gas analyses. Hence, three data sets are utilized to determine the origin of the Questa Climax-type porphyry molybdenum system and its associated molybdenite mineralization.

BACKGROUND

Climax-type deposits

Climax-type deposits are high fluorine (> 0.1% F), low copper (Cu:Mo=1:100 to 1:50) porphyry molybdenum deposits that are genetically related to rhyolite/granite source intrusions of mainly mid-Tertiary age. Climax-type porphyry molybdenum deposits occur in rift zones rather than the subduction zone/orogenic belt setting of the low fluorine, higher copper (Cu:Mo=1:30 to 1:1) Quartz Monzonite-type porphyry-Mo deposits. In addition, Climax-type deposits have a higher grade (0.3-0.45% MoS_2) than the subduction related Quartz Monzonite-type (0.1-0.2% MoS_2). Climax, Henderson/Urad, and Mount Emmons, CO and Questa, NM (area of study) are classified as Climax-type porphyry-Mo deposits (White et al., 1981; Cox and Singer, 1986;

Guilbert and Park, 1986; White et al., 1990; Carten et al., 1993; Sinclair, 1995; Donahue, 2002).

Location

The Questa Climax-type porphyry molybdenum system (Questa system) is located in north-central New Mexico in the Taos Range of the Sangre de Cristo Mountains (Figure 1). The Questa system is sited on the southern flank of the Tertiary Questa Caldera in the Latir volcanic field. Mineralization of the Questa system follows a structural trend along the southern flank of the caldera, referred to as the Red River Trench, with a N70^{o}E to N75^{o}E orientation (Figure 2) (Lipman, 1992; Ross, 2002; Ross et al., 2002). Mineralization occurs as three distinct Mo deposits from west to east – the Log Cabin, Central, and Spring Gulch deposits. The Central deposit is the only site of molybdenum mining in the district. It is horseshoe-shaped and consists of two distinct ore zones, the Northeast and Southwest. Several distinct orebodies exist within these ore zones and are defined by a 0.2% MoS_2 grade cutoff (Figure 3) (Ross, 2002; Ross et al., 2002).

The Goat Hill Orebody

The Goat Hill orebody (area of study), located in the Southwest ore zone of the Central deposit at the Questa Mine, occurs between the western-most orebody (Southwest Extension) and the D-orebody of the Southwest ore zone (Figure 3). Underground mining of the Goat Hill orebody occurred from 1983 to 2000 by the block-caving method with a total production of 21.11 Mt of ore at 0.318% MoS_2 (Schilling, 1956; Bloom, 1981).

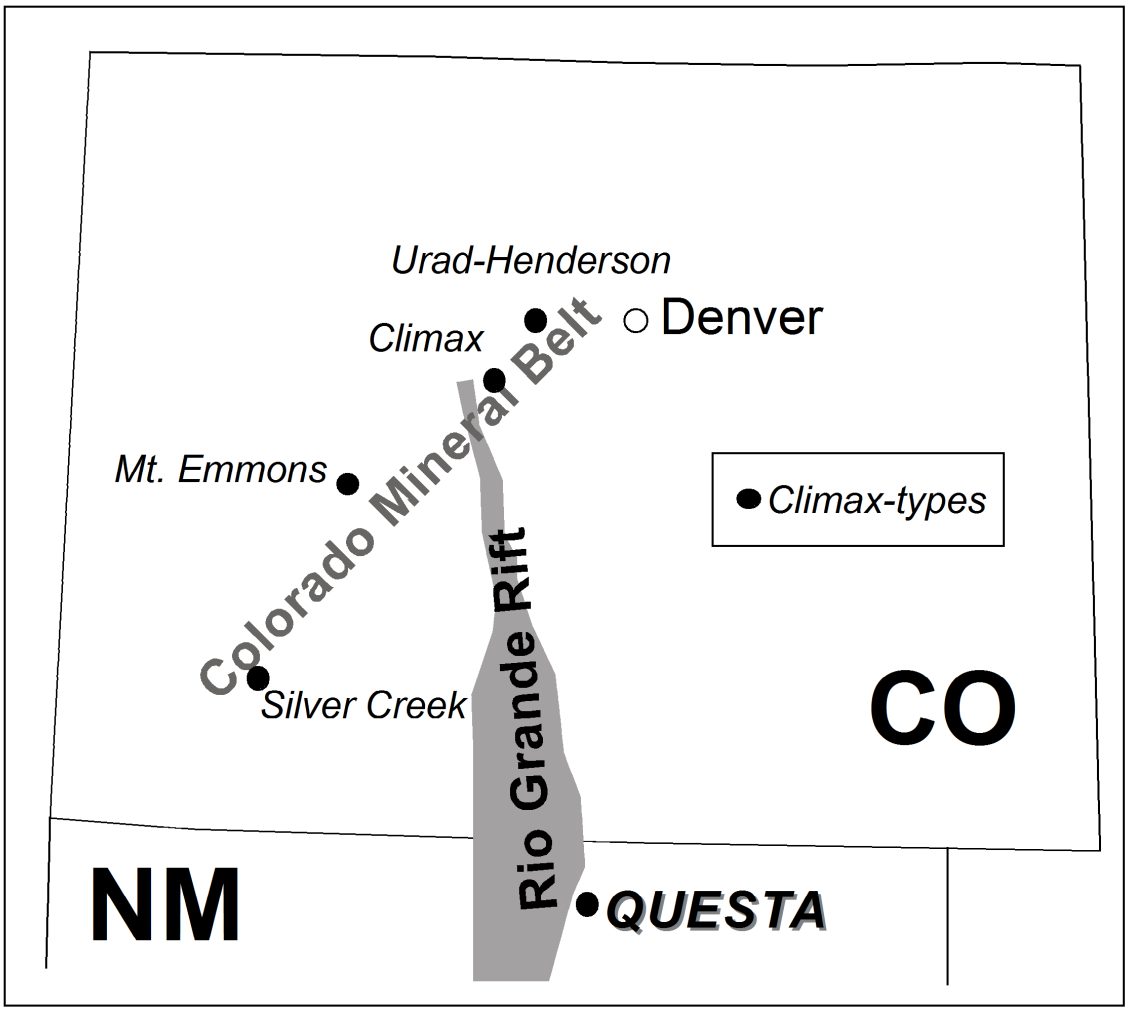

Figure 1. Mine location map showing the relative location of the Climax-type deposits of NM and CO that occur along the Rio Grande Rift. Not to scale.

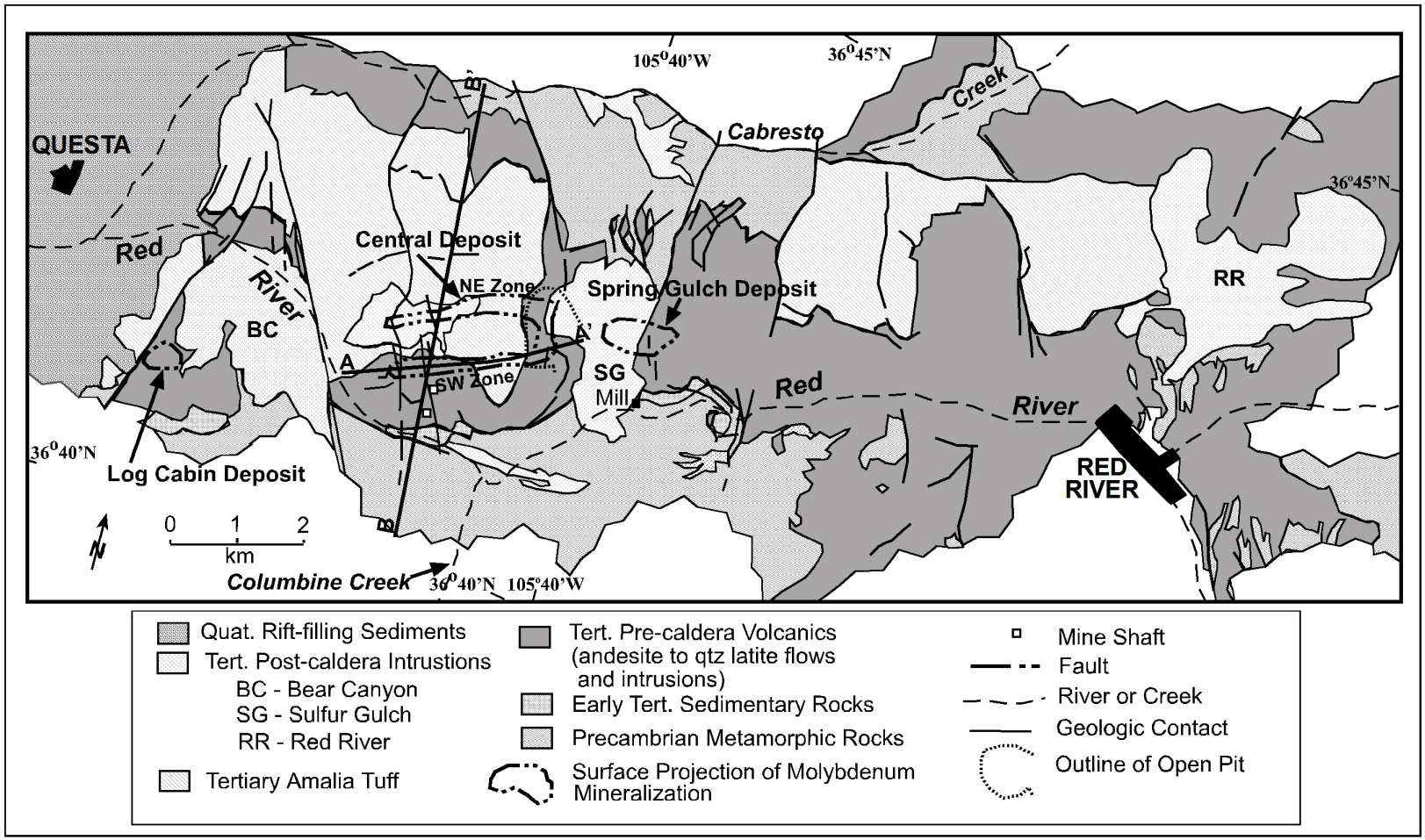

Figure 2. Geologic map of the Questa-Red River area. A-A' and B-B' are cross-section lines for Figure 3. Modified from Meyer and Foland (1991).

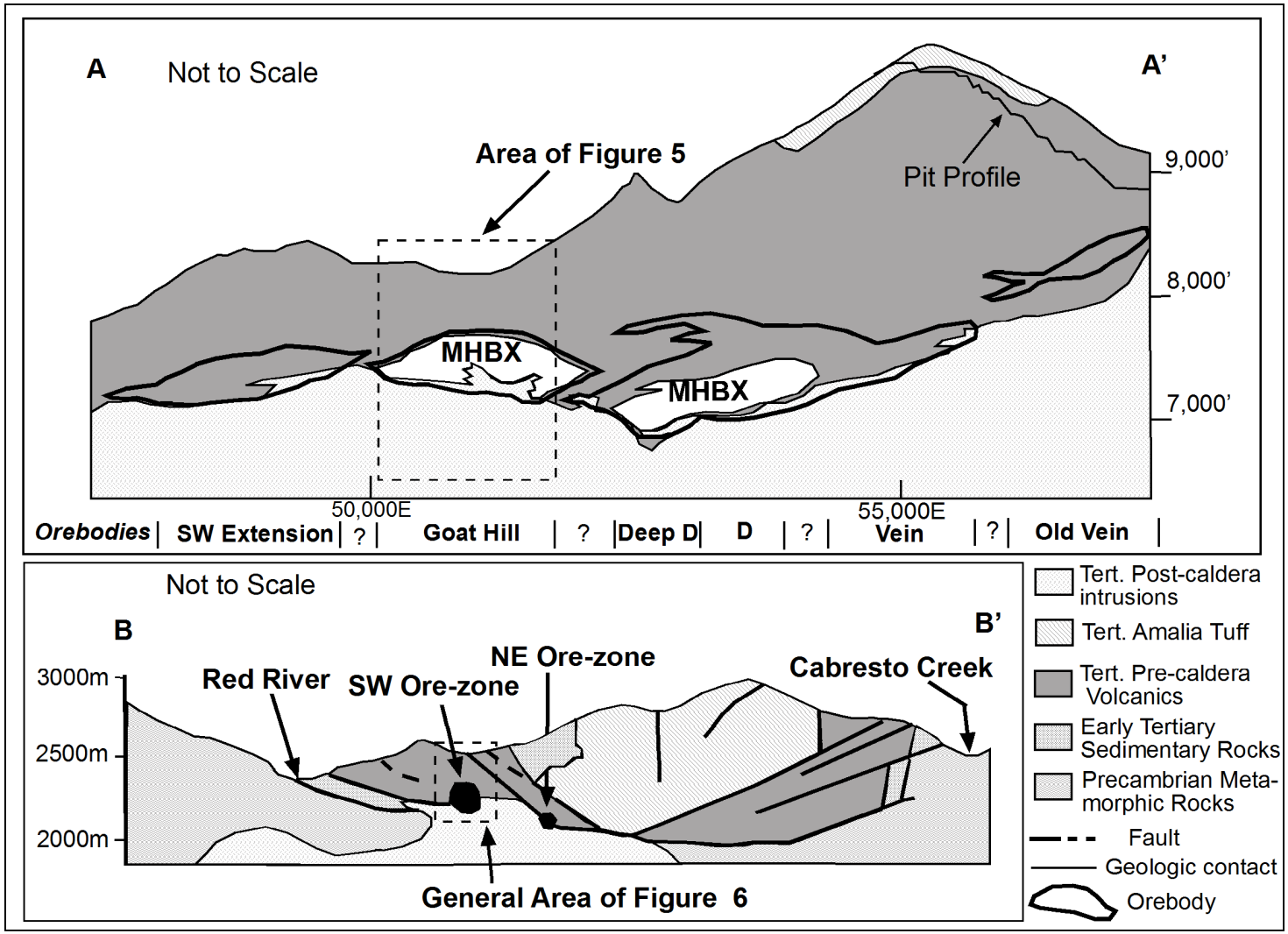

Figure 3. Respective cross-sections A-A' and B-B' from Figure 2. General areas for Figures 5 and 6 in dashed boxes. Modified from Ross (2002) and Walker (1997).

The Goat Hill orebody is hosted in a Tertiary volcanic package (Tan) consisting of interbedded andesite flows and volcaniclastic sediments, and partially in an aplitic source intrusion. Molybdenite mineralization within the Goat Hill orebody occurs within a magmatic-hydrothermal breccia (MHBX) and later quartz-molybdenite (qtz-mo) stockwork veinlets that exceed the confines of the MHBX (Figure 4). MHBX-related molybdenite mineralization contributed approximately 40% of grade (0.2% MoS_2 cutoff) to the orebody, whereas the later stockwork veinlets contributed the remaining 60% of the molybdenite mineralization (Ross, 2002; Ross et al., 2002). The Goat Hill orebody exhibits typical Climax-type porphyry alteration with that is centered on the orebody and evolves above and outward of the source intrusion. The earliest alteration occurs farthest from the source intrusion and is a regional pre-mineralization/pre-brecciation propylitization of the Tertiary andesite, associated with interaction of the country rock with meteoric water. The first alteration type associated with the intrusion of the source aplite and release of magmatic hydrothermal fluids is a poorly defined high silica zone closest to the source intrusion. Moving outward from the source intrusion in spatial and temporal order are potassic and phyllic alteration. Lastly, local argillic alteration occurred in fracture zones (Leonardson et al., 1983; Meyer, 1991).

The Magmatic-hydrothermal Breccia (MHBX)

The MHBX was formed by hydraulic fracturing of andesite and premineral dikes by ore-bearing fluids that evolved from a crystallizing water-saturated granitic magma which was emplaced at depths of 3 to 5 km (lithostatic pressures of 0.8-1.4 kbars) below surface (Ross, 2002; Ross et al., 2002; Molling, 1989; Cline and Bodnar, 1994).

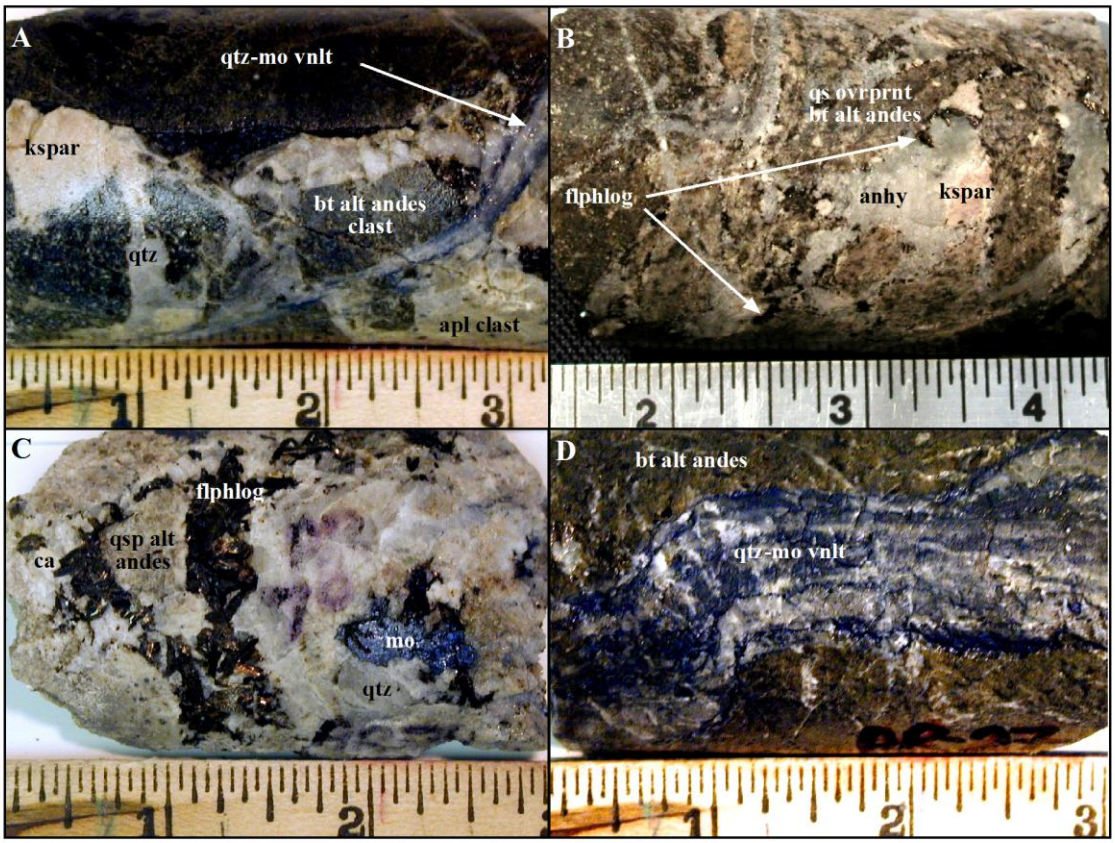

Figure 4. Hand sample photographs showing the two different types of ore and the difference between the MHBX facies. Scale in inches. Note the differences in the two end-members of the MHBX (A and E facies) and the C-facies that is intermediate between the two. (A) MHBX from A3-facies with quartz(qtz)-potassium feldspar(kspar)-trace molybdenite(mo) matrix and aplite and biotite altered andesite clasts. A qtz-mo veinlet crosscuts the MHBX. (B) MHBX from the C-facies with fluorophlogopite(flphlog)-kspar-qtz-mo-trace calcite(ca)-anydrite(anhy) matrix and biotite altered and quartz-sericite-pyrite(qsp) overprinting biotite altered andesite clasts. (C) MHBX from the E-facies with qtz-flphlog-mo-ca matrix and corroded qsp altered andesite clasts. (D) qtz-mo veinlet from unbrecciated andesite from within the orebody but outside of the MHBX.

Volumetrically, the breccia body is >$6x10^6$ m^3. It is located above and southward of the apex of an aplitic stock, which is believed to be the source for the mineralizing fluids (Figures 5 and 6). The upper contact of the breccia dips 18° to the north and is thought to follow a pre-breccia fabric, either representing a fracture zone or volcanic bedding, in which the magmatic-hydrothermal fluids were focused (Ross, 2002; Ross et al., 2002).

Ross (2002) defined 5 distinct stratified facies (A-E) within the MHBX based upon matrix mineralogy, and clast alteration and textures (Table 1; Fig. 5 and 6). Facies A occurs at the bottom of the MHBX, adjacent to the source aplite intrusion, and is divided into 3 subfacies (A_1, A_2, and A_3). Facies D and E occur at the top of the MHBX, most distal to the source intrusion. The MHBX matrix is mineralogically zoned from the bottom of the breccia and closest to the source intrusion to the top and distal edges of the breccia. The major matrix constituents of the MHBX consist of aplite, quartz, potassium feldspar and trace molybdenite in the A facies; quartz, potassium feldspar and trace molybdenite in the B facies; quartz, potassium feldspar, fluorophlogopite, calcite, molybdenite and fluorite in the C facies; quartz, fluorophlogopite, calcite, molybdenite and fluorite D and E facies. The MHBX clast alteration also evolves from the bottom of the breccia to the top and distal edges. The major alteration types in the MHBX consist of biotite and potassium feldspar alteration in the A facies; biotite alteration in the B facies; biotite alteration and quartz-sericite-pyrite (QSP) alteration in the C facies; QSP alteration overprinting biotite alteration in the D facies; and QSP alteration in the E facies. It was proposed that the differences in the breccia facies is due to evolution of the

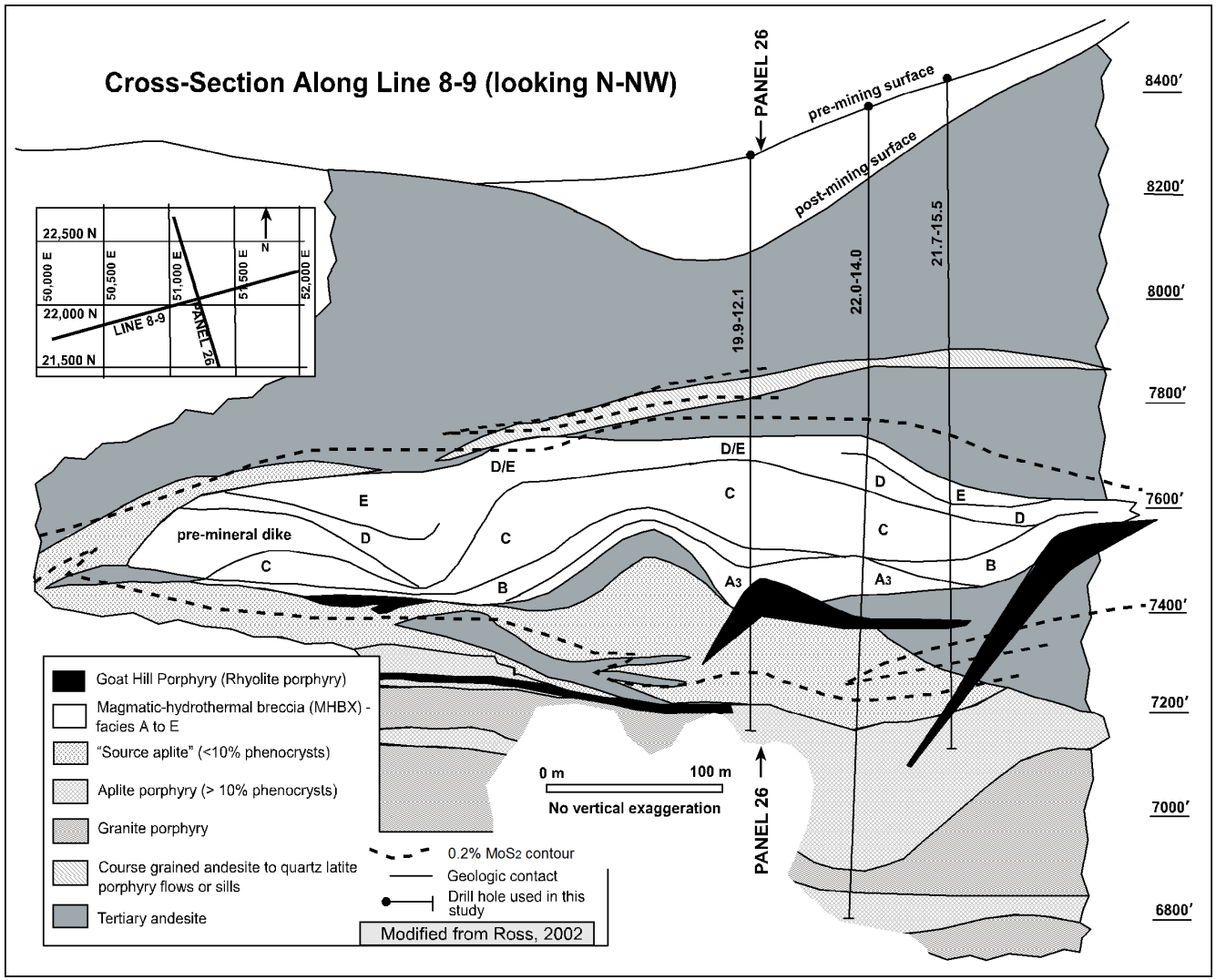

Figure 5. Long-section of the Goat Hill orebody along Line 8-9. Drillholes 19.9-12.1, 22.0-14.0 and 21.7-15.5 used in this study.

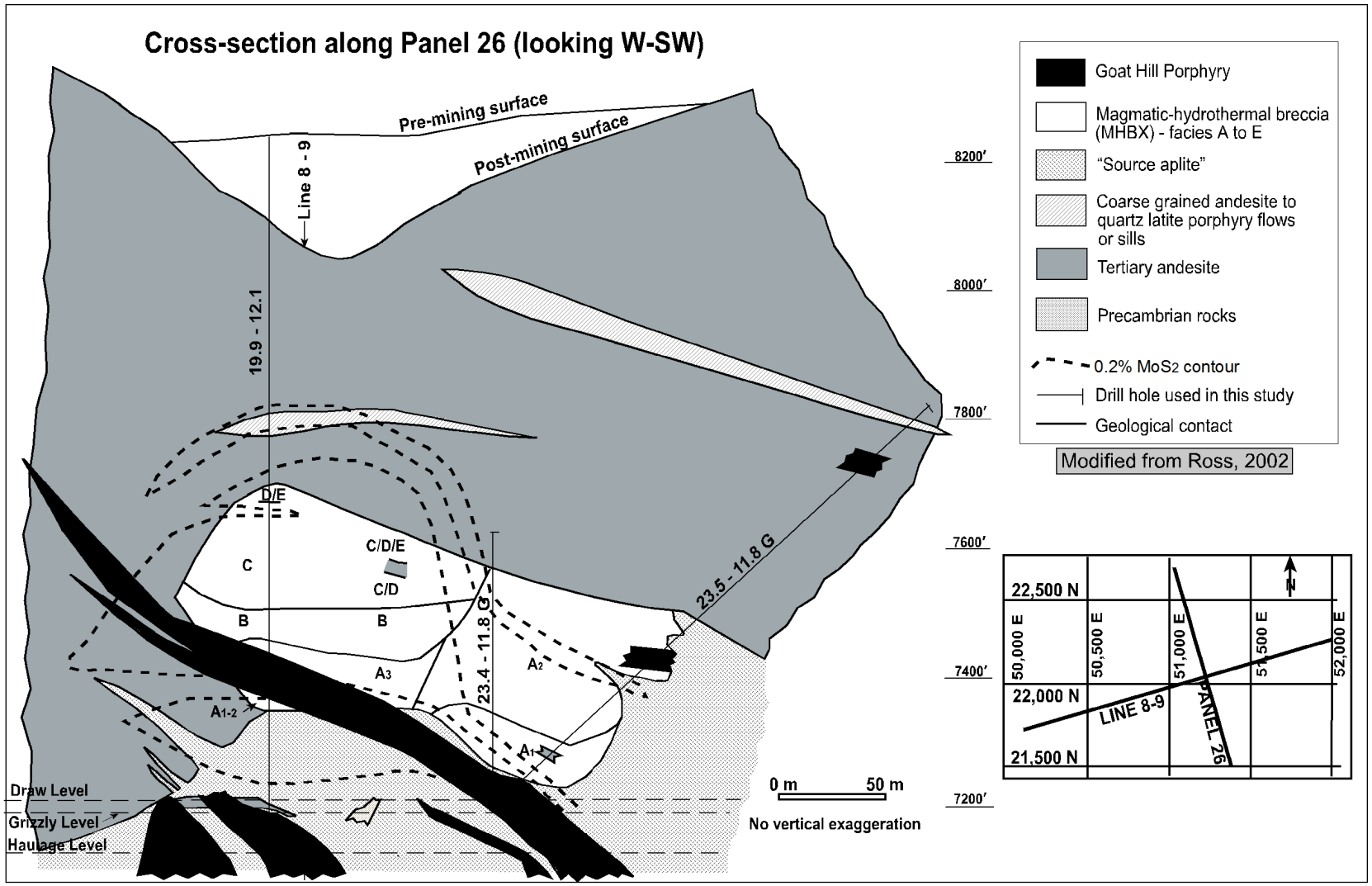

Figure 6. Short-section of the Goat Hill orebody along Panel 26. Drillholes 19.9-12.1, 23.4-22.8G and 23.5-11.8G used in this study.

Table 1. MHBX Classification by Ross et al. (2002).

MATRIX			ANDESITE FRAGMENTS				
Facies	***%***	***Composition***	***Alteration***	***Shape***	***Corrosion***	***Size (cm)***	***Fabric***
E	5 - 30	qtz, flphlog, ca, mo, +/-fl	qsp	rounded to angular	present	0.1 - 10	none
D	?	qtz, flphlog, ca, mo, +/-fl, vugs	qsp ovrprnt bt	rounded to angular	present	0.1 - 10	shingle BX
C	5 - 50	qtz, flphlog, kf, ca, mo, +/-fl	bt, qsp ovrprnt bt	rounded to angular	present	0.1 - 10	shingle BX
B	5 - 30	qtz, kf, tr mo	bt	angular	none	<1 - >10	mosaic
A_3	5 - 40	qtz-kf, tr mo, minor aplite	bt	angular	none	<1 - >10	mosaic
A_2	10 - 95	qtz-kf+/-mo>aplite	bt core, kfp margin	angular	none	2 - 20	mosaic
A_1	50 - 95	aplite, minor qtz+/-kf +/-mo	bt core, kfp margin	irregular to angular	none	3 - 30	inclusion BX

Abbreviations: BX = breccia, bt = biotite, ca = calcite, fl = fluorite, flphlog = fluorophlogpite, kf = K-feldspar, mo = molybdenite, qtz = quartz, ovrprnt = overprinting, qsp = quartz-sericite-pyrite, tr = trace

magmatic-hydrothermal fluid away from its source, differing intensities of water/rock interaction, and/or differing breccia forming processes (Ross, 2002; Ross et al., 2002).

Previous Stable Isotope and Fluid Inclusion Gas Analysis Studies on Questa

Smith (1983) performed a stable isotope and fluid inclusion gas analysis study at Questa, NM. Quartz, potassium feldspar, and biotite associated with vein mineralization were analyzed for oxygen and hydrogen stable isotopes. The sampling was not spatially or temporally constrained for this study and the MHBX was not as understood at the time of this study as it is today and was lumped in with vein mineralization. Quartz, potassium feldspar, and biotite associated with the potassic alteration stage of mineralization yielded $\delta^{18}O$ values of 6.8-12‰, 1.8-8.5‰, and 1.2-5.4‰, respectively. Quartz associated with QSP alteration yielded $\delta^{18}O$ values of 9.3 and 9.7 Biotites yielded a δD range of -110 to -117‰. The $\delta^{18}O_{water}$ from quartz associated with potassic alteration was calculated using fluid inclusion temperatures of 550°C and 400°C with $\delta^{18}O_{water}$ values of 7.8‰ and 1.6-7.6‰, respectively. The $\delta^{18}O_{water}$ from quartz associated with sericitic alteration was calculated using the fluid inclusion temperature of 320°C with values of 2.3 and 1.9‰. As observed at Climax in Hall et al. (1979), quartz and potassium feldspar were not found to be in isotopic equilibrium due to tendency of K-feldspar to exhibit isotopic exchange with later, lighter meteoric water. The stable isotope data revealed oxygen and hydrogen values that are not purely magmatic, but intermediate between magmatic and Oligocene meteoric water. Based upon this observation, Smith (1983) concluded that molybdenum mineralization originated from a mixture of magmatic and exchanged meteoric fluids.

Fluid inclusion gas analyses were performed by Smith (1983) utilizing an older method (thermal decrepitation) and older quadrupole mass spectrometer model than what was used for this study. The methods of Smith (1983) only allow for analysis of He, H_2, CO_2, CO, H_2O, H_2S, N_2, and mole% water. In addition, the Smith (1983) study occurred prior to new methods on reporting fluid inclusion gas analysis data as developed by later authors (Norman et al., 1997; Norman and Moore, 1999; Moore et al., 2001; Norman and Blamey, 2001; Blamey and Norman, 2002; Norman et al., 2002). Results indicated a lower concentration in H_2S in quartz associated with potassic alteration than the quartz associated with sericitic alteration.

Stein and Hannah (1985) and Stein (1988) reported the $\delta^{34}S$ for four molybdenite samples from Questa for Climax-type comparison studies. The four molybdenite samples had a narrow $\delta^{34}S$ range of 1.0-1.1‰. These values are consistent with a magmatic reservoir for the sulfur contributing to molybdenite mineralization at Questa.

Ross et al. (2002) performed a limited oxygen and hydrogen stable isotope study on the Goat Hill MHBX matrix quartz (9 samples) and fluorophlogopite (3 samples). The MHBX matrix quartz and fluorophlogopite exhibited a narrow $\delta^{18}O$ range of 6.8-8.6‰ and 3.2-5.7‰, respectively. The three matrix fluorophlogopites that were also analyzed for hydrogen resulted in δD values of -112, -137, and -138‰, a fairly wide range. Ross et al. (2002) calculated fractionation temperatures using quartz-mica pairs, yielding a temperature range of 380-620°C assuming a phlogopite composition or 305-515°C assuming a fluorophlogpite composition. Ross et al. (2002) did not perform a fluid inclusion study to correspond with the stable isotope study performed, but instead chose 550°C to use for $\delta^{18}O_{H2O}$ and δD_{H2O} calculations. The 550°C temperature was

chosen based upon the quartz-phlogopite fractionation temperatures, the biotite-apatite geothermometer of Molling (1989), fluid inclusion temperatures (300-600°C) of Smith (1983) and experimental studies on the liquidus of water- and F-rich granitic melts (550-600°C) of Manning (1981) and Manning and Pichavant (1984). The calculated $\delta^{18}O_{H2O}$from qtz and biotite ranged from 5.1 to 8.6‰ and 5.2 to 8.1‰, respectively. The calculated δD_{H2O} from biotite exhibited a range of -93 to -121‰. Based upon magmatic textures of the A-facies, the proximity to the source intrusion, and the $\delta^{18}O_{H2O}$ and δD_{H2O} values, Ross et al. (2002) concluded a magmatic origin to the ore-forming fluids with little to no meteoric contribution.

METHODS

Stable Isotopes

Oxygen, hydrogen, carbon, and sulfur stable isotope analyses were performed on various appropriate phases (quartz, fluorophlogopite, potassium feldspar, fluorite, calcite, molybdenite, pyrite, anhydrite, and whole rocks) from the MHBX and stockwork veinlets of the Goat Hill orebody. Stable isotope samples were collected from among five different drillholes (19.9-12.1, 21.7-15.5, 22.0-14.0, 23.4-11.8G, 23.5-11.8G) in the eastern portion of the Goat Hill MHBX (Figures 5 and 6). Three background samples (one qtz-mo veinlet and two barren pegmatitic quartz) outside of the MHBX were also taken within the source aplite stock. Paragenetic relationships between mineral phases were determined in Rowe (2011) or Chapter I prior to stable isotope sample preparations and laboratory analysis (Figure 7). In addition, quartz oxygen and hydrogen stable isotope samples are matching pairs to those utilized in the fluid inclusion study of Rowe

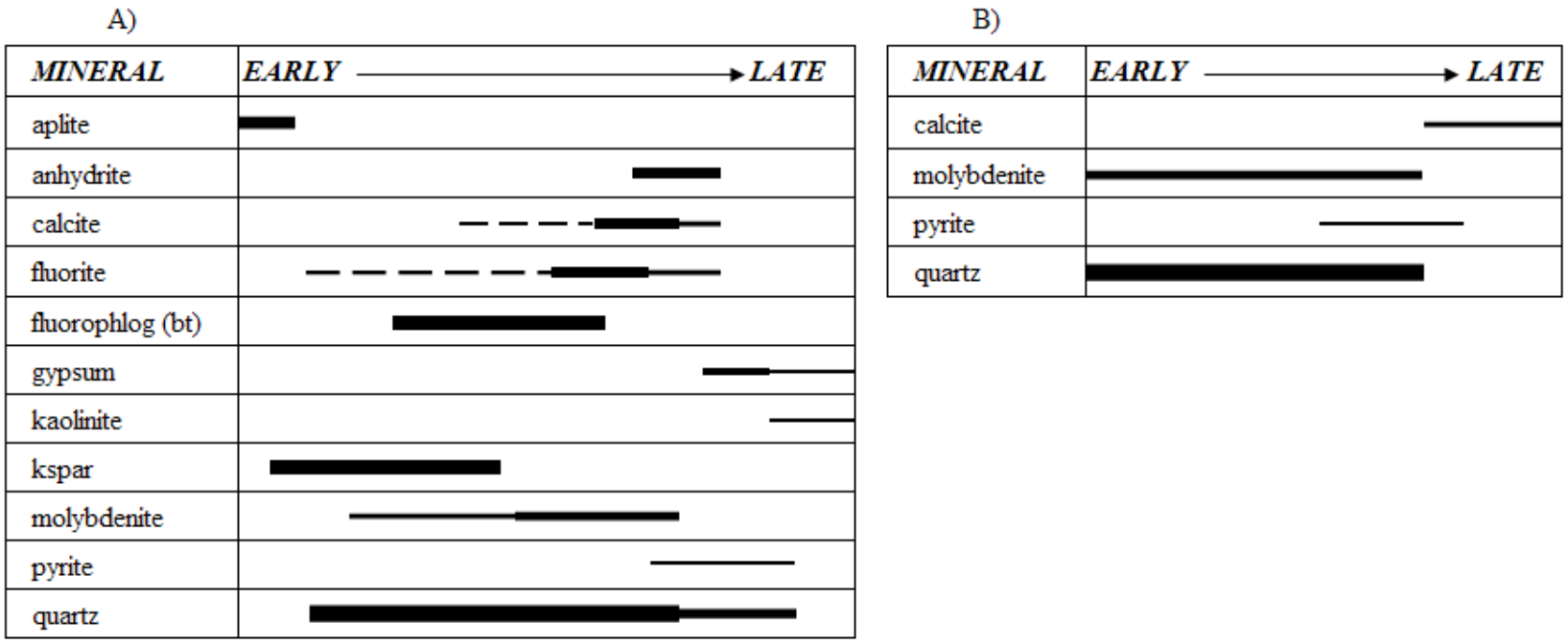

Figure 7. A) MHBX matrix paragenesis. B) Veinlet paragenesis. Thickness of line represents abundance of mineral.

(2011) or Chapter I (two matrix and two veinlet samples from each of the MHBX facies and three background samples) in order to be able to apply temperatures to oxygen and hydrogen water calculations. With the exception of quartz, which occurs in all facies of the MHBX and in veinlets, mineral phase and alteration sample locations were limited by the mineralogic and alteration evolution within the MHBX and by veinlet mineralogy. All stable isotope analyses were performed utilizing either a FinniganMAT Delta E or FinniganMAT Delta Plus XP isotope ratio mass spectrometer at the New Mexico Tech Stable Isotope Laboratory, except for hydrogen on fluorophlogopite and whole rocks, which were run by the Stable Isotope Laboratory of the University of New Mexico's Department of Earth & Planetary Sciences.

Oxygen

Oxygen stable isotope analyses were performed on 15 veinlet and 19 MHBX matrix quartz (facies A-E, Source Aplite Barren Quartz, Source Aplite veinlet), seven MHBX matrix potassium feldspar (facies A2, B, and C), 18 MHBX matrix fluorophlogopite (facies C-E), two MHBX matrix fluorite (facies C and D), 10 MHBX matrix calcite (facies C-E), and seven MHBX clast whole rocks (bt alteration from A and B facies, QSP overprinting bt alteration from C and D facies, and QSP alteration from D and E facies). Reproducibility of $\delta^{18}O$ isotope values for all mineral species analyzed was ±0.15‰ or less.

Silicates

Sample preparation for silicates (quartz, potassium feldspar, fluorophlogopite, and whole rocks) involved separation of mineral species from undesirable material, crushing with a mortar and pestle, sieving, and placing a predetermined weight of sample based

upon percent of oxygen in respective mineral in a sample vessel for analysis. Reference samples were similarly prepared and include NBS-28 (National Bureau of Standards quartz standard), NBS-30 (biotite standard) and various in-house standards. The known reference values were used to make a correction factor that was applied to the unknown samples for correction to their actual stable isotope values. The samples are baked for 8 hours at 60°C to drive off atmospheric water. After baking, the samples were reacted with ClF_3 for 8 hours at 450°C on a silicate extraction line and the oxygen converted to CO_2 by reacting with a hot carbon rod. CO_2 is transferred to the dual inlet system of either the FinniganMAT Delta E or FinniganMAT Delta Plus XP isotope ratio mass spectrometer and measured with reference to a Oztech CO_2 reference gas (Velador, 2010; Earthman, 2010).

Calcite

Calcite was reacted on a heating block at 45°C by the standard acidification technique involving 100% phosphoric acid. CO_2 was then extracted from the samples into the Gasbench system with autosampler and ran on the Finnigan MAT Delta Plus XP isotope ratio mass spectrometer in continuous flow mode. The samples are corrected to mineral standards analyzed in each run (Velador, 2010).

Fluorite

Fluid inclusion waters in fluorite were analyzed for oxygen stable isotopes. Sample preparation for fluorite involved mineral separation, baking to drive off atmospheric water, and loading small chips (40 mg) of fluorite into 3x5 mm Costech silver cups. Reference samples were also loaded into silver cups and include benzoic acid (HEKA isotope standard), NBS $BaSO_4$ standard and Hansonburg Fluorite in-house

standard. The filled sample cups were loaded into an automated turret and individually dropped into a Finnigan MAT TC/EA (high temperature carbon reduction elemental analyzer) at 1450°C. When the sample is dropped into the carbon reactor, the fluid inclusions decrepitate and release their water, which is quickly converted to H_2 and CO by the hot glassy carbon in the reactor tube. H_2 and CO are swept into the FinniganMAT Delta Plus XP isotope ratio mass spectrometer by a He carrier gas and analyzed in continuous flow mode against a carbon monoxide reference gas standard. The known reference values were used to make a correction factor that was applied to the unknown samples for correction to their actual oxygen isotope values. Due to the variability of the abundance of fluid inclusions, and hence fluid inclusion water, that exist in any given sample, the samples were also corrected for peak height/size. This ensures proper comparison to standard peak height and the most accurate stable isotope values.

Hydrogen

Hydrogen stable isotope analyses were performed on the same quartz (fluid inclusion waters), fluorophlogopite, whole rock, and fluorite (fluid inclusion waters) samples that oxygen stable isotopes were performed, for the purpose of producing oxygen and hydrogen pairs. Sample preparation for quartz and fluorite involved mineral separation, baking to drive off atmospheric water, and loading grains or small chips (~40 mg) into 3x5 mm Costech silver cups. Reference samples were also loaded into silver cups and include CH_7 (IAEA isotope standard) and benzoic acid (HEKA isotope standard). The known reference values were used to make a correction factor that was applied to the unknown samples for correction to their actual hydrogen isotope values. The analytical procedure for fluid inclusion water hydrogen stable isotope analysis is

almost exactly the same for the oxygen as described for fluorite in the previous section. The only difference is that the hydrogen is analyzed by the FinniganMAT Delta Plus XP isotope ratio mass spectrometer against a hydrogen reference gas standard. A peak height/size correction was similarly applied to the samples for hydrogen as it was for the fluid inclusion water oxygen analyses. Reproducibility of δD isotope values for fluid inclusion water analyses was quite variable. Matrix fluid inclusion δD analysis yielded a reproducibility range of 0.7 to 22.0‰, with an average of 11.8‰. Veinlet fluid inclusion δD analysis yielded a reproducibility range of 0.7 to 62.1‰ with an average of 16.5‰. Eliminating the three duplicates that yielded differences of 38.31, 38.97, and 62.1‰ would show reproducibility in veinlet fluid inclusion δD analysis of 0.7 to 19.1‰ with an average of 8.4‰.

The hydrogen stable isotope analyses on fluorophlogopite and whole rocks were performed by the Stable Isotope Laboratory of the University of New Mexico's Department of Earth & Planetary Sciences. Reproducibility of δD isotope values for fluorophlogopite and whole rocks was 1.5‰ to 7.1‰.

Carbon

Carbon stable isotopes are obtained from calcites in the same run as the oxygen.

Sulfur

Sulfur stable isotope analyses were performed on seven veinlet and 13 MHBX matrix (facies B-E) molybdenite, five veinlet and one MHBX matrix (facies B) pyrite, and seven MHBX matrix (facies C-E) anhydrite in the New Mexico Tech Stable Isotopes Laboratory. Sample preparation involved separation of mineral species from undesirable material, crushing with a mortar and pestle, and placing a predetermined weight of

sample based upon percent of sulfur in respective mineral into Costech 3x5 mm pressed tin cups. Vanadium pentaoxide (V_2O_5) (6.0 mg) was added to the anhydrite, as well as the sulfate standard, to aid in the combustion process. Reference samples were similarly prepared and include in-house pyrite, pyrrhotite, barite, and sphalerite standards. The known reference values were used to make a correction factor that was applied to the unknown samples for correction to their actual stable isotope values.

The filled tin cups were loaded into an automated turret and individually dropped into a Costech Elemental Combustion System (EA) at 1020°C and combusted to SO_2 with a pulse of high purity oxygen. The SO_2 gas is carried through a gas chromatograph and into the FinniganMAT Delta Plus XP isotope ratio mass spectrometer through a continuous flow of helium. The sample is then measured with reference to an SO_2 reference gas. Reproducibility of $\delta^{34}S$ isotope values is ±0.3‰ (Earthman, 2010).

Fluid Inclusion Gas Analysis

Fluid inclusion gas analyses were performed on the same quartz and fluorite samples in which oxygen and hydrogen stable isotope analyses and fluid inclusion microthermometry of Rowe (2011) or Chapter I were performed. Fluid inclusion volatiles were analyzed utilizing the crush-fast-scan (CFS) method as described in Norman et al. (1996) on a dual (Balzers QME125 and Pfeiffer Vacuum Prisma) quadrupole mass spectrometer system. Samples were prepared to weigh approximately 0.2g, which is about the size of the head of a matchstick. The samples were cleaned with a 10% NaOH solution and distilled water, then dried at approximately 60°C to remove any atmospheric water from the sample. An individual sample is loaded in the crusher and evacuated to a pressure of $<10^{-7}$ Torr. Crushing of the sample then involves opening

fluid inclusions with a swift crush, which in turn releases fluid inclusion volatiles. The volatiles are then quickly vacuumed to the mass spectrometer and analyzed by the dual mass spectrometer system in fast scan mode. Each sample is crushed and analyzed 5 to 20 times. The gas species analyzed are H_2, He, CH_4, H_2O, N_2, O_2, H_2S, Ar, CO_2, SO_2, and C_{2-7} organic compounds. The data is reported in mol.%.

The mass spectrometers are calibrated using commercial gas mixtures, synthetic fluid inclusions, and in-house standards. Based upon instrument calibrations, the gas-water ratios are measured better than 0.2%, and measurement precision for major gas species is <5% and approximately 10% for the minor gas species.

RESULTS

Stable Isotopes

Oxygen stable isotope analyses of MHBX matrix quartz, fluorophlogopite, K-feldspar, and calcite yielded a $\delta^{18}O$ range of 6.0-8.2‰, 2.0-5.6‰, 1.5-5.4‰, and 5.4-8.5‰, respectively (Table 2). Fluorite fluid inclusion waters produced $\delta^{18}O$ values of -4.0 and -1.7‰. Similar to the fluid inclusion data of Rowe (2011) or Chapter I, oxygen stable isotope analyses on veinlet quartz yielded $\delta^{18}O$ range (6.1-8.4‰) that was essentially analytically indistinguishable from the $\delta^{18}O_{qtz}$ for the MHBX. Whole rock $\delta^{18}O$ values for biotite altered andesite, QSP overprinting biotite altered andesite, and QSP altered andesite are -0.4-5.7‰, 0.9-3.5‰, and 0.9-3.7‰, respectively.

Hydrogen stable isotope analyses performed on MHBX matrix fluorophlogopite produced results with a δD range of -115 to -59‰ (Table 2). Fluid inclusion water δD values from MHBX matrix quartz and fluorite ranged from -101 to -71‰ and -109 to

Table 2. Oxygen and hydrogen stable isotope data for whole rocks, quartz, K-feldspar, fluorophlogopite, fluorite, and calcite. $\delta^{18}O_{H2O}$ and δD_{H2O} measured directly from fluid inclusions for fluorite. δD_{H2O} measured directly from fluid inclusions for quartz. Temperatures used for H_2O calculations are 380°C for quartz, fluorophlogopite, and Kspar (main mode of mineralization from Rowe, 2011 or Ch. I) and 200°C for calcite due its association with this temperature from Rowe, 2011 or Ch. I (Clayton et al., 1972; Zheng,1993; Zheng, 1993a; Zheng, 1999). Abbreviations: WR - whole rock qtz - quartz Kspar - potassium feldspar flphlog - fluorophlogopite fl - fluorite ca - calcite bt alt Tan - biotite altered Tertiary andesite QSP ovrprnt bt - quartz-sericite-pyrite alteration overprinting biotite alteration QSP alt Tan - quartz-sericite-pyrite altered Tertiary andesite BQ - barren quartz SA - source aplite M - matrix V - veinlet min - mineral meas - measured calc - calculated

Sample ID	Sample Media	Facies	Phase	$\delta^{18}O_{min}$ ‰	$\delta^{18}O_{H2O}$ meas ‰	δD_{min} ‰	δD_{H2O} meas ‰	$\delta^{18}O_{H2O}$ calc @ 200°C ‰	$\delta^{18}O_{H2O}$ calc @ 380°C ‰	δD_{H2O} calc @ 380°C ‰
AR-90WR	WR	A_3	Bt alt Tan	-0.4	--	-122	--	--	--	--
AR-14WR	WR	A_3	Bt alt Tan	5.7	--	-117	--	--	--	--
AR-169WR	WR	B	Bt alt Tan	2.3	--	-118	--	--	--	--
AR-86WR	WR	C	QSP ovrprnt bt	1.8	--	-106	--	--	--	--
AR-83WR	WR	C	QSP ovrprnt bt	0.9	--	-108	--	--	--	--
AR-146WR	WR	D	QSP ovrprnt bt	0.9	--	-112	--	--	--	--
AR-164WR	WR	D	QSP alt Tan	3.7	--	-117	--	--	--	--
AR-64WR	WR	E	QSP ovrprnt bt	3.5	--	-106	--	--	--	--
AR-3WR	WR	E	QSP alt Tan	0.9	--	-123	--	--	--	--
AR-97	qtz	SA	BQ	7.4	--	--	-93	--	2.9	--
AR-173	qtz	SA	BQ	7.2	--	--	-92	--	2.7	--
AR-105	qtz	A_1	M	7.9	--	--	-71	--	3.3	--
AR-112	qtz	A_1	M	7.9	--	--	-85	--	3.4	--
AR-106	qtz	A_2	M	7.8	--	--	-71	--	3.3	--
AR-118	qtz	A_2	M	7.5	--	--	-84	--	3.0	--
AR-91	qtz	A_3	M	7.5	--	--	-95	--	3.0	--
AR-93	qtz	A_3	M	7.2	--	--	-101	--	2.7	--
AR-12	qtz	B	M	8.0	--	--	--	--	3.5	--
AR-13	qtz	B	M	7.7	--	--	-90	--	3.2	--
AR-169	qtz	B	M	8.2	--	--	--	--	3.7	--
AR-131	qtz	C	M	7.7	--	--	-91	--	3.2	--
AR-8	qtz	C	M	7.9	--	--	-73	--	3.4	--
AR-10	qtz	D	M	7.7	--	--	-92	--	3.2	--
AR-164	qtz	D	M	6.0	--	--	-72	--	1.5	--
AR-6A	qtz	D	M	7.6	--	--	--	--	3.0	--
AR-78	qtz	D	M	8.0	--	--	-89	--	3.5	--
AR-5	qtz	E	M	7.6	--	--	-72	--	3.1	--
AR-64	qtz	E	M	8.1	--	--	-77	--	3.6	--
AR-174	qtz	SA	V	7.9	--	--	-81	--	3.4	--
AR-102	qtz	A_1	V	6.6	--	--	--	--	2.0	--
AR-115	qtz	A_1	V	6.1	--	--	--	--	1.6	--
AR-110	qtz	A_2	V	7.5	--	--	-52	--	3.0	--
AR-119	qtz	A_2	V	8.1	--	--	-64	--	3.6	--
AR-14	qtz	A_3	V	7.3	--	--	-113	--	2.8	--
AR-90	qtz	A_3	V	7.5	--	--	-99	--	3.0	--
AR-147	qtz	B	V	7.3	--	--	-97	--	2.8	--
AR-167	qtz	B	V	7.9	--	--	-103	--	3.3	--
AR-11	qtz	C	V	7.4	--	--	-66	--	2.9	--
AR-81	qtz	C	V	7.6	--	--	--	--	3.1	--
AR-143	qtz	D	V	7.0	--	--	-143	--	2.4	--
AR-146	qtz	D	V	7.4	--	--	-98	--	2.9	--
AR-138	qtz	E	V	7.5	--	--	-123	--	3.0	--
AR-3	qtz	E	V	8.4	--	--	-94	--	3.9	--
AR-106kspar	Kspar	A_2	M	1.5	--	--	--	--	-1.1	--
AR-118kspar	Kspar	A_2	M	1.5	--	--	--	--	-1.1	--
AR-169kspar	Kspar	B	M	2.7	--	--	--	--	0.2	--
AR-130kspar	Kspar	C	M	5.4	--	--	--	--	2.9	--
AR-131kspar	Kspar	C	M	4.8	--	--	--	--	2.3	--
AR-132kspar	Kspar	C	M	2.3	--	--	--	--	-0.2	--
AR-83kspar	Kspar	C	M	1.5	--	--	--	--	-1.1	--

Sample ID	Sample Media	Facies	Phase	$\delta^{18}O_{min}$ ‰	$\delta^{18}O_{H2O}$ meas ‰	δD_{min} ‰	δD_{H2O} meas ‰	$\delta^{18}O_{H2O}$ calc @ 200°C ‰	$\delta^{18}O_{H2O}$ calc @ 380°C ‰	δD_{H2O} calc @ 380°C ‰
AR-130bt	flphlog	C	M	4.2	--	-105	--	--	6.0	-79.3
AR-131bt	flphlog	C	M	4.4	--	-109	--	--	6.2	-84
AR-166bt	flphlog	C	M	3.9	--	-59	--	--	5.7	-33
AR-81bt	flphlog	C	M	5.6	--	-103	--	--	7.4	-77
AR-83bt	flphlog	C	M	5.1	--	-100	--	--	6.9	-74
AR-84bt	flphlog	C	M	2.7	--	-93	--	--	4.5	-68
AR-163bt	flphlog	D	M	4.1	--	-102	--	--	5.9	-77
AR-164bt	flphlog	D	M	4.4	--	-113	--	--	6.1	-88
AR-69bt	flphlog	D	M	4.5	--	-96	--	--	6.3	-71
AR-6Abt	flphlog	D	M	2.0	--	-107	--	--	3.8	-82
AR-78bt	flphlog	D	M	5.0	--	-89	--	--	6.7	-63
AR-137bt	flphlog	E	M	4.0	--	-107	--	--	5.8	-82
AR-160bt	flphlog	E	M	3.9	--	-100	--	--	5.7	-75
AR-3bt	flphlog	E	M	3.8	--	-115	--	--	5.6	-89
AR-4bt	flphlog	E	M	3.3	--	-102	--	--	5.1	-77
AR-64bt	flphlog	E	M	4.1	--	-109	--	--	5.9	-83
AR-166fl	fl	C	M	--	-1.7	--	-106	--	--	--
AR-164fl	fl	D	M	--	-4.0	--	-109	--	--	--
AR-8ca	ca	C	M	5.4	--	--	--	-4.3	--	--
AR-82ca	ca	C	M	7.7	--	--	--	-2.1	--	--
AR-166ca	ca	C	M	7.5	--	--	--	-2.3	--	--
AR-10ca	ca	D	M	7.4	--	--	--	-2.4	--	--
AR-144ca	ca	D	M	8.5	--	--	--	-1.3	--	--
AR-146ca	ca	D	M	8.3	--	--	--	-1.5	--	--
AR-164ca	ca	D	M	7.8	--	--	--	-2.0	--	--
AR-4ca	ca	E	M	8.1	--	--	--	-1.7	--	--
AR-5ca	ca	E	M	6.9	--	--	--	-2.8	--	--
AR-142ca	ca	E	M	8.4	--	--	--	-1.4	--	--

-106, respectively. Whole rock δD values from biotite altered andesite, QSP overprinting biotite altered andesite, and QSP altered andesite ranged from -122 to -117‰, -112 to -106‰, and -123 to -117‰, respectively. Unlike the quartz $\delta^{18}O$, fluid inclusion water δD values from veinlet quartz (-143 to -52‰) exhibited a larger range of values than the MHBX matrix quartz. It is intriguing that the veinlet δDs are so different considering that the fluid inclusion (Rowe, 2011 or Chapter I) and $\delta^{18}O$ data between the MHBX and veinlets exhibit no analytical differences. A couple of minor differences exist between the MHBX and veinlet quartz when looking at the fluid inclusions petrographically that might explain the difference in δDs between the two quartz phases: the veinlet fluid inclusions were smaller and less abundant than the fluid inclusions in the MHBX matrix. Smaller and less abundant fluid inclusions in the veinlets resulted in smaller sample peaks during analysis. As previously mentioned in the Methods section of this paper, the reproducibility of the fluid inclusion δDs in veinlet quartz was much more variable (0.7-62.1‰) than the MHBX quartz (0.7-22.0‰), hence the sporadic and widespread range in veinlet δDs could very well be attributed to analytical error associated with small sample peaks. Two other possibilities exist for the veinlet δD variability - these ranges are real or there is a geologic role in the range of values – and will be discussed in the Data Interpretation section of this paper.

Carbon stable isotope analyses performed on MHBX matrix calcite and sulfur stable isotope analyses performed on MHBX matrix anhydrite, molybdenite, and pyrite demonstrated a $\delta^{13}C$ range of -6.2 to -5.0‰ (Table 3) and a $\delta^{34}S$ range of 6.6-10‰, 0.4-2.3‰, and 1.6–2.5‰ (Table 4), respectively. $\delta^{34}S$ values from veinlet molybdenite and pyrite ranged from 1.1-2.0‰ and 1.7-2.5‰, respectively.

Table 3. Carbon stable isotope data. Temperature used for CO_2 calculation (Ohmoto and Rye, 1979) is from mode temperature (200°C) of Stage 4 of Rowe (2009) in which calcite is associated.
Abbreviations: min - mineral calc - calculated

Sample	Facies	Phase	$\delta^{13}C_{min}$ ‰	$\delta^{13}C_{CO2}$ calc @ 200°C ‰
AR-8ca	C	matrix	-5.5	-5.3
AR-82ca	C	matrix	-5.9	-5.7
AR-166ca	C	matrix	-5.4	-5.2
AR-10ca	D	matrix	-5.5	-5.3
AR-144ca	D	matrix	-5.9	-5.7
AR-146ca	D	matrix	-6.2	-6.0
AR-164ca	D	matrix	-5.8	-5.6
AR-4ca	E	matrix	-5.9	-5.7
AR-5ca	E	matrix	-5.9	-5.7
AR-142ca	E	matrix	-5.0	-4.9

Table 4. Sulfur stable isotope data. Abbreviations: anhy - anhydrite mo - molybdenite py - pyrite M - matrix V - veinlets min - mineral SA - source aplite

Sample	Mineral	Facies	Phase	$d^{34}S_{min}$ ‰
AR-134anhy	anhy	C	M	9.4
AR-89anhy	anhy	C	M	9.6
AR-163anhy	anhy	D	M	8.0
AR-165anhy	anhy	D	M	6.6
AR-6Aanhy	anhy	D	M	9.8
AR-139anhy	anhy	E	M	10.0
AR-141anhy	anhy	E	M	8.5
AR-150mo	mo	B	M	1.1
AR-149mo	mo	B	M	0.8
AR-130mo	mo	C	M	1.5
AR-131mo	mo	C	M	1.2
AR-80mo	mo	C	M	2.3
AR-8mo	mo	C	M	0.4
AR-163mo	mo	D	M	1.3
AR-164mo	mo	D	M	1.1
AR-78mo	mo	D	M	1.2
AR-76mo	mo	D	M	2.1
AR-165mo	mo	D	M	1.8
AR-4mo	mo	E	M	1.4
AR-64mo	mo	E	M	1.1
AR-98mo	mo	SA	V	2.0
AR-113mo	mo	A_1	V	1.1
AR-110mo	mo	A_2	V	1.3
AR-119mo	mo	A_2	V	1.6
AR-81mo	mo	C	V	1.5
AR-145mo	mo	D	V	1.3
AR-3mo	mo	E	V	1.7
AR-149py	py	B	M	1.6
AR-110py	py	A_2	V	2.2
AR-90py	py	A_3	V	2.5
AR-166py	py	C	V	1.7
AR-82py	py	C	V	2.2
AR-161py	py	E	V	1.9

Fluid Inclusion Gas Analysis

Two important criteria need to be established in order for a fluid inclusion volatile analysis to be relevant: inclusions have not leaked since the fluids were trapped and the compositions of the volatile phases were not modified during analysis (Smith, 1983; Norman et al., 1996). Due to the high diffusion rates of H_2 and He through various minerals, the occurrence of measurable amounts of H_2 and He in fluid inclusions is evidence that there has been little to no loss of fluids from inclusions after trapping (Smith, 1983; Norman and Musgrave, 1994; Norman et al., 1996). Measurable amounts of H_2 and He were detected in all the samples analyzed (Table 5), evidence that the fluid inclusions at Questa have not experienced post-entrapment modification through leakage. Predetermined sensitivity factors, peak-stripping algorithms, and in-house designed matrix-inversion programs are used to determine the concentration of each volatile species. This method, in combination with instrument calibration and QA/QC analyses, ensures that there was no modification of the fluid inclusion gases during analysis. The averages of the crushes for each sample for the fluid inclusion volatiles analyzed are presented in Table 5.

DATA ANALYSIS AND INTERPRETATION

Oxygen and Hydrogen Stable Isotopes

Oxygen Isotope Geothermometry

Oxygen mineral pairs were utilized to calculate fractionation temperatures for MHBX matrix quartz-potassium feldspar, fluorophlogopite-potassium feldspar and quartz-fluorophlogopite. Four mineral pairs were available for oxygen isotope

Table 5. Averages for fluid inclusion gas analyses. All gas species in mol % except for short-chain hydrocarbons (C_nH_n), which are in ppm. All samples are quartz except for the two samples AR-164fl and AR-166fl which are fluorite. Pearsons Correlation Coefficient (cc) of gas species versus MHBX facies is included. Average gas data for Smith (1983) samples associated with potassic and QSP alteration also included. Abbreviations: BQ - barren quartz SA - source aplite M - matrix V - veinlet

Sample	Phase	Facies	H_2	He	CH_4	H_2O	N_2	H_2S	Ar	CO_2	SO_2	O_2	C_2H_4	C_2H_6	C_3H_6	C_3H_8	C_4H_8	C_4H_{10}	C_5H_{12}	C_6H_6	C_7H_{10}	Total Gas
Correl. Coeff. (cc)	*Matrix*	*All*	*0.13*	*-0.25*	*0.12*	*0.21*	*-0.15*	*-0.11*	*-0.19*	*-0.18*	*0.11*	*-0.08*	*0.21*	*-0.07*	*-0.15*	*0.43*	*0.11*	*0.25*	*0.29*	*0.14*	*0.12*	--
AR-173	BQ	SA	0.055	0.0004	0.021	98.24	0.35	0.00037	0.0040	0.98	0.0007	0.32	0	166.88	9.23	1.22	2.03	85.42	11.29	3.76	1.63	1.76
AR-97	BQ	SA	0.034	0.0002	0.012	98.34	0.48	0.00187	0.0092	0.61	0.0006	0.45	0	572.55	14.34	0	2.64	22.17	16.21	3.07	1.43	1.66
AR-105	M	A_1	0.026	0.0003	0.012	95.19	0.70	0.00238	0.0126	2.34	0.0026	1.43	0	2564.78	160.83	0.79	4.66	39.13	32.48	6.38	2.97	4.81
AR-112	M	A_1	0.033	0.0006	0.040	98.60	0.46	0.00183	0.0053	0.74	0.0005	0.11	3.11	74.97	7.55	0.55	2.80	12.38	4.14	1.12	0.39	1.40
AR-106	M	A_2	0.037	0.0005	0.016	94.92	0.73	0.00119	0.0106	3.01	0.0022	1.13	0	1230.14	125.49	0	1.83	19.61	25.79	6.21	2.74	5.08
AR-118	M	A_2	0.047	0.0002	0.011	98.45	0.39	0.00139	0.0063	0.75	0.0003	0.31	1.03	324.60	12.77	1.93	1.23	10.20	10.13	2.08	0.98	1.55
AR-93	M	A_3	0.033	0.0002	0.013	96.16	0.83	0.00214	0.0138	2.09	0.0022	0.73	0	1095.06	74.88	0	4.29	35.15	27.59	4.64	2.13	3.84
AR-91	M	A_3	0.078	0.0005	0.073	97.90	0.36	0.00002	0.0032	1.26	0.0007	0.31	0	139.89	11.22	11.81	2.05	13.12	11.00	1.79	0.93	2.10
AR-12	M	B	0.057	0.0006	0.022	94.93	1.13	0.00050	0.0155	3.22	0.0008	0.61	0.37	105.85	39.70	7.79	0.01	3.27	7.57	14.88	4.69	5.07
AR-13	M	B	0.063	0.0004	0.026	97.51	0.55	0.00103	0.0057	1.61	0.0008	0.21	0	117.22	7.10	16.84	3.04	20.14	13.86	10.61	3.52	2.49
AR-169	M	B	0.026	0.0004	0.015	99.50	0.12	0.00045	0.0022	0.22	0.0002	0.10	0.83	35.12	0.76	0.62	1.56	10.32	6.77	1.27	0.54	0.50
AR-131	M	C	0.045	0.0005	0.023	98.51	0.30	0.00203	0.0036	0.84	0.0005	0.25	0	163.05	11.60	3.01	1.16	11.87	14.80	2.61	1.39	1.49
AR-166fl	M	C	0.043	0.0002	0.014	99.46	0.08	0.00005	0.0019	0.02	0.0001	0.23	113.23	47.56	0	0.68	1.88	1203.92	23.00	4.21	1.45	0.54
AR-8	M	C	0.044	0.0001	0.035	97.14	0.18	0.00042	0.0025	2.59	--	--	--	--	--	--	--	--	--	--	--	2.86
AR-10	M	D	0.053	0.0003	0.052	98.76	0.32	0.00092	0.0035	0.67	0.0003	0.13	2.15	44.80	2.64	22.41	3.45	20.50	16.74	4.46	1.46	1.24
AR-78	M	D	0.034	0.0003	0.066	96.24	1.21	0.00252	0.0141	1.64	0.0014	0.66	1.34	1239.31	57.78	9.04	3.71	27.13	23.33	7.40	2.86	3.76
AR-6A	M	D	0.041	0.0002	0.009	97.30	0.56	0.00247	0.0123	1.15	0.0008	0.78	0	1356.65	65.17	0	1.44	23.40	22.11	5.48	2.83	2.70
AR-164fl	M	D	0.059	0.0001	0.012	99.28	0.11	0.00093	0.0026	0.04	0.0004	0.35	50.07	172.40	0	6.48	5.30	1145.55	63.92	3.53	1.58	0.72
AR-164	M	D	0.057	0.0002	0.015	98.48	0.32	0.00003	0.0026	0.92	0.0003	0.19	0	70.74	0	4.27	5.25	67.99	28.95	2.88	1.08	1.52
AR-5	M	E	0.045	0.0005	0.025	98.14	0.41	0.00124	0.0043	1.13	0.0004	0.24	0	100.27	6.69	17.48	1.19	12.49	14.23	3.76	1.43	1.86
AR-64	M	E	0.030	0.0002	0.016	98.18	0.29	0.00116	0.0067	0.69	0.0008	0.66	0	1107.97	41.38	0	2.68	23.89	18.86	3.97	1.98	1.82
Average	**M**	**All**	**0.045**	**0.0003**	**0.025**	**97.68**	**0.47**	**0.00119**	**0.007**	**1.26**	**0.0008**	**0.46**	**8.61**	**536.49**	**32.46**	**5.25**	**2.61**	**140.38**	**19.64**	**4.71**	**1.90**	**2.32**
Average w/out Fl	**M**	**All**	**0.044**	**0.0003**	**0.026**	**97.50**	**0.51**	**0.00126**	**0.007**	**1.39**	**0.0009**	**0.480**	**0.49**	**583.88**	**36.06**	**5.43**	**2.50**	**25.45**	**16.99**	**4.80**	**1.94**	**2.50**
AR-174	V	SA	0.060	0.0004	0.012	98.62	0.22	0	0.0025	0.74	0.0005	0.33	0	173.30	2.81	0.43	2.28	16.22	13.60	2.33	1.15	1.38
AR-102	V	A_1	0.047	0.0002	0.103	98.78	0.46	0.00106	0.0092	0.43	0.0002	0.15	0	198.65	1.53	5.72	2.45	16.40	11.56	1.99	0.84	1.22
AR-110	V	A_2	0.068	0.0003	0.047	98.36	0.95	0.00276	0.0138	0.41	0.0002	0.13	0	157.31	2.05	0	4.28	15.93	7.32	1.35	0.61	1.64
AR-119	V	A_2	0.048	0.0008	0.051	99.00	0.28	0.00068	0.0030	0.50	0.0001	0.11	1.21	51.91	3.21	9.82	0.43	4.33	7.23	2.00	0.60	1.00
AR-14	V	A_3	0.063	0.0009	0.030	94.96	0.98	0.00038	0.0113	3.42	0.0017	0.50	0	172.88	34.61	71.74	0.39	2.12	9.76	9.40	3.39	5.04
AR-90	V	A_3	0.086	0.0006	0.033	95.47	1.62	0.00280	0.0256	2.27	0.0011	0.44	0	465.48	35.42	0	5.45	19.47	11.21	3.99	1.60	4.53
AR-147	V	B	0.042	0.0009	0.086	97.80	0.48	0.00050	0.0070	1.42	0.0008	0.16	2.47	66.02	4.78	5.41	2.87	17.23	12.29	1.87	0.90	2.20
AR-167	V	B	0.031	0.0005	0.018	97.66	0.53	0	0.0050	1.43	0.0006	0.31	0	125.13	13.09	8.75	2.53	14.20	8.07	2.60	1.15	2.34
AR-81	V	C	0.033	0.0004	0.016	98.70	0.58	0.00042	0.0076	0.47	0.0002	0.19	0.05	69.70	2.68	5.60	1.97	9.37	6.27	1.24	0.57	1.30
AR-11	V	C	0.032	0.00004	0.342	98.28	0.19	0.00063	0.0043	1.14	--	--	--	--	--	--	--	--	--	--	--	1.72
AR-143	V	D	0.014	0.0001	0.005	99.72	0.08	0.00040	0.0014	0.10	0.0001	0.08	0.09	40.17	0.95	0.25	0.50	4.17	4.60	0.81	0.40	0.28
AR-146	V	D	0.039	0.0003	0.054	99.21	0.17	0.00015	0.0019	0.39	0.0002	0.13	0.17	46.24	0.47	9.13	1.78	9.68	6.89	2.15	0.80	0.79
AR-3	V	E	0.062	0.0003	0.038	99.14	0.35	0.00119	0.0053	0.30	0.0002	0.10	7.66	29.03	0	15.94	2.36	11.72	4.95	2.68	0.94	0.86
AR-138	V	E	0.024	0.0001	0.002	99.66	0.09	0.00026	0.0017	0.07	0.0001	0.14	0.22	59.55	0	0.02	0.78	6.05	5.21	0.84	0.41	0.34
Average	**V**	**All**	**0.046**	**0.0004**	**0.060**	**98.239**	**0.499**	**0.001**	**0.007**	**0.93**	**0.0005**	**0.21**	**0.91**	**127.34**	**7.82**	**10.22**	**2.16**	**11.30**	**8.38**	**2.56**	**1.03**	**1.76**
Average	**M & V**	**All**	**0.045**	**0.0004**	**0.039**	**97.902**	**0.482**	**0.001**	**0.007**	**1.13**	**0.0007**	**0.36**	**5.58**	**375.31**	**22.75**	**7.20**	**2.43**	**89.53**	**15.20**	**3.86**	**1.56**	**2.10**
Smith (1983) Avg.	K Alteration		0.041	0.00007	--	99.20	0.027	0.041	--	0.64	0.033	--	--	--	--	--	--	--	--	--	--	0.80
Smith (1983) Avg.	QSP Alteration		0.05	--	--	97.55	0.09	0.84	--	0.895	0.515	--	--	--	--	--	--	--	--	--	--	2.45

geothermometry using quartz and potassium feldspar. The resultant temperatures, calculated utilizing Zheng (1993), O'Neil and Taylor (1969), Zheng (1993) and Clayton et al. (1972), were too low (<125°C) and/or too high (>>600°C) for the system, indicating that quartz and K-feldspar were not in isotopic equilibrium. The disequilibrium demonstrated by the temperatures that were too low can most likely be attributed to the susceptibility of feldspars to post-deposition alteration and corresponding isotopic exchange.

Six quartz-fluorophlogpite mineral pairs were utilized to calculate fractionation temperatures utilizing quartz-fluorophlogopite and quartz-phlogopite fractionation equations. The calculated quartz-fluorophlogopite fractionation temperatures ranged from 270-475°C with one outlier of >600°C (370°C average) (Clayton and Keiffer ,1991 and Chacko, 1996), 250-402°C (311°C average) (Fortier, 1994 and Sharp and Kirchner, 1994), and 200-350°C (265°C average) (Zheng, 1999 and Fortier, 1994). All of the temperature ranges derived from the quartz-fluorophlogopite equations correlate with fluid inclusion temperatures and Stages 1 through 3 of Rowe (2011) or Chapter I, however the temperatures (270-475°C, 370°C average) of Clayton & Keiffer (1991) and Chacko (1996) best correlated with established temperatures for the system (Rowe, 2011 or Chapter I) (Figure 8). The temperatures calculated for quartz-phlogopite, rather than fluorophlogopite, where too high with an average temperature of 740°C (Zheng 1993 and 1993a).

MHBX Facies

It was hypothesized that the oxygen stable isotope data would reflect the mineralogic/alteration evolution that occurs within the Goat Hill MHBX (Ross, 2002),

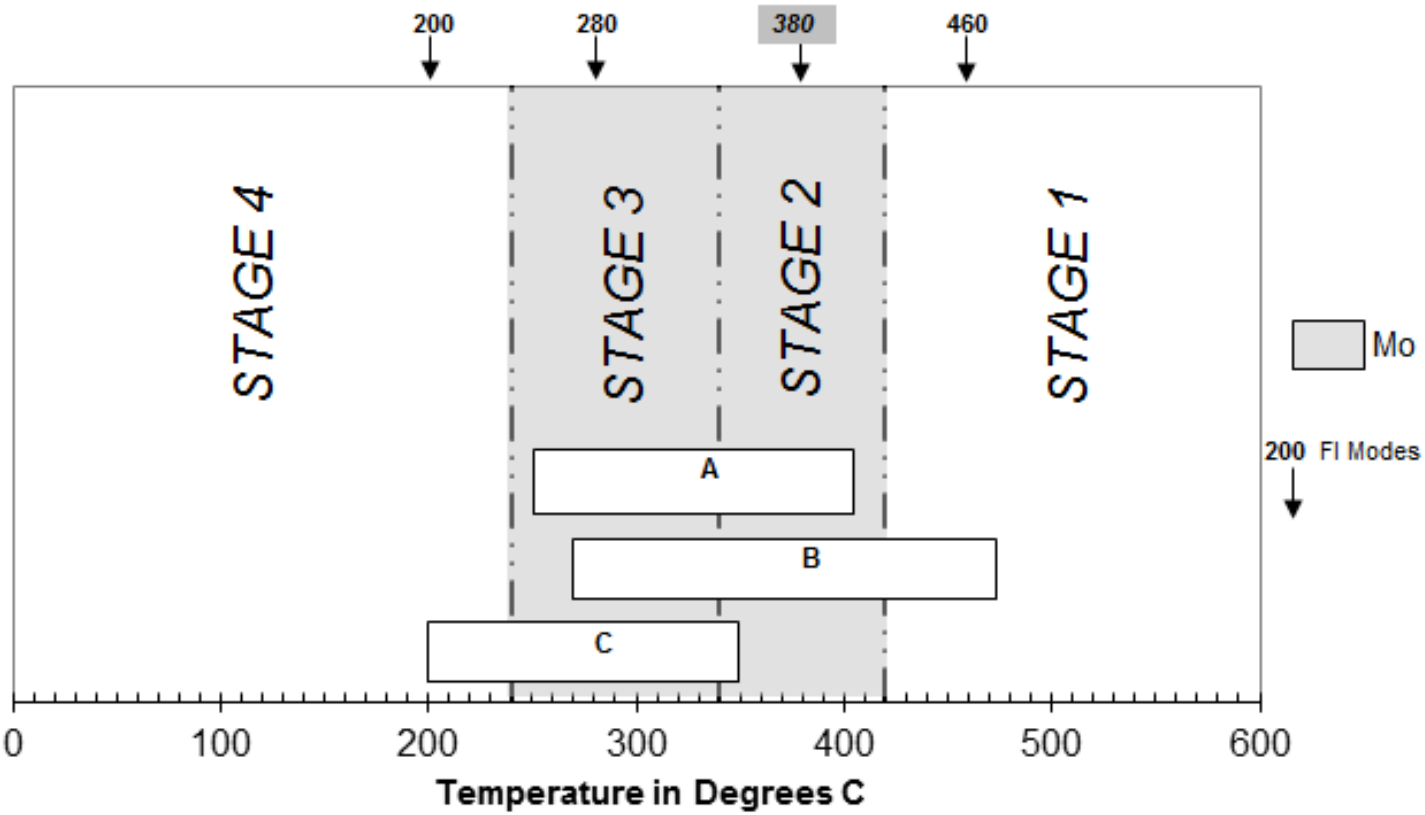

Figure 8. Fluid inclusion temperatures, stages, and modes of Rowe (2011) or Ch. I with quartz-fluorophlogopite oxygen stable isotope fractionation temperature ranges calculated from A) Fortier (1994) and Sharp & Kirschner (1999), B) Clayton & Keiffer (1991) and Chacko (1996), and C) Zheng (1999) and Fortier (1994). Shaded areas are stages of molybdenite mineralization from Rowe (2011) or Ch. I. Arrows indicate fluid inclusion Th modes within stages. 380°C mode is shaded because it is the largest Th mode in the data set and is considered to be the main mode of mineralization. Stages 1 and 2 are associated with potassic alteration and Stages 3 and 4 are associated with phyllic or QSP alteration.

with the heaviest, most magmatic values occurring closest to the source intrusion (Facies A and B) and the lightest, more meteoric stable isotope values occurring most distal to the source intrusion (Facies D and E). Whole rock analysis results for MHBX clasts of the three major alteration types (biotite, QSP overprinting biotite, and QSP) from bottom of the MHBX to the top (facies A_3-E) did not support this hypothesis (Table 2 and Figure 9). The biotite (facies A_3 and B)(-0.4-2.3‰) and QSP (facies D and E)(0.9-3.7‰) altered clasts do not demonstrate the heaviest and lightest values, respectively, but rather a variable range. In addition, the intermediate QSP overprinting biotite alteration (0.9-3.5‰) does not fall in between the two end member alteration values, but rather overlaps the other two alteration types. The lack of any evolutionary pattern in the clast stable isotope values based upon alteration type and/or facies may be due to the fact that the samples were whole rock bulk analysis and may contain variable amounts of relict potassium feldspar from early potassic alteration or accessory minerals such as magnetite, etc. that contributed to a result that was different than expected. It may also be that this hypothesis is wrong. A Pearson's correlation was used in an attempt to quantify the degree of correlation between facies and alteration types, $\delta^{18}O_{WR}$, and δD_{WR}, or the lack thereof. If the absolute value of a correlation coefficient (|cc|) is 0.5 and greater, then it is considered to represent a correlation between the variables. All |cc|s between facies and other variables were <0.5, with values of 0.05-0.28, demonstrating that there is no facies correlation with alteration type, $\delta^{18}O_{WR}$, or δD_{WR}.

Oxygen and hydrogen stable isotopes are especially valuable when they are used in conjunction with fluid inclusion temperatures to calculate the $\delta^{18}O_{H2O}$ and δD_{H2O} values of the mineralizing fluids which can constrain the source (magmatic, meteoric, or

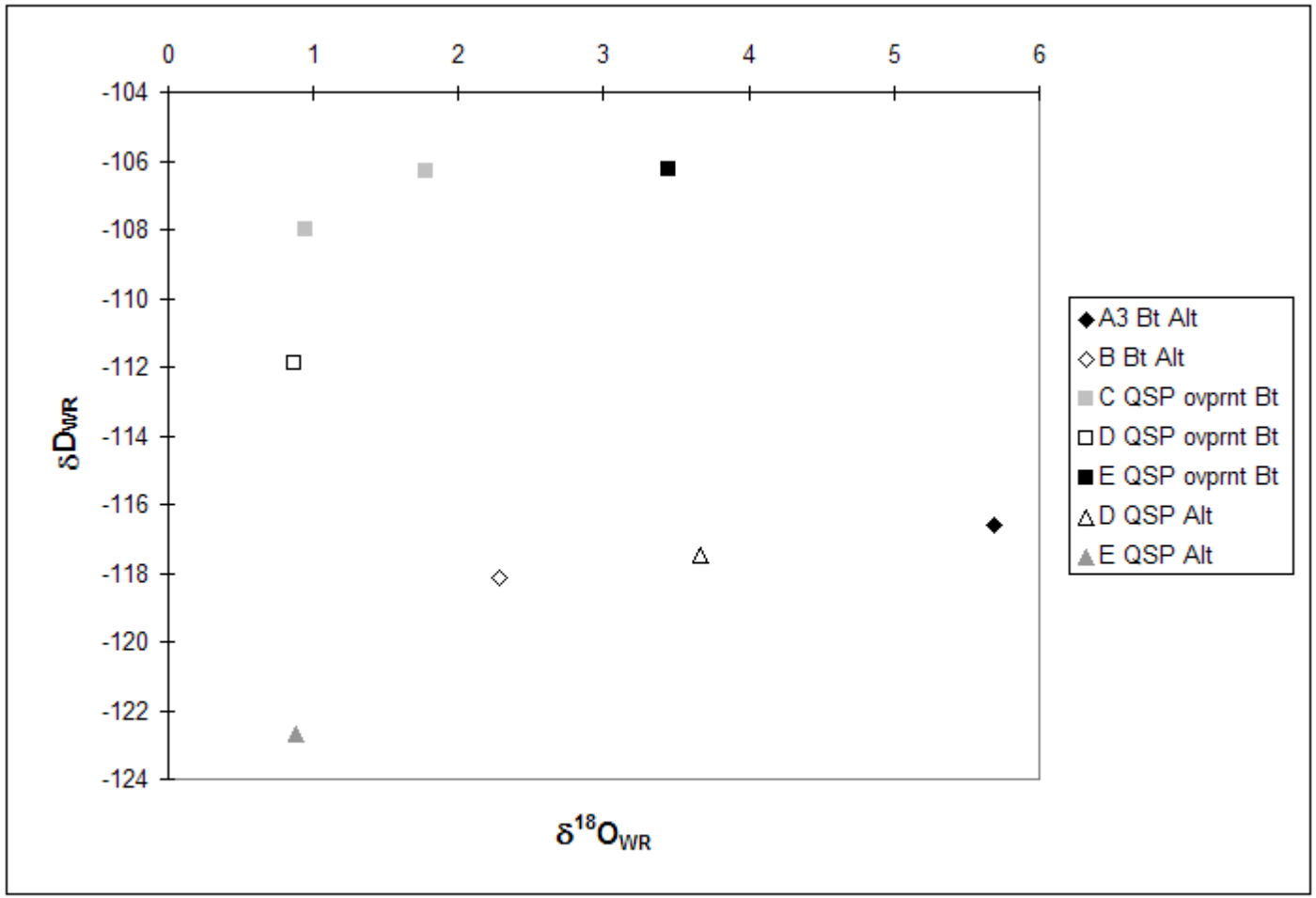

Figure 9. δD vs. $\delta^{18}O$ for whole rocks. No evolutionary pattern is evident based upon facies and/or alteration type.

both) and evolution of the fluid in the ore-forming system (Table 2). The $\delta^{18}O_{H2O}$ values for MHBX quartz (1.5-3.7‰), fluorophlogopite (3.8-6.9‰), and K-feldspar (-1.1-2.9‰) were calculated at 380°C, using the equations of Clayton et al. (1972), Zheng (1993), and Zheng (1993a), respectively. 380°C was chosen because it is the main mode temperature for the associated fluid inclusion data of Rowe (2011) or Chapter I and is related to Stage 2 of Rowe (2011) or Chapter I, a main stage of molybdenite mineralization that is also associated with those minerals (Figure 8). Similarly, 380°C was also chosen to calculate the δD_{H2O} for the fluorophlogopites (-89 to -33‰) using the equation of Suzuoki & Epstein (1976). The $\delta^{18}O_{H2O}$ for fluorite was taken directly from fluid inclusion waters, as mentioned in the previous sections. The associated fluid inclusion temperature for those same fluorite samples is 200°C from Stage 4 of Rowe (2011) or Chapter I. 200°C was used to calculate the $\delta^{18}O_{H2O}$ of calcite (-4.3 to -1.3‰) using the equation of Zheng (1999), due to it being syn-genetic or post-genetic with fluorite in the Goat Hill MHBX paragenetic sequence (Figure 7 and 10). Hence, calcite would have a similar, if not lower, temperature of deposition. The δD_{H2O} for quartz and fluorite were taken directly from fluid inclusion waters, as mentioned in the previous sections.

No evolutionary pattern is evident in the quartz $\delta^{18}O$ and δD calculated waters based upon facies, opposite of what was hypothesized (Figure 11). The quartz data exhibit a very tight range of $\delta^{18}O_{H2O}$ and a slight variation in δD_{H2O}, with a random distribution of the facies. A Pearson's correlation was performed on the quartz hydrogen and oxygen data to determine if the data has a correlation between facies. The |cc| was 0.02 for the oxygen data and 0.23 for the hydrogen data, revealing there is no facies correlation with the quartz oxygen and hydrogen stable isotope data. In addition, there is

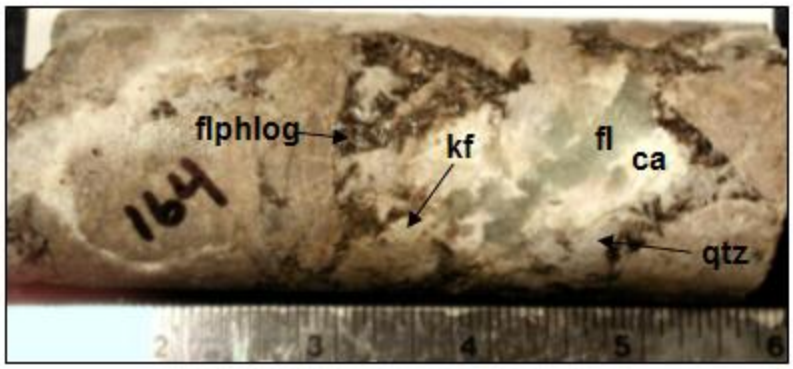

Figure 10. Sample AR-164 demonstrating mineral paragenesis: kf→flphlog→qtz→fl→ca. Scale is in inches.

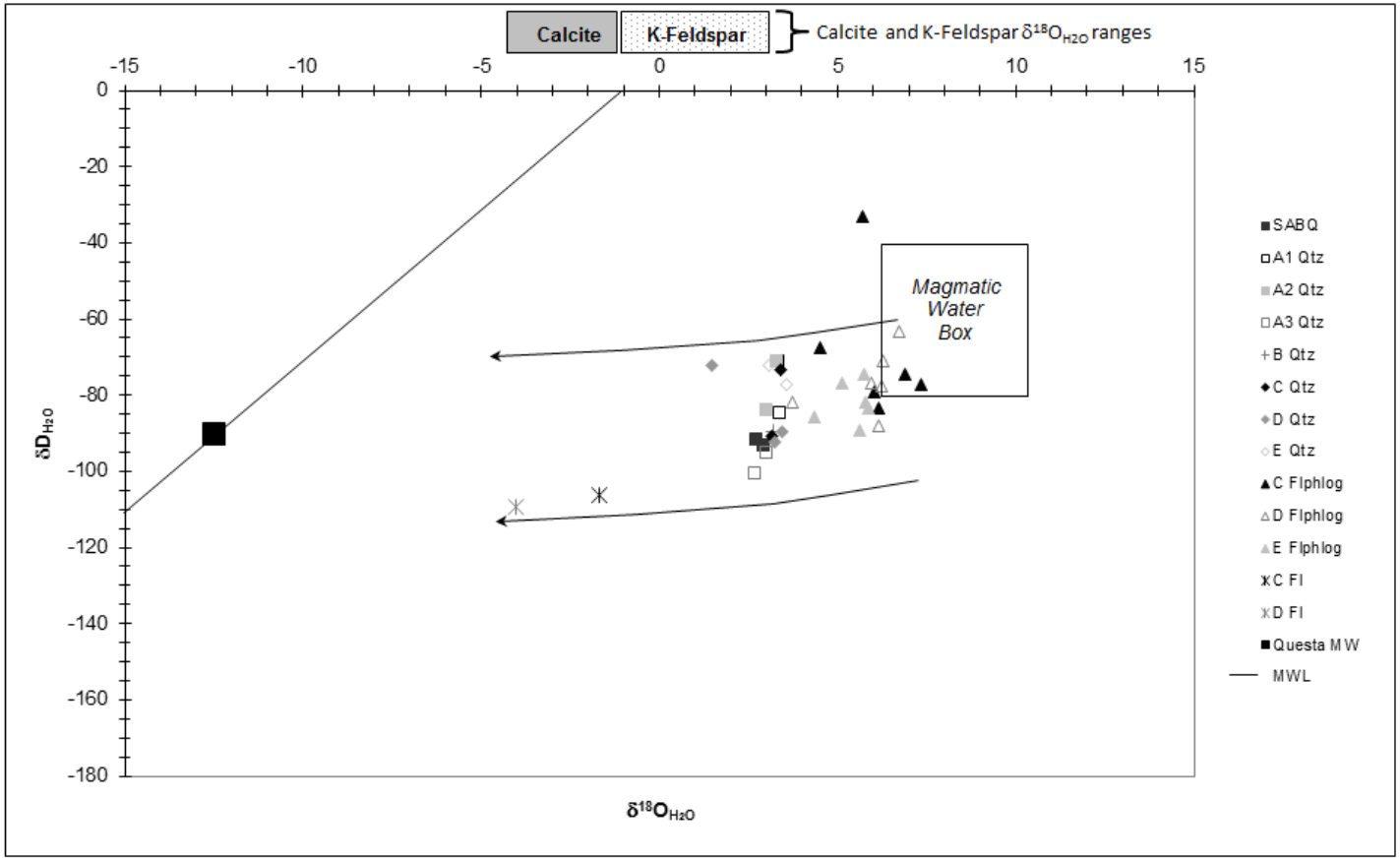

Figure 11. $\delta^{18}O_{H2O}$ vs. δD_{H2O} of matrix minerals by facies. $\delta^{18}O_{H2O}$ for quartz, fluorophlogopite and K feldspar calculated at 380°C. $\delta^{18}O_{H2O}$ for calcite calculated at 200°C. δD_{H2O} for fluorophlogopite calculated at 380°C. See text for reason for temperatures and references. δD_{H2O} for quartz and fluorite was taken directly from fluid inclusion water. No evolutionary pattern based upon facies is evident in either quartz or fluorophlogopite. Evolution is apparent between the different mineral phases of the MHBX paragenesis (fluorophlogopite→quartz→fluorite→ calcite). The exception to this trend is K-feldspar, which is lighter than expected due to post-deposition alteration. Arrows in the diagram show the evolution of the different mineral species from magmatic to magmatic-dominated magmatic-meteoric mixing to meteoric-dominated magmatic-meteoric mixing. Magmatic water box from Taylor (1997). Questa meteoric water is the mid-Tertiary meteoric water for the area from Johnson et al. (1990).

no facies correlation with the fluorophlogpite oxygen and hydrogen stable isotope data (Figure 11). The fluorophlogopite $\delta^{18}O_{H2O}$ data is slightly wider spread than the $\delta^{18}O_{H2O}$ data of quartz. The fluorophlogopite $\delta^{18}O_{H2O}$ data also exhibits a random facies distribution with the C-facies containing the heaviest and one of the lightest $\delta^{18}O_{H2O}$ values and the D-facies containing the lightest $\delta^{18}O_{H2O}$ value. The δD_{H2O} values have a similar spread as the quartz, also with a random facies distribution. A Pearson's correlation was also performed on the fluorophlogpite $\delta^{18}O$ and δD data versus facies, with a |cc| of 0.33 and 0.43, respectively. This indicates no facies correlation with the oxygen and hydrogen stable isotope data for fluorophlogopites.

Similarly to the stable isotope data of this study, the associated fluid inclusion data in Rowe (2011) or Chapter I demonstrated no evolutionary pattern in quartz based upon facies. Rowe (2011) or Chapter I did conclude however, that there is an evolution between the mineral phases of the MHBX matrix paragenetic sequence (quartz and fluorite), which in turn does reflect the mineralogic evolution of the Goat Hill MHBX. Likewise, the evolution between the different mineral phases is evident in the oxygen and hydrogen stable isotope data of fluorophlogopite, quartz, K-feldspar, fluorite, and calcite, where the minerals that are first in the paragenetic sequence (fluorophlogopite, quartz, and K-feldspar) are the heaviest, most magmatic, and the minerals last in the paragenetic sequence (fluorite and calcite) are the lightest, least magmatic with meteoric input (Figure 11). K-feldspar is lighter than would be expected, however, especially since it is first in the paragenetic sequence and occurs in the facies closest to the source intrusion. The lighter values are most likely due to the susceptibility of feldspars to post-deposition alteration and isotopic exchange.

A good example of the oxygen and hydrogen isotope data reflecting the mineralogic evolution of the MHBX is AR-164, which has results for fluorophlogopite ($\delta^{18}O_{H2O}$=6.1 and δD_{H2O}=-88‰), quartz ($\delta^{18}O_{H2O}$=1.5 and δD_{H2O}=-72‰), fluorite ($\delta^{18}O_{H2O}$=-4 and δD_{H2O}=-109‰), and calcite ($\delta^{18}O_{H2O}$=-4.3‰) (Figure 10, Figure 11, and Table 2). As you can see, fluorophlogopite is first in the paragenetic sequence and has the most magmatic values, with minimal magmatic-meteoric mixing. Quartz, which is next in the paragenetic sequence, is less magmatic with more meteoric input than the fluorophlogopite and is evolving towards Questa paleo-meteoric water (Johnson et al., 1990). Fluorite, next in mineral paragenesis, resulted in values that reflect even more of a meteoric input, placing these values even closer to Questa paleo-meteoric water. Lastly, calcite had the lightest, most meteoric $\delta^{18}O_{H2O}$ values and is last in the mineral paragenesis.

In summary, an evolution is apparent demonstrating that the minerals that are first in the paragenesis of the Goat Hill orebody are the most magmatic, and as paragenesis evolves, so do the isotopic values of the fluid from predominantly magmatic to magmatic-dominant magmatic-meteoric mixing to a meteoric-dominant mixed magmatic-meteoric fluid (Figure 12). In addition, based upon the fact that there is no correlation or evolutionary pattern in the quartz data based upon facies, but there is an evolution evident between the different mineral phases of the MHBX, it appears that performing oxygen and hydrogen stable isotope analyses on the different mineral phases of the MHBX is what reflects the mineral evolution of this system. The main mode of molybdenite mineralization is associated with Stage 2 of Rowe (2011) or Chapter I at 380°C and a $\delta^{18}O_{H2O}$ and δD_{H2O} range of 7.4‰ (from fluorophlogopite) to 1.5‰ (from

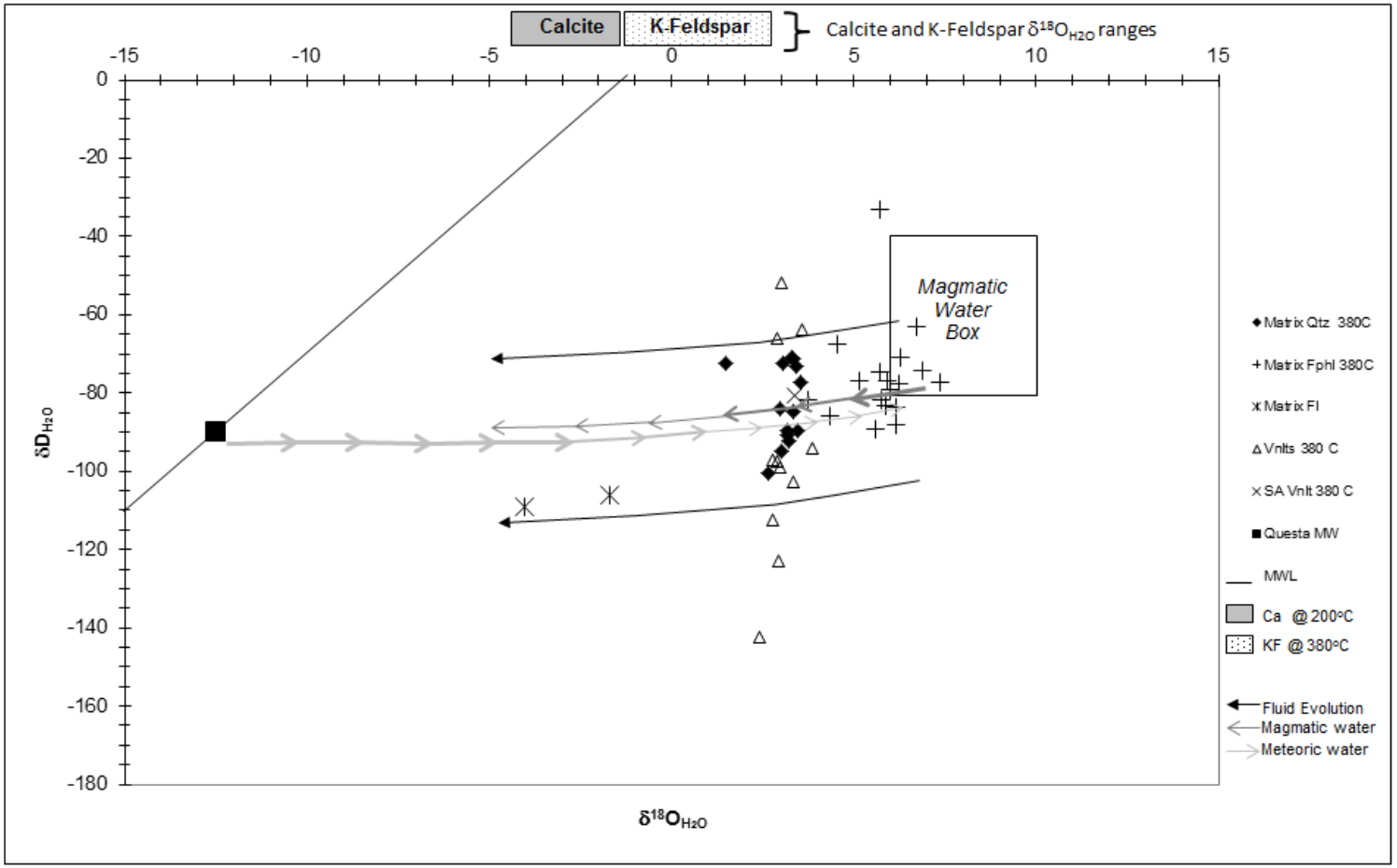

Figure 12. $\delta^{18}O_{H2O}$ vs. δD_{H2O} diagram demonstrating fluid evolution for MHBX and veinlets based upon mineral paragenesis and mode temperatures from respective stages of Rowe (2011). 380°C was applied to the $\delta^{18}O_{H2O}$ calculations for matrix fluorophlogopite, K-feldspar, and quartz, veinlet quartz, and the δD_{H2O} calculations for fluorophlogopite. 200°C was applied to the $\delta^{18}O_{H2O}$ calculations for matrix calcite. The δD_{H2O} for matrix fluorite and quartz and veinlet quartz were obtained directly from fluid inclusions. Where the magmatic water arrows overlap the meteoric water arrows is a zone of magmatic and meteoric mixing. Thickness of arrows demonstrates amount of component, where thicker means more and thinner means less.

quartz) and -63‰ (from fluorophlogpite) to -101‰ (from measured δD_{H2O} in quartz). Fluorophlogopite data produced an outlier (AR-166bt) that was excluded from the above conclusion, due to the dissimilarity to the dataset.

Veinlets

It was concluded by Rowe (2011) or Chapter I that the fluid inclusion temperature and salinity data for the veinlets are essentially indistinguishable from the MHBX, and hence both the MHBX matrix and veinlet fluids underwent a similar evolutionary history. Due to the similar evolutionary history, the $\delta^{18}O_{H2O}$ values for veinlet quartz were also calculated using the main mineralization mode temperature of 380°C, as was done for the MHBX (Table 2 and Figure 12). The veinlet quartz exhibited a tight range of $\delta^{18}O_{H2O}$ values, both similar in the value and the narrow range as the MHBX matrix quartz $\delta^{18}O_{H2O}$ values for 380°C. As discussed in the previous section, the δD_{H2O} for veinlet quartz was taken directly from fluid inclusion waters and exhibited a wide range of values that exceed the range of δD_{H2O} values for the MHBX quartz. If analytical error is not the cause for this broad range and dissimilarity in veinlet δD_{H2O} values, then the range is either real or attributed to a geologic factor. The previous studies performed on Questa did not analyze fluid inclusion water δD in quartz, therefore comparison Questa data is unavailable to aid the argument that the veinlet δD values are real. A possible geologic contributor to the large veinlet quartz δD_{H2O} range is interstitial water. A small amount of structurally-bonded molecular water can occur in a quartz crystal, fractionate with the hydrothermal fluid and/or be released during thermal decrepitation, producing sporadic and widespread, typically lighter, δD values (Hoefs, 1997). The veinlet quartz is different than the MHBX matrix in that the veinlets have smaller, more abundant quartz

grains. This could perhaps contribute to a higher amount of interstitial water in the veinlets compared to the MHBX. Another possibility is that the lesser amount of fluid that was produced by the smaller and less abundant veinlet fluid inclusions was more susceptible to exchange and dilution by interstitial water hydrogen, resulting in variable veinlet quartz δD_{H2O} values compared to the MHBX. In other words, the fluid inclusion water to quartz interstitial water ratio is higher in the matrix and lower in the veinlets, hence the interstitial water having more of an effect isotopically on the veinlets. The widespread range of veinlet fluid inclusion δDs could also be a result of both analytical error, as discussed in the Results section, and any combination of the geologic factors discussed above.

Based upon the veinlet $\delta^{18}O_{H2O}$ values and the fluid inclusion data of Rowe (2011) or Chapter I, it is likely that the quartz-molybdenite veinlets underwent the same isotopic evolutionary history as the Goat Hill MHBX matrix. The variable δD_{H2O} values may, in part, not accurately represent the veinlet fluid. Similar to the MHBX, veinlet molybdenite mineralization is associated with Stage 2 of Rowe (2011) or Chapter I at 380°C and $\delta^{18}O_{H2O}$ values of 3.9‰ to 1.6‰.

Carbon Stable Isotopes

The dominant carbon-bearing aqueous species from Climax-type magmas is CO_2 (Ohmoto & Goldhaber, 1997), hence the $\delta^{13}C_{CO2}$ was calculated for calcites at 200°C (Ohmoto and Rye, 1979)(Table 3). The temperature was determined by the association of calcite with Stage 4 of Rowe (2011) or Chapter I and fluorite, as previously mentioned. The calculation revealed a tight range in $\delta^{13}C_{CO2}$ of -6.0 to -4.9‰. Typically, the $\delta^{13}C_{CO2}$ and $\delta^{18}O_{H2O}$ for calcite would be plotted on an X-Y diagram in order to

identify trends attributed to degassing, fluid/rock interaction, and/or fluid mixing, however this study does not offer such an opportunity due to such a small range in the $\delta^{13}C_{CO_2}$ (1.1‰) and the $\delta^{18}O_{H_2O}$ (3‰) values. Bicarbonate $\delta^{13}C$ was not calculated due to the fact that the HCO_3^- content of hydrothermal fluid is negligible at temperatures >100°C (Hoefs, 1997) and all low salinity fluid inclusions associated with calcite precipitation and meteoric influx in Stage 4 (Rowe, 2011 or Chapter I) demonstrated homogenization temperatures at >100°C.

The $\delta^{13}C_{CO_2}$ data demonstrates that the carbon in all facies analyzed (C-E) came from a magmatic source (Deines and Gold, 1973) Hoefs, 1997; Ohmoto & Goldhaber, 1997). The source is different for carbon (magmatic) compared to oxygen (mixed meteoric/magmatic with meteoric dominance) for Questa calcites. This is possible because the amount of carbon in meteoric fluid is negligible. Hence, the magmatic signature of the carbon remains in the meteoric-dominant mixed magmatic-meteoric fluid despite the fact that the oxygen has evolved to reflect the meteoric-dominant fluid (Ohmoto, 1986). A Pearson's correlation was performed to determine if there is a correlation between $\delta^{13}C_{CO_2}$, $\delta^{18}O_{H_2O}$, and facies. The |cc| was 0.03 to 0.42, showing there is no correlation between $\delta^{13}C_{CO_2}$, $\delta^{18}O_{H_2O}$, and facies. Lastly, due to the reverse solubility of calcite, precipitation cannot occur by simple cooling (Hoefs, 1997). Fluid mixing, which was determined to have occurred at Questa based upon $\delta^{18}O_{H_2O}$ and δD_{H_2O} data and fluid inclusion microthermometry data, is the probable mechanism of calcite precipitation (Rowe, 2011 or Chapter I).

Sulfur Stable Isotopes

Sulfur stable isotopes were analyzed for MHBX matrix anhydrite, molybdenite, and pyrite, and veinlet molybdenite and pyrite. Molybdenite and pyrite mineral pairs could not be used for geothermometry due to the fact that these minerals exhibit little fractionation at temperatures greater than 200°C (Ohmoto & Goldhaber, 1997) and molybdenite mineralization in the Goat Hill orebody commenced at ≤420°C and ceased at 220°C (Rowe, 2011 or Chapter I). Also, sulfide-sulfate (i.e., molybdenite/pyrite-anhydrite) mineral pairs could not be utilized for geothermometry because they are not in equilibrium at temperatures below 350°C (Hoefs, 1997; Ohmoto & Lasaga, 1982) and MHBX anhydrite is paragenetically associated with Stage 4 of Rowe (2011) or Chapter I, which has a mode temperature of 200°C. In addition, molybdenite deposition occurred at 240-420°C (Rowe, 2011 or Chapter I). MHBX matrix and veinlet molybdenite and pyrite have a very narrow $\delta^{34}S$ range of 0.8-2.5‰, compatible with a magmatic source for sulfur (Table 4) (Hoefs, 1997 and Ohmoto & Goldhaber, 1997). MHBX matrix anhydrite also has a narrow range of 6.6-10.0‰, also demonstrating a magmatic source (Hoefs, 1997 and Ohmoto & Goldhaber, 1997). Similar to carbon, the magmatic signature of sulfur can remain despite any meteoric component to the mineralizing fluid (as reflected in $\delta^{18}O_{H2O}$ and δD_{H2O} values) because of the negligible amount of sulfur in meteoric fluid. A Pearson's correlation was performed to determine if there is a correlation between $\delta^{34}S_{anhy}$, $\delta^{34}S_{mo}$, and facies. The absolute values of the correlation coefficients for $\delta^{34}S_{anhy}$ and $\delta^{34}S_{mo}$ vs. facies were 0.08 to 0.22, respectively, showing there is no correlation between $\delta^{34}S_{anhy}$, $\delta^{34}S_{mo}$, and facies.

Fluid Inclusion Gas Analysis

Fluid inclusion gas analysis is a bulk assay of the fluid inclusion gases in a given sample, which means primary, pseudosecondary, and secondary inclusions are subject to extraction during crushing. Based upon fluid inclusion microthermometry analyses in Rowe (2011) or Chapter I, primary and pseudosecondaries are dominant in the samples compared to secondary inclusions. Consequently, the results of the fluid inclusion gas analyses of this study are principally representative of the primary fluids of the system. This is supported by the fact that the results of the fluid inclusion gas analyses are in intimate correspondence with the fluid inclusion data of Rowe (2011) or Chapter I and the oxygen and hydrogen stable isotope data of this study.

Certain species of fluid inclusion gas analysis, specifically CO_2/CH_4, N_2/Ar, and Ar/He ratios, can be indicators of fluid sources and evolution within the system. The gas data in this paper is reported in terms of two data plots by Norman and Moore (1999) and Blamey and Norman (2002) - N_2/Ar vs. CO_2/CH_4 (Figure 13) and N_2/Ar vs. Ar/He (Figure 14), respectively. The data is plotted in this fashion to show both processes and sources for a number of reasons pertaining to geologic factors, corresponding gas species behaviors, and the relationships of these factors and behaviors with known fluid source reservoirs. The N_2/Ar vs. CO_2/CH_4 plot of Norman and Moore (1999) identifies the ratio values for magmatic, shallow meteoric, evolved (crustal), organic (crustal), and evolved magmatic fluid sources. On the N_2/Ar vs. Ar/He plot of Blamey and Norman (2002), the interior of the 5-sided box represents the calc-alkaline magmatic gas compilation of

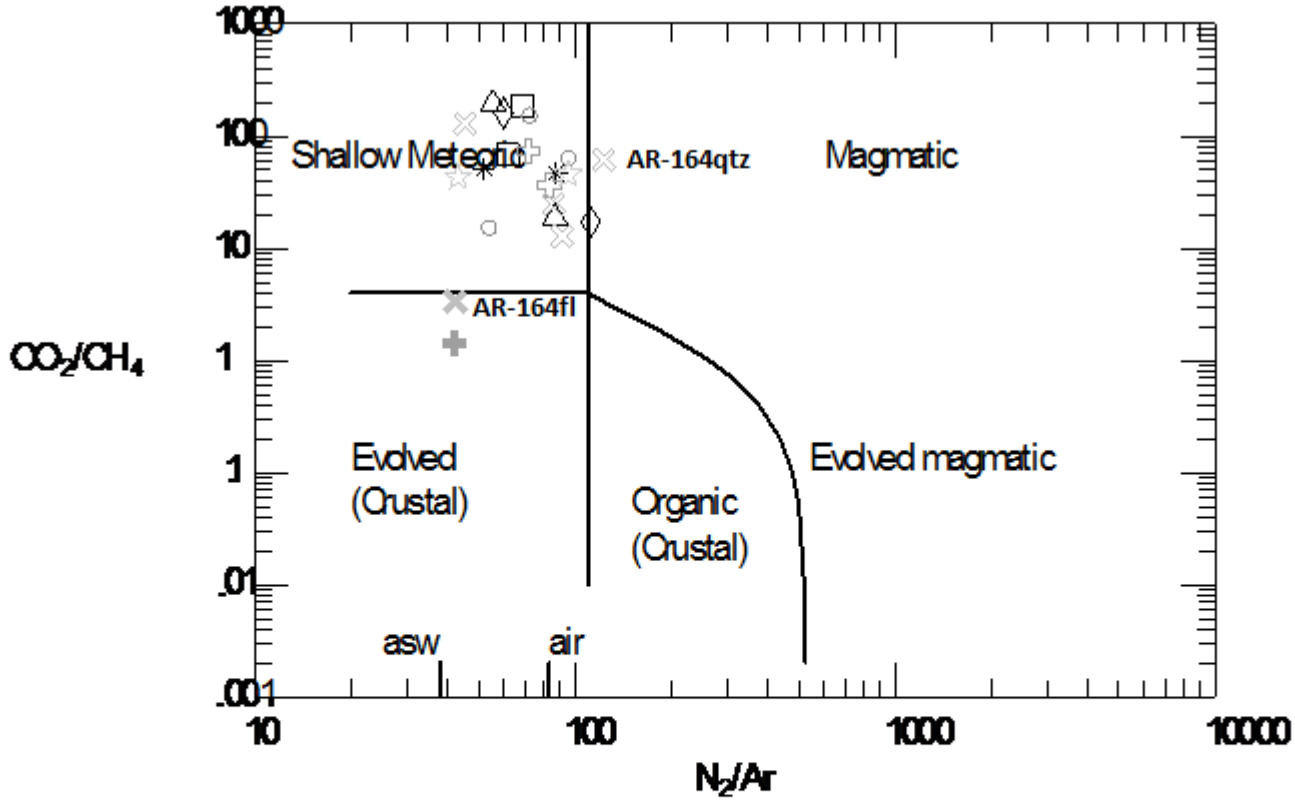

Figure 13. N_2/Ar vs. CO_2/CH_4 diagram for MHBX matrix gas analysis data by facies. In mol.%. Facies symbols: black asterisk – source aplite barren quartz, black open triangle – A_1 quartz, black open square – A_2 quartz, black open diamond – A_3 quartz, dark gray open circle – B quartz, dark gray open cross – C quartz, dark gray filled cross – C fluorite, medium gray open X – D quartz, medium gray filled X – D fluorite, light gray open star – E quartz. See text for explanation. Diagram from Norman and Moore (1999).

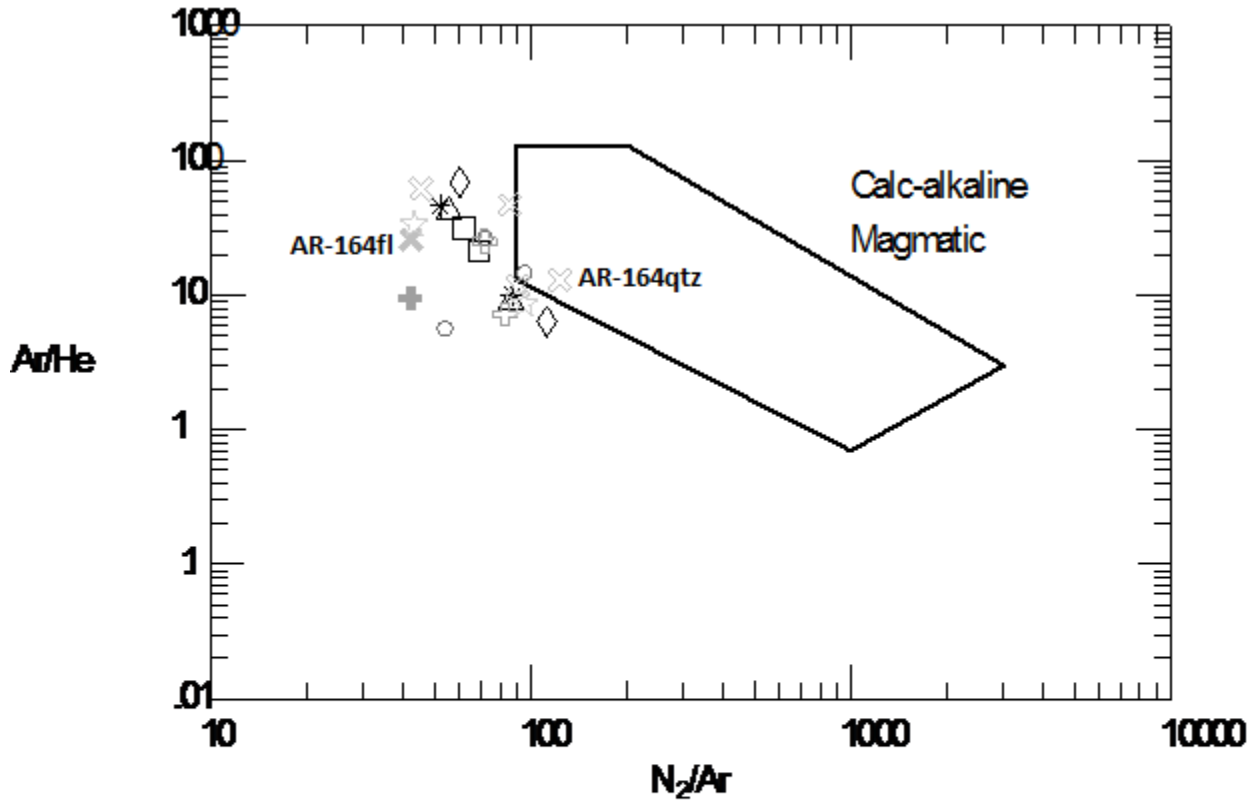

Figure 14. N_2/Ar vs. Ar/He diagram for MHBX matrix gas analyses by facies. In mol.%. Facies symbols: black asterisk – source apite barren quartz, black open triangle – A_1 quartz, black open squares – A_2 quartz, black open diamonds – A_3 quartz, dark gray open circle – B quartz, dark gray open cross – C quartz, dark gray filled cross – C fluorite, medium gray open X – D quartz, medium gray filled X – D fluorite, light gray open star – E quartz. See text for explanation. Diagram from Blamey & Norman (2002).

Giggenbach (1996). On this diagram, meteoric fluids occur to the left and above the 5-sided box (Blamey and Norman, 2002). A caveat in utilizing the 5-sided magmatic plot for data interpretation in this study is that the source intrusion for the Questa system is peralkaline/granitic not calc-alkaline. Therefore, due to lack of fluid inclusion gas analysis data on Climax-type systems, it is unknown whether the calc-alkaline magmatic box would apply. Look to Norman and Moore (1999) and Blamey & Norman (2002) for more details on how these diagrams were derived.

MHBX Facies

Similar to the oxygen and hydrogen stable isotopes, it was hypothesized that the fluid inclusions gases in quartz from each facies would reflect the mineralogic/alteration zonation in terms of an evolutionary pattern in the fluid inclusion gas analysis data, i.e. facies closest to the source intrusion would have a magmatic gas signature and facies distal to the source intrusion would have a gas signature signifying meteoric input. This is not the case, however. There is no distinct evolutionary pattern based upon facies in the quartz data (Figures 13 and 14). All facies quartz is randomly placed in near magmatic and/or shallow meteoric box of the N_2/Ar vs. CO_2/CH_4 diagram. Similarly, all facies quartz occurs randomly from just within to outside of the calc-alkaline magmatic box of the N_2/Ar vs. Ar/He plot. A Pearson's correlation was used for quartz and fluorite in attempts to identify a correlation between facies and H_2, He, CH_4, H_2O, N_2, H_2S, Ar, CO_2, SO_2, O_2, and alkane/alkene organic compounds to see if there is a geochemical evolution that corresponds to the mineralogic/alteration evolution of the MHBX (Table 5). If the absolute value of a correlation coefficient (|cc|) is 0.5 and greater, then it is considered to represent a correlation between the variables. All |cc|s between facies and

the various gas species were below 0.5, with values of 0.07-0.43, demonstrating that there is no facies correlation with the analyzed fluid inclusion gas species in quartz and fluorite.

Analogous to the oxygen and hydrogen stable isotope data of this study and the fluid inclusion data of Rowe (2011) or Chapter I, an evolution is evident between the different mineral phases of the matrix paragenetic sequence - early quartz and later fluorite (Figures 13 and 14). The two MHBX fluorite samples contained less CO_2 (not more CH_4) than the quartz samples of the MHBX (Table 5) and occur in the evolved (crustal) box of the CO_2/CH_4 vs. N_2/Ar plot, along the border of shallow meteoric (Figure 13). The lack of CO_2 in the fluorites, which occur in the last stage of evolution (Stage 4 of Rowe (2011) or Chapter I fluid inclusion data and last in hydrogen and oxygen stable isotope evolution of this study), is a possible indicator of CO_2 degassing or mixing at the very end of evolution of the MHBX when quartz and calcite were deposited. This degassing, in combination with magmatic and meteoric fluid mixing (per oxygen and hydrogen stable isotope data of this study and Stage 4 of Rowe (2011) or Chapter I), are the probable mechanisms for precipitation of reversely soluble calcite in the Goat Hill MHBX. On the Ar/He vs. N_2/Ar diagram, the fluorites have the lowest N_2/Ar ratios and are somewhat set apart from the quartz samples, although it is not as obvious on this plot as it is on the N_2/Ar vs. CO_2/CH_4 diagram. On both plots, samples of quartz and fluorite from AR-164 have very different ratios (Figures 13 and 14). The quartz sample from AR-164 plots in the magmatic field in both diagrams. The AR-164 fluorite sample plots in the evolved (crustal) gas field of the N_2/Ar vs. CO_2/CH_4 diagram and to the left, in the meteoric gas field, of the calc-alkaline magmatic gas box on the N_2/Ar vs. Ar/He

diagram. The fluorite samples also demonstrated a significantly higher amount of C_2H_4 (50.07-113.23 mole %) and C_4H_{10} (1203.92-1145.55 mole %) hydrocarbons than the MHBX quartz with a range of 0-3.11 and 3.27-85 mole %, respectively (Table 5). The presence of significant C_{2-7} hydrocarbons in fluid inclusions is evidence for evolved crustal waters that have underwent significant wall-rock reactions (Moore et al., 2001). All of the above clearly reflect the mineralogic evolution of the system.

The Goat Hill MHBX quartz fluid inclusion gas analysis data displays a magmatic to meteoric source, with samples occurring in and/or along the magmatic gas field to well into the shallow meteoric field of the N_2/Ar vs. CO_2/CH_4 plot (Figure 13). Likewise, quartz samples occur within or along the calc-alkaline magmatic gases box to well out of the magmatic box and into the meteoric input area for the N_2/Ar vs. Ar/He diagram (Figure 14). Both FIGA diagrams are comparable to the fluid source demonstrated by the hydrogen and oxygen stable isotope data. The difference in comparison of the oxygen/hydrogen stable isotope and fluid inclusion gas analysis data sets is that the gas data yields an interpretation of magmatic-meteoric mixing with primarily a meteoric source to the system, whereas the oxygen/hydrogen stable isotope data shows an evolution of a mixed fluid from a predominantly magmatic to a predominantly meteoric source (Figure 12). Two possible mechanisms could explain the interpreted meteoric dominance of the gas analysis data. First, fluid inclusion gas analysis is a bulk method which may obtain all types of inclusions that occur in samples, including often meteorically-derived secondaries. As mentioned previously however, in samples for this study, secondaries are minute in abundance compared to fluid inclusions that represent primary fluids, so they would not influence the results significantly. A second possible

explanation for the meteoric dominance of the gas analysis is that it is a newer method, with newer reporting techniques based upon limited data, and perhaps peralkaline and/or granite-related ore deposit systems occur in a genre separate from the established fields of Norman and Moore (1999) and Blamey and Norman (2002). In other words, perhaps granite-related systems have a lower N_2/Ar ratio in reference to the magmatic gas sources used for deriving the N_2/Ar vs. CO_2/CH_4 and N_2/Ar vs. Ar/He diagrams. Despite the questionable meteoric dominance displayed by the gas analysis data, the importance is that there is a meteoric input to the system with magmatic-meteoric mixing indicated and evolution from magmatic to meteoric is displayed with a definite difference in the quartz and fluorite, most importantly in the same sample. Since fluid inclusion gas analysis is a fairly new technique with little ore deposit data reported, and the $\delta^{18}O_{H2O}$ vs. δD_{H2O} is a well-established and reported method, more confidence is allotted to the oxygen/hydrogen isotope results that indicate magmatic-dominant magmatic-meteoric mixing for the quartz.

The fluid inclusion microthermometry data of Rowe (2011) or Chapter I indicates boiling was a dominant occurrence at Questa and was a mechanism for molybdenite deposition. The total gas content of the fluid inclusions can also be a gauge for whether boiling has occurred in the system or not. Total gas content is calculated by taking the amount of H_2O detected in the fluid inclusions and subtracting it from 100. If the total gas content is greater than 1.5 mole %, then excess gas levels due to boiling are indicated (Norman et al., 2002). The average total gas content for the MHBX is 2.32 mole %, demonstrating that boiling of the fluids occurred. This supports the same conclusion from the fluid inclusion microthermometry data in Rowe (2011) or Chapter I.

Veinlets

Veinlet quartz analyzed for fluid inclusion gases was essentially analytically indistinguishable from the fluid inclusion gas analyses of the MHBX quartz (Figure 15 and 16), again similar to the fluid inclusion data (Rowe, 2011 or Chapter I) and the oxygen stable isotope data of this study. On the N_2/Ar vs. CO_2/CH_4 diagram, the veinlet data plotted mainly in the shallow meteoric field with a few samples bordering magmatic and evolved crustal. On the N_2/Ar vs. Ar/He diagram, the veinlet data occurs from slightly in the magmatic box to meteoric input area (above and left of box), indicating an evolution from magmatic to meteoric sources to the system. Similar to the MHBX, the veinlet gas analysis data also indicates boiling occurred with an average total gas content of 1.76 mole %. The total gas content of the veinlets is slightly lower than that for the MHBX, but is still greater than 1.5 mole %. The difference in fluid inclusion gas content may indicate that the veinlets originated from a slightly more evolved magmatic-hydrothermal fluid than the MHBX, as was also suggested in Chapter I or Rowe (2011) based upon minor differences in fluid inclusion size, type, and abundance between the MHBX and veinlets. Since the veinlet fluid inclusion gas analysis data is essentially analytical indistinguishable from the MHBX matrix quartz data with only a slight difference in gas content, it is concluded that the veinlets underwent the same evolutionary history as the Goat Hill MHBX. This is in conjunction with the conclusions derived from the corresponding fluid inclusion microthermometry data of Rowe (2011) or Chapter I and oxygen/hydrogen stable isotope data of this study. Hence, the meteoric dominance argument applied to the MHBX matrix quartz in the previous section also applies to the Goat Hill quartz-molybdenite veinlets.

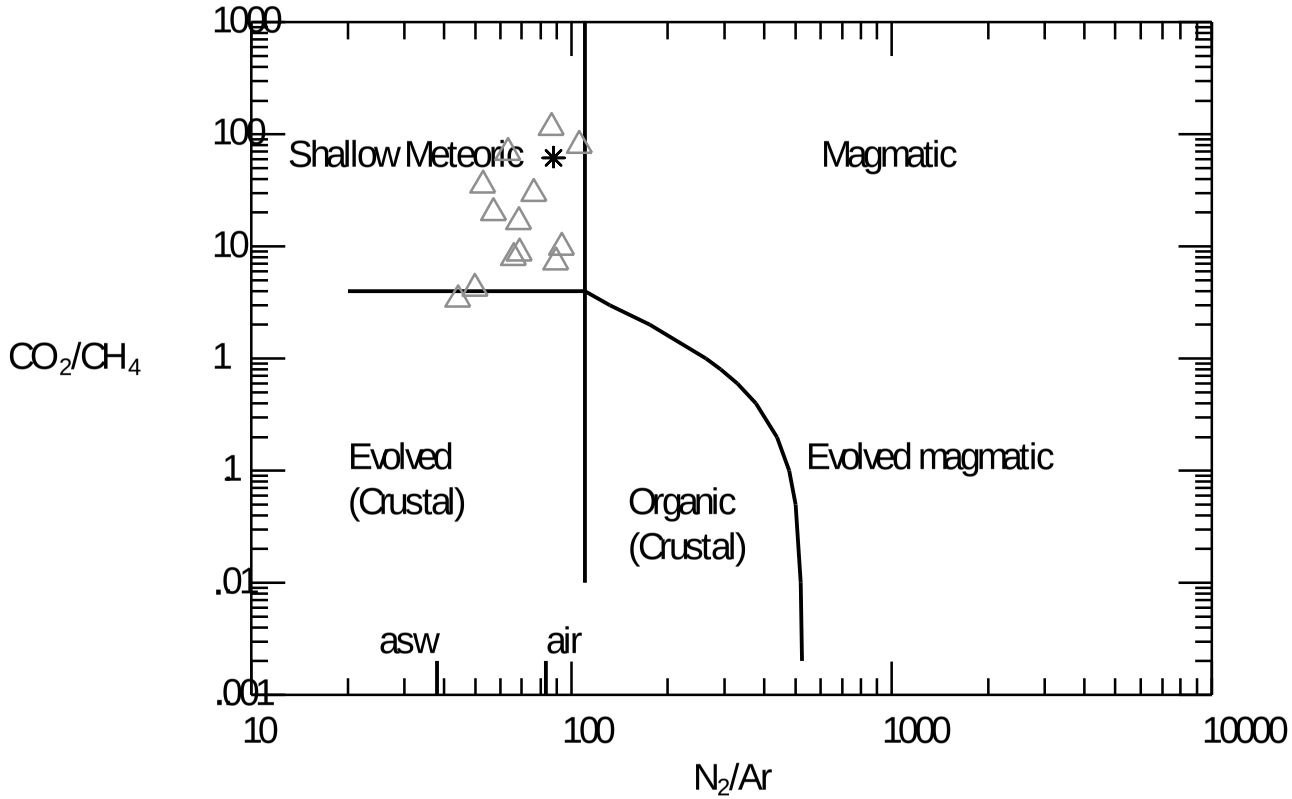

Figure 15. N_2/Ar vs. CO_2/CH_4 diagram for veinlets. In mol.%. Symbols: black asterisk - source aplite veinlet, dark gray open triangles - veinlets. See text for explanation. Diagram from Norman & Moore (1999).

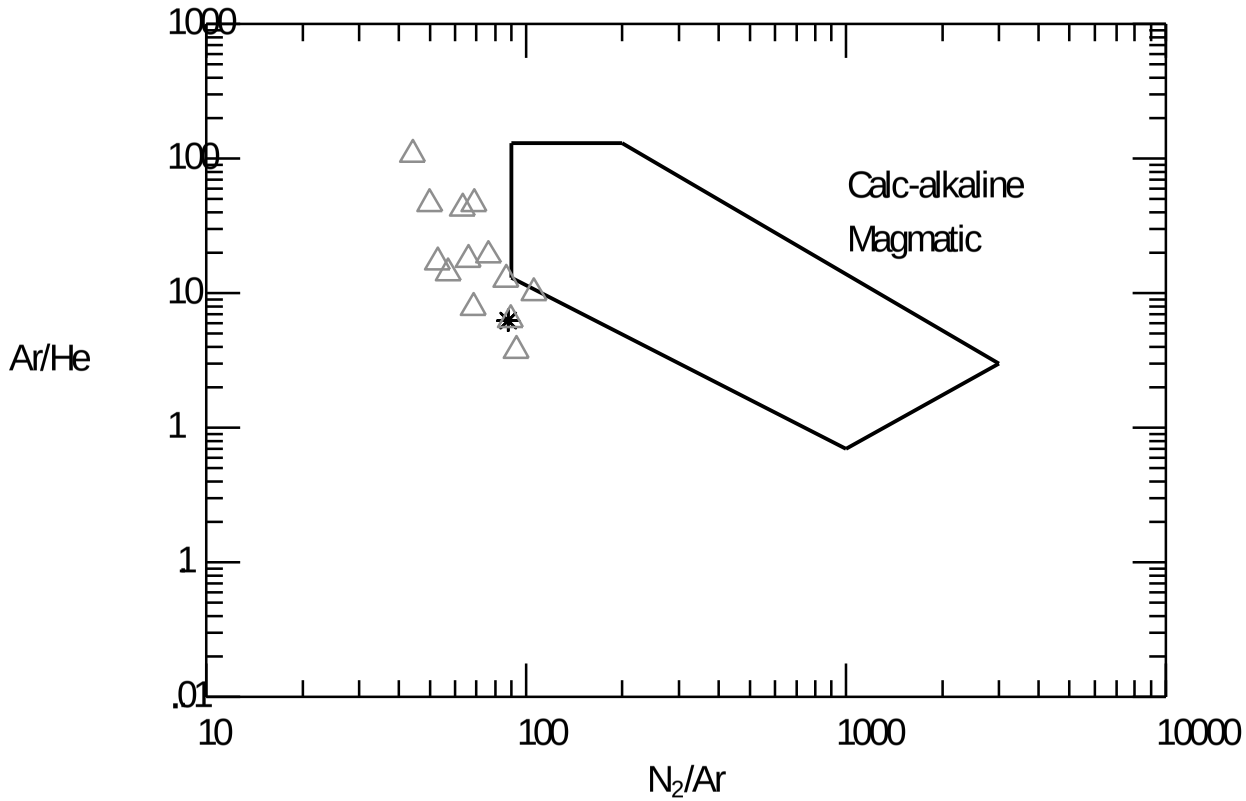

Figure 16. N_2/Ar vs. Ar/He diagram for veinlets. In mol.%. Symbols: black asterisk - source aplite vienlet, dark gray open triangles - veinlets. See text for explanation. Diagram from Blamey & Norman (2002).

COMPARISON WITH PREVIOUS QUESTA SI AND FIGA STUDIES

The data set from this study exhibited similarities and differences to the previous stable isotope and fluid inclusion gas analysis studies on Questa (Smith, 1983; Stein & Hannah, 1985; Stein, 1988; Ross et al., 2002) in terms of oxygen and hydrogen stable isotope values, oxygen isotope geothermometry, sulfur stable isotopes, and fluid inclusion gas analysis results. In addition, there are similarities and differences in the data interpretation between the various authors and this study. Comparing previous stable isotope and fluid inclusion gas analysis data sets and interpretations with those of this study will aid in deriving an ore genesis model for the Questa system. In addition, incorporating the ore genesis conclusions from the fluid inclusion microthermometry study (Rowe, 2011 or Chapter I) with those of this study can offer an ore genesis model derived from three supporting data sets and several different studies.

Stable Isotopes

Oxygen and Hydrogen

The $\delta^{18}O_{KF}$ values of Smith (1983) correlate well with this study with ranges of 1.8-8.5‰ and 1.5-5.4‰, respectively (Figure 17 and Table 6). Smith (1983) obtained a value up to 3.1‰ heavier than this study for potassium feldspar, however. A possible explanation for this variable range in $\delta^{18}O_{KF}$ values is the susceptibility of potassium feldspar to alteration and fractionation from later stage, isotopically lighter waters. Smith (1983) may have sampled more pristine, less altered K-feldspar as well as K-feldspars that were similarly altered to those sampled in this study. Support of this theory would be disequilibrium between cogenetic quartz-KF mineral pairs demonstrated by

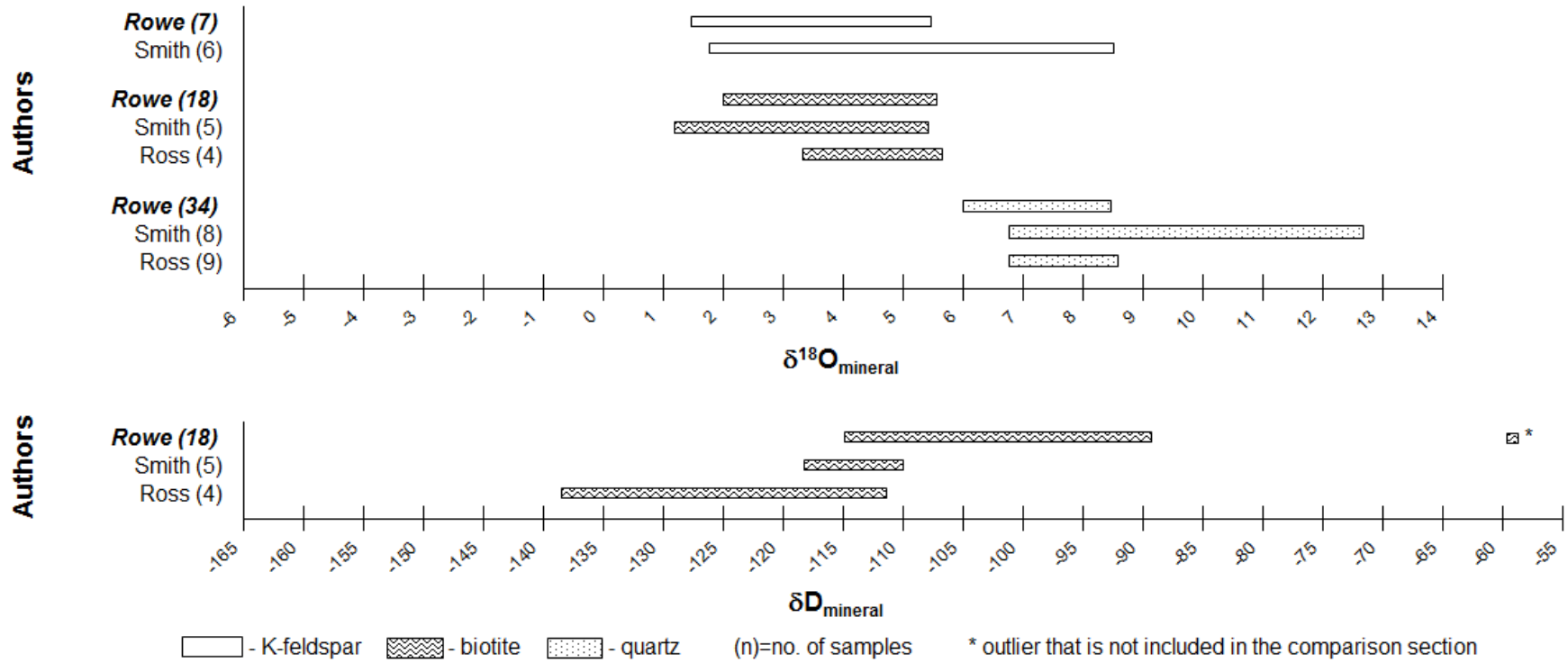

Figure 17 - $\delta^{18}O_{mineral}$ and $\delta D_{mineral}$ ranges for various authors (Rowe, 2011; Smith, 1983; Ross et al., 2002)

Authors	$\delta^{34}S$ (‰)	$\delta^{18}O$ (‰)	δD (‰)	$\delta^{18}O_{H2O}$ from FIs (‰)	δD_{H2O} from FIs (‰)	Calc $\delta^{18}O_{H2O}$ @ 550°C (‰)	Calc δD_{H2O} @ 550°C (‰)	Calc $\delta^{18}O_{H2O}$ @ 400°C (‰)	Calc $\delta^{18}O_{H2O}$ @ 380°C (‰)	Calc δD_{H2O} @ 380°C (‰)	Calc $\delta^{18}O_{H2O}$ @ 320°C (‰)	Calc $\delta^{18}O_{H2O}$ @ 200°C (‰)
Questa												
This Study												
MHBX qtz		6.0-8.2			-101 to -71				1.5-3.7			
MHBX bt		2.0-5.6	-115 to -89, -59*						3.8-7.4	-89 to -63, -33*		
MHBX fl				-4.0 to -1.7	-109 to -106							
MHBX kf		1.5-5.4							-1.1-2.9			
MHBX ca		5.4-8.5										-4.3 to -1.3
vnlt qtz		6.1-8.4			-143 to -52				1.6-3.9			
MHBX mo	0.4-2.3											
vnlt mo	1.1-2.0											
Smith (1983)												
qtz		6.8-12.8				7.8		1.6-7.6			1.9-2.3	
kf		1.8-8.5										
bt		1.2-5.4	-117 to -110			3.6-7.8	-95 to -93		3.0-7.2	-87 to -85		
Ross (2002)												
qtz		6.8-8.6				5.1-6.9			2.3-4.1			
bt		3.3-5.7	-138 to -112			5.2-8.1	-121 to -93		5.1-7.5	-113 to -88		
Stein (1985, 1988)												
mo	1.0-1.1											

Table 6 - Oxygen, hydrogen, and sulfur stable isotope ranges for various authors. The calculated water values reported by other authors are included. See these references for fractionation equations used in their calculations. Values in the gray box were calculated from the main mineralization mode temperature of 380°C from this study using the equations of Clayton et al. (1972), Zheng (1993a), and Suzuoki & Epstein (1976) for comparison purposes. All water values for this study were calculated using the equations of Clayton et al. (1972), Zheng (1993), Zheng (1993a), Zheng (1999), and Suzuoki & Epstein (1976).

* outlier that is not included in the comparison section of this paper

fractionation temperatures that were either too high or too low for this type of system. This was the case for five out of six quartz-KF mineral pairs for Smith (1983), where the fractionation temperatures are <200°C for the system. Similarly, this study found that quartz and K-feldspar are not in equilibrium as well. As previously mentioned, the disequilibrium is most likely attributed to post-depositional alteration of K-feldspar by isotopically lighter water and quartz being resistant to this process.

The biotite $\delta^{18}O$ values of Smith (1983) and Ross et al. (2002) correlate well with this study (Figure 17 and Table 6). Ross et al. (2002) obtained a slightly smaller $\delta^{18}O$ range (3.3-5.7‰) and the range of Smith (1.2-5.4‰) extends slightly lighter than this study (2.0-5.6‰) for biotite. The quartz oxygen values of Smith (1983) and Ross et al. (2002) are also quite comparable to the values of this study with ranges of 6.8-12.8‰, 6.8-8.6‰, and 6.0-8.4‰, respectively (Figure 17 and Table 6). A difference is that Smith (1983) reported a larger $\delta^{18}O_{qtz}$ range compared to this study and Ross et al. (2002) with values up to 4.4‰ heavier. It is unknown why Smith (1983) obtained heavier values for $\delta^{18}O_{qtz}$, but what is most important is that the range of this study and of Ross et al. (2002) fall within that of Smith (1983). Based upon this fact and the overlapping ranges for $\delta^{18}O_{bt}$, it is concluded that Questa has a $\delta^{18}O_{qtz}$ value of 6.0-8.6‰ and $\delta^{18}O_{bt}$ value of 1.2-5.7‰ associated with molybdenite mineralization.

Differences in biotite δD values are revealed by the data comparison of Smith (1983) (-117 to -110‰) and Ross et al. (2002) (-138 to -112‰) to this study (-115 to -89 ‰) (Figure 17 and Table 6). First, the δD_{bt} values for this study ranged up to 21‰ heavier than the upper limit of δD_{bt} of Smith (1983) and Ross et al. (2002) (Figure 17). Second, the lower limits of the δD_{bt} range of Ross extends up to 23‰ lighter than the

lower limits of the biotite δD range for this study and that of Smith (1983). Lastly, a much tighter biotite δD range was reported by Smith (1983), which falls in the middle of the data set for this study and that of Ross et al. (2002). The variation in the biotite δD data for Questa reported by Smith (1983) and Ross et al. (2002) is puzzling, since the biotite $\delta^{18}O$ values correlate well between the studies. It may be that this study sampled more pristine, less sericitically altered biotites than the other studies on Questa, which would reveal heavier values for this study. Also, hydrogen isotopes are more readily susceptible to fractionation than oxygen stable isotopes, which could cause such a large range in δD_{bt} values from the same deposit. Another factor to keep in mind is that this study analyzed 18 biotites for oxygen and hydrogen stable isotopes, whereas Smith (1983) and Ross et al. (2002) only analyzed five and four biotite samples, respectively. This study exemplifies a more statistically representative data set that could possibly be viewed with more weight than the other studies. Also for consideration is the fact that the biotite δD_{H2O} values calculated for this study at the established mode temperature of 380°C do fit well with the calculated quartz δD_{H2O} values and the fluid evolution story for the system (Figure 12). Despite the biotite δD differences, the most important factor is that all three data sets do overlap for the biotite δDs. Based upon this fact, the number of samples analyzed in this study compared to the other authors, and the fluid evolution stages of Rowe (2011) or Chapter I, it is concluded that Questa has a biotite δD value of -117 to -89‰. No δDs were analyzed from quartz fluid inclusion waters in either Smith (1983) or Ross et al. (2002).

The temperatures utilized to calculate the $\delta^{18}O_{H2O}$ and δD_{H2O} values, how those temperatures were derived, and the interpretation of the origin of the fluids varied

between this study, Smith (1983), and Ross et al. (2002). Smith (1983) utilized 400°C for calculating most of the quartz $\delta^{18}O_{H2O}$ values and calculated one sample at 550°C (Table 6 and Figure 18). These two temperatures were applied to samples considered to be associated with potassic alteration. 400°C was based upon the largest mode in fluid inclusion homogenization temperatures of Smith (1983), which is comparable to the 380°C main mode of this study that is also associated with potassic alteration (Rowe, 2011 or Chapter I). The temperature of 550°C for Smith (1983) came from the fractionation temperature revealed by mineral pairs (qtz-KF, qtz-bt, KF-bt) in one sample. The temperature obtained from fluid inclusion microthermometry on 70 inclusions is likely more reliable than a fractionation temperature from mineral pairs in one sample. Smith also utilized the 550°C to calculate biotite $\delta^{18}O_{H2O}$ and δD_{H2O} values (Table 6 and Figure 18). Smith (1983) also applied a temperature of 320°C to calculate $\delta^{18}O_{H2O}$ from quartz associated with sericitic alteration (Table 6 and Figure 18).

Similar to the oxygen and hydrogen mineral values of Smith (1983) being fairly comparable to this study, so are the calculated $\delta^{18}O_{H2O}$ and δD_{H2O} values despite the variation in temperatures used (Figure 18 and Table 6). However, since 550°C was utilized to calculate the biotite $\delta^{18}O_{H2O}$ and δD_{H2O} values for Smith (1983), and that temperature is based solely on mineral pairs from one sample, the main mode temperature from this study (380°C) was applied to demonstrate its effects (Table 6 and Figure 18). This temperature change puts the biotites entirely within range of the $\delta^{18}O_{H2O}$ and δD_{H2O} values for this study. Another interesting fact to note is regarding the fluid evolution Stages of Rowe (2011) or Chapter I (Figure 8). Even though the second main mode temperature (280°C) for molybdenite mineralization from Stage 3 of Rowe (2011)

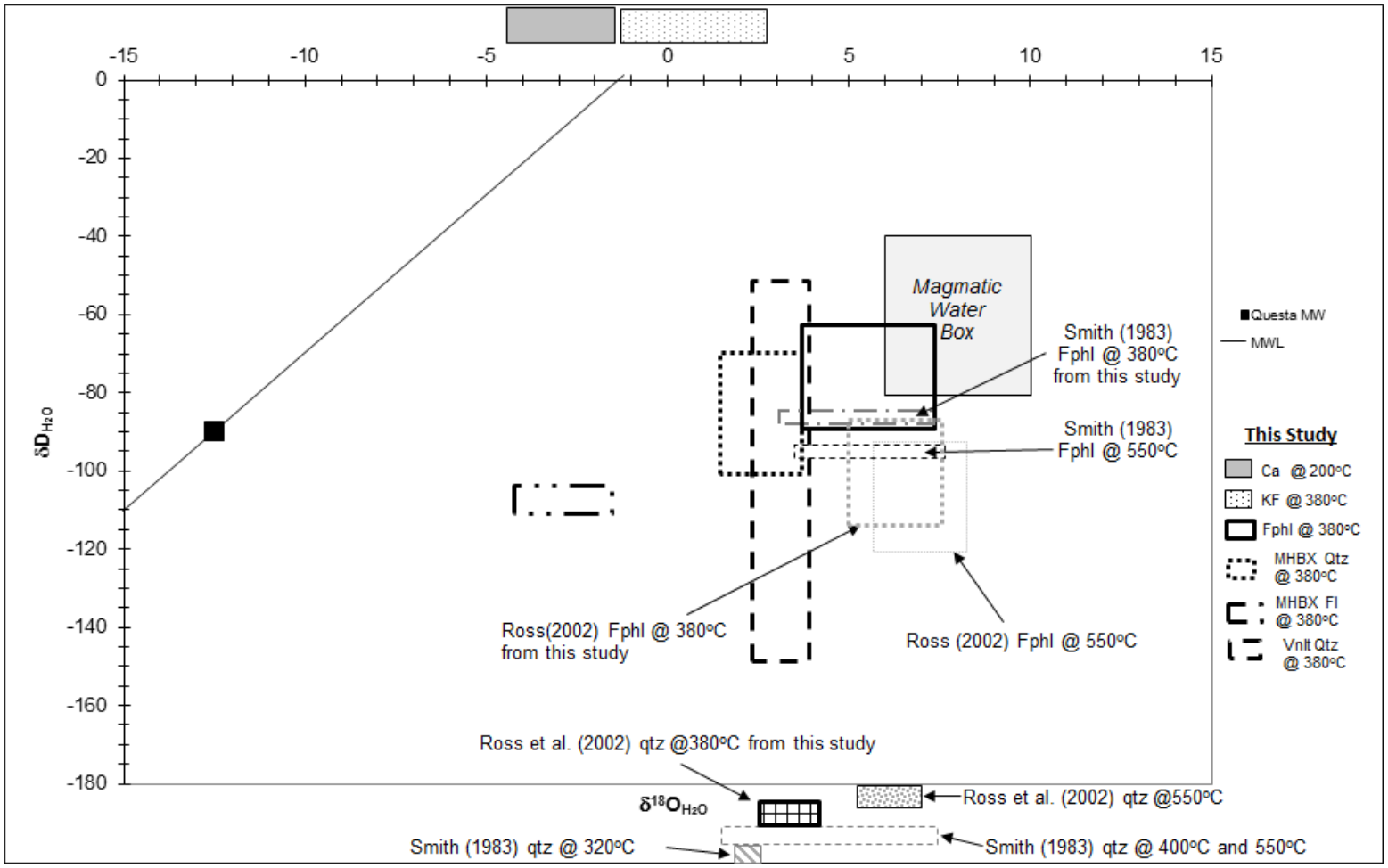

Figure 18. $\delta^{18}O_{H2O}$ vs. δD_{H2O} diagram. Water compositions from fluid inclusions or calculated from quartz, K-feldspar, calcite, and fluorophlogopite isotope ranges for various authors at their chosen temperatures and at 380°C from this study. See Table 6 for references. K-feldspar of Smith (1983) is not included due to established post-deposition alteration and associated fractionation. Calcite and K-feldspar from this study are also included.

or Chapter I was not applied to the stable isotope data, the temperature of 320°C from Smith (1983) is in agreement with the temperature range (340-240°C) for Stage 3, which is also associated with sericitic alteration. The quartz $\delta^{18}O_{H2O}$ values calculated from 320°C of Smith (1983) are pulled closer to the meteoric water line and further support the evolution of the system in terms of mineralogy and Stages 1-4 of Rowe (2011) or Chapter I (Figures 8 and 18). Not only was the data of Smith (1983) fairly comparable to this study, but the conclusion of the source for mineralizing fluid source is also comparable with this study - mixed magmatic and meteoric.

Ross et al. (2002) applied a temperature of 550°C to the quartz and biotite $\delta^{18}O_{H2O}$ and the biotite δD_{H2O} calculations (Table 6 and Figure 18). This temperature was not obtained from a complimentary fluid inclusion study. Instead, 550°C was chosen based upon temperatures derived by previous studies (biotite-apatite geothermometer for temperature of crystallization from Molling, 1989; fractionation temperature from mineral pairs of Smith, 1983; liquidus temperature in water and fluorine-rich granitic melts from Manning, 1981 and Manning & Pichavant, 1984) and from his fractionation temperatures derived from quartz-biotite mineral pairs. Ross et al. (2002) calculated fractionation temperatures between quartz and biotite assuming a phlogopite composition for biotites (380-620°C) and a fluorophlogopite composition for biotites (305-515°C). Despite the fact that the MHBX matrix biotites at Questa are fluorophlogopite in composition (Molling, 1989; Cline & Bodnar, 1994), Ross chose the quartz-phlogopite (rather than quartz-fluorophlogopite) temperature because it fit with the above mentioned previous studies to make a temperature determination of 550°C. Based upon the fluid inclusion studies at Questa (Rowe, 2011 or Chapter I; Bloom, 1981; Smith, 1983; Cline

& Bodnar, 1994; Cline & Vanko, 1995; Klemm et al., 2004), the quartz-fluorophlogopite geothermometer of Ross et al. (2002) and Rowe (2011) or Chapter I, and the aqueous geochemistry of Smith (1983), 550°C is considered too high a temperature to be associated with molybdenite mineralization. Applying a temperature that is too high (550°C) is going to result in $\delta^{18}O_{H2O}$ values that are heavier than what is representative of the system. Hence, the main mineralization mode temperature for this study (380°C) was applied to calculate the $\delta^{18}O_{H2O}$ of Ross et al. (2002) and demonstrates that the $\delta^{18}O_{H2O}$ values for both quartz and fluorophlogopite (i.e. biotite) are in the same range as reported for this study at 380°C (Figure 18). These values are considered by this study to be more representative of the ore fluid. The mode temperature of 380°C was also applied to the δD_{H2O} calculations of Ross et al. (2002), however the δD_{H2O} values are still much lighter than this study with minor overlap (Figure 18).

Ross et al. (2002) concluded a magmatic origin with little to no meteoric contribution based upon calculated $\delta^{18}O_{H2O}$ values from quartz and biotite, δD_{H2O} values from biotite, and the temperature (550°C) that was chosen for the isotope water calculations. Unlike this study where the biotites range from magmatic to lighter than magmatic values, the biotite δD_{H2O} values of Ross are definitely not magmatic, regardless of the temperature used in the calculation (Figure 18). Ross attributed the non-magmatic δD_{H2O} values to either post-depositional hydrogen exchange with meteoric water or a previously degassed magma chamber. If either of these were the case, this would likely be reflected in the hydrogen data for this study, which is not the case. At 550°C, the quartz $\delta^{18}O_{H2O}$ values of Ross et al. (2002) are mostly magmatic, however it has been established that 550°C is too high for the system and 380°C should be applied. At 380°C,

the quartz $\delta^{18}O_{H2O}$ values of Ross et al. (2002) are definitely mixed magmatic-meteoric, similarly to this study.

Sulfur

The $\delta^{34}S$ values for molybdenite (0.4-2.3‰) in this study are comparable to the molybdenite sulfur values of Stein & Hannah (1985) and Stein (1988) (1.0-1.1‰) (Table 6). Despite the fact that the $\delta^{34}S$ values from this study have a slightly broader range than those of Stein & Hannah (1985) and Stein (1988), the source for the molybdenite sulfur is in agreement between the studies – a magmatic source.

Fluid Inclusion Gas Analysis

The fluid inclusion gas analysis of Smith (1983) did not include Ar or CH_4, so the data cannot be plotted on the N_2/Ar vs. CO_2/CH_4 and N_2-Ar-He and diagrams for comparison to this study in terms of fluid origin (Table 5, Figures 15 and 16). In terms of the gas constituents that were analyzed by both studies (H_2, He, H_2O, N_2, H_2S, CO_2, SO_2, and calculated Total Gas), there are some similarities and differences. As previously mentioned, a total gas content of >1.5 mol% is an indicator of boiling. The average total gas content of quartz associated with potassic alteration of Smith (1983) (0.80 mole %) shows no boiling occurred and is much less than that of this study (2.10 mole%) where boiling is indicated by the total gas. Conversely, the average total gas content for quartz associated with QSP alteration (2.45 mole %) for Smith (1983) is similar to this study and indicates boiling as well. The hydrogen content from the gas analysis of Smith (1983) is comparable to that of this study. As previously mentioned, measurable H_2 in fluid inclusion volatile analysis is significant as supporting evidence that the fluid inclusions have not experienced post-entrapment modification through leakage. H_2 content being

the same between the gas analyses of each study further demonstrates that no leakage or gas modification has occurred at Questa, which aids in supporting the Trapped Halite Phenomenon of Rowe (2011) or Chapter I and the gas analysis data of this study. The CO_2 content of Smith (1983) (0.64-0.9 mole%) is comparable to this study (1.13 mole%), however the N2 content of Smith (1983) (0.03-0.09 mole%) is significantly lower than this study (0.482 mole%). Without Ar and CH4 however, it is not possible to determine if there is any significance to these relationships regarding fluid source. Lastly, the gas analysis data of Smith (1983) reveals substantially more sulfur-bearing gases (H_2S and SO_2) than this study (Table 6). Smith (1983) stated that the SO_2 reading is not reliable and is therefore disregarded. Lower H_2S values can be a result of the sulfur being removed from the system by sulfide mineralization (i.e. molybdenite±pyrite). The lower H_2S values of this study (0.001 mole%) compared to Smith (1983) (0.041 to 0.84 mole%) may be an indicator that the sampling that was based on rigorous temporal-spatial constraints for this study more accurately sampled quartz that was associated with molybdenite mineralization.

CONCLUSIONS

Although the Goat Hill orebody MHBX consists of a defined mineralogic and alteration zonation, the quartz $\delta^{18}O_{H2O}$, δD_{H2O}, and fluid inclusion gas analysis data do not reflect a fluid evolution based upon facies. The $\delta^{18}O_{H2O}$, δD_{H2O}, and fluid inclusion gas analysis data do reflect an evolution between the different mineral phases of the MHBX matrix paragenetic sequence, however. With the $\delta^{18}O_{H2O}$ vs. δD_{H2O} data, the evolution follows the paragenetic sequence (fluorophlogopite→quartz→fluorite→calcite) where the minerals that are first in the paragenetic sequence exhibit the heaviest, most magmatic

signature with the least amount of meteoric mixing and the minerals that are last in the paragenetic sequence are the lightest, least magmatic fluids with the most amount of meteoric mixing. The fluid evolution is also evident by quartz and fluorite in the fluid inclusion volatile analyses. Paragentically earlier quartz demonstrates magmatic to predominantly meteoric CO_2/CH_4, N_2/Ar, and Ar/He gas ratios, whereas later fluorite has significantly less CO_2 and lower N_2/Ar ratios indicating an even more evolved fluid (from shallow meteoric to evolved crustal). All of the above is complimentary to the data and conclusions of the fluid inclusion microthermometry of Rowe, 2011 or Chapter I.

Due to the fact that the $\delta^{18}O_{H2O}$ and fluid inclusion gas analysis data is essentially analytically indistinguishable between MHBX and the later veinlets that crosscut the MHBX, it is concluded that the MHBX matrix and veinlet fluid underwent the same fluid evolution history. The one minor difference between the MHBX and veinlets (total gas content) may indicate that the veinlets originated from a slightly more evolved magmatic-hydrothermal fluid, but still underwent a similar fluid evolution history as the MHBX. Based upon the oxygen and hydrogen stable isotope data of this study, Smith (1983), and Ross et al. (2002), factors discussed in this section, the fluid inclusion microthermometry of Rowe (2011) or Chapter I and Smith (1983), and the fluid inclusion gas analyses of this study, it is concluded that both phases of molybdenite mineralization are from similar source fluids that evolved from magmatic to mixed magmatic-meteoric of variable degrees with a $\delta^{18}O_{H2O}$ range of 1.5-7.6‰ and a δD range of -113 to -63‰ and are associated with both potassic and phyllic alteration (Smith, 1983 and Rowe, 2011 or Chapter I). The veinlets are paragenetically later, demonstrating that the system evolved this way at least twice.

REFERENCES

Blamey, N. J. F., and Norman, D. I., New Interpretations of Geothermal Fluid Inclusion Volatiles: Ar/He and N2/Ar ratios - A Better Indicator of Magmatic Volatiles and Equilibrium Gas Geothermometry, *in* Proceedings 27th Geothermal Reservoir Engineering, Stanford, San Francisco, 2002.

Bloom, M. S., 1981, Chemistry of inclusion fluids; stockwork molybdenum deposits from Questa, New Mexico, Hudson Bay Mountain and Endako, British Columbia: Economic Geology v. 76, no. 7, p. 1906-1920.

Carten, R. B., 1987, Evolution of immiscible Cl- and F-rich liquids from ore magmas, Henderson porphyry molybdenum deposit, Colorado [abs.]: Geological Society of America Abstracts with Programs, v. 19, no. 613.

Carten, R. B., Rye, R. O., and Landis, G. P., 1988, Effects of igneous and hydrothermal processes on the compositions of ore-forming fluids; stable-isotope and fluid-inclusion evidence, Henderson molybdenum deposit, Colorado, *in* Anonymous, ed., Geological Society of America 1988 centennial celebration, Volume 20, Geological Society of America (GSA), p. 94.

Carten, R. B., White, W. H., and Stein, H. J., 1993, High-grade granite-related molybdenum systems; classification and origin: Mineral deposit modeling, v. 40, p. 521-554.

Chacko, T., Hu, X., Mayeda, T. M., Clayton, R. N., and Goldsmith, J. R., 1996, Oxygen isotope fractionations in muscovite, phlogopite, and rutile: Geochimica et Cosmochimica Acta, v. 60, no. 14, p. 2595-2608.

Clayton, R. N., and Keiffer, S. W., 1991, Oxygen isotopic thermometer calibrations, *in* Taylor, H. P., O'Neil, J.R. & Kaplan, I.R., ed., Stable Isotope Geochemistry: A tribute to Samuel Epstein, The Geochemical Society, Special Publication no.3, p. 3-10.

Clayton, R. N., O'Neil, J. R., and Mayeda, T. K., 1972, Oxygen Isotope Exchange between Quartz and Water: Journal of Geophysical Research, v. 77, no. 17, p. 3057-3067.

Cline, J. S., and Bodnar, R. J., 1994, Direct evolution of brine from a crystallizing silicic melt at the Questa, New Mexico, molybdenum deposit: Economic Geology, v. 89, no. 8, p. 1780-1802.

Cline, J. S., and Vanko, D. A., 1995, Magmatically generated saline brines related to molybdenum at Questa, New Mexico, USA, *in* Thompson, J. F. H., ed., Magmas, Fluids, and Ore Deposits: Mineralogical Association of Canada Short Course Series, Victoria, B.C., Canada, Volume 23, p. 153-174.

Cox, D. P., and Singer, D. A., 1986, Mineral deposit models, Reston, VA, U. S. Geological Survey, 379 p.:

Donahue, K. M., 2002, Geochemistry, geology and geochronology of the Victorio mining district, Luna County, New Mexico: Linking skarn and porphyry systems to carbonate-hosted lead-zinc replacement deposits [Master of Science Thesis]: New Mexico Institute of Mining & Technology, 186 p.

Earthman, M. A., 2010, Sulfur Isotope and Fluid Inclusion Study of Fluid Sources within the Fresnillo Southwest Silver District, Zacatecas, Mexico [Master of Science in Geochemistry Thesis]: New Mexico Institute of Mining & Technology, 66 p.

Fortier, S. M., Luettge, A., Satir, M., and Metz, P., 1994, Oxygen isotope fractionation between fluorophlogopite and calcite; an experimental investigation of temperature dependence and F (super -) OH (super -) effects: European Journal of Mineralogy, v. 6, no. 1, p. 53-65.

Giggenbach, W. F., 1996, Chemical composition of volcanic gases, *in* Scarpa, R., Tilling, R. I., and Springer, V., eds., Monitoring and mitigation of volcano hazards: Berlin.

Guilbert, J. M., and Park, C. F., Jr., 1986, The Geology of Ore Deposits, New York, NY, W. H. Freeman and Company, 985 p.:

Hall, W. E., Friedman, I., and Nash, J. T., 1974, Fluid Inclusion and Light Stable Isotope Study of the Climax Molybdenum Deposits, Colorado: Economic Geology, v. 69, no. 6, p. 884-901.

Hannah, J. L., and Stein, H. J., 1986, Oxygen isotope compositions of selected Laramide-Tertiary granitoid stocks in the Colorado mineral belt and their bearing on the origin of climax-type granite-molybdenum systems: Contributions to Mineralogy and Petrology, v. 93, no. 3, p. 347-358.

Hoefs, J., 1997, Stable isotope geochemistry, Berlin, Springer, 201 p.:

Johnson, C. M., Lipman, P. W., and Czamanske, G. K., 1990, H, O, Sr, Nd, and Pb isotope geochemistry of the Latir volcanic field and cogenetic intrusions, New Mexico, and relations between evolution of a continental magmatic center and modifications of the lithosphere: Contributions to Mineralogy and Petrology, v. 104, no. 1, p. 99-124.

Kamilli, R. J., 1978, The genesis of stockwork molybdenite deposits; implication from fluid inclusion studies at the Henderson Mine [abs.]: The Geological Society of America (91st annual meeting), v. 10, p. 431.

Klemm, L. M., and Pettke, T. H. C. A., 2004, Early magmatic-hydrothermal evolution of the Questa porphyry Mo deposit, New Mexico, USA, *in* Muhling, J., Goldfarb, R. J., Vielreicher, N., Bierlein, F. P., Stumpfl, E. F., Groves, D. I., Kenworthy, S., and Knox-Robinson, C. M., eds., SEG 2004, Volume 33, University of Western Australia Geology Department and Extension Service, p. 431.

Klemm, L. M., Pettke, T. H. C. A., and Heinrich, C. A., 2008, Fluid and source magma evolution of the Questa porphyry Mo deposit, New Mexico, USA: Mineralium Deposita, v. 43, no. 5, p. 533-552.

Leonardson, R. W., Dunlop, G., Starquist, V. L., Bratton, G. P., Meyer, J. W., and Osborne, L. W., Jr., 1983, Preliminary geology and molybdenum deposits at Questa, New Mexico, *in* Babcock, J. W., ed., Denver Region Exploration Geologists Society symposium; the genesis of Rocky Mountain ore deposits; changes with time and tectonics: Wheat Ridge, CO, Denver Reg. Explor. Geol. Soc.

Lipman, P. W., 1992, Ash-flow calderas as structural controls of ore deposits; recent work and future problems, *in* Thorman, C. H., ed., Application of structural geology to mineral and energy resources of the Central and Western United States, U. S. Geological Survey, p. L1-L12.

Manning, D., and Pichavant, M., 1984, Experimental studies of the role of fluorine and boron in the formation of late-stage granitic rocks and associated mineralization: International Geological Congress, v. 27, p. 386-387.

Manning, D. A. C., 1981, The effect of fluorine on liquidus phase relationships in the system Qz-Ab-Or with excess water at 1 kb: Contributions to Mineralogy and Petrology, v. 76, no. 2, p. 206-215.

Meyer, J. W., 1991, Volcanic, plutonic, tectonic and hydrothermal history of the southern Questa Caldera, New Mexico [Doctor of Philosophy Dissertation]: University of California Santa Barbara, 348 p.

Molling, P. A., 1989, Applications of the reaction progress variable to hydrothermal alteration associated with the deposition of the Questa molybdenite deposit, NM [Doctor of Philosophy Dissertation]: Johns Hopkins Univ., 249 p.

Norman, D. I., Groff, J., Kamali, C., Musgrave, J., and Moore, J. N., 1996, Gaseous species in fluid inclusions; indicators of magmatic input into ore-forming geothermal systems: Geological Society of America, 28th annual meeting, v. 28, p. 401.

Norman, D. I., and Moore, J. N., Methane and excess N2 and Ar in geothermal fluid inclusions, *in* Proceedings Twenty-fourth Workshop of Geothermal Reservoir Engineering, Stanford University, Stanford, California, January 22-24 1999, p. 233-240.

Norman, D. I., and Musgrave, J. A., 1994, N_2-Ar-He compositions in fluid inclusions; implicators of fluid source: Geochimica et Cosmochimica Acta, v. 58, no. 3, p. 1119-1131.

Ohmoto, H., 1986, Stable isotope geochemistry of ore deposits, *in* J.W. Valley, H. P. T., Jr., and J.R. O'Neil, ed., Reviews in Mineralogy Volume 16: Stable Isotopes in High Temperature Geological Processes: Mineralogical Society of America, p. 491-559.

Ohmoto, H., and Goldhaber, M. B., 1997, Sulfur and carbon isotopes, *in* Barnes, H. L., ed., Geochemistry of hydrothermal ore deposits: New York, NY, John Wiley and Sons, p. 517-611.

Ohmoto, H., and Lasaga, A. C., 1982, Kinetics of reactions between aqueous sulfates and sulfides in hydrothermal systems: Geochimica et Cosmochimica Acta, v. 46, no. 10, p. 1727-1745.

Ohmoto, H., and Rye, R. O., 1979, Isotope of sulfur and carbon, *in* Barnes, H. L., ed., Geochemestry of Hydrothermal deposits, John Wiley & Sons, p. 509-567.

O'Neil, J. R., and Taylor, H. P., Jr., 1967, The oxygen isotope and cation exchange chemistry of feldspars: American Mineralogist, v. 52, p. 1414-1437.

Ross, P. S., 2002, Magmatic-hydrothermal Breccia Formation in Porphyry Mo Systems: A Horizontal Stratified Body at Questa, New Mexico [Master of Science Thesis]: Earth Sciences Dept. University of Quebec in Montreal.

Ross, P.-S., Jebrak, M., and Walker, B. M., 2002, Discharge of hydrothermal fluids from a magma chamber and concomitant formation of a stratified breccia zone at the Questa porphyry molybdenum deposit, New Mexico: Economic Geology v. 97, no. 8, p. 1679-1699.

Rowe, A., 2011, Fluid Evolution of the Magmatic Hydrothermal Breccia of the Goat Hill Orebody, Questa Climax-type Porphyry Mo System, New Mexico - A Fluid Inclusion Study: Submitted to Economic Geology, December 2011.

Schilling, J. H., 1956, Geology of the Questa molybdenum (Moly) mine area, Taos County, New Mexico: New Mexico Bureau of Mines and Mineral Resources

Bulletin 51, p. 87.
Seedorff, E., and Einaudi, M. T., 2004, Henderson Porphyry Molybdenum System, Colorado: II. Decoupling of Introduction and Deposition of Metals during Geochmical Evolution of Hydrothermal Fluids: Economic Geology, v. 99, p. 39-72.
Sharp, Z. D., and Kirschner, D. L., 1994, Quartz-calcite oxygen isotope themometry:a calibration based on natural isotopic variations: Geochimica et Cosmochimica Acta, v. 58, p. 4491-4501.
Sinclair, W. D., 1995, Porphyry Mo (climax-type): Selected British Columbia mineral deposit profiles, p. 105-108.
Sinclair, W.D., 1995, Porphyry Mo (low-F-type): Selected British Columbia mineral deposit profiles, p. 93-95.
Smith, R. W., 1983, Aqueous chemistry of molybdenum at elevated temperatures and pressures with applications to porphyry molybdenum deposits [Doctor of Philosophy Dissertation]: New Mexico Institute of Mining and Technology, 311 p.
Stein, H. J., 1988, Genetic traits of climax-type granites and molybdenum mineralization, Colorado mineral belt, *in* Taylor, R. P., and Strong, D. F., eds., CIM conference on Granite-related mineral deposits, Volume 39, Canadian Institute of Mining and Metallurgy, p. 394-401.
Stein, H. J., and Hannah, J. L., 1985, Movement and origin of ore fluids in climax-type systems: Geology, v. 13, no. 7, p. 469-474.
Suzuoki, T., and Epstein, S., 1976, Hydrogen isotope fractionation between OH-bearing minerals and water: Geochimica et Cosmochimica Acta, v. 40, no. 10, p. 1229-1240.
Taylor, H. P., Jr., 1997, Oxygen and hydrogen isotope relationships in hydrothermal mineral deposits, *in* Barnes, H. L., ed., Geochemistry of hydrothermal ore deposits: New York, NY, John Wiley and Sons.
Velador, J. A., 2010, Timing and origin of intermediate sulfidation epithermal veins and geochemical zoning in the Fresnillo District, Mexico: Constrained by 40Ar/39Ar geochronology, fluid inclusions, gas analysis, stable isotopes, and metal ratios [Doctorate of Philosophy Dissertation]: New Mexico Institute of Mining & Technology, 185 p.
White, W. H., Bookstrom, A. A., Kamilli, R. J., Ganster, M. W., Smith, R. P., Ranta, D. E., and Steininger, R. C., 1981, Character and origin of climax-type molybdenum deposits: Economic Geology, Seventy-fifth anniversary volume (1905-1980).
White, W. H., Carten, R. B., Bookstrom, A. A., and Stein, H. J., 1990, A Model for Climax-tpe Molybdenum Deposits [abs.], 8th IAGOD Symposium in Conjunction with International Conference in Mineral Deposit Modeling - Program with Abstracts, p. 133-134.
Zheng, Y.-F., 1993, Calculation of oxygen isotope fractionation in anhydrous silicate minerals: Geochimica Cosmochimica Acta, v. 57, p. 1079-1091.
Zheng, Y.-F., 1993a, Calculation of oxygen isotope fractionation in hydroxyl-bearing silicates: Earth and Planetary Science Letters, v. 120, no. 3-4, p. 247-263.
Zheng, Y.-F., 1999, Oxygen isotope fractionation in carbonate and sulfate minerals: Geochemical Journal, v. 33, no. 2, p. 109-126.

CHAPTER III.

A Comparison of Genetic Fluid Origin of the Questa Climax-type Porphyry Molybdenum System, New Mexico with the Climax-type Deposits of the Colorado Mineral Belt, Colorado

ABSTRACT

The Climax-type porphyry molybdenum systems of New Mexico (Questa) and the Colorado Mineral Belt (COMB) (Climax, Henderson, Mount Emmons, and Silver Creek) possess a unique set of physical characteristics that set them apart from other porphyry-Mo deposits and put them together in a class of their own. The genetic origin of Climax-type deposits has been debated throughout the economic geology community with only a magmatic source as the predominantly accepted origin (Cline & Bodnar, 1994; Cline & Vityk, 1995; Ross et al., 2002; Klemm et al, 2004; Klemm et al., 2008; Kamilli, 1978; White et al., 1981; Carten, 1987; Carten et al., 1988; Seedorff & Einaudi, 2008) followed by mixed magmatic-meteoric origin (Bloom, 1981; Smith, 1983; Hall et al., 1974; Larson, 1987).

Fluid inclusion microthermometry, stable isotope analysis, and fluid inclusion gas analysis data of the Questa Climax-type deposit indicate a magmatic to mixed magmatic-meteoric genetic origin of the molybdenite-mineralizing fluids with a $\delta^{18}O_{H2O}$ and δD_{H2O} range of 1.5-7.6‰ and -53 to -143‰, a mode temperature of mineralization at 380-400°C, salinities of 0-64 eq. wt.% NaCl, and N_2-Ar-He and CO_2-CH_4-N_2-Ar fluid inclusion gas ratios plotting in near-magmatic to meteoric source fields on diagrams of Blamey & Norman (2002) and Norman & Moore (1999) . A comparison of the geochemical data of Questa with the data of the Climax-type deposits of the COMB revealed that the deposits of the COMB do indeed possess similar genetic origins and

fluid evolution histories to Questa with common fluid inclusion types, non-magmatic raw homogenization temperature modes ranging from 320-400°C, and magmatic to mixed magmatic-meteoric $\delta^{18}O_{H2O}$ and δD_{H2O} ranges of 2-9.7‰ and -140 to -83‰ associated with molybdenite mineralization. Another similarity between the deposits is a magmatic source for sulfur with a $\delta^{34}S_{molybdenite}$ range of 0.4-5.3‰ for all of the deposits.

As to be expected, minor differences exist between Questa and some of the COMB deposits as well, i.e. boiling, Tshl>>Tlv fluid inclusions, and source of carbon in post-mineralization calcites. These differences are minimal compared to the similarities that demonstrate a mixed magmatic-meteoric fluid source for Climax-type deposits.

INTRODUCTION

Despite the recent economic downturn, the elevated price of molybdenum in the past 8 years has amplified interest in the world-class high-grade porphyry molybdenum deposits of the Climax-type (Figure 1). Amplified interest often calls for a re-visitation of past data and interpretations, in addition to performing and reporting new studies. Various interpretations have been made about the genetic origin of Climax-type porphyry molybdenum systems and the characteristics that define them as a Climax-type (Bloom, 1981; Carten, 1981; Carten et al., 1988; Carten et al., 1993; Cline & Bodnar 1994; Cline & Vanko, 1995; Hall et al., 1974; Hannah & Stein, 1986; Kamilli, 1978; Klemm & Pettke, 2004; Klemm et al., 2008; Ross et al., 2002; Seedorff & Einaudi, 2004; Smith, 1983; Stein, 1988; Stein & Hannah, 1985; White et al., 1990; White et al., 1981). These interpretations reflect similarities and differences from deposit to deposit, analysis to analysis, and author to author. This paper is a summary and comparison of the geology and geochemistry of the Questa Climax-type porphyry molybdenum system (Questa) with the Climax-type deposits of the Colorado Mineral Belt (COMB) – Climax, Henderson, Mt. Emmons, and Silver Creek.

BACKGROUND

Climax-type Deposits

Climax-type deposits are set apart from the traditional quartz monzonite-type porphyry-Mo deposits by their high grade and distinctive characteristics, most significantly the tectonic setting, age range, source intrusion composition, geochemistry, and copper to molybdenum ratio (Table 1). The tectonic setting that is unique to Climax-type deposits is a rift environment. Not all rift zones have potential for Climax-type

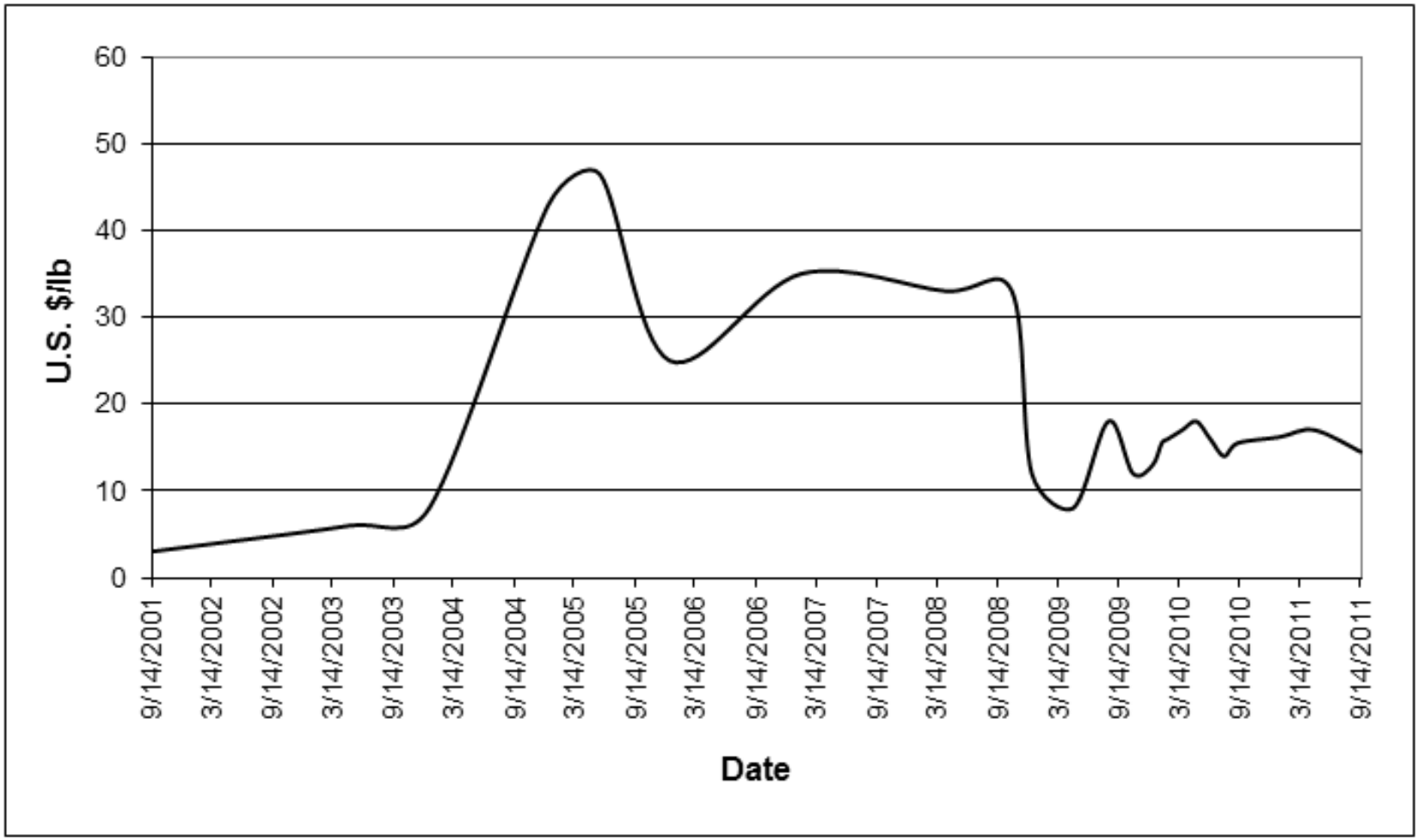

Figure 1. Molybdenum price (10 year). Modified from Infomine, Inc., 1990-2011.

Characteristic	Climax-type	Quartz monzonite-type
Source Intrusion	Granite porphyry	Quartz monzonite porphyry
Magma Chemistry	High silica, peralkaline, F-rich (0.1 to >1% F)	Calc-alkaline, low F content (<0.1% F)
Deposition	Multiple intrusions of granite	Composite intrusions of diorite to quartz monzonite
Age range	Paleozoic to Tertiary, but mainly Mid-Tertiary	Archean to Tertiary, but most commonly Mesozoic and Tertiary
Tectonic Setting	Rift zones in areas of thick crust	Subduction zones related to arc-continent or continental collision
Average ore grade	0.3-0.45% MoS_2 (0.18-0.27% Mo)	0.1-0.2% MoS_2 (0.06-0.12% Mo)
Cu:Mo ratio	1:100 to 1:50	1:30 to 1:1
Examples of Deposit Type	Colorado: Climax, Henderson, Silver Creek, Urad, Mount Emmons, Redwell Basin; **New Mexico: Questa**; Utah: Pine Grove; Greenland: Malmbjerg, Erzberg; Norway: Nordli	British Colombia, Canada: Endako, Boss Mountain, Kitsault, Adanac, Carmi, Bell Moly, Red Bird, Trout Lake, Storie Moly, Ajax; Yukon, Canada: Boswell River, Red Mountain; Alaska: Quartz Hill; Montana: Cannivan; Idaho: Thomson Creek, White Cloud, Cumo; Nevada: Nevada Moly, Pine Nut, Buckingham; Peru: Compaccha; Russia: East Kounrad; Mexico: Creston; China: Jinduicheng

Table 1. Comparison of Climax-type and quartz monzonite type porphyry molybdenum deposits. Data taken from or modified from Donahue (2002), Ludington (1986), Ludington et. al. (1995), Sinclair (1995), Theodore (1986), White et. al. (1981), Ludington and Plumlee, 2009.

mineralization, however. Climax-type deposits occur in areas of shallow subduction where the tectonic environment shifts from compression to atectonic to rifting (Wallace, 1995). Shallow subduction promotes fractional partial melting of upper mantle and lower crust which causes thermal weakening of the crust, resulting in rifting (Meyer, 1991; White et al., 1981).

The age range for Climax-type deposits is Paleozoic to Tertiary. However, the majority of Climax-type deposits are concentrated in the Mid-Tertiary, when their unique tectonic environment was prevalent on earth. The high-silica peralkaline granite source intrusions for Climax-type deposits are extreme differentiates of the upper mantle and lower crust parent magmas that began their partial melting process during shallow subduction. These granitic source magmas are cupolas of stocks that belong to a larger, deeper batholith. The cupolas coarsen with depth (aplite to granite), where the shallower aplite/rhyolite to aplite/rhyolite porphyry is the phase associated with mineralization. Multiple stages of intrusion of the source magmas are directly associated with multiple stages of mineralization for Climax-type deposits. Typically, there is a younging of intrusions with depth, where the oldest intrusion is the shallowest, and the youngest is the deepest intrusion.

Due to the highly evolved nature of the source magma, these deposits are high silica, alkali-rich and calcium poor. The extreme differentiation process of these magmas also resulted in other unique geochemical aspects of these deposits. The source plutons have elevated concentrations of incompatible elements: fluorine (0.1 to >1%), rubidium, cesium, beryllium, lithium, niobium, tantalum, and most importantly molybdenum (Cox & Singer, 1986; Ludington, 1986; Ludington, 1995; Sinclair, 1995; Theodore, 1986;

Ludington, 1986; Ludington & Plumlee, 2009; Donahue, 2002; White et al., 1981; White et al., 1990; Carten et al., 1993; Ross et al., 2002; Lipman, 1992). The fluorine plays an important role in molybdenum mineralization as a complex for the Mo rather than the chlorine complex in traditional Cu-Mo deposits (Smith, 1983). Climax-type deposits are also elevated in tin, thorium, uranium, and tungsten. Tin and tungsten were actually recovered as a by-product of mining at the Climax mine in Colorado. Additionally, the evolution process of the source magmas results in clean and homogeneous ore with a very low copper to molybdenum ratio (Cu:Mo = 1:100 to 1:50).

Climax-type deposits possess additional common features from deposit to deposit as well. An important structural feature that occurs in Climax-type systems controlled the emplacement of the highly evolved magmas - the juxtaposition of a Precambrian shear zone with rift centers. The molybdenum ore zones are draped about the apex of the stock or cupola. Alteration types follow a similar pattern with high silica zones closest to source intrusion, then potassic, phyllic, and argillic alteration zoned sequentially outward from the source intrusion. Local argillic alteration also occurs along structures. Propylitic alteration occurs distally both above and outward from the intrusive center. In some cases, a tungsten ore shell will mimic the molybdenum ore shell and occur both within and above the Mo zone. Base-metal (Zn, Pb, and Cu) mineralization occurs outward and distally from the source intrusion and molybdenum ore shell (Cox & Singer, 1986; Ludington, 1986; Ludington, 1995; Sinclair, 1995; Theodore, 1986; Ludington, 1986; Ludington & Plumlee, 2009; Donahue, 2002; White et al., 1981; White et al., 1990; Carten et al., 1993; Ross et al., 2002; Lipman, 1992).

Molybdenum mineralization in Climax-type deposits occurs as open-space filling stockwork veinlets, replacement veinlet stockworks, magmatic-hydrothermal breccias, and minimal disseminations. Some vein minerals that occur in Climax-type systems are quartz, potassium feldspar, fluorine-rich biotite, fluorite, molybdenite, anhydrite, calcite, pyrite, magnetite, hubnerite, wolframite, cassiterite, beryl, rutile, apatite, rare earth oxides, rhodochrosite, dolomite, fluorine-rich topaz, and creedite.

Questa and the COMB

This paper focuses on the most well-known Climax-type systems – Questa in New Mexico and those of the COMB (Climax, Henderson, Mt. Emmons, and Silver Creek) (Figure 2). All of the NM and CO deposits occur along the Rio Grande Rift. As mentioned in the previous section, Precambrian shear zones are additional necessary structural features that occur in Climax-type areas. The deposits in CO occur along the Precambrian shear zone similarly termed the Colorado Mineral Belt (Carten et al., 1993; White et al., 1981). Questa in NM does not occur along this particular shear zone, but does occur along a shear zone of similar age and named the Jemez Lineament (Lipman, 1992; Meyer and Leonardson, 1990; Meyer and Foland, 1991; Ross et al., 2002). Both of these Precambrian shear zones helped control emplacement of the large-scale batholiths of highly evolved source magmas for the Climax-type systems. Magmatism for all of the Climax-type deposits of the NM and CO occurred during the Tertiary period. The oldest deposits are those in closest proximity to the Rio Grande Rift (Climax, Henderson, and Questa), with Oligocene ages of 33-24 Ma, 30-27 Ma, and 25-24 Ma, respectively (White et al., 1990; White et al., 1981; Czmanske, 1990; Zimmerer, 2008; Shannon et al., 2004; Ludington & Plumlee, 2009). The next youngest is the Miocene-aged Mt. Emmons (17

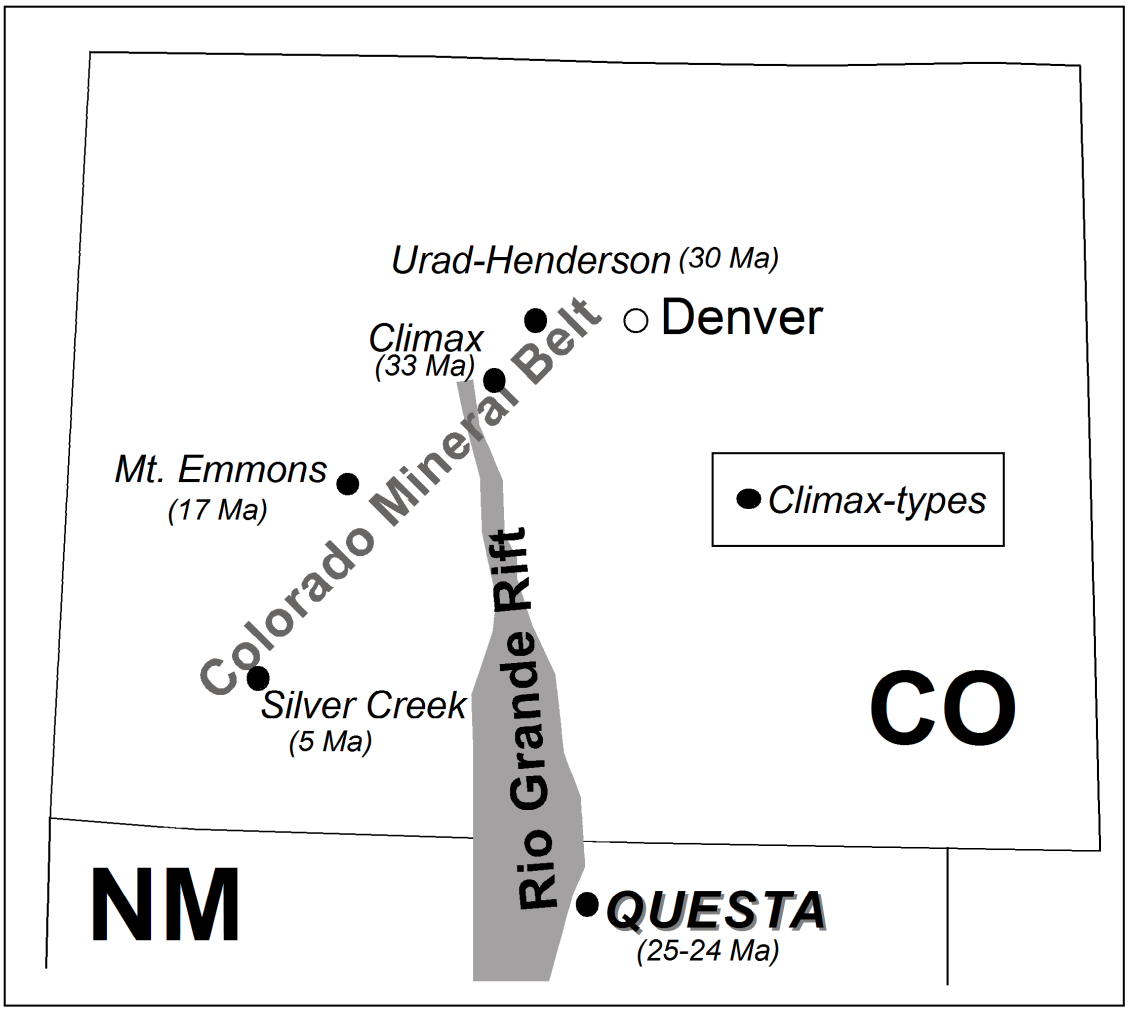

Figure 2. Mine location map showing the relative location of the Climax-type deposits of NM and CO that occur along the Rio Grande Rift. Not to scale. Ages from Wallace (1995), Shannon et al. (2004), Zimmerer (2008), Thomas and Galey (1982), Cameron et al. (1986).

Ma) (White et al., 1981; Thomas and Galey, 1982). The youngest of the NM and CO Climax-type deposits is Silver Creek at a Pliocene age of 5 Ma (Larson et al., 1987; Larson, 1994; Cameron et al., 1985). For the COMB, the age of the Climax-type deposits appears to be proportional to the distance from the rift center. New Mexico's Questa deposit is an exception to this trend.

Molybdenum mineralization in Climax-type systems is independent of host rock lithology since the source of Mo in Climax-type deposits is the extreme differentiates of the upper mantle and lower crust. Host rock lithology is variable from deposit to deposit in the COMB and NM, where each deposit has a different country rock type (Table 2). Despite the fact that host rock lithology is not related to Mo mineralization, host rock lithology may be a possible contributor to some differences between the deposits. For instance, at Climax, the only deposit where tungsten was recovered (0.027-0.030% WO_3), half of the host rocks are mostly Precambrian meta-igneous schists and gneisses which were already anomalous with respect to tungsten. The other deposits do not have metamorphic basement rocks that are anomalous in tungsten (Wallace, 1995). Another difference that is likely attributable to host rock lithology is mineralization style. Questa is the only deposit that has prevalent magmatic-hydrothermal breccia (MHBX) mineralization style (Table 2). The weak, deuterically altered, volcanic and volcaniclastic host rocks at Questa could not withstand the pressures caused by the magmatic-hydrothermal system, resulting in substantial MHBX formation. Climax and Henderson country rocks are competent igneous or meta-igneous rocks which are not as favorable to MHBX formation as the weak volcanics of Questa. There is a smaller, lower grade deposit (Redwell) neighboring Mt. Emmons that has a post-Mo mineralization MHBX,

	Questa	Climax	Henderson	Mt. Emmons	Silver Creek
Location	New Mexico	Colorado	Colorado	Colorado	Colorado
Tectonic Associations					
Rift	Rio Grande	Rio Grande	Rio Grande	Rio Grande	Rio Grande
Precambrian Shear Zone	Jemez Lineament	Colorado Mineral Belt	Colorado Mineral Belt	Colorado Mineral Belt	Colorado Mineral Belt
Age of Associated Intrusive Activity	25-24 Ma	33-24 Ma	30-27 Ma	17 Ma	5 Ma
Host Rock	Tertiary volcanic package (andesite and volcaniclastic sediments) and minor aplite	Precambrian schist and gneiss, Precambrian metalamprophyre and Silver Plume granite, late Cretaceous dikes and sills of diorite to quartz monzonite	Tertiary rhyolite porphyry	Cretaceous carbonaceous shales and sandstones	Precambrian quartzite and greenstone, Paleozoic and Mesozoic sedimentary rocks
Source Intrusion(s)	Aplite porphyry	Rhyolite porphyry	Rhyolite porphyry	Rhyolite porphyry	Alaskite Rhyolite Porphyry
Source Morphology	Lateral and stacked cupolas	Stacked cupolas	Stacked cupolas	Single intrusive event	Dikes
Depth of Emplacement	9,850 - 16,400 ft	10,000 feet	9,850 feet	1,900 ft up to 13,700ft	6,500 ft
Orebody Distribution	Lateral	Stacked	Stacked	Single	Single
Mo Mineralization					
Phase	MHBX and later composite stockwork vnlts, paints and slips	Some open space vnlts, later molybdenite replacement veinlets	Open space vnlts and later molybdenite replacement vnlts	Stockwork veinlets, minor disseminations, minor later replacement vnlts	Composite open-space stockwork veinlets
Grade	0.318% MoS_2 (0.19% Mo) *	0.4% MoS_2 (0.24% Mo)	0.38% MoS_2 (0.23% Mo)	0.44% MoS_2 (0.26% Mo)	0.52% MoS_2 (0.31% Mo)
Contained Mo	442 Mt	1,790 Mt	1,070 Mt	344 Mt	124 Mt
Percentage of Grade	MHBX - 40% * Stockworks, paints, slips - 60% *	Replacement vnlts dominant	Open space vnlts - 45% Replacement vnlts - 55%	Open space vnlts dominant	Open space vnlts dominant
W Mineralization	Trace	0.027-0.030% WO_3 by-product	Trace	Trace	Trace

Table 2 - Comparison of Climax-type characteristic features between deposits. Data taken from Wallace et al. (1968), Hall et al. (1974), Seedorff & Einaudi (2004), Larson (1987), Carten et al. (1993), Thomas and Galey (1982), Larson et al (1994), Cameron et al. (1985), and Ludington and Plumlee (2009).

* Applies to the Goat Hill orebody

but for whatever reasons, the sedimentary hosted Mt. Emmons deposit favored open-space veinlet formation for mineralization phase (Thomas & Galey, 1982). The same goes for the meta-sedimentary and sedimentary hosted Silver Creek deposit.

In Climax-type deposits, multiple stages of intrusion and associated ore shells often occur, as at Climax, Henderson, and Questa. These multiple stages of intrusion, with their associated ore shells, provide these deposits with their large tonnages and render them economically desirable. The difference between Questa and Climax/Henderson is that the source intrusions and associated ore shells at Questa mostly occur laterally, whereas at Climax/Henderson they are stacked (Table 2). A pre-existing structural fabric associated with the Tertiary Questa caldera is the likely culprit for the lateral source intrusion morphology and orebody distribution at Questa. There is evidence of some stacking of source intrusions at Questa by minor vertical ore shell stacking, but the dominant morphology is lateral, not vertical. The Mt. Emmons deposit is considered to be the result of a single intrusive event, which would explain its small size (Wallace et al.,1968; Hall et al.,1974; Seedorff & Einaudi, 2004; Larson, 1987; Carten et al., 1993; Thomas and Galey, 1982; Larson et al.,1994; Cameron et al., 1985; Ludington and Plumlee, 2009) (Table 2). At the Redwell deposit, despite both lateral and vertical source intrusion morphology and orebody distribution, the grades and volumes are subeconomic. Little is known about the source intrusion of the Silver Creek deposit in the Rico district. What minimal exploration drilling that has been done has not intersected the source intrusion, only dikes of alaskite porphyry that are believed to be the source of the mineralization. Silver Creek appears to be one orebody from one intrusive event based upon drilling and its small size (Table 2) (Cameron et al., 1985).

GEOCHEMISTRY OF CLIMAX-TYPE DEPOSITS

An ore genesis geochemical study was performed on the Goat Hill orebody at Questa (2011a and b or Ch. I and II) utilizing three supporting data sets (fluid inclusion (FI) microthermometry, stable isotope (SI) analysis, and fluid inclusion gas analysis) and well-defined temporal and spatial constraints. Fluid inclusion microthermometry and gas analyses were performed on MHBX matrix quartz and fluorite, and quartz from later stockwork veinlets. Oxygen, hydrogen, carbon, and sulfur stable isotope analyses were performed on the respective MHBX matrix mineral species of quartz, fluorophlogopite, K-feldspar, calcite, and molybdenite and on stockwork veinlet quartz and molybdenite. Oxygen stable isotope analyses were also performed on fluid inclusion waters in MHBX matrix fluorite. Hydrogen stable isotope analyses were performed on fluid inclusion waters in MHBX matrix quartz and fluorite and stockwork veinlet quartz. Please refer to Rowe (2011a and b or Ch I and II) for detailed methodologies.

This paper will focus on the interpretation of the geochemistry and the ore genesis model for Questa derived from this study and previous studies on Questa in comparison to data interpretations and models for the Climax-type deposits of the COMB. Note that fluid inclusion gas analyses were not performed on any of the COMB deposits and hence are not available for comparison to Questa. The fluid inclusion gas analyses are an important aspect in telling the fluid evolution and ore genesis story for Questa, however, and will be included in the summary on Questa. Comparison between Questa and the Climax-type deposits of the COMB is invaluable in determining the fluid evolution of this type of system, what geochemical conditions are associated with molybdenite

mineralization, and generating an ore genesis model for Climax-type porphyry Mo deposits.

Fluid Inclusion Microthermometry

Fluid Inclusion Types

Based upon visible phases at room temperature, four major fluid inclusion types (I-IV) were identified at Questa (Figure 3, Table 3, Table 4). Type I inclusions contain liquid and vapor, and are divided into three subtypes (a, b, and c). Type Ia fluid inclusions are liquid-rich and contain opaque (op) and/or hematite (hm) and/or unknown other translucent (ot) daughter minerals. The opaque daughter minerals may be molybdenite, fluorophlogopite, pyrite, or rutile. The unknown ot daughter minerals could be anhydrite, nahcolite, fluorite, or calcite. Type Ib inclusions, the most abundant of the fluid inclusion types, are liquid-rich with no daughter minerals present. Type Ic inclusions are vapor-rich and may contain one or more op, ot, or hm daughter minerals. Type II fluid inclusions contain liquid, vapor and halite, and are subdivided into four subtypes (a, b, c, and d). Type IIa, IIb, and IIc inclusions are liquid-rich and contain no additional daughters, contain op and/or hm daughters, and contain ot±hm±op daughters, respectively. Type IId are vapor-rich inclusions containing halite and possible op, hm, and ot daughter minerals. Type III fluid inclusions are divided into two subtypes (a and b). Type IIIa and IIIb are liquid-rich and vapor-rich aqueous inclusions, respectively and contain a halite crystal and sylvite±hm±op±ot daughter minerals. No microthermometry was performed on types IId and IIIb due to the difficulty in observing any phase changes with these inclusions and the minimal number of these inclusions observed in the samples. Type IV fluid inclusions, the least abundant of the fluid inclusion types, are

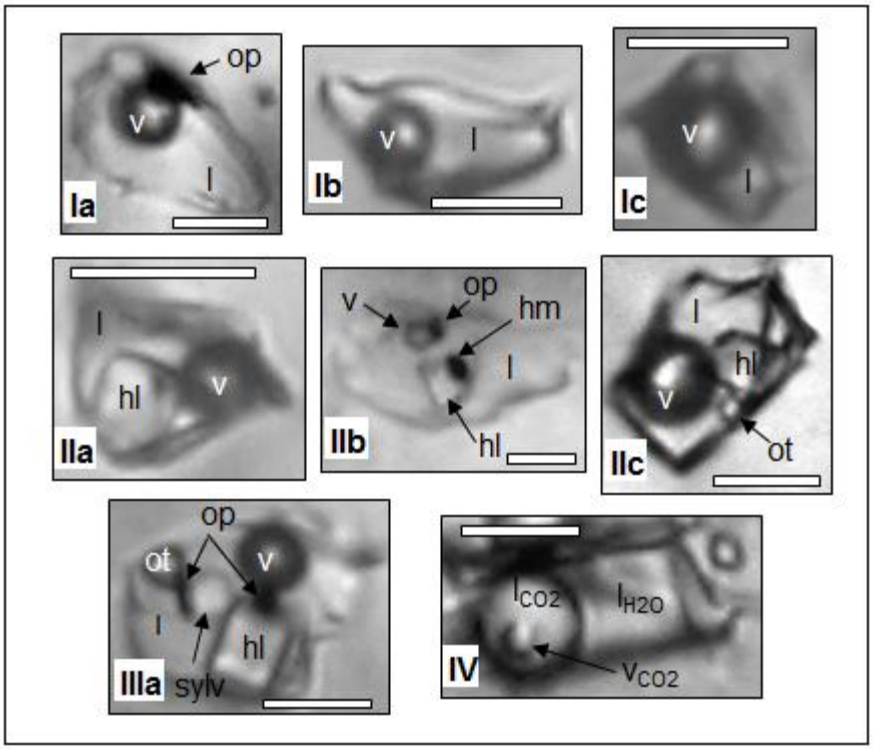

Figure 3. Microphotographs of fluid inclusion types. A) Type Ia B) Type Ib C) Type Ic D) Type IIa E) Type IIb F) Type IIc G) Type IIIa H) Type IV. White bar is approximately 5 μm. No pictures are available for types IId and IIIb.

Table 3. Questa fluid inclusion types and their microthermometric data from Rowe (2011 or Chapter I).

FI Type	# of FIs	Phases	Tlv Range in °C	Salinity Range in eq. wt.% NaCl±KCl±$CaCl_2$	Mode of Final Th
Ia	31	l+v+s; l>v; s=hm,op, ot	88-520	0-25	vbd
Ib	114	l+v; l>v	105-540	0-25	vbd
Ic	87	l+v±s; v≥l; s=op, hm, ot	240-560	0-25	ld or cb
IIa	41	l+v+s; l>v; s=hl	145-520	30-59	hd or vbd
IIb	76	l+v+s; l>v; s=hl±op±hm	62-480	24-64	hd or vbd
IIc	67	l+v+s; l>v; s=hl+ots±hm±op	68-560	32-64	hd, vbd, or otd
IId*	min.	l+v+s; v>>l; s=hl±hm±op±ot	-------	-------	-------
IIIa	14	l+v+s; l>v; s=hl+sylv±hm±op±ot	178-325	39-63	hd or otd
IIIb*	min.	l+v+s; v>>l; s=hl+sylv±hm±op±ot	-------	-------	-------
IV	4	$l_{H2O}+l_{CO2}+v_{CO2}$; $l_{H2O}>l_{CO2}+v_{CO2}$	130-260	0-9	l_{H2O}

l=liquid v=vapor s=solid hm=hematite op=opaque(s) hl=halite ot=other translucent daughter(s) sylv=sylvite vbd=vapor bubble disappearance hd=halite dissolution ld=liquid disappearance cb=critical behavior otd=other translucent daughter dissolution SABQ=source aplite barren qtz SAV=source aplite veinlet min.=minimal # observed

* IId and IIIb were observed in some samples, but were not used in this study due to the inability to observe phase changes with these types of inclusions.

Table 4 - Comparison of fluid inclusion data from this study to previous authors.

Deposit	Author	Type Equivalent to Rowe (2011 or Chapter I)	Missing Type Equivalent	Final Th in °C*	Salinity	Boiling	Mo Mineralization	Origin
Questa	**Rowe (Chapter I and II)**	**Ia-Ic IIa-IIc IIIa, IIIb IV**	**--**	**All Types: MHBX Tlv =68-520 w/ modes (from largest to smallest) at 380, 180, 460, 280; vnlt Tlv = 62-560 w/ modes (from largest to smallest) at 380, 200, 280 All Types: MHBX Final Th = 88-537 w/largest mode at 380; vnlt Final Th = 169-560 w/largest mode at 380**	**All: MHBX 0-64 eq. wt.% NaCl±KCl±$CaCl_2$; vnlts 0-63 eq. wt.% NaCl±KCl±$CaCl_2$**	**Yes**	**≤420-240°C with a 380°C mode and 0-64 eq. wt.% NaCl±KCl±CaCl2**	**Mixed magmatic and meteoric*** **
	Bloom (1981)	Ia, Ib Ic IIa, IIb IIIa IV	IIIb	300 to >600, mode at 390 300 to >600, mode at 390 320 to >600, mode at 390	5-15 eq. wt.% NaCl+KCl 30-60 eq. wt.% NaCl+KCl 40-70 eq. wt.% NaCl+KCl	Yes	500-300°C with a mode @390°C and 5-15 and/or 30-60 eq. wt.% NaCl±KCl	Mixed magmatic and meteoric
	Smith (1983)	Ib, Ic IIa, IIb IIIa	Ia IIc, IId IIIb IV	All: 300-600 w/a mode at 380, secondaries - 200-370	All: 5-65 eq. wt.% NaCl	Yes	550-350°C with a mode @380°C and 5-57 eq. wt.% NaCl±KCl	Mixed magmatic and meteoric**
	Cline & Bodnar (1994) and Cline & Vanko (1995)	Ia, Ib Ic IIa, IIb, IIc, IIIa	IId, IIIb IV	150-370 360-500 200-500, mode @ 360-400; Tlv = 55-490	0-12 eq. wt.% NaCl 2-26 eq. wt.% NaCl 31-57 eq. wt.% NaCl	No	500-150°C with a mode @ 380°C and 0-26 and 31-57 eq. wt.% NaCl±KCl	Magmatic
	Klemm et al. (2004 and 2008)	Ia, Ib Ic IIa, IIb IIIa IV	IIc, IId IIIb	Range of 250-500 for all types in MHBX and qtz-mo veinlets	Range of 2-17 and 30-50 eq. wt.% NaCl for all types in MHBX and qtz-mo veinlets	Yes	420-350°C (no mode reported) and 33-45 eq. wt.% NaCl±KCl	Magmatic
Climax	Hall (1974)	Ia, Ib Ic IIa-IIc, IIIa IV	IId, IIIb	200-400 350-600 200-400 200-400 Mode @ 250-350 for all types	0-12 eq. wt.%NaCl 35-43 eq. wt.% NaCl	No	385-335°C, 0-12 and 35-43 eq. wt. % NaCl	Mixed magmatic and meteoric**
Henderson	Kamilli (1978)	Ia, Ib Ic IIa	IIb-IId IIIa, IIIb IV	Range of 250 to >600 in all inclusions	<2 eq. wt.% NaCl 5-20 eq. wt.% NaCl 30-60 eq. wt.% NaCl	Yes	500°C no salinities reported	Magmatic
	White et al. (1981)	Ia, Ib Ic IIa	IIb-IId IIIa, IIIb IV	Range of 250 to >600 in all inclusions with a mode @ 400	0-65 eq. wt.% NaCl for all types	No report	650-500°C (pressure corrected), mode of 400°C (not pressure corrected) and 30-65 eq. wt.% NaCl	Magmatic

Deposit	Author	Type Equivalent to Rowe (2011 or Chapter I)	Missing Type Equivalent	Final Th in °C*	Salinity	Boiling	Mo Mineralization	Origin
Henderson cont'd	Carten (1987) and Carten et al.(1988)	Ia IIIa	Ib, Ic IIa-IId IIIb IV	Tlv: 346+/-30 (F-rich) Tlv: 280+/-35 (Cl-rich)	~2-7 eq. wt.% NaCl (F-rich) 16-20 to 62 eq. wt.% NaCl (Cl-rich)	No	376-316°C and 2-7 eq. wt% NaCl	Magmatic**
	Seedorff & Einaudi (2004)	Ia-Ic IIa-IIc IIIa	IId IIIb IV	600-460 (mod. high), 530-310 (mod), 390-200 (low)	28-65 eq. wt.% NaCl+KCl to <29 eq. wt.% NaCl	No	600-460°C and <29 eq. wt.% NaCl	Magmatic
Silver Creek	Larson (1987)	Ia, Ib, IIa-IIc, IIIa Ic IV	IId, IIIb	Tlv: 225-415 Tlv: 355-425	0-7 eq. wt.% NaCl	Yes	420-350°C and 0-7 eq. wt.% NaCl	Mixed magmatic and meteoric**

* All studies reported in Final Th whereas this study was reported in this table as both Tlv homogenization and Final Th.
** Conclusion derived based upon both FI and stable isotope data.
*** Conclusion derived based upon fluid inclusion, stable isotope, and fluid inclusion gas analysis data.

Table 4 - Comparison of fluid inclusion data from this study to previous authors.

carbonic-bearing inclusions that contain liquid water, liquid CO_2, and vapor CO_2 (double bubble). The water phase is greater than the carbonic phases in Type IV inclusions.

Comparable fluid inclusion types to this study were identified in all of the Climax-type deposits of the COMB that had fluid inclusion microthermometry studies performed (Climax, Henderson, and Silver Creek), with a few minor differences (Table 4). No vapor-rich halite-bearing Type IId or vapor-rich multi-solid Type IIIb fluid inclusions were identified in the COMB deposits. It is a possibility however, that these inclusions were overlooked due to the vapor-rich property and the inability to observe phase changes in this type of inclusion as was the likely case in some previous studies on Questa. Also, carbonic fluid inclusions were not identified at Henderson. The lack of liquid CO_2-bearing inclusions at Henderson reveals that the system is low in CO_2 (<5%), since 5% CO_2 is required for Type IV inclusions to exist (Shepherd et al., 1985).

Tshl>>Tlv Inclusions

Before discussing fluid inclusion temperatures, it is important to first convey that the temperature data for this Questa study is reported in terms of homogenization temperature of the liquid-vapor phase (Tlv) rather than by final homogenization temperature (Final Th) due to the trapped halite phenomenon (Rowe, 2011a or Chapter I). The majority of the fluid inclusions that contained halite daughter minerals (Types II and III) at Questa demonstrated Final Th by halite dissolution (Tshl), with a significant number of inclusions exhibiting halite dissolution temperatures substantially higher (up to 339°C) than homogenization of the liquid-vapor phase. Based upon phase equilibria constraints, homogeneous trapping of this type of fluid inclusion would require lithostatic pressures much too great for any system (Bodnar, 1994; Bodnar & Vityk, 1994; Cline &

Bodnar, 1994; Gunter et al., 1983; Bodnar, 2003; Kamilli, 1978; Becker et al., 2008), which corresponds to an unrealistic depth of emplacement for the Goat Hill orebody. This study has determined that heterogeneous trapping, or the entrapment or capture of halite crystals from a heterogeneous fluid that is saturated with respect to halite (trapped halite phenomenon), is the favored mechanism for producing the Tshl>>Tlv fluid inclusions at Questa. A two-phase fluid that was exsolved directly from the parent magma (Figure 4A - Stage 1) became saturated with respect to halite by pervasive boiling (Figure 4A – Stage 2) and/or simple cooling (Figure 4A – Stages 2, 3, and 4) in the latter stages of fluid evolution at Questa. The fluid inclusions that exhibit Tshl>>Tlv are a result of heterogenous trapping, i.e. a saturated saline fluid and a halite crystal. Hence, reporting the temperature in terms of Tlv rather than Final Th is more representative of the real fluid from which these inclusions originated. In Figure 4A, the fluid inclusions above the Halite Saturation Curve (HSC) homogenized by Tshl>>Tlv and represent this saturated saline fluid and a trapped halite crystal. The true representation of the fluid would be the salinity on the HSC for those fluid inclusions at their Tlv temperature, as represented by the dark gray line along the HSC (also see the schematic diagram in Figure 5). The inclusions along the HSC in Figure 4B are those same fluid inclusions that are above the HSC in Figure 4A, but at the temperature in which the trapped halite crystal dissolved (Final Th), rather than Tlv, and the false fluid salinity that is calculated from that temperature. This is how data is typically reported in fluid inclusion studies, even when these types of inclusions occur. The fluid inclusions above the HSC in Figure 4B contain sylvite, placing them above the HSC. They also represent temperatures and

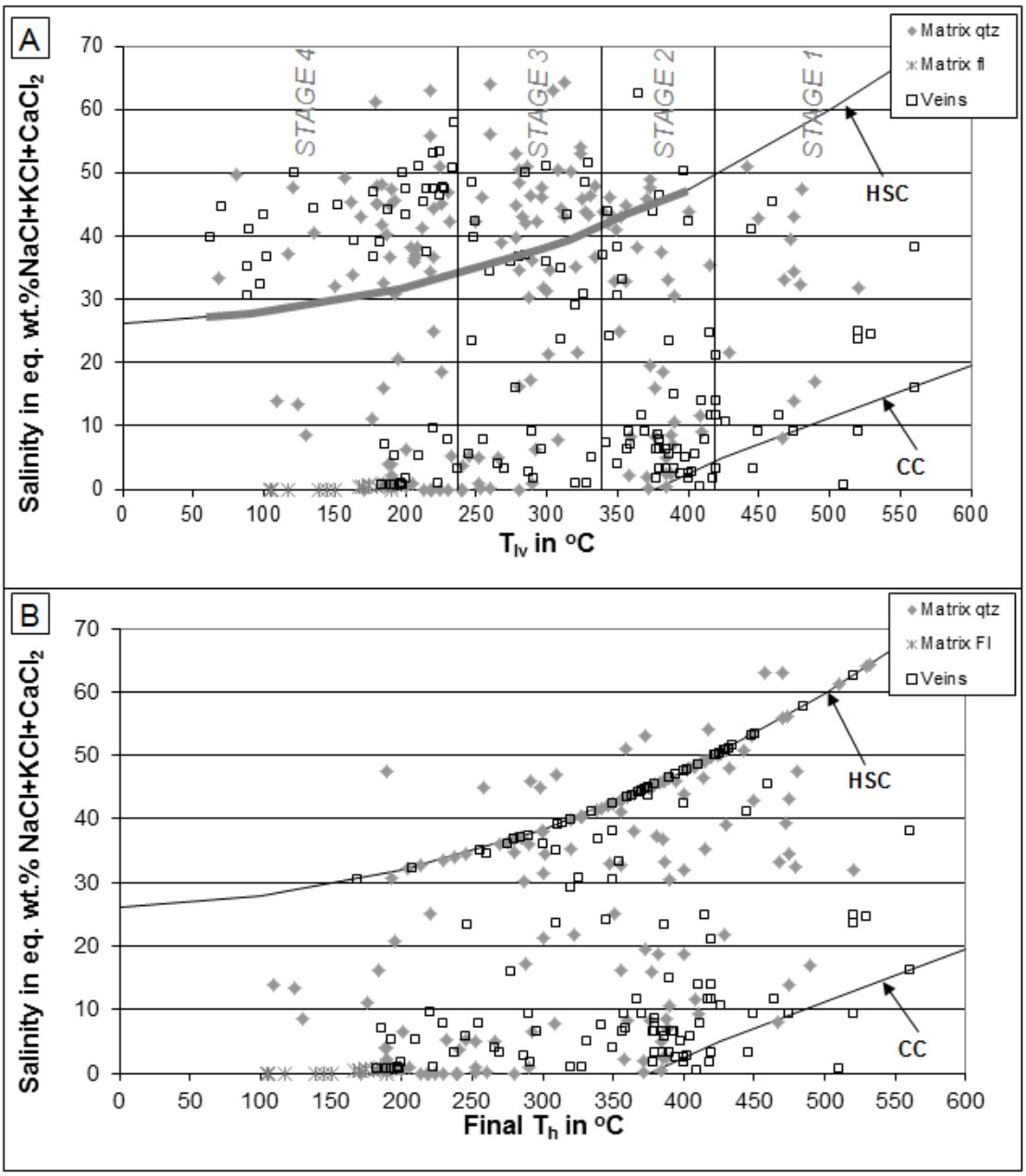

Figure 4. - Temperature vs. salinity diagrams demonstrating differences when reporting in terms of Tlv vs. Final Th. A) Temperature of homogenization in terms of Tlv vs. Salinity. All of the FIs above the Halite Saturation Curve (HSC) homogenized by Tshl and do not represent the true salinity of the fluid due to the Trapped Halite Phenomenon. The real salinity of the fluid is the same temperature, but projected down to the HSC (thick gray line). B) Temperature of homogenization in terms of Final Th vs. Salinity. All of the FIs on the HSC homogenized by Tshl. FIs above the HSC contain sylvite. The FIs on or above the HSC represent temperatures and salinities that higher than real fluid due to the Trapped Halite Phenomenon. Also see related Figure 5. Note the differences between these two diagrams: the Tlv diagram has more FIs at lower temperatures and less FIs at higher temperatures than the Final Th diagram. This demonstrates how the data can be skewed depending on how it is reported.

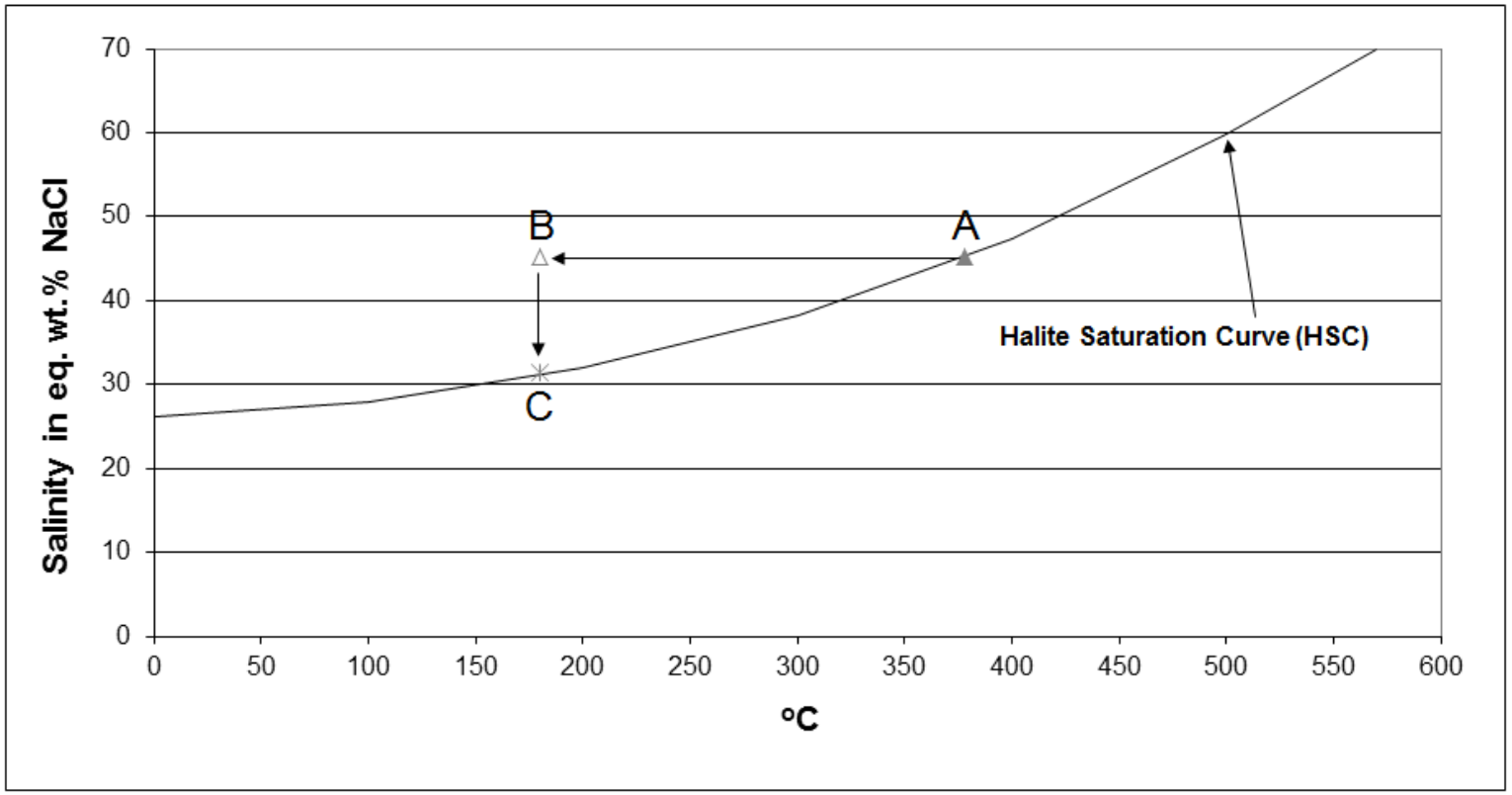

Figure 5 - A schematic diagram demonstrating the true fluid representation of a Tshl>>Tlv fluid inclusion. The Final Th of the FI is plotted at (A), where Tshl occurs at 378°C and corresponds to a salinity of 45 eq. wt.% NaCl. Due to the trapped halite phenomenon, (A) does not represent the true fluid temperature and salinity. In order to find the true temperature and salinity of the fluid, the Tlv (180°C) of the fluid inclusion is plotted against the salinity defined by Tshl for that inclusion (at (B)). (B) represents the miniumum temperature of trapping (Tt) for the fluid inclusion, a saturated saline fluid, and a trapped halite crystal, which is why B plots above the HSC. From here, the true salinity of the FI can be determined by intersecting the HSC at the temperature of Tlv (at (C)). At (C), the Tshl=Tlv, giving way to the minimum Tt and the salinity of the halite saturated fluid (31 eq. wt.% NaCl). The difference in salinity and temperature between this point and that of the Final Th (A) is attributed to the halite crystal that was floating in the halite saturated fluid and was trapped by the fluid inclusion.

salinities that are not real when plotted in terms of Final Th. Tshl>>Tlv fluid inclusions were noted at Henderson, but not at Climax or Silver Creek, and the suggested mechanism for their origin was not the trapped halite phenomenon as at Questa. Kamilli (1978), Carten (1987), Carten et al. (1988), and White et al. (1988) concluded that overpressures caused by exsolution and evolution of the hydrothermal fluid from the source magma, produced this type of fluid inclusion at Henderson. Overpressures are discounted by this study for Questa based upon the low tensile strength (35 bars average) of the altered andesite and volcaniclastic country rock at Questa that would fracture before significant

overpressures could occur (Rowe, 2011a or Chapter I) and various supporting evidence for the trapped halite phenomenon at Questa (solid inclusions of halite, other daughter minerals that do not dissolve upon heating, cogenetic liquid-rich brine inclusions and v-rich inclusions, Type IId and Type IIIb inclusions, variable halite to liquid phase ratios, and inclusions containing more than one halite crystal). In contrast, the tensile strength of the competent rhyolite porphyry country rock at Henderson is much higher than the altered andesite and volcaniclastics of Questa and could possibly withstand the calculated overpressures from the Tshl>>Tlv inclusions at Henderson (White et al., 1981). Due to this fact, and without reported evidence for Henderson that would support the trapped halite phenomenon as the origin of the Tshl>>Tlv fluid inclusions, overpressures cannot be discounted for the origin of this type of fluid inclusion at the Henderson deposit. However, based upon evidences described by various authors on this type of fluid inclusion (Erwood et al., 1979; Campbell et al., 1995; Eastoe, 1978; Wilson, 1978; Kodera et al., 2004; Campbell et al., 2001; Becker et al., 2008), the trapped halite

phenomenon cannot be discounted for this type of fluid inclusion at Henderson either. Further investigation to identify if any evidence of trapped halite phenomenon exists at Henderson is warranted to determine which mechanism created the Tshl>>Tlv fluid inclusions.

Fluid Inclusion Temperatures

The various fluid inclusion microthermometry studies at Questa reflected a variable and wide range of homogenization temperatures (62 to >600°C), however the main mode was similar for each study at 380-400°C (Figure 6) (Rowe, 2011a or Chapter I; Bloom, 1981; Smith, 1983; Cline & Bodnar, 1994; Cline & Vanko, 1995; Klemm et al., 2004; Klemm et al., 2008). Homogenization temperatures for Climax were similar to Questa with a range of 200-600°C, however Climax did not exhibit any temperatures corresponding to the lower range of Questa (62-200°C) (Hall et al., 1974). The temperature mode for Climax was 250-350°C, which is different than the 380-400°C mode for Questa. The lower end of the Climax mode is comparable, however, to the Stage 3 temperature mode associated with Mo mineralization at Questa of 280°C and the upper end of the Climax mode is comparable to the temperature mode (380-400°C) associated with the main stage of mineralization (Stage 2) at Questa (Figure 7a) (Rowe, 2011 or Chapter I). Henderson exhibited a similar homogenization temperature range to Climax (250 to >600°C), which is also comparable to Questa (Kamilli, 1978; White et al., 1981; Carten, 1987; Carten et al., 1988; Seedorff & Einaudi, 2004). The only temperature mode that was reported for Henderson was 500-650°C (White et al., 1981). However, this temperature range was a pressure correction based upon the Tshl>>Tlv fluid inclusions and the actual measured raw temperature mode was 400°C. If the

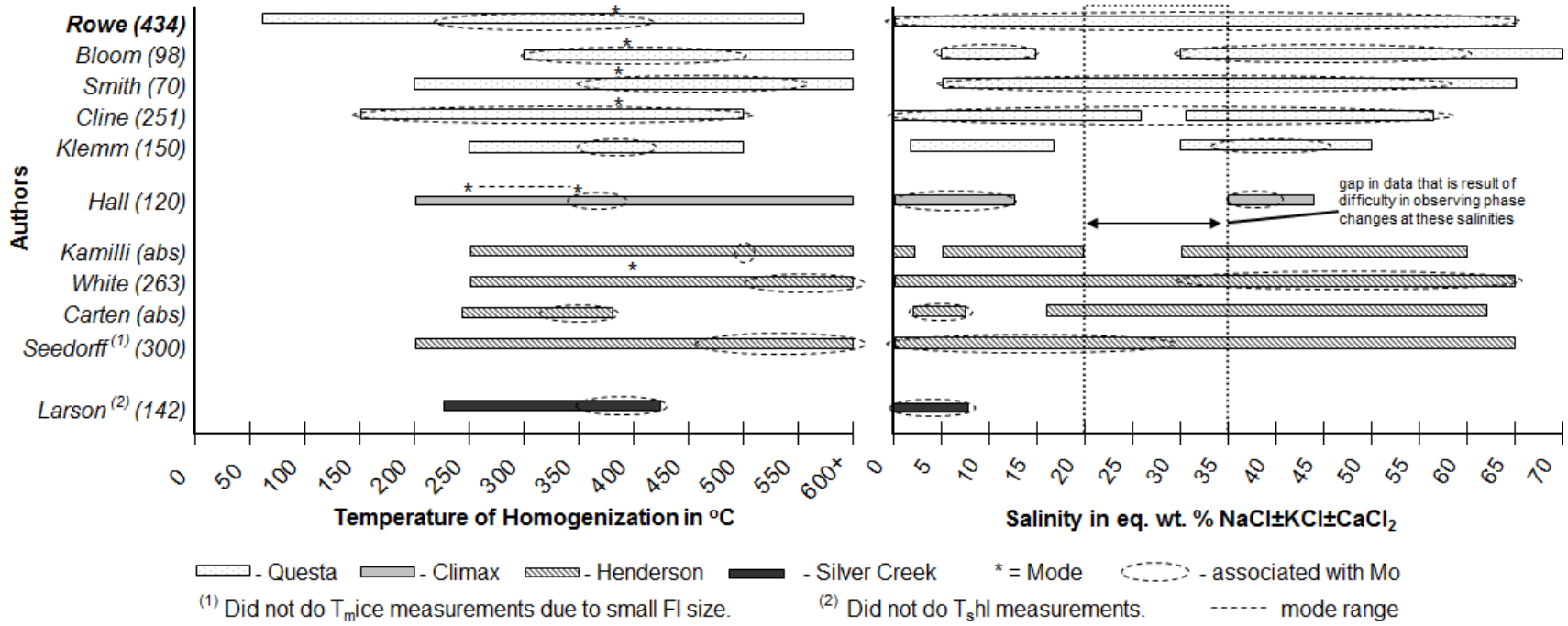

Figure 6. Temperatures of homogenization and salinities for various authors on Climax-types (Rowe, 2011; Bloom, 1981; Smith, 1983; Cline & Bodnar, 1994; Cline & Vanko, 1995; Klemm & Pettke, 2004; Klemm et al., 2008; Hall et al., 1974; Kamilli, 1978; White et al., 1981; Carten, 1987; Seedorff & Einaudi, 2004; Larson, 1987). The number in paranthesis next to author is the number of fluid inclusions analyzed. The number of FIs was not available for Kamilli or Carten due to the limitations of abstract reference material. All temperatures are Final Th except for Rowe, Carten, and Larson, which are Tlv.

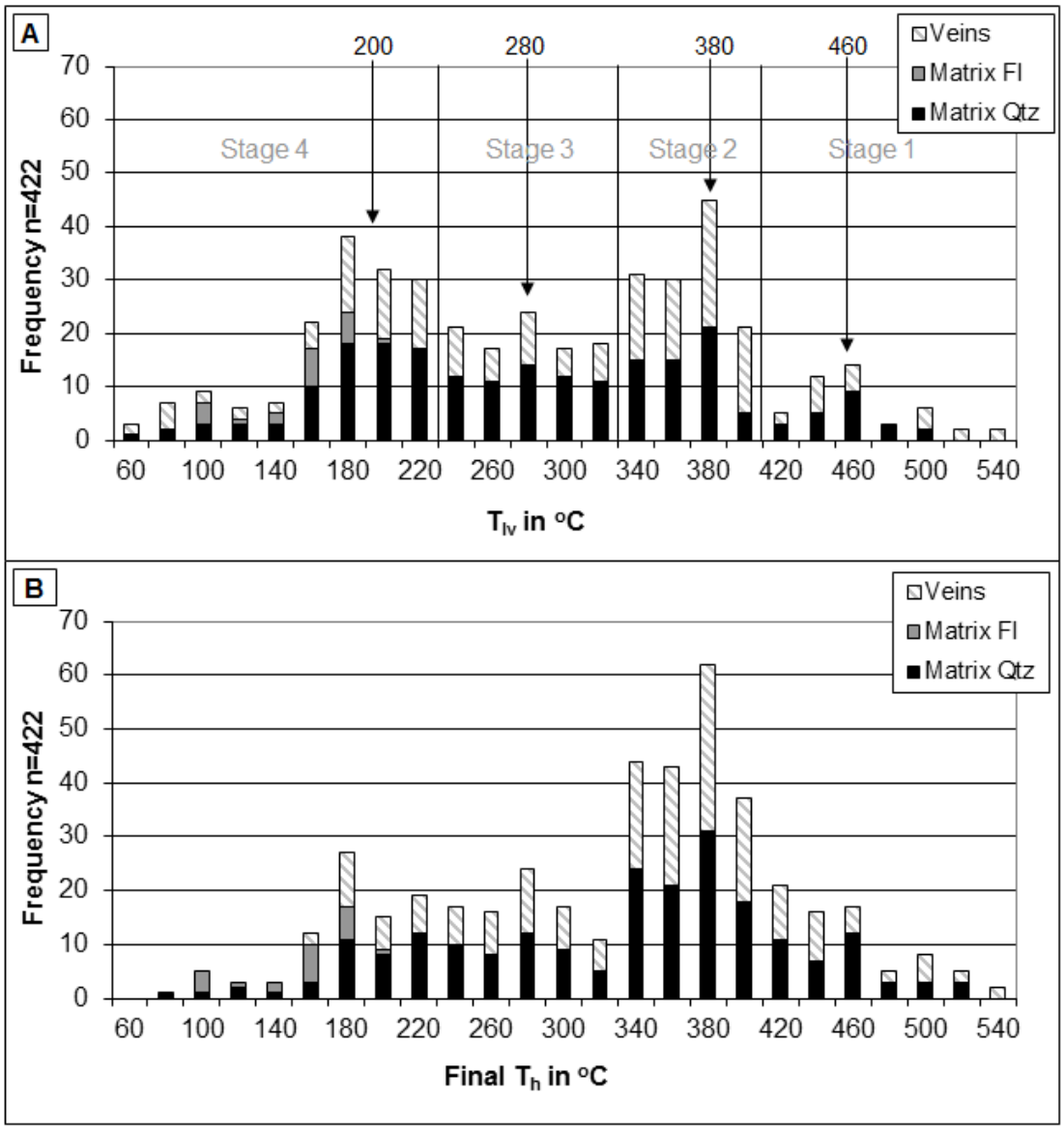

Figure 7. - Histograms demonstrating difference in temperature distribution when reporting in terms of Tlv vs. Final Th.

trapped halite phenomenon was considered for the Tshl>>Tlv fluid inclusions at Henderson, then the 400°C mode would correspond with the 380-400°C mode of Questa and the upper limit of the temperature mode (350°C) for Climax. Silver Creek exhibited a narrower temperature range of 225-425°C compared to Questa and the other COMB deposits (Larson, 1987).

Questa exhibited the widest range of fluid inclusion temperatures compared to the Climax-type deposits of the COMB (Figure 6). However, as previously mentioned, the data for this study is reported in terms of Tlv rather than Final Th and the lower temperatures for Questa are mostly attributed to this study. Note the temperature and salinity distribution differences when reporting in terms of Tlv versus Final Th (Figure 4 and Figure 7). Reporting temperatures in Tlv allowed for more data on the lower temperature end and less data on the higher temperature end when comparing Tlv and Final Th methods. This might be a possible explanation why this study reveals lower temperatures compared to several other studies (Bloom, 1981; Smith, 1983; Klemm, 2008; Hall, 1974; Kamilli, 1978; White et al., 1981; Seedorff & Einaudi, 2004) that reported their data in terms of Final Th (all except Carten,1987; Carten et al., 1988; and Larson,1987) (Figure 6). If the homogenization temperature data is looked at in terms of Tlv for Cline & Bodnar (1994) and Cline & Vanko (1995), rather than the reported Final Th, the temperature range is 55-490°C (as opposed to 150-500°C for Final Th), similar to this study. Again, this reveals that lower temperatures are brought out from reporting Tlv rather than Final Th on the Tshl>>Tlv fluid inclusions.

Fluid Inclusion Salinities

Questa exhibited a large range of fluid inclusion salinities with eq. wt.% NaCl measurements from 0-70 (Figure 6) (Rowe, 2011a or Chapter I; Bloom, 1981; Smith, 1983; Cline & Bodnar, 1994; Cline & Vanko, 1995; Klemm et al., 2004; Klemm et al., 2008). The salinities exhibited by Climax fluid inclusions reflected a bimodal distribution with values of 0-12 and 35-45 eq. wt.% NaCl, rather than a continuous range as at Questa (Hall et al., 1974). The upper salinity limit for Climax (45 eq. wt. % NaCl) is much lower than the upper limit for Questa (70 eq. wt.% NaCl) as well. These differences between Questa and Climax salinities may prove to be a significant dissimilarity. As previously mentioned, Tshl>>Tlv fluid inclusions were not observed at Climax. The lack of Tshl>>Tlv inclusions is the reason that the upper salinity limit for Climax is so much lower than Questa's. Climax equivalent Type II and III (halite-bearing) fluid inclusions needed to be on or below the halite saturation curve (Tshl≤Tlv) to have a salinity of 35-43 eq. wt.% NaCl at 200-400°C. As established by this study, boiling is the mechanism for fluid oversaturation with respect to halite, which in turn gives way to the trapped halite phenomenon and Tshl>>Tlv fluid inclusions (Rowe, 2011a or Chapter I). It was reported that boiling did not occur at Climax (Hall et al., 1974), which supports the lack of Tshl>>Tlv inclusions and the lower salinities than Questa (Table 4). The bimodality of the Climax salinities is also likely due to the absence of boiling, heterogeneous trapping, and the trapped halite phenomenon, since both of these mechanisms give way to variable salinities from low to moderate to brines such as at Questa (Rowe, 2011a or Chapter I).

Fluid inclusion salinities for Henderson are very similar to those of Questa with a continuous range of 0-65 eq. wt.% NaCl (Figure 6) (Kamilli, 1978; White et al., 1981; Carten, 1987; Carten et al., 1988; Seedorff & Einaudi, 2004). Boiling was indicated by one study on Henderson (Kamilli, 1978) and could likely be the cause of the variable salinities as was at Questa (Table 4). The salinity range (0-7 eq. wt.%NaCl) for Silver Creek is much smaller and lower compared to Questa and the other COMBs (Figure 6) (Larson, 1987). Higher salinities do exist for the Silver Creek deposit since halite-bearing comparable Type II and III inclusions were reported, however they were not measured for Tshl to get the brine salinities (Larson, 1987). Due to this fact, it is difficult to compare salinities between Silver Creek and Questa. What can be compared is that there are low-moderate salinity inclusions and high salinity brines, similar to all of the Climax-type systems.

Molybdenite Mineralization and Fluid Origin

At Questa, it was determined that the main mode of molybdenite mineralization occurred at 380°C and 0-64 eq. wt.%NaCl±KCl±$CaCl_2$ as a result of heat loss from boiling. Boiling was evident by cogenetic l-rich and v-rich fluid inclusions that homogenized at the 380°C mode. Based upon a mixing pattern in the temperature vs. salinity fluid inclusion data, it was also concluded that meteoric mixing with the evolved parent magmatic fluid occurred during this mode as well, causing a temperature decrease and subsequent molybdenite mineralization. A temperature of mineralization of 380°C is too low to be entirely magmatic, and with the supporting evidence from T-X data and the concept of the trapped halite phenomenon, it was concluded that the Questa system is magmatic with significant meteoric input. As is common in porphyry systems, a post-

mineralization late-stage meteoric influx also occurred in the system at 200°C with a salinities of ≤1 eq. wt.% NaCl and is associated with secondary inclusions and fluorite and calcite mineralization (Chapter I or Rowe, 2011a).

Fluid inclusion evidence reported by Hall et al., (1974) for Climax revealed a temperature of 360±25°C and low to moderate (0-12 eq. wt.% NaCl) to brine (35-40 eq. wt.% NaCl) salinities for molybdenite mineralization. Similar to Questa, Hall et al. (1974) concluded that molybdenite mineralization was a result of temperature decrease at Climax. The temperature decrease was solely the result of meteoric mixing with primary magmatic fluids however, rather than both a heat loss and temperature decrease due to boiling and magmatic-meteoric mixing as was at Questa. Also similar to Questa, Climax FI data demonstrated a late-stage meteoric-dominant fluid source for fluorite mineralization at 190-275°C and <1 eq. wt.% NaCl (Hall et al., 1974). Despite the lack of boiling, these conclusions make Climax exceptionally comparable to Questa.

A magmatic source was concluded to be the origin of the mineralizing fluids at Henderson (Kamilli, 1978; White et al., 1982; Carten , 1987; Carten et al., 1988; Seedorff & Einaudi, 2004). This conclusion was mostly based upon a pressure corrected temperature range of 460-650°C from a raw data mode of approximately 400°C (Kamilli, 1978; White et al., 1982; Seedorff & Einaudi, 2004). The temperatures were pressure corrected to the higher temperatures not because of the lack of evidence of boiling, but to explain the Tshl>>Tlv fluid inclusions. As previously mentioned, the Tshl>>Tlv fluid inclusions at Henderson were defined as being a result of overpressures, however the trapped halite phenomenon could also be a likely mechanism in creating this type of inclusion. If further investigation revealed the trapped halite phenomenon as the cause

for the Tshl>>Tlv fluid inclusions at Henderson, no pressure correction would be necessary and the raw mode temperature of 400°C, which is too low to be entirely magmatic, would be the temperature of molybdenite mineralization. This indicates that Henderson is comparable to Questa. If overpressure was the mechanism for Tshl>>Tlv fluid inclusions at Henderson, this would set Henderson apart from Questa with a much higher temperature of mineralization (460-650°C). One author did however, report a temperature of mineralization at 316-376°C at Henderson, with no pressure correction and a suggested magmatic source (Carten, 1987 and Carten et al., 1988). Again, this temperature is too low to be entirely magmatic as was reported and the temperature is comparable to Questa mineralization temperatures. In summary, with the recent interpretations of the trapped halite phenomenon to explain Tshl>>Tlv inclusions (Campbell et al., 2001; Becker et al., 2008; Kodera et al., 2004; Bodnar, 2003) in combination with the temperatures of mineralization reported by Carten (1987) and Carten et al. (1988) for Henderson and similar temperatures for Questa and Climax, it may be that the temperature of mineralization at Henderson is the 400°C raw mode.

The salinities that were reported to be associated with molybdenite mineralization at Henderson were quite variable (30-65 eq. wt.% NaCl from White et al., 1981; 2-7 eq. wt.% NaCl from Carten, 1987 and Carten et al., 1988; and <29 eq. wt.% NaCl from Seedorff & Einaudi, 2004), inhibiting the ability to conclude a summarized salinity for Henderson (Figure 6 and Table 4). Based upon this fact, it may be that all reported salinities are associated with mineralization (2-65 eq. wt.% NaCl), which would indicate that Henderson is comparable to Questa.

Fluid inclusions at Silver Creek revealed a temperature and salinity range of 350-420°C and 0-7 eq. wt.% NaCl for the primary mineralizing fluid, conducive to a mixed magmatic-meteoric source for the origin of Silver Creek (Figure 6) (Larson, 1987). The mineralization temperature range is compatible with Questa, along with Henderson's raw temperature mode and the temperatures of Climax, as well. However, the salinity that was reported to be associated with molybdenite mineralization at Silver Creek is an exceptionally low and narrow range compared to Questa and the COMB (Figure 6). Halite-bearing inclusions that would produce higher salinities were observed at Silver Creek, but Tshl measurements were not taken on these inclusions to obtain the NaCl concentration (Larson, 1987). Boiling was indicated by the cogenesis of liquid- and vapor-rich fluid inclusions at Silver Creek, so no pressure correction was applied to the data to derive the 350-420°C temperature range. A late stage, lower temperature (225-350°C), low salinity fluid that represents meteoric influx onto the system was indicated by secondary inclusions at Silver Creek. The temperature range for this stage of the Silver Creek Climax-type system is slightly higher, but comparable, to similar stages for Questa and Climax.

Stable Isotopes

Oxygen and Hydrogen Analyses and Fluid Evolution

$\delta^{18}O_{mineral}$ values associated with molybdenite mineralization at Questa ranged from 6.0 to 8.6‰ for quartz, 1.2-5.7‰ for biotite, and 1.5-8.5‰ for K-feldspar (Table 5 and Figure 8). $\delta D_{mineral}$ values for Questa fluorophlogopite (biotite) ranged from -117 to -89‰. The $\delta^{18}O_{H2O}$ and δD_{H2O} values associated with the molybdenite-bearing fluid

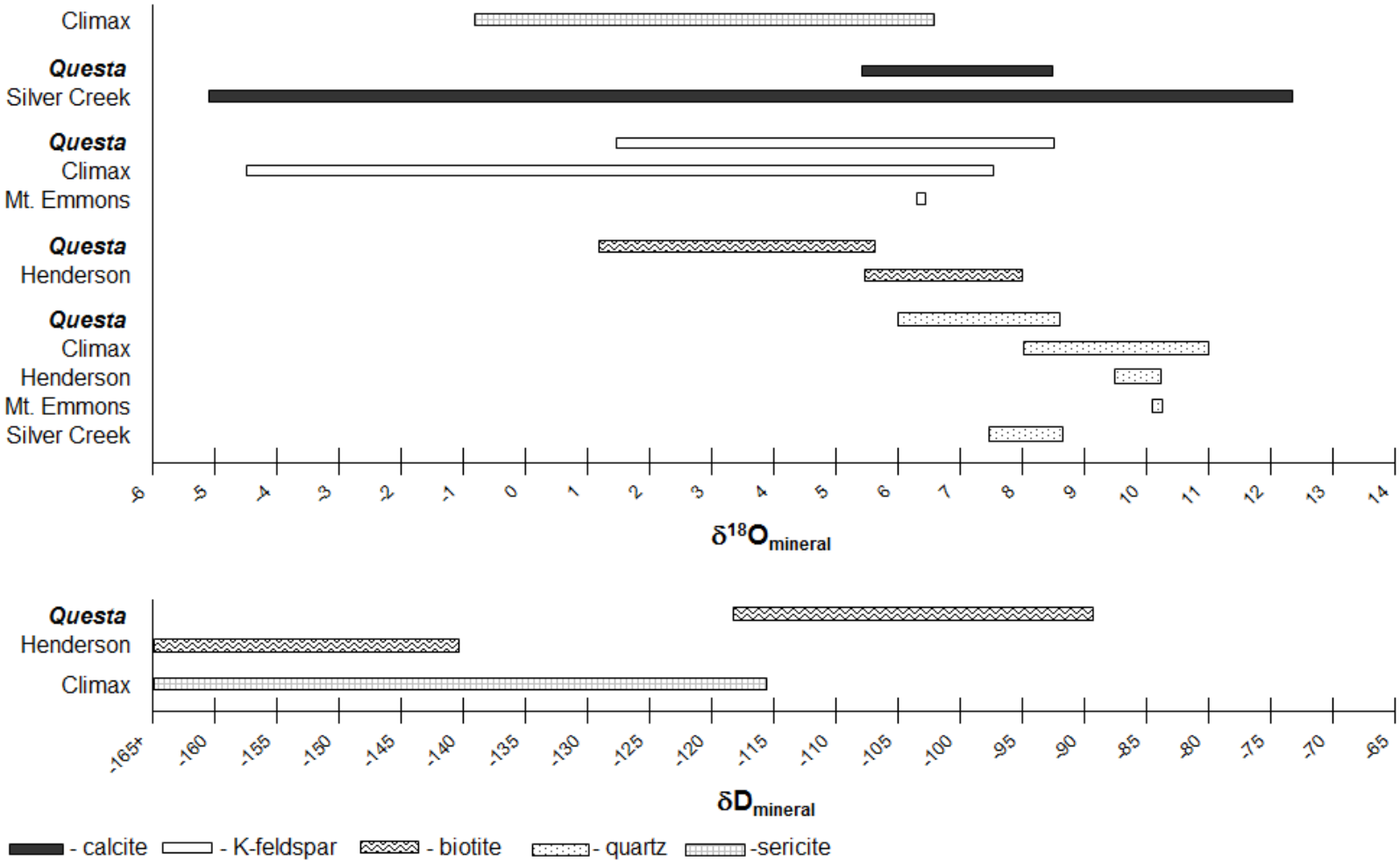

Figure 8 - $\delta^{18}O_{mineral}$ and $\delta D_{mineral}$ ranges for various Climax-type deposits. References are as follows: Rowe, 2011a; Smith, 1983; Ross et al., 2002; Hall et al., 1974; Carten et al., 1988; Stein & Hannah, 1985; Stein, 1988; Larson, 1987; Wareham et al., 1998.

Authors	$\delta^{34}S$ (‰)	$\delta^{13}C$ (‰)	$\delta^{18}O$ (‰)	δD (‰)	$\delta^{18}O_{H2O}$ from FIs (‰)	δD_{H2O} from FIs (‰)	Calc $\delta^{18}O_{H2O}$ @ 550°C (‰)	Calc δD_{H2O} @ 550°C (‰)	Calc $\delta^{18}O_{H2O}$ @ 400°C (‰)	Calc $\delta^{18}O_{H2O}$ @ 380°C (‰)	Calc δD_{H2O} @ 380°C (‰)	Calc $\delta^{18}O_{H2O}$ @ 350°C (‰)	Calc δD_{H2O} @ 350°C (‰)	Calc $\delta^{18}O_{H2O}$ @ 320°C (‰)	Calc $\delta^{18}O_{H2O}$ @ 275°C (‰)	Calc δD_{H2O} @ 275°C (‰)	Calc $\delta^{18}O_{H2O}$ @ 200°C (‰)
Questa																	
This Study																	
MHBX qtz			6.0-8.2			-101 to -71				1.5-3.7							
MHBX bt			2.0-5.6	-115 to -89						3.8-7.4	-89 to -63						
MHBX fl					-4.0 to -1.7	-109 to -106											
MHBX kf			1.5-5.4							-1.1-2.9							
MHBX ca		-6.2 to -5.0	5.4-8.5														-4.3 to -1.3
vnlt qtz			6.1-8.4			-143 to -52				1.6-3.9							
MHBX mo	0.4-2.3																
vnlt mo	1.1-2.0																
Smith (1984)																	
qtz			6.8-12.8				7.8		1.6-7.6					1.9-2.3			
kf			1.8-8.5														
bt			1.2-5.4	-117 to -110			3.6-7.8	-95 to -93		3.0-7.2	-92 to -86						
Ross (2002)																	
qtz			6.8-8.6				5.1-6.9			2.3-4.1							
bt			3.3-5.7	-138 to -112			5.2-8.1	-121 to -93		5.1-7.5	-113 to -88						
Stein (1985, 1988)																	
mo	1.0-1.1																
Climax																	
Hall et al. (1974)																	
qtz			8.4-10.9			-140 to -88						3.0-5.2					
kf			-4.5-7.5									-8.5 to 3.5					
ser			-0.8-7.4	-168 to -116											-3.1-5.0	-144 to -92	
Stein (1985, 1988)																	
mo	2.5-3.6																
Henderson																	
Carten et al. (1988)																	
qtz			9.5-10.2			-137 to -92						4.2-4.9					
bt			5.5-8.0	-165 to -141								7.2-9.7	-107 to -83				
Stein (1985, 1988)																	
mo	4.7-5.3																
Mt. Emmons																	
Stein (1985, 1988)																	
kf			6.4														
qtz			10.1														
mo	3.7-4.6																
Silver Creek																	
Larson (1987)																	
qtz			7.5-8.7			-104 to -90								2[1]			
Wareham (1998)																	
mo	0.5-4.6																
ca		-7.5-1.1	-5.1-12.4														-14.9-2.5

Table 5 - Oxygen, hydrogen,sulfur, and carbon stable isotope ranges for various authors. The calculated water values reported by other authers is included. See these references for fractionation equations used in their calculations. Values in the gray box were calculated from the main mineralization mode temperature of 380°C from this study using the equations of Clayton et al. (1972), Zheng (1993a), and Suzuoki & Epstein (1976) for comparison purposes. All water values for this study were calculated using the equations of Clayton et al. (1972), Zheng (1993), Zheng (1993a), Zheng (1999), and Suzuoki & Epstein (1976). [1] Larson reported that a temperature range of 320-360°C was utilized in his calculations for qtz.

($\delta^{18}O_{H2O}$ = 1.5-7.6‰ for quartz and biotite and -1.1 to 6‰ for K-feldspar; δD_{H2O} = -112 to -63‰) were calculated from these mineral values utilizing the main mineralization mode temperature of 380-400°C (Table 5 and Figure 9). δD_{H2O} values in quartz were obtained directly from fluid inclusion waters revealing δD_{H2O} values of -101 to -71‰ for MHBX quartz and -143 to -53‰ for veinlet quartz (Rowe, 2011b or Chapter II; Smith, 1983; Ross et al., 2002).

The $\delta^{18}O_{H2O}$ and δD_{H2O} values for quartz and biotite at Questa reveal that the molybdenite mineralizing fluids are not of a purely magmatic origin, but rather evolved from a magmatic to mixed magmatic-meteoric origin, as demonstrated by the a shift to lighter oxygen and hydrogen values. The δD_{H2O} range for the veinlet quartz is significantly larger than the MHBX matrix quartz or biotite at Questa (Table 5 and Figure 9). This difference in the veinlets may be attributed to low water/rock ratios, small sample peaks due to smaller and less abundant fluid inclusions than the MHBX matrix quartz, a higher amount of interstitial fractionated water in the veinlets as a result of smaller and more abundant quartz grains than the MHBX matrix quartz, or a lower fluid inclusion water to quartz interstitial water ratio than the MHBX (Rowe 2010b or Ch. II). Another option is that the veinlet fluid may actually be different isotopically for hydrogen than the MHBX matrix quartz. Based upon mineral paragenesis and quartz and biotite oxygen values, the $\delta^{18}O_{H2O}$ values for K-feldspar were isotopically too light and variable for a Climax-type system. This is likely a result of subjection of K-feldspar to post-mineralization alteration and isotope fractionation. K-feldspar at Questa also revealed unrealistic mineral pair fractionation temperatures, further supporting that this mineral

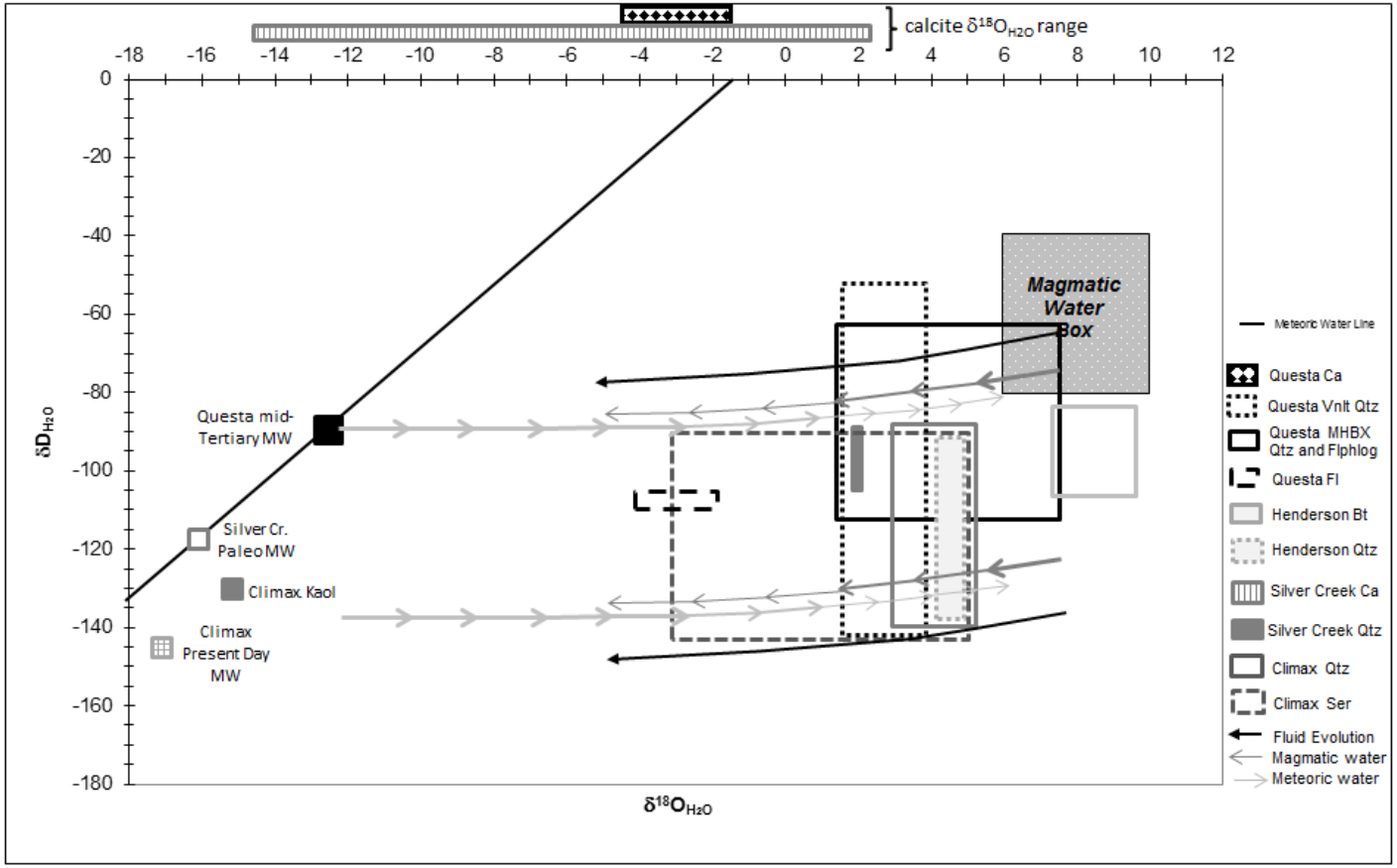

Figure 9. $\delta^{18}O_{H2O}$ vs. δD_{H2O} diagram for Climax-type deposits. Water composition either measured from fluid inclusions or calculated from quartz, fluorophlogopite/biotite, and calcite, and fluorite isotopic ranges. K-feldspar is not included here due to all deposits demonstrating post-mineralization alteration and fractionation of the mineral. See Table 5 and text for any calculation temperatures and references. Where the magmatic water arrows overlap the meteoric water arrows is a zone of magmatic and meteoric mixing. Thickness of arrows demonstrates amount of component, where thicker means more and thinner means less. Questa mid-Tertiary meteoric water (MW) from Johnson et al., 1990. Silver Creek paleo MW from Larson et al., 1987. Climax kaolinite (kaol) demonstrating paleo MW and Climax present day MW from Hall et al., 1974. Ca = calcite Qtz = quartz Flphlog = fluorophlogopite (biotite) Fl = fluorite Bt = biotite Ser = sericite

was not in equilibrium with this system (Rowe, 2011b or Chapter II; Smith, 1983; Ross et al., 2002).

Fluid inclusion waters from post-mineralization fluorite exhibited a meteoric-dominant fluid source with a $\delta^{18}O_{H2O}$ and δD_{H2O} range of -4.0 to -1.7‰ and -109 to -106‰, respectively (Table 5 and Figure 10). Post-mineralization Questa calcites produced a $\delta^{18}O_{mineral}$ range of 5.4-8.5‰. The calcite at Questa is associated with the same stage of fluid evolution (Stage 4 of Chapter II or Rowe, 2011b) as fluorite, hence the mode temperature (200°C) associated with Stage 4 and fluorite was applied to calculate the $\delta^{18}O_{H2O}$ values for calcite (Figure 4a and Figure 7a). Calcite at Questa exhibited a meteoric-dominant source with $\delta^{18}O_{H2O}$ values of -4.3 to -1.3‰, almost identical to fluorite. The isotope values for quartz, biotite, calcite and fluorite demonstrate the evolution of the Questa system from a magmatic to magmatic-dominant magmatic-meteoric mixed fluid to a meteoric-dominant mixed magmatic-meteoric fluid (Figure 9).

Climax $\delta^{18}O_{mineral}$ values are fairly comparable to Questa for quartz and K-feldspar with ranges of 8.4-10.9‰ and -4.5-7.5‰ (Table 5 and Figure 8). The $\delta^{18}O_{H2O}$ values associated with the molybdenite-bearing fluid at Climax ($\delta^{18}O_{H2O}$ = 3.0-5.2‰ for quartz and -8.5-3.5‰ for K-feldspar) were calculated utilizing the main mineralization mode temperature of 350°C (Table 5 and Figure 9). Fluid inclusion water δD_{H2O} ranged from -140 to -88‰ for Climax. Similar to Questa, the Climax K-feldspars likely underwent isotope fractionation associated with post-mineralization alteration, hence the extremely light oxygen isotope values for Climax K-feldspars and unreasonable fractionation temperatures for cogenetic quartz-K-feldspar mineral pairs (Hall et al.,

1974). Climax $\delta^{18}O_{H2O}$ values from quartz are comparable to Questa, with values overlapping in part with both Questa MHBX and veinlet quartz (Table 5 and Figure 9). Climax δD_{H2O} values from quartz are fairly comparable to Questa with a δD_{H2O} range overlapping with Questa veinlets and overlapping in part and extending to lighter δD_{H2O} values than Questa MHBX. The δD_{H2O} values that are lighter than Questa MHBX may be attributed to lighter paleo meteoric water for the COMB compared to Questa (Figure 9 - Silver Creek and Climax paleo meteoric water) (Johnson et al., 1990; Larson et al., 1987; Hall et al., 1974). Another possible contributor to the lighter δD_{H2O} range at Climax is that the quartz δD_{H2O} values were obtained from fluid inclusions in veinlets (no MHBX) and therefore may be a result of similar factors as Questa veinlet δDs involving fluid inclusion size and/or interstitial water. Regardless of this minor difference, Climax is analogous to Questa in that the oxygen and hydrogen stable isotope values for Climax demonstrate that the mineralizing fluid is not from a purely magmatic source, but is rather mixed magmatic-meteoric in origin.

Sericite associated with post-mineralization alteration at Climax revealed $\delta^{18}O_{mineral}$ and $\delta D_{mineral}$ values of -0.8-7.4 and -116 to -168‰, respectively (Table 5 and Figure 8). The $\delta^{18}O_{H2O}$ and δD_{H2O} values for this post-mineralization fluid ranged from -3.1-5.0‰ and -144 to -92‰ at 275°C, respectively and revealed a meteoric-dominant source (Hall et al., 1974) (Table 5 and Figure 9). Sericite was not analyzed for oxygen or hydrogen stable isotopes at Questa; however, this post-mineralization Climax fluid is comparable to the meteoric-dominant post-mineralization fluid at Questa that was recorded by fluorite and calcite. The Climax water values from sericite also overlap in part with Climax and Questa quartz water values, but again have lower δD_{H2O} values

which is likely attributable to a lighter paleo meteoric water for Climax. The overlapping with Questa quartz may demonstrate that Climax sericite is associated with molybdenite mineralization and post-mineralization fluids. This could be possible, since there is evidence of a molybdenite mineralization stage at Questa (Stage 3) that is associated with phyllic alteration and a temperature mode of 280°C.

Henderson quartz and biotite associated with molybdenite mineralization exhibited $\delta^{18}O_{mineral}$ values of 9.5-10.2‰ and 5.5-8.0‰, respectively and biotite $\delta D_{mineral}$ values of -165 to -141‰ (Table 5 and Figure 8)(Carten et al., 1988). The mineral oxygen and hydrogen isotope values for Henderson are fairly different than Questa with slightly heavier $\delta^{18}O$ values and significantly lighter δD values. The calculated water values from Henderson at the mineralization temperature of 350°C exhibited $\delta^{18}O_{H2O}$ values of 4.2-4.9‰ and 7.2-9.7‰ for quartz and biotite, respectively, and δD_{H2O} values of -107 to -83‰ for biotite (Table 5 and Figure 9) (Carten, 1987; Carten et al., 1988). Fluid inclusion waters from quartz at Henderson exhibited a δD_{H2O} range of -137 to -92‰ (Carten et al., 1988). The Henderson biotite values are magmatic for $\delta^{18}O$ and are shifted to lighter than magmatic water for δD_{H2O}, but still correlate slightly with Questa. The Henderson quartz values are shifted to lighter than magmatic water for both $\delta^{18}O_{H2O}$ and δD_{H2O} and also correlate slightly with Questa. Similar to Climax, the δD_{H2O} values for Henderson quartz ranges lighter than Questa MHBX and correlates best with Questa veinlets. As with Climax, this may be attributed to the lighter paleo meteoric water for the COMB region (Figure 9) or to the fact that Henderson quartz samples are veinlets and may have effects from small, less abundant fluid inclusions and/or interstitial water.

The $\delta^{18}O_{H2O}$ and δD_{H2O} values for Henderson biotite and quartz demonstrate a fluid evolution similar to Questa (Chapter II or Rowe, 2011b), where the biotite is mostly magmatic and the quartz is mixed magmatic-meteoric (Figure 9). The molybdenite mineralizing fluids at Henderson have been concluded to be magmatic in origin, despite non-magmatic temperatures of mineralization and mixed magmatic-meteoric origin for molybdenite-associated quartz (Carten, 1987; Carten et al., 1988).

Mount Emmons $\delta^{18}O_{mineral}$ values for quartz and K-feldspar associated with molybdenite mineralization are 6.4 and 10.1‰, respectively (Table 5 and Figure 8)(Stein & Hannah, 1985; Stein, 1988). These values are compatible with the $\delta^{18}O_{mineral}$ values for Questa. No fluid inclusion temperatures were available to calculate the $\delta^{18}O_{H2O}$ values for this deposit.

Silver Creek $\delta^{18}O_{mineral}$ values for quartz are comparable to Questa with a range of 7.5-8.7‰ (Table 5 and Figure 8). Calculated water values from quartz revealed a $\delta^{18}O_{H2O}$ of 2‰ at 320-360°C and fluid inclusion waters revealed a δD_{H2O} range of -104 to -90‰ for Silver Creek (Table 5 and Figure 9)(Larson, 1987). These temperatures and values make Silver Creek genetically similar to Questa with a mixed magmatic-meteoric source for mineralizing fluids.

Silver Creek post-mineralization calcites exhibited a very large $\delta^{18}O_{mineral}$ range of -5.1-12.3‰ (Table 5 and Figure 8) (Wareham, 1998). The calcite $\delta^{18}O_{mineral}$ range for Silver Creek is significantly larger than Questa, with $\delta^{18}O_{ca}$ values of up to 4.1‰ heavier and 11.1‰ lighter than this study. Fluid inclusion homogenization temperatures indicate a deposition temperature of 200°C for Silver Creek calcites (Larson, 1987; Wareham, 1998). The associated calculated $\delta^{18}O_{H2O}$ values at this temperature for calcite ranged

from -14.9 to 2.5‰ (Figure 9). This wide range of $\delta^{18}O_{H2O}$ values reflects several different sources from purely meteoric to meteoric-dominant mixed magmatic-meteoric to magmatic-dominant mixed magmatic-meteoric. It is unlikely that all of these different sources are the origin of the oxygen in the calcite-depositing fluids for Silver Creek. The large $\delta^{18}O_{H2O}$ range for calcite at Silver Creek is likely due to post-depositional isotopic re-equilibration with later meteoric-sourced epithermal fluids or the calcite was not deposited in isotopic equilibrium with the hydrothermal waters (Wareham, 1998).

Carbon

Carbon stable isotope values from calcite at Questa revealed a narrow $\delta^{13}C$ range of -6.2 to -5.0‰ (Table 5). Similar to $\delta^{18}O_{CO2}$, $\delta^{13}C_{CO2}$ values (-6.0 to -4.9‰) for Questa calcites were calculated using 200°C using the fractionation equation of Ohmoto & Rye (1979) due to the association of calcites with Stage 4 of Rowe (2011a) or Chapter I, fluorite, and meteoric-dominant secondary fluids. The narrow carbon stable isotope range for Questa is conducive to a magmatic source for carbon, despite the fact that oxygen stable isotopes in calcites are associated with meteoric-dominant hydrothermal CO_2. This is possible because the calcite parent fluid evolved from a magmatic to mixed magmatic-meteoric to meteoric-dominant, but not pure meteoric, fluid. The carbon was hence inherited from the magmatic-dominant portion and the oxygen from the meteoric-dominant portion of the system. The magmatic carbon signature can remain due to the low concentration of carbon in meteoric fluid and the oxygen evolved due to the abundance of light oxygen in meteoric water.

Silver Creek calcites demonstrated a much broader span of carbon stable isotope values compared to Questa, with a $\delta^{13}C$ range of -7.5 to 1.1‰ (Table 5) (Wareham et al.,

1998). The calcite at Silver Creek is associated with an average temperature of 200°C (similar to Questa), revealing calculated $\delta^{13}C_{CO2}$ values of -7.3 to 1.3‰ (Larson, 1987; Wareham et al., 1998; Ohmoto & Rye, 1979). Due to the variability in the Silver Creek carbon stable isotope values, the calcites are a result of multiple sources for carbon. A magmatic component is present as demonstrated by the lighter carbon isotopes, however a variable sedimentary source of carbon is dominant for this system (Wareham et al., 1998). This reveals a significant difference between Questa and Silver Creek. Precambrian metasediments, Cretaceous sedimentary rocks, and tertiary volcaniclastic sediments do exist in the Questa area, however they were not contributors to the source of carbon in Questa calcites.

Sulfur

Sulfur isotope values for Questa molybdenite ranged from a $\delta^{34}S$ of 0.4 to 2.3‰, which is conducive to a magmatic source for sulfur (Table 5) (Chapter II or Rowe, 2011b; Stein & Hannah, 1985; Stein, 1988). All of the COMB Climax-type deposits, with the exception of Silver Creek, revealed a magmatic sulfur source with higher $\delta^{34}S$ values than Questa at 2.5-3.6‰ for Climax, 4.7-5.3‰ for Henderson, and 3.7-4.6‰ for Mount Emmons (Stein & Hannah, 1985; Stein, 1988; Wareham et al., 1998). Silver Creek demonstrated the largest range out of the Climax-type deposits with a $\delta^{34}S$ range of 0.5-4.6‰, which spans the ranges of Questa, Climax, and Mount Emmons, but not Henderson, but also reflects a magmatic source. If the source of the Climax-type sulfur was not purely magmatic, but rather was evolved from the variable country rocks at each deposit, then the $\delta^{34}S$ values would be highly variable between the deposits and is not the case (Stein and Hannah, 1985). Sulfur can be of a magmatic source, despite the fact that

the mineralizing fluids were of mixed magmatic-meteoric origin, due to the fact that the sulfur originated from the magmatic portion of the fluids (Wareham, 1998). Also, the fluid can keep the magmatic sulfur signature due to the low concentration of sulfur in meteoric water. The minor variation in magmatic $\delta^{34}S$ values between the deposits, despite the fact that they are all magmatic in origin, could be attributed to magma source, fractionation, or fO_2 (Wareham, 1998; Stein & Hannah, 1985).

Fluid Inclusion Gas Analysis

An additional data set (fluid inclusion gas analysis) that identifies fluid source is available for Questa, but not for the Climax-type deposits of the COMB. The Ar-He-N_2 diagram of Blamey & Norman (2002) demonstrates that Questa MHBX matrix (open circles) and veinlet quartz (crosses) are not purely magmatic, since the majority of the samples did not plot within the Calc-Alkaline magmatic box (Figure 10). Instead, the majority of the samples at Questa plotted to the left of the magmatic box, demonstrating that there is a strong meteoric component to the gases associated with mineralization. The MHBX matrix fluorite (solid circles) plots the farthest to left, indicating that the fluorites are the most meteoric and evolved fluids. The N_2/Ar vs. CO_2/CH_4 diagram of Norman & Moore (1999) also demonstrates that Questa MHBX matrix and veinlet quartz associated with mineralization are not purely magmatic, but have a strong shallow meteoric input (Figure 11). Similar to the Ar-He-N_2 diagram, MHBX matrix fluorite plots apart from the quartz samples, demonstrating a further evolved fluid than the quartz. The difference between the fluid inclusion gas analysis and the oxygen/hydrogen stable isotope results for Questa is that the gas analyses demonstrate a greater meteoric component to the magmatic-meteoric mixed source for the mineralizing fluids, whereas

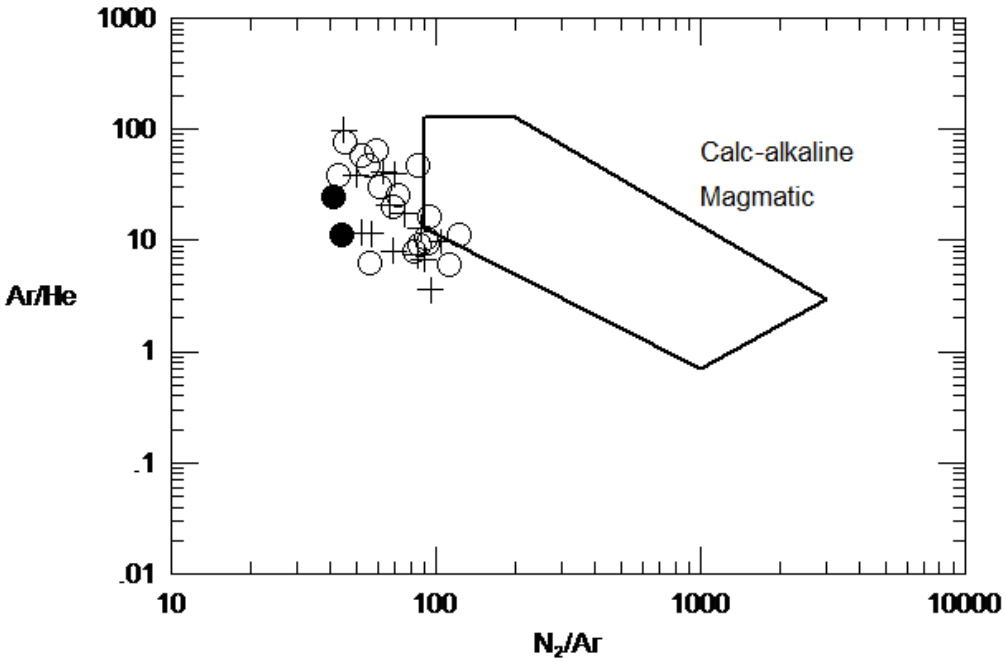

Figure 10. N2-Ar-He diagram from fluid inclusion gas analyses at Questa. Open circles are MHBX matrix quartz, solid circles are MHBX matrix fluorite, and cross symbols are veinlets. Diagram from Blamey & Norman, 1999.

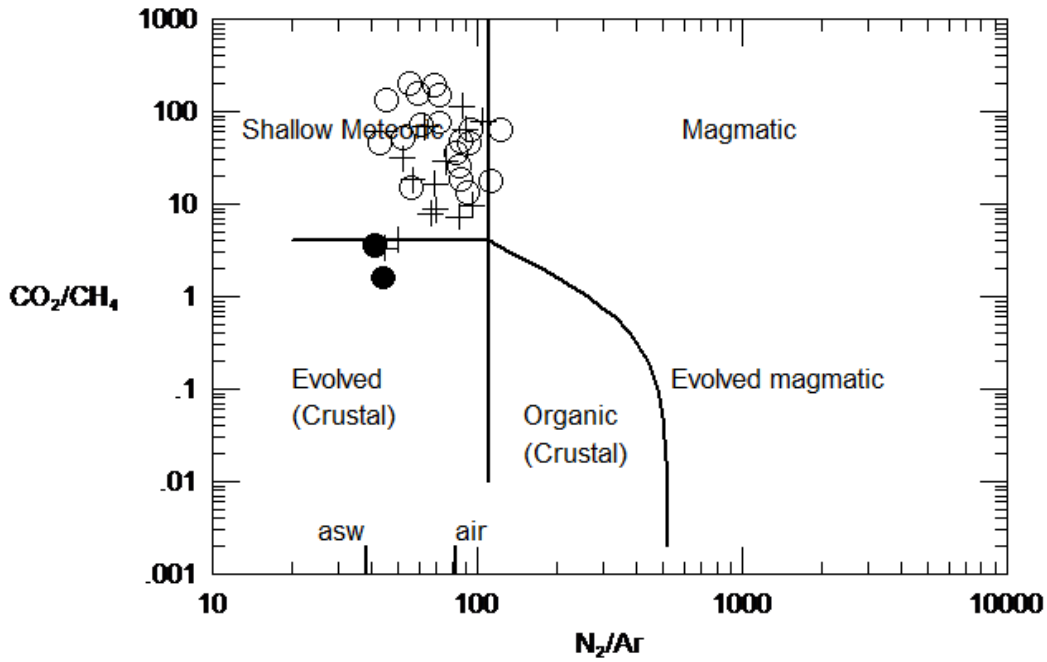

Figure 11. CO_2/CH_4 vs. N_2/Ar diagram from fluid inclusion gas analyses at Questa. Open circles are MHBX matrix quartz, closed circles are MHBX matrix fluorite, and cross symbols are veinlets. Diagram from Norman & Moore, 2002.

the oxygen and hydrogen stable isotope analyses exhibit a mixed magmatic-meteoric source with a more dominant magmatic contribution to the mineralizing fluids. Both analyses do demonstrate, however, that the system further evolves to meteoric for post-mineralization fluorite (Chapter II or Rowe, 2011b). The importance of the fluid inclusion gas analysis is that it is an additional analysis that supports the conclusions derived from fluid inclusion microthermometry and oxygen/hydrogen stable isotope analyses that the Questa Climax-type mineralizing fluid is not from a purely magmatic source.

SUMMARY

Fluid inclusion microthermometry, oxygen and hydrogen stable isotope analyses, and fluid inclusion gas analysis at Questa all revealed that the genetic origin of the Questa Climax-type mineralizing fluids evolved from magmatic to mixed magmatic-meteoric origin with a $\delta^{18}O_{H2O}$ and δD_{H2O} range of 1.5-7.6‰ and -53 to -143‰, a temperature of mineralization at approximately 380-400°C, and a large range of salinities from 0-64 eq. wt.% NaCl. Temperature decrease caused by both mixing with meteoric fluids and simple cooling due to boiling is the mechanism for molybdenite mineralization at this temperature. Following mineralization, the fluids further evolved to a meteoric-dominant mixed magmatic-meteoric fluid at temperature of 200°C, a low salinity of $\leq$1% eq. wt.% NaCl, and a $\delta^{18}O_{H2O}$ and δD_{H2O} range of -4.3 to -1.3‰ and -109 to -106‰. Carbon and sulfur isotope analyses revealed a magmatic source of carbon for late-stage calcite and sulfur for molybdenite for the Questa system, which further demonstrates that the fluids evolved from a magmatic to meteoric-dominant mixed magmatic-meteoric

fluid. These conclusions prove significant because many previous authors on Questa (Cline & Bodnar, 1994; Cline & Vityk, 1995; Ross et al., 2002; Klemm et al., 2004; Klemm et al., 2008) and COMB Climax-type deposits (Kamilli, 1978; White et al., 1981; Carten, 1987; Carten et al., 1988; Seedorff & Einaudi, 2004) have deemed molybdenite mineralizing fluids to be purely magmatic in origin, with a post-mineralization meteoric contribution to the system only. An additional significance is that three complimentary data sets (fluid inclusion microthermometry, stable isotope analyses, and fluid inclusion gas analyses) support the conclusions of this study, whereas the previous studies on Questa or the Climax-type deposits of the COMB derived their conclusions from only one or two data sets (fluid inclusion microthermometry and/or stable isotope analyses).

In comparison of Questa fluid inclusion microthermometry and stable isotope data with the Climax-type deposits of the Colorado Mineral Belt (Climax, Henderson, Mount Emmons, and Silver Creek), it was found that these deposits are very genetically similar to Questa in terms of fluid inclusion types, temperature of mineralization, source of the mineralizing fluids, fluid evolution, and source for sulfur. This finding proves significant in that not only do Climax-type deposits possess similar characteristics listed in Table 1 that place them in a deposit class together, but these deposits also possess similar genetic origins and fluid evolution histories. Most significantly, the genetic model for not just Questa, but also for the Climax-types of the COMB, includes a meteoric component to molybdenite mineralization rather than the purely magmatic origin concluded by many previous authors (Cline & Bodnar, 1994; Cline & Vityk, 1995; Ross et al., 2002; Klemm et al., 2004; Klemm et al., 2008; Kamilli, 1978; White et al., 1981; Carten, 1987; Carten et al., 1988; Seedorff & Einaudi, 2004).

There are also some minor differences between Questa and the some of the Climax-type deposits of the COMB, that add a factor of uniqueness to some of the COMB deposits. For Climax, Tshl>>Tlv fluid inclusions and boiling were not identified and the overall salinity was lower. Climax also reflected bimodal salinities associated with mineralization. These differences between Climax and Questa are likely interrelated in that the lack in boiling at Climax would explain the deficiency of both intermediate salinities and Tshl>>Tlv fluid inclusions, as well as the overall lower salinity for the system due to no Tshl>>Tlv fluid inclusions. For Henderson, the $\delta^{18}O_{H2O}$ values for biotite are heavier than Questa, indicating that the fluid source was more magmatic to start with compared to Questa. Lastly, the Silver Creek calcites are different than Questa. The source of $\delta^{18}O_{H2O}$ for Silver Creek calcites is questionable, likely because of post-deposition fractionation and re-equilibration with later, cooler, epithermal fluids. Additionally, the source of carbon for Silver Creek calcite is primarily sedimentary host rocks, whereas Questa carbon is magmatic. These differences between Questa and the Climax-type deposits of the COMB are minimal compared to the prominent similarities that render all of these deposits members of the same genre that possesses a distinctive genetic model.

REFERENCES

Becker, S. P., Fall, A., and Bodnar, R. J., 2008, Synthetic Fluid Inclusions. XVII. PVTX Properties of High Salinity H2O-NaCl Solutions (>30 wt% NaCl): Application to Fluid Inclusions that Homogenize by Halite Disappearance from Porphyry Copper and Other Hydrothermal Ore Deposits: Economic Geology, v. 103, p. 539-554.

Blamey, N. J. F., and Norman, D. I., New Interpretations of Geothermal FLuid Inclusion Volatiles: Ar/He and N_2/Ar ratios - A Better Indicator of Magmatic Volatiles and Equilibrium Gas Geothermometry, *in* Proceedings 27th Geothermal Reservoir Engineering, Stanford, San Francisco, 2002.

Bloom, M. S., 1981, Chemistry of inclusion fluids; stockwork molybdenum deposits from Questa, New Mexico, Hudson Bay Mountain and Endako, British Columbia: Economic Geology v. 76, no. 7, p. 1906-1920.

Bodnar, R. J., and Vityk, M. O., 1994, Interpretation of Microthermometric data for H2O-NaCl fluid inclusions, *in* B., D. V., and M.L., F., ed., Fluid Inclusions in Minerals: Methods and Applications: Blacksburg, VA, Virginia Tech.

Bodnar, R. J., 1994, Synthetic fluid inclusions. XII. Experimental determination of the liquidus and isochores for a 40 wt.% H2O-NaCl solution: Geochimica Cosmochimica Acta v. 58, p. 1053-1063.

Bodnar, R.J., 2003, Introduction to aqueous-electrolyte fluid inclusions, *in* Samson, I. M., Anderson, A. J., and Marshall, D., ed., Fluid Inclusions: Analysis and Interpretation, Volume 32: Vancouver, B.C., Mineralogical Association of Canada, p. 81-100.

Cameron, D. E., Barrett, L.F., and Wilson, J.C., 1986, Discovery of the Silver Creek molybdenum deposit, Rico, Colorado: American Institute of Mining, Metallurgical, and Petroleum Engineers Transactions, v. 280, p. 2099–2105.

Campbell, A. R., Banks, D. A., Phillips, R. S., and Yardley, B. W. D., 1995, Geochemistry of Th-U-REE mineralizing magmatic fluids, Capitan Mountains, New Mexico: Economic Geology, v. 90, p. 1271-1287.

Campbell, A. R., Lundberg, S. A. W., and Dunbar, N. W., 2001, Solid inclusions of halite in quartz: evidence for the halite trend: Chemical Geology (including Isotope Geoscience), v. 173, p. 179-191.

Carten, R. B., 1987, Evolution of immiscible Cl- and F-rich liquids from ore magmas, Henderson porphyry molybdenum deposit, Colorado [abs.]: Geological Society of America Abstracts with Programs, v. 19, no. 613.

Carten, R. B., Rye, R. O., and Landis, G. P., 1988, Effects of igneous and hydrothermal processes on the compositions of ore-forming fluids; stable-isotope and fluid-inclusion evidence, Henderson molybdenum deposit, Colorado, *in* Anonymous, ed., Geological Society of America 1988 centennial celebration, Volume 20, Geological Society of America (GSA), p. 94.

Carten, R. B., White, W. H., and Stein, H. J., 1993, High-grade granite-related molybdenum systems; classification and origin: Mineral deposit modeling, v. 40, p. 521-554.

Clayton, R. N., O'Neil, J. R., and Mayeda, T. K., 1972, Oxygen Isotope Exchange between Quartz and Water: Journal of Geophysical Research, v. 77, no. 17, p.

3057-3067.
Cline, J. S., and Bodnar, R. J., 1994, Direct evolution of brine from a crystallizing silicic melt at the Questa, New Mexico, molybdenum deposit: Economic Geology, v. 89, no. 8, p. 1780-1802.
Cline, J. S., and Vanko, D. A., 1995, Magmatically generated saline brines related to molybdenum at Questa, New Mexico, USA, Magmas, Fluids, and Ore Deposits: Mineralogical Association of Canada Short Course Series, Victoria, B.C., Canada, p. 153-174 p.:
Cox, D. P., and Singer, D. A., 1986, Mineral deposit models, Reston, VA, U. S. Geological Survey, 379 p.:
Czamanske, G. K., Foland, K. A., Kubacher, F. A., and Allen, J. C., 1990, The $^{40}Ar/^{39}Ar$ chronology of caldera formation, intrusive activity and Mo-ore deposition near Questa, New Mexico, *in* Bauer, P. W., Lucas, S. G., Mawer, C. K., and McIntosh, W. C., eds., New Mexico Geological Society Forty-first annual field conference, Volume 41, New Mexico Geological Society, p. 355-358.
Donahue, K. M., 2002, Geochemistry, geology and geochronology of the Victorio mining district, Luna County, New Mexico: Linking skarn and porphyry systems to carbonate-hosted lead-zinc replacement deposits [Master of Science Thesis]: New Mexico Institute of Mining & Technology, 186 p.
Eastoe, C. J., 1978, A fluid inclusion study of the Panguna porphyry copper deposit, Bougainville, Papua New Guinea:: Economic Geology, v. 73, p. 721-748.
Erwood, R. J., Kessler, S. E., and Cloke, P. L., 1979, Compositionally distinct, saline hydrothermal solutions, Naica mine, Chihuahua, Mexico: Economic Geology, v. 74, p. 95-108.
Gunter, W. D., Chou, I.-M., and Girsperger, S., 1983, Phase relations in the system NaCl-KCl-H2O II: Differential thermal analysis of the halite liquidus in the NaCl-H2O binary above 450C: Geochimica Cosmochimica Acta v. 47, p. 863-873.
Hall, W. E., Friedman, I., and Nash, J. T., 1974, Fluid Inclusion and Light Stable Isotope Study of the Climax Molybdenum Deposits, Colorado: Economic Geology, v. 69, no. 6, p. 884-901.
Hannah, J. L., and Stein, H. J., 1986, Oxygen isotope compositions of selected Laramide-Tertiary granitoid stocks in the Colorado mineral belt and their bearing on the origin of climax-type granite-molybdenum systems: Contributions to Mineralogy and Petrology, v. 93, no. 3, p. 347-358.
InfoMine, Inc., 1990-2011, http://www.infomine.com/chartsanddata/chartbuilder.aspx?z=f&g=127676&dr=15y, Molybdenum Oxide Price - Chart Builder, InfoMine, Inc.
Kamilli, R. J., 1978, The genesis of stockwork molybdenite deposits; implication from fluid inclusion studies at the Henderson Mine [abs.]: The Geological Society of America (91st annual meeting), v. 10, p. 431.
Klemm, L. M., and Pettke, T. H. C. A., 2004, Early magmatic-hydrothermal evolution of the Questa porphyry Mo deposit, New Mexico, USA, *in* Muhling, J., Goldfarb, R. J., Vielreicher, N., Bierlein, F. P., Stumpfl, E. F., Groves, D. I., Kenworthy, S., and Knox-Robinson, C. M., eds., Seg 2004, Volume 33, University of Western Australia Geology Department and Extension Service, p. 431.
Klemm, L. M., Pettke, T. H. C. A., and Heinrich, C. A., 2008, Fluid and source magma

evolution of the Questa porphyry Mo deposit, New Mexico, USA: Mineralium Deposita, v. 43, no. 5, p. 533-552.
Kodera, P., Lexa, J., Rankin, A. H., and Fallick, A. E., 2004, Fluid evolution in a subvolcanic granodiorite pluton related to Fe and Pb-Zn mineralization, Banska Stiavnica Ore District, Slovakia: Economic Geology, v. 99, p. 1745-1770.
Larson, P. B., 1987, Stable isotope and fluid inclusion investigations of epithermal vein and porphyry molybdenum mineralization in the Rico mining district, Colorado: Economic Geology, v. 82, p. 2141–2157.
Larson, P. B., Cunningham, C.G., and Naeser, C.W., 1994, Large-scale alteration effects in the Rico paleothermal anomaly: Economic Geology, v. 89, p. 1769-1779.
Lipman, P. W., 1992, Ash-flow calderas as structural controls of ore deposits; recent work and future problems, *in* Thorman, C. H., ed., Application of structural geology to mineral and energy resources of the Central and Western United States, U. S. Geological Survey, p. L1-L12.
Ludington, S., and Plumlee, G. S., 2009, Climax-type Porphyry Molybdenum Deposits: U.S. Geological Survey Open-File Report 2009-1215, p. 16.
Ludington, S. D., 1986, Descriptive model of Climax Mo deposits: Mineral deposit models, p. 73.
Ludington, S. D., Bookstrom, A. A., Kamilli, R. J., Walker, B. M., and Klein, D. P., 1995, Climax Mo deposits: Preliminary compilation of descriptive geoenvironmental mineral deposit models, p. 70-74.
Meyer, J., and Foland, K. A., 1991, Magmatic-tectonic interaction during early Rio Grande Rift extension at Questa, New Mexico: Geological Society of America Bulletin, v. 103, no. 8, p. 993-1006.
Meyer, J. W., 1991, Volcanic, plutonic, tectonic and hydrothermal history of the southern Questa Caldera, New Mexico [Doctor of Philosophy Dissertation]: University of California Santa Barbara, 348 p.
Meyer, J. W., and Leonardson, R., 1990, Tectonic, hydrothermal and geomorphic controls on alteration scar formation near Questa, New Mexico, Tectonic development of the Southern Sangre do Cristo Mountains, New Mexico: New Mexico Geological Society Guidebook, 41st Annual Field Conference, p. 417-422.
Norman, D. I., and Moore, J. N., Methane and excess N_2 and Ar in geothermal fluid inclusions, *in* Proceedings Twenty-fourth Workshop of Geothermal Reservoir Engineering, Stanford University, Stanford, California, January 22-24 1999, p. 233-240.
Ohmoto, H., and Rye, R. O., 1979, Isotope of sulfur and carbon, *in* Barnes, H. L., ed., Geochemestry of Hydrothermal deposits, John Wiley & Sons, p. 509-567.
Ross, P.-S., Jebrak, M., and Walker, B. M., 2002, Discharge of hydrothermal fluids from a magma chamber and concomitant formation of a stratified breccia zone at the Questa porphyry molybdenum deposit, New Mexico: Economic Geology v. 97, no. 8, p. 1679-1699.
Rowe, A., 2011a, Fluid Evolution of the Magmatic Hydrothermal Breccia of the Goat Hill Orebody, Questa Climax-type Porphyry Mo System, New Mexico - A Fluid Inclusion Study: Submitted to Economic Geology, December 2011.
Rowe, A., 2011b, Fluid Evolution of the Magmatic-hydrothermal Breccia and Stockwork

Veinlets of the Goat Hill Orebody, Questa Climax-type Porphyry Mo System, New Mexico – A Stable Isotope and Fluid Inclusion Gas Analysis Study: Submitted to Economic Geology, December 2011.

Seedorff, E., and Einaudi, M. T., 2004, Henderson Porphyry Molybdenum System, Colorado: II. Decoupling of Introduction and Deposition of Metals during Geochmical Evolution of Hydrothermal Fluids: Economic Geology, v. 99, p. 39-72.

Shannon, J. R., Nelson, E. P., and Golden, R. J. J., 2004, Surface and underground geology of the world-class Henderson molybdenum porphyry mine, Colorado, *in* Nelson, E. P., and Erslev, E. A., eds., Field trips in the southern Rocky Mountains, USA: Geological Society of America Field Guide 5, p. 207–218.

Shephard, T. J., Rankin, A. H., and Alderton, D. H. M., 1985, A Practical Guide to Fluid Inclusion Studies, Glasgow, Blackie & Son Limited, 239 p.:

Sinclair, W. D., 1995, Porphyry Mo (climax-type): Selected British Columbia mineral deposit profiles, p. 105-108.

Sinclair, W.D., 1995, Porphyry Mo (low-F-type): Selected British Columbia mineral deposit profiles, p. 93-95.

Smith, R. W., 1983, Aqueous chemistry of molybdenum at elevated temperatures and pressures with applications to porphyry molybdenum depositsPhD Dissertation]: New Mexico Institute of Mining and Technology, 311 p.

Stein, H. J., 1988, Genetic traits of climax-type granites and molybdenum mineralization, Colorado mineral belt, *in* Taylor, R. P., and Strong, D. F., eds., CIM conference on Granite-related mineral deposits, Volume 39, Canadian Institute of Mining and Metallurgy, p. 394-401.

Stein, H. J., and Hannah, J. L., 1985, Movement and origin of ore fluids in climax-type systems: Geology, v. 13, no. 7, p. 469-474.

Suzuoki, T., and Epstein, S., 1976, Hydrogen isotope fractionation between OH-bearing minerals and water: Geochimica et Cosmochimica Acta, v. 40, no. 10, p. 1229-1240.

Theodore, T. G., 1986, Descriptive model of porphyry Mo, low-F: Mineral deposit models, p. 120.

Thomas, J. A., and Galey, J. T., Jr., 1982, Exploration and geology of the Mt. Emmons molybdenite deposits, Gunnison County, Colorado: Economic Geology, v. 77, p. 1085–1104.

Wallace, S. R., Muncaster, N.K., Jonson, D.C., MacKenzie, W.B., Bookstrom, A.A., and Surface, V.E., 1968, Multiple intrusion and mineralization at Climax, Colorado, *in* Ridge, J. D., ed., Ore deposits of the United States, 1933–1967, Volume The Graton-Sales Volume: New York, American Institute of Mining, Metallurgical, and Petroleum Engineers, p. 605–640.

Wallace, S. R., 1995, Climax-type molybdenite deposits—What they are, where they are, and why they are (SEG presidential address): Economic Geology, v. 90, p. 1359–1380.

Wareham, C. D., Rice, C.M., Boyce, A.J., and Rogers, Graeme, 1998, S, C, Sr, and Pb sources in the Pliocene Silver Creek porphyry Mo system, Rico, Colorado: Economic Geology, v. 93, p. 32-46.

White, W. H., Bookstrom, A. A., Kamilli, R. J., Ganster, M. W., Smith, R. P., Ranta, D.

E., and Steininger, R. C., 1981, Character and origin of climax-type molybdenum deposits: Economic Geology, Seventy-fifth anniversary volume (1905-1980).

White, W. H., Carten, R. B., Bookstrom, A. A., and Stein, H. J., 1990, A Model for Climax-tpe Molybdenum Deposits [abs.], 8th IAGOD Symposium in Conjunction with International Conference in Mineral Deposit Modeling - Program with Abstracts, p. 133-134.

Wilson, J. W. J., 1978, Fluid inclusion geochemistry of the Granisle and Bell Copper porphyry deposits, B.C. [Master of Science Thesis]: University of Toronto, 117 p.

Zheng, Y.-F., 1993, Calculation of oxygen isotope fractionation in anhydrous silicate minerals.: Geochim. Cosmochim. Acta, v. 57, p. 1079-1091.

Zheng, Y.-F., 1993a, Calculation of oxygen isotope fractionation in hydroxyl-bearing silicates: Earth and Planetary Science Letters, v. 120, no. 3-4, p. 247-263.

Zheng, Y.-F., 1999, Oxygen isotope fractionation in carbonate and sulfate minerals: Geochemical Journal, v. 33, no. 2, p. 109-126.

Zimmer, M. J., 2008, The $^{40}Ar/^{39}Ar$ Geochronology and Thermochronology of the Latir Volcanic Field and Associated Intrusions: Implications for Caldera-related Magmatism [Master of Science Thesis], 113 p.

APPENDIX A – PETROGRAPHIC ANALYSIS

Legend for Petrographic Analyses

assoc – association
crs - coarse
d.z. – digital zoom
defm'n – deformation
dissem – disseminated
f.g. – fine grained
grn(ed) – grain(ed)
lg – large
med - medium
MHBX – magmatic-hydrothermal breccia
pln – plane light
reflect – reflected light
sm – small
trans – transmitted light
vnlt – veinlet
xcuts – cross-cuts
xpol – cross polars
+ occurring after bt, kspar, QSP, etc. – addition of these minerals in alteration
> - greater than

Rocks and Minerals

alt – alteration
anhy – anhydrite
ap - apatite
blch - bleached
bt – biotite (aka fluorophlogopite)
ca – calcite
chlor - chlorite
cp – chalcopyrite
fl – fluorite
grn – green
gyp - gypsum
kaol – kaolinite
kspar – potassium feldspar
mo – molybdenite
mt - magnetite
par – paragonite (green mica)
pheno(s) – phenocryst(s)
plag – plagioclase feldspar
py – pyrite
QSP – qtz-ser-py alteration
qtz – quartz
rtl – rutile
SABQ – source aplite barren quartz
ser – sericite
Tan – Tertiary andesite
Tlgp – Tertiary late granite porphyry
tpz – topaz
tr – trace
uTan – unbrecciated Tertiary andesite
uTana – unbrecciated Tertiary andesite above the breccia body
uTanb – unbrecciated Tertiary andesite below the breccia body

Paragenesis

+ included in time assemblage
+/- may or may not be included in time assemblage
→later assemblage

Sample: AR-173
Facies: Source Aplite
Phase: Barren Qtz
Borehole: 19.9-12.1
Elevation: 7283'

Macroscopic

Source aplite with larger, more phenos, possibly partially digested latite with barren, early qtz vn; <5% mo.

Microscopic

- *Source aplite with barren qtz:*
  - kspar-qtz-tr mo-bt-rtl-py-ser-tr ca
  - aplite contains very fine grned qtz
  - kspar alt to ser and kaol
  - crs grned qtz in barren matrix areas
  - py is subhedral to anhedral; py-rtl assoc; py-bt assoc
  - ser often occurring on grn bound of qtz and/or rtl; ser also occurring as centers of relict kspar
  - rtl in and on edges of bt grn; rtl-bt assoc
  - barren qtz contains qtz-rtl-py-ser-some kspar-some aplite; qtz grns vary from 10-200 microns
  - xcutting ca or ser vnlt

Paragenesis

Barren qtz:

aplite→kspar→qtz+rtl+/-py→ser/ca

Source aplite:

qtz+kspar→qtz+kspar+/-bt+/-rtl→qtz+kspar+/-mo+/-bt+/-rtl→qtz+ser+py→qtz+ca+ser→kaol

Macroscopic

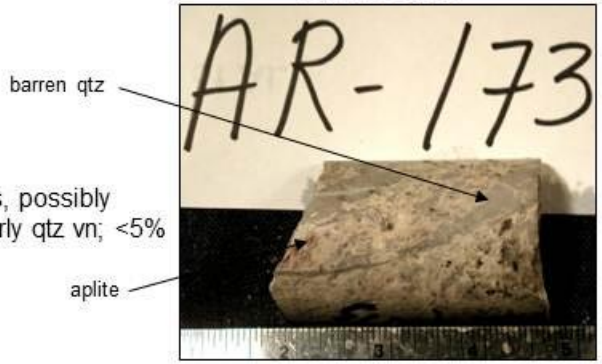

Petrographic

Microscopic

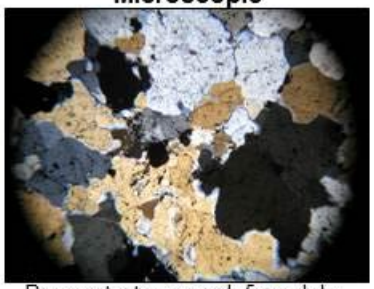

Barren qtz; trans; xpol; 5x and d.z.

Aplite (kspar-bt-qtz-rtl-py-ser); trans; pln; 5x and d.z.

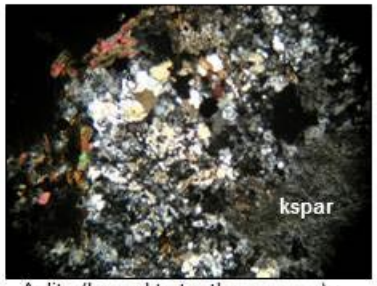

Aplite (kspar-bt-qtz-rtl-py-ser-mo); trans; xpol; 5x/d.z.

Sample: AR-97
Facies: Source Aplite
Phase: Barren Quartz
Borehole: 22.0-14.0
Elevation: 7289'

Macroscopic

Aplite with primarily barren quartz vein material that resembles matrix in MHBX; later molybdenite veinlets.

Microscopic

- *Matrix:*
  - aplite = qtz + kspar → sericite and tr kaolinite + pyrite + rutile
  - extremely fine-grained fluorite in qtz and aplite
  - qtz and kspar as "vein" or matrix material
  - kspar is partially altered to sericite and kaolinite
  - sericite or carbonate veinlets and stringers throughout
  - py also in qtz and kspar "vein" or matrix material
  - py-fluorite and py-rutile association
  - no molybdenite observed

Paragenesis

Matrix:

aplite→qtz+kspar+rtl+fl→qtz+ser+py→kaol

Petrographic Section

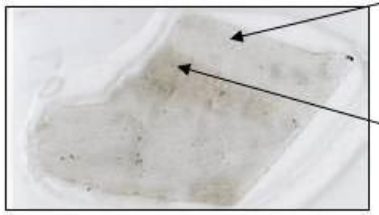

Macroscopic

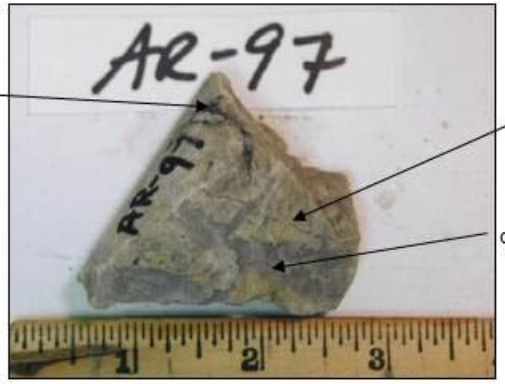

Quartz vein material that resembles MHBX matrix.

Microscopic

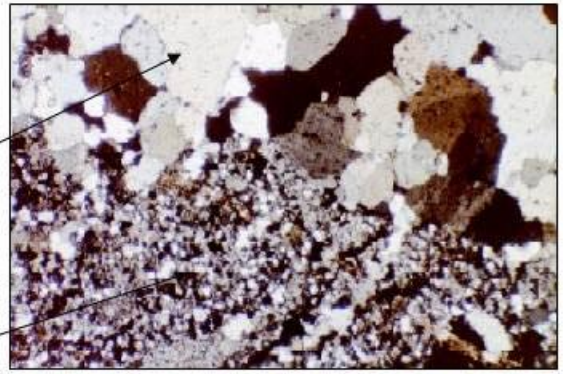

Transmitted light; cross-polars; source aplite and qtz "vein" or matrix material; 5x

Sample: AR-174
Facies: Source Aplite
Phase: Vein
Borehole: 19.9-12.1
Elevation: 7277'

Macroscopic

Source aplite with qtz-mo vn.

Microscopic

- *Vein:*
  - qtz-mo-py-fl-ser
  - fl-mo assoc; fl on rims of mo grns
  - mo is anhedral to euhedral blades and hexagons; mostly occurring at vn/aplite interface; some mid-vn
  - some interstitial crs grn ser between qtz grns
  - qtz is anhedral to subhedral; coarsest grns in center of vn (80-200 microns); sm-med grned qtz along vn/aplite interface
  - ser often occurring at or near areas with mo; where crs grned ser at vn/aplite interface, qtz has stress features
- *Source Aplite:*
  - kspar-qtz-mo-py-ser-bt-rtl-kaol-ca-fl
  - some barren qtz vnlts xcutting aplite, possibly related to MHBX matrix
  - fl dissem in clast
  - some interstitial ca
  - kspars being altered to ser and kaol
  - inclusions of rtl in bt; bt-tpz assoc
  - some crs grned rtl; rtl-py assoc
  - py often occurring with ser; py-ser assoc

Macroscopic

Microscopic

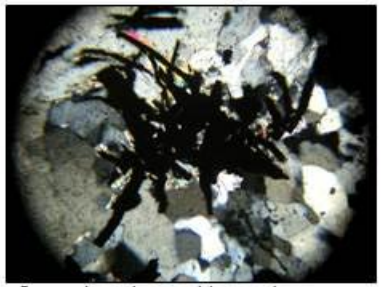

Qtz and mo in vn with ser along grn boundaries; trans; xpol; 10x and d.z.

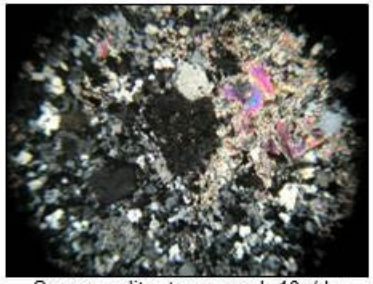

Source aplite; trans; xpol; 10x/d.z.

Paragenesis

Vein:

qtz→qtz+mo+fl+/-py→qtz+ser+/-py

Source Aplite:

qtz+kspar→qtz+kspar+rtl+bt+/-tpz+/-fl→qtz+py+/-ser→qtz+mo+fl→qtz+ser+/-py→ca+kaol

Petrographic Section

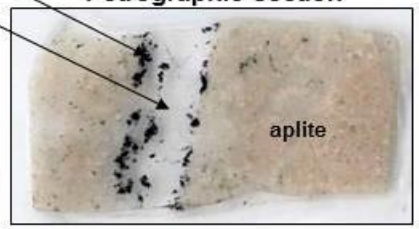

Sample: AR-105
Facies: A1
Phase: Matrix
Borehole: 23.4-11.8G
Elevation: 7343'

Macroscopic

Biotite altered Tan clasts with aplite-qtz-tr mo matrix.

Microscopic

• *Matrix:*

- ➢ mostly quartz; subhedral to anhedral, with few euhedral grains; 100-1750 microns; stress features
- ➢ minor aplite; consists of qtz and kspar altering to ser and tr kaol
- ➢ minor kspar; altered to sericite and trace kaolinite
- ➢ fluorite disseminated throughout; fl pocket and vein
- ➢ interstitial calcite between fine grained quartz grains
- ➢ abundant rutile
- ➢ trace moly within kspar grain; < 75 microns
- ➢ trace pyrite; <75 microns
- ➢ sericite stringers throughout

Paragenesis

Matrix:

aplite→qtz+kspar+fl+mo+rtl+/-ca→qtz+rtl+tr tpz+fl+/-ca →qtz+ser+py+/-ca+/-rtl→kaol

Macroscopic

Microscopic

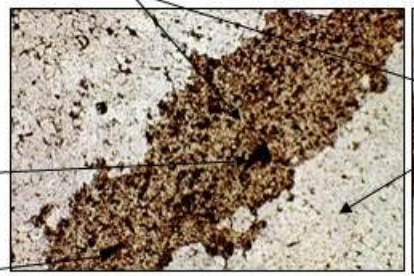

Aplite matrix with rutile, molybdenite and quartz; trans; pln; 5x.

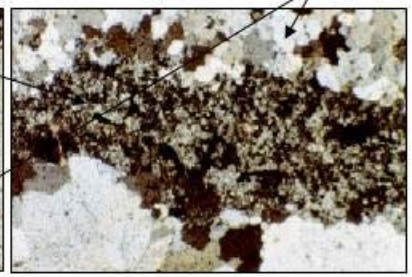

Same; trans; xpol; 5x.

Petrographic Section

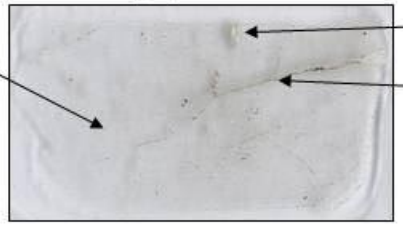

Sample: AR-112
Facies: A1
Phase: Matrix
Borehole: 23.5-11.8G
Elevation: 7259.5'

Macroscopic

Predominantly source aplite and some Tlgp clasts; qtz-mo matrix.

Microscopic

- predominantly matrix with small piece of clast
- *Matrix:*
  - very large grains of qtz; med grains of qtz variable size; small grains of qtz associated with QSP
  - very little rutile (tr)
  - some mo; mo with sericite and some fluorite; ser most likely was originally kspar
  - minor kspar
  - tr pyrite
  - ca-qtz and/or ser-qtz vnlts xcut matrix qtz
  - disseminated fl; fl vnlt xcuts matrix
- *Clast:*
  - ser-fl-qtz

Paragenesis

Matrix:

qtz+kspar+mo+fl+/-tr rtl→qtz+ser+tr py+/-tr rtl

Clast:

qtz+fl→qtz+fl+ser

Macroscopic

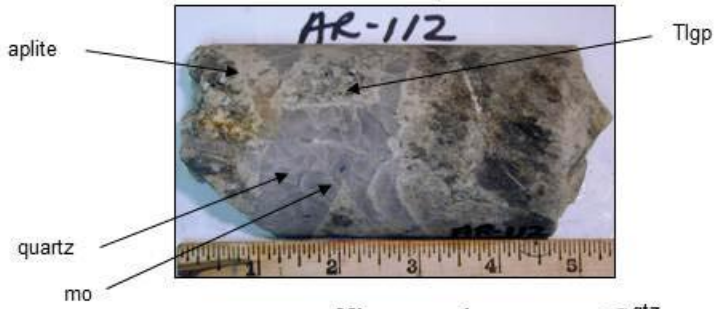

Microscopic

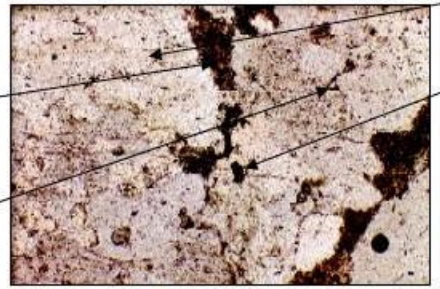

qtz-mo-fl-ser; relict kspar replaced by ser; trans; pln; 10x.

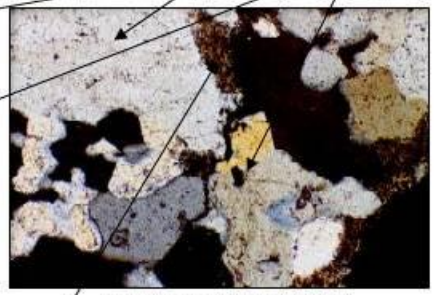

same; trans; xpol; 10x.

Petrographic Section

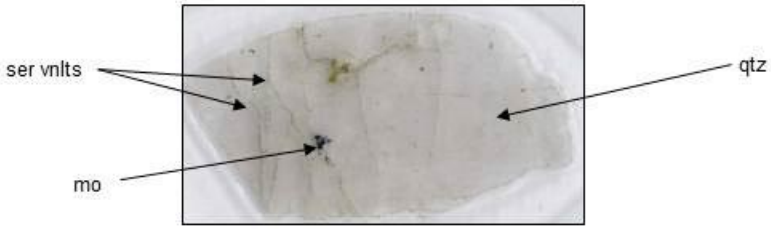

Sample: AR-115
Facies: A1
Phase: Vein
Borehole: 23.5-11.8G
Elevation: 7290.5'

Macroscopic

Aplite-qtz-mo-Tlgp matrix; aplite and Tlgp clasts; qtz-mo vn.

Microscopic

- *Vein:*
  - qtz-mo vn partially "digesting" aplite/Tlgp; bt, very fine grained qtz and/or kspar in vn from digestion; rutile stringers in these areas
    pyrite and rutile in vn; py-rtl association
  - fl dissem throughout; fl-mo association
  - mo is euhedral blades and hexagons to anhedral; small grains as outer part of vein, large grains in center, i.e. sm→lg←sm
  - ser or ca stringers xcut vn

- *Clast/Matrix:*
  - kspar-qtz-ser-bt-rtl-py-fl-topaz
  - kspar altered to ser and/or kaol
  - tpz association with bt and rtl; tpz altering to ser
  - rtl and py xcutting and/or included in bt and rest of clast; py-rtl association; rtl bt association
  - large euhedral inclusions of rtl in bt
  - some mo as envelope from vn
  - ser and/or ca stringers xcut clast and matrix

Macroscopic

Microscopic

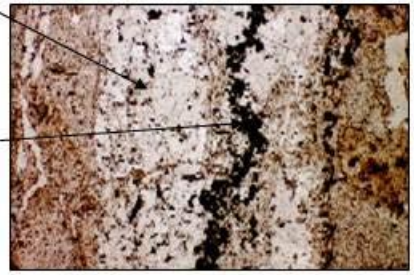

qtz-mo vn and clast/matrix; trans; pln; 5x.

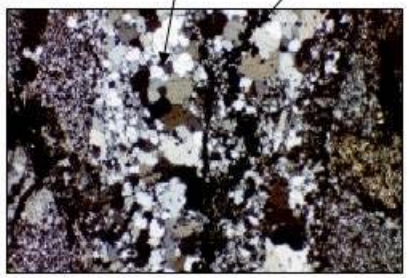

same; trans; xpol; 5x.

Paragenesis

Vein:
qtz→qtz+mo+fl→qtz+ser+py+rtl+/-ca

Vein Envelope:
qtz+kspar+bt→qtz+fl+mo+/-bt→bt+rtl+tpz→qtz+ser+py+/-rtl+/-tpz→ca+/-kaol

Petrographic Section

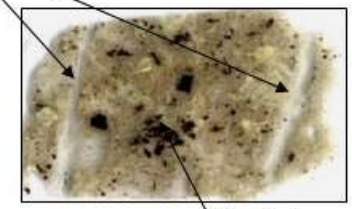

Sample: AR-102
Facies: A1
Phase: Vein
Borehole: 23.4-11.8G
Elevation: 7275.5'

Macroscopic

Qtz-mo vn xcutting latite; structural deformation causing vein to be "chewed up".

Microscopic

- *Vein:* not typical vn appearance, i.e. layering, etc.
  - qtz-mo-fl-rtl-py-ser-leucoxene(?)-ca
  - mo-fl association
  - qtz is med to sm grned, but no real grn pattern; may be due to structural defm'n
  - mo is euhedral blades and hexagons to anhedral
  - rtl takes vn-like attitude; rtl-py association
  - some interstitial ca in vn
  - sericite with py; py is subhedral to anhedral
  - ser vnlts and/or ca vnlts xcut vn and clast
- *Clast:*
  - bt-qtz-kspar-fl-tpz-py-rtl-ser-ca-kaol
  - relict kspars altering to ser and kaol
  - qtz – some pockets and some very fine grned
  - bt often containing euhedral inclusions of rtl
  - rtl dissem throughout; bt-rtl association; rtl-py association
  - py is anhedral to euhedral; dissem throughout
  - fl dissem throughout; fl included in tpz
  - tpz in few areas in clast
  - no mo in clast
  - some ca replacement in clast; may be from vn

Macroscopic

Microscopic

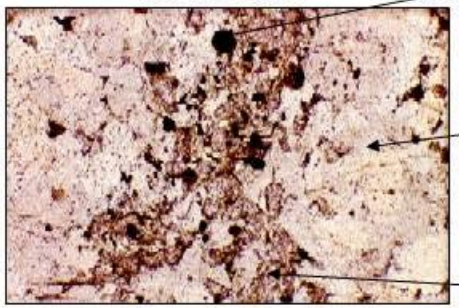

Mo and fl in qtz-mo vn; trans; pln; 10x.

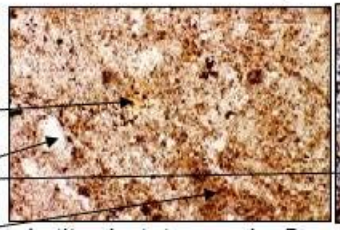

Latite clast; trans; pln; 5x.

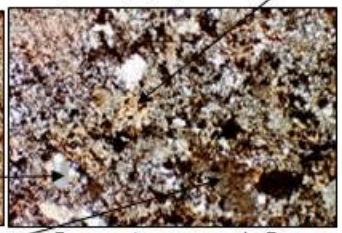

Same; trans; xpol; 5x.

Petrographic Section

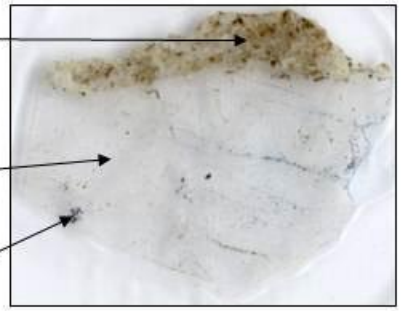

Paragenesis

Vein:
qtz→qtz+mo+fl→qtz+ser+py+rtl+/-ca →ca

Vein Envelope:
qtz+kspar→bt+qtz+fl→rtl+tpz+fl+qtz +ser+py→ca+/-kaol

Sample: AR-106
Facies: A2
Phase: Matrix
Borehole: 23.4-11.8G
Elevation: 7363'

Macroscopic

Qtz-mo-kspar-aplite matrix; source aplite, bt alt Tan, and blch ovrprnt bt alt Tan clasts matrix.

Microscopic

- *Matrix:*
  - minor aplite-qtz-kspar-mo-fl-rtl-bt-py-ser-ca-kaol
  - qtz is subhedral to anhedral; finer grned generation and coarser grnd generation, 25 microns to 2200 microns; highly fractured
  - relict subhedral kspar grains; kspar alt to ser and/or kaol; bt association; mo association
  - euhedral-subhedral mo blades and hexagons; associated with finer grned qtz and kspar
  - fl dissem throughout and as vnlts; fl-mo association
  - tr bt occurring along clast/matrix interface and with kspar; anhedral to subhedral; 25 microns to 250 microns
  - rtl occurring throughout; association with fluorite, py, and sericite
  - py is euhedral to anhedral
  - ca vn xcutting matrix and fl vnlt

Macroscopic

Microscopic

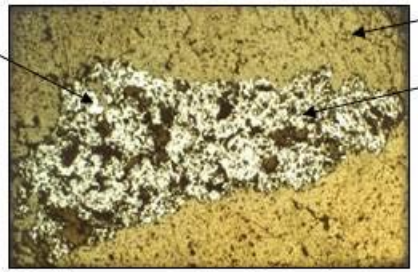

Rutile, ser, qtz, fl; reflect; pln; 5x.

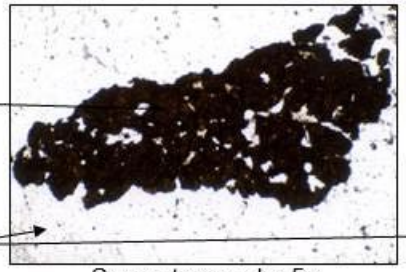

Same; trans; pln; 5x.

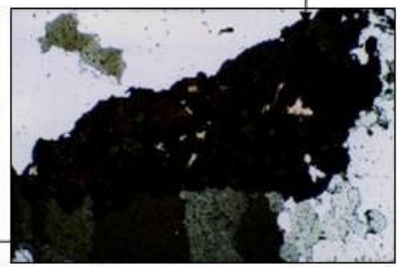

Same; trans; xpol; 5x.

Petrographic Section

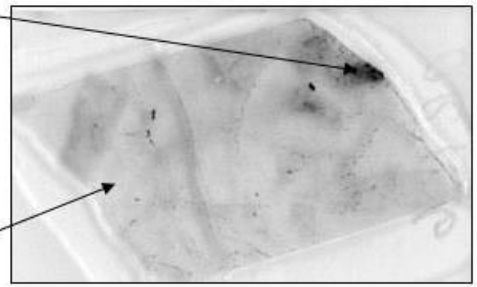

Paragenesis:

Matrix:

aplite→qtz+kspar+fluorite+mo+/-
bt→bt+fl+rtl+/-mo+/-qtz+/-
kspar→qtz+ser+py+rtl→ca+/-kaol

Sample: AR-118
Facies: A2
Phase: Matrix
Borehole: 23.5-11.8G
Elevation: 7397'

Macroscopic

Aplite-kspar-qtz-mo-Tlgp matrix

Microscopic

• *Matrix:*

- aplite-kspar-qtz-mo-rtl-py-ser-ca-tr bt-tr fl
- aplite consists of qtz+kpar+rtl+py+ser+/-kaol
- smaller qtz grains…associated with QSP?
- xcut by minor ser or ca vnlts
- lots of fluid inclusions

Paragenesis:

Matrix:

aplite→qtz+kspar+/-tr mo+/-bt→bt+rtl+/-mo→rtl+qtz+ser+py→ca+/-kaol

Macroscopic

Petrographic Section

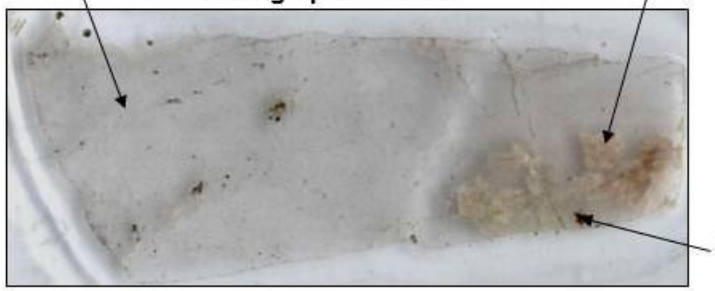

Microscopic

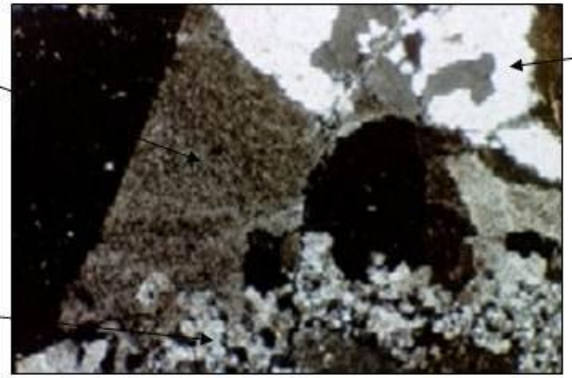

Aplite-qtz-kspar matrix; trans; xpol; 5x.

Sample: AR-110
Facies: A2
Phase: Vein
Borehole: 23.4-11.8G
Elevation: 7517'

Macroscopic

Macroscopic
Qtz-mo vn with blch alteration clast.

Microscopic

- *Vein:*
  - ➢qtz-mo-fl-py-rtl-bt-ser-ca-kaol
  - ➢different stages of qtz deposition within vn; size variation 30-600 microns in some areas and 10-1100 microns in other areas
  - ➢ fl dissem throughout vn; some euhedral (hexagonal) fl grains; fl-mo association, fl often surrounding the mo grain
  - ➢ euhedral (hexagonal and blades) to anhedral mo; often occurs along boundaries of varying qtz grn size; often occuring with smaller, zoned subhedral-anhedral qtz
  - ➢ some rtl in vn, may be from clast digestion
  - ➢ some ser-qtz-kaol pockets, may be from clast digestion
  - ➢py in vn; euhedral to subhedral; 10-250 microns; often occurring with ser pockets
  - ➢ some bt, prob from clast digestion
  - ➢ fl vnlt xcuts qtz-mo vn
  - ➢ ca vnlts and/or ser vnlts xcut qtz-mo vn
- *Clast:*
  - ➢ ser-kaol-rtl-qtz-py-mo-tr fl
  - ➢ fairly crs to fine grned ser
  - ➢ py-ser association
  - ➢ some fl dissem throughout clast
  - ➢ mo xcuts QSP alteration/clast

Paragenesis:

Vein:
qtz+mo+fl+/-py→ser+/-py→ca

Vein Envelope:
bt→rtl+ser+py+qtz→mo+qtz+fl+/-py→ser+/-py→ca

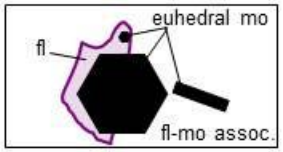

Microscopic

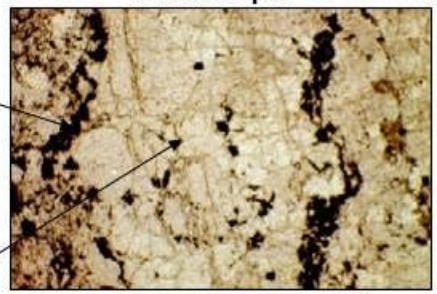

Qtz grn size and mo relationship; trans; pln; 5x.

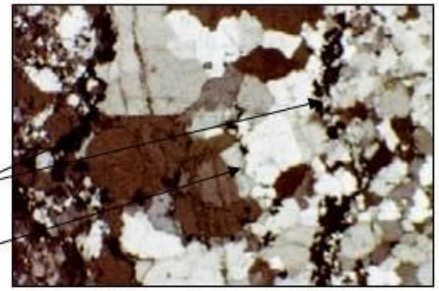

Same; trans; xpol; 5x.

Petrographic Section

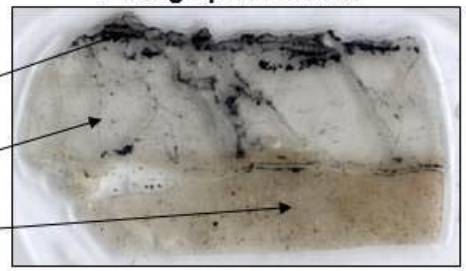

Sample: AR-119
Facies: A2
Phase: Vein
Borehole: 23.5-11.8G
Elevation: 7434'

Macroscopic

Bt alt; blch ovrprnt bt alt; kspar-qtz-mo matrix with rtl; qtz-mo-py-ca vn.

Microscopic

• *Vein:*

- qtz-mo-ca-fl-py-ser
- large qtz crystals; anhedral to subhedral; vn grains vary from 60 to 2000 microns
- ca occurring in center of vein
- mo in vn is euhedral blades or hexagons; 20 to 200 microns
- py in vn euhedral to anhedral; 20 to 50 microns; some py occurring with mo
- fl dissem throughout vein; fl-mo and fl-rtl-py association
- xcutting ser vnlts and ca vnlts

• *Clast:*

- qtz-kspar-ser-bt-rtl-py-fl-mo-ca
- mo dissem in clast
- py dissem in clast; occurring often with rtl
- kspar altered to ser and/or kaol
- some bt; rtl-bt assoc
- xcutting ser vnlts and ca vnlts
- rtl often occurring in vnlts and pockets of crs grn qtz

Macroscopic

Microscopic

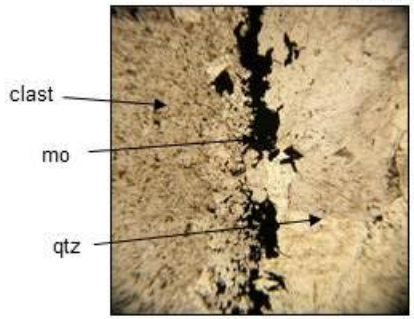

Clast-vn interface; trans; pln; 5x.

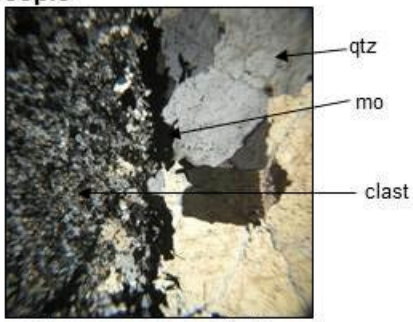

Same; trans; xpol; 5x.

Petrographic Section

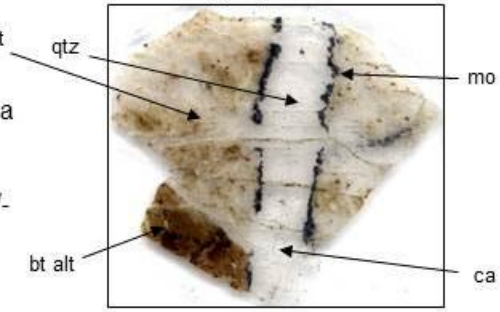

Paragenesis

Vein:

qtz+mo+fl+py→ca→qtz+ser+/-py→ca

Vein Envelope:

kspar+qtz→qtz+rtl+/-bt→qtz+rtl+bt+/-py+/-fl→qtz+ser+py+/-rtl+/-fl→qtz+mo+fl→ser→kaol→ca

Sample: AR-93
Facies: A3
Phase: Matrix
Borehole: 22.0-14.0
Elevation: 7391.5'

Macroscopic

Bt alt Tan; qtz-kspar-tr mo matrix.

Microscopic

• *Matrix:*

- qtz-aplite-kspar-tr bt-tr rtl-tr py
- some very large qtz grns in matrix (> field of view), med and sm grns also
- aplite – qtz+kspar and some minor bt and ser; "digested" into matrix;
- bt alt Tan may also be slightly digested into matrix
- minor bt within matrix; rtl-bt association; poss tpz-bt assoc
- fl dissem throughout; fl-bt assoc
- ser and/or ca stringers
- no visible mo; however very thin blades occur in qtz matrix, may be mo, rtl, or fluid inclusions
- kspar alt to ser and kaol in some areas

• *Clast:*

- bt altered clast; bt-qtz-kspar+fl+rtl+/-tpz
- ser and/or ca stringers

Macroscopic

Microscopic

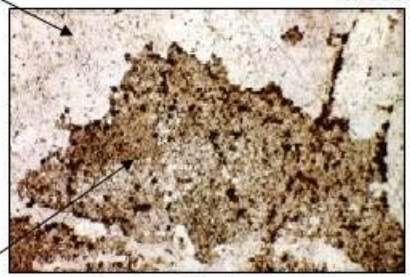

Aplite-qtz matrix; trans; pln; 5x.

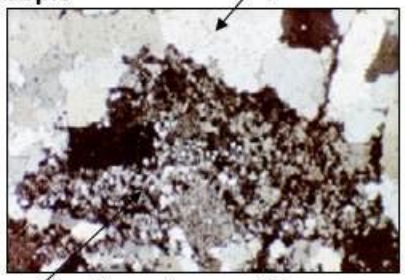

Same; trans; xpol; 5x.

Paragenesis

Matrix:
aplite→qtz+kspar+fl→qtz+rtl+bt+fl→qtz+ser+/-rtl+/-py→kaol→ser/ca

Clast:
qtz+kspar→bt+qtz→bt+qt+tpz→bt+qtz+rtl+tpz→qtz+rtl+py→ser/ca

Petrographic Section

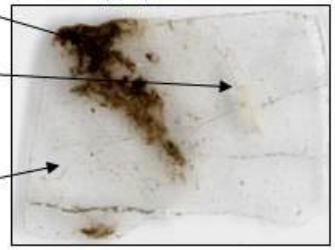

Sample: AR-91 (replaced AR-170 due to insufficient material)
Facies: A3
Phase: Matrix
Borehole: 22.0-14.0
Elevation: 7426.5'

Macroscopic

Microscopic

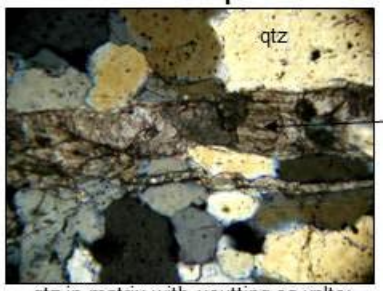

qtz in matrix with xcutting ca vnlts; trans; xpol; 10x and d.z.

Macroscopic
Bt alt Tan clasts; qtz-tr mo-kspar matrix.

Microscopic

- *Matrix:*
  - kspar-aplite-qtz-mo-fl
  - qtz is fine to lg grned; 5 to 200 microns; anhedral; random grn distribution; qtz and kspar cogenetic
  - kspars fairly pristene, but altered slightly to ser and kaol; some kspars well altered to ser and/or kaol; kspars are anhedral; 5-50 microns
  - f.g. fl dissem in matrix
  - mo as anhedral to subhedral grns
  - some clast "digestion"
  - ser and/or ca vnlts xcutting matrix and clast

- *Clast:*
  - qtz-bt-rtl-tr tpz-fl-py-ser-kaol-mt?
  - typical bt alt clast
  - lots of kspar @ clast/matrix interface
  - leucoxene or clay replacing plag phenos; relict plag phenos are replaced by ruddy dk brown-black material and ser/clays
  - rtl-bt assoc

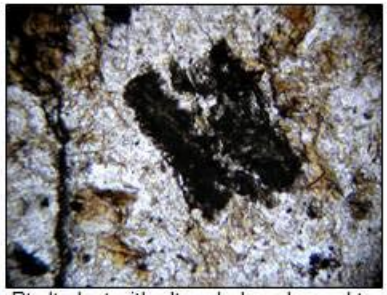

Bt alt clast with altered plag pheno, bt, ser, qtz, and rtl; trans; pln; 10x and d.z.

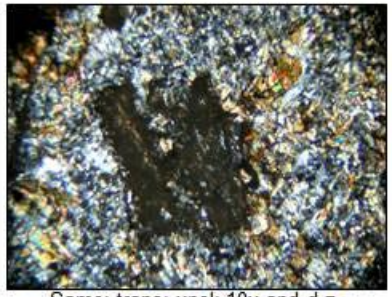

Same; trans; xpol; 10x and d.z.

Paragenesis

Matrix:
aplite→qtz+kspar+/-fl→qtz+mo+fl→ ser/ca

Clast:
qtz+bt+/-rtl+/-tpz+/-fl→qtz+bt+rtl+tpz +/-fl→qtz+fl→qtz+ser+py→ser/ca→ kaol

Petrographic Section

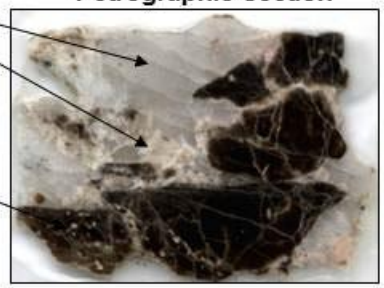

Sample: AR-90
Facies: A3
Phase: Vein
Borehole: 22.0-14.0
Elevation: 7430'

Macroscopic

Bt alt Tan clasts, qtz-mo-kspar-aplite matrix, qtz-mo vn.

Microscopic

• *Vein:*

- qtz-mo-ca-py-fl-tr rtl-tr bt-tr kspar
- small→large←small grn relationship in qtz; mo assoc with sm-lg grn boundary and sm grn qtz-clast substrate
- mo is euhedral blades and hexagons to anhedral
- ca assoc with lg qtz grns in center of vn (open space filling); euhedral qtz crystals in contact with ca; wherever ca, minor amt of bt in w/ca and qtz
- lots of dissem anhedral fluorite; mo-fl assoc
- no topaz observed in vn→this may support that its assoc w/matrix
- small amt of kspar assoc w/ sm qtz grns (digested clast?)
- rtl dissem throughout vn
- lg grn of very tarnished py; 1050x850 microns; contains inclusions of euhedral mo, plus qtz, bt, and rtl; other sm grns of py in vn, but not abundant

Macroscopic

• *Clast:*

- bt-qtz-fl-rtl-py-ser-kaol
- relict plag phenos altering to bt, ser, and kaol
- rtl-bt assoc
- no visible topaz, may be altered to ser
- fl dissem throughout; prob from vn
- no mo dissem in clast; mo along substrate of clast and vn only
- minor py throughout

Paragenesis

Vein:

qtz+mo+fl→qtz+mo+fl+/-kspar+/-bt+/-rtl→qtz+py+/-mo+/-rtl+/-bt→ca

Vein Envelope:

qtz+bt+rtl→qtz+bt+fl→qtz+ser+py→kaol

Microscopic

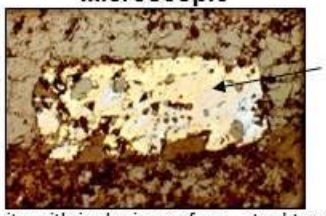

Pyrite with inclusions of mo, qtz, bt, and rtl; in qtz-mo vn along vn/clast substrate; reflect; pln; 10x.

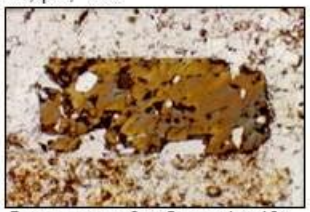

Same; trans & reflect; pln; 10x.

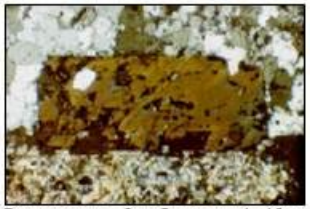

Same; trans & reflect; xpol; 10x.

Petrographic Section

Sample: AR-14
Facies: A3
Phase: Vein
Borehole: 21.7-15.5
Elevation: 7395'

Macroscopic

Microscopic

qtz-mo vn; qtz-mo-ser; trans; pln; 10x.

Macroscopic
Bt alt Tan and qtz-mo vn.

Microscopic

• *Vein:*
- ➢ qtz-ca-mo-py-bt-fl-ser-tr kspar
- ➢ subhedral and anhedral qtz with variable grn size; 50-300 microns
- ➢ "digestion" of bt alt Tan; giving way to bt in vn and bt alt to ser; ser pockets in vn; grn of kspar being alt to ser in vn
- ➢ fl dissem throughout
- ➢ mo is anhedral to subhedral; no particular qtz grn size assoc with mo
- ➢ minor interstitial ca
- ➢ minor py dissem throughout
- ➢ ca and/or ser vnlts xcutting vn

• *Clast:*
- ➢ bt-qtz-rtl-py-fl-tr mo
- ➢ bt alt Tan with subhedral to anhedral bt grns; <10-150 microns;
- ➢ possible relict kspar or plag phenos alt to bt, qtz, ser, and kaol
- ➢ rtl (5-50 microns) occurring with py and bt
- ➢ a few qtz pockets but predom bt-qtz mixture; qtz grn size same variability as bt

Clast cont'd
- ➢ fl dissem throughout
- ➢ py in clast (prob assoc with lg qtz pockets); 5-50 microns; possible mt replacement of some py
- ➢ poss mo in clast
- ➢ ca and/or ser vnlts xcutting clast

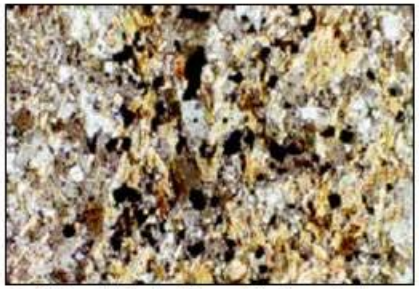

bt alt clast; bt-qtz-rtl-py-mt?-minor fl; trans; xpol; 20x.

Paragenesis

Vein:
qtz→qtz+mo+fl→qtz+ser+py+rtl→ca/ser

Vein Envelope:
qtz+bt→qtz+fl+mo+/-bt→qtz+ser+py+rtl+/-mt→ca/ser→kaol

Petrographic Section

Sample: AR-169
Facies: B
Phase: Matrix
Borehole: 19.9-12.1
Elevation: 7459'

Macroscopic

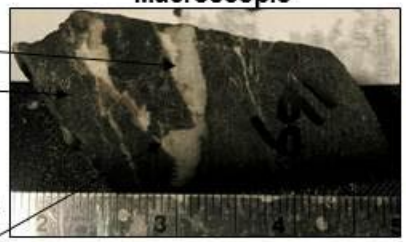

Microscopic

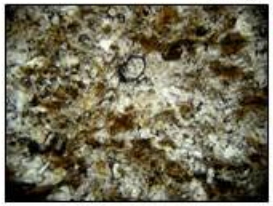

bt-tpz-rtl-apatite-qtz in bt alt clast; trans; pln; 10x and digital zoom

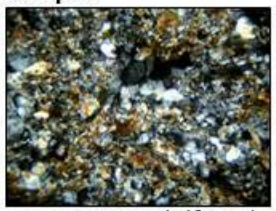

same; trans; xpol; 10x and digital zoom

Macroscopic

Qtz-kspar-tr mo matrix and bt alt Tan; xcutting ca vnlts

Microscopic

- *Matrix:*
  - qtz-kspar-mo-py-fl-minor ca-tr bt-tr rtl
  - some very lg qtz grns farthest from clast; finer grn qtz closest to clast
  - kspar and mo mostly close to clast
  - mo is euhedral hexagons and blades to anhedral; mostly assoc w/ fine-med grn qtz
  - some ca matrix material
  - fl dissem throughout
  - kspar altered to ser and kaol in some areas
  - partially "digested" clast contributing some bt and rtl; tr hydrothermal bt also
  - xcutting ca-fl vnlt

- *Clast:*
  - bt-qtz-fl-rtl-py-mo-tpz-ap-some kspar-tr mt
  - fine grned kspar along matrix-clast boundary
  - bt-rtl-tpz-ap-qtz groundmass
  - abundant crs grn topaz
  - py dissem throughout clast

qtz and mo in matrix; trans; pln; 5x and digital zoom

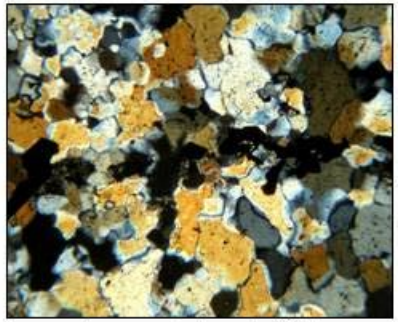

same; trans; xpol; 5x and digital zoom

Paragenesis

Matrix:
"digested" clast (bt+qtz+tpz+rtl)→ qtz+kspar+mo+fl→qtz+mo+fl→qtz+py →ca+fl

Clast:
qtz+bt+/-tpz+/-ap→qtz+bt+rtl+tpz+ap→ qtz+mo+fl→qtz+py→ca+fl

Petrographic Section

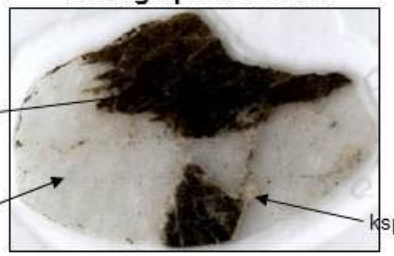

Sample: AR-12
Facies: B
Phase: Matrix
Borehole: 21.7-15.5
Elevation: 7430'

Macroscopic

Macroscopic

Bt alt clasts; kspar-qtz-mo-ca matrix; some py throughout.

Microscopic

• *Matrix:*

- qtz-kspar-mo-fl-bt-ca-tpz-ap-py-ser-kaol-tr hm-tr rtl
- bt-ca-tpz and/or kspar assoc
- bt dissem throughout sparsely, but appear to be in stringer-like orientations rather than completely random
- some kspar alt to ser and kaol; most kspar along matrix/clast interface; kspar is subhedral to anhedral
- few grns of subhedral py; 3-8 microns
- qtz is variable in size; 5-150 microns; anhedral to subhedral
- fl dissem throughout; occurs with mo, kspar, bt and qtz
- ca is interstitial between qtz grns
- mo is subhedral blade to anhedral; mo-kspar assoc
- ser stringers xcut matrix
- tpz-ap-tr rtl-some bt from clast digestion?

kspar-qtz matrix; bt alt clast; trans; pln; 10x and digital zoom

same; trans; xpol; 10x and digital zoom

• *Clast:*

- qtz-bt-rtl-py-tpz-ap
- inclusions of rtl in bt
- qtz pockets
- ca and kspar (prob from matrix)
- py dissem throughout; euhedral-anhedral
- rtl occurring often in stringers or pockets; crs grned
- crs grned bt
- possible mt in clast

Paragenesis

Matrix:

"digested clast" (bt+qtz+tpz+rtl)→ kspar+qtz+mo+fl→qtz+kspar+ca+/-bt+/-mo+/-fl→qtz+ser+py+/-rtl→kaol

Clast:

bt+qtz→bt+qtz+rtl+tpz+ap→kspar+ca+qtz (from matrix)→qtz+py+/-ser→kaol

Microscopic

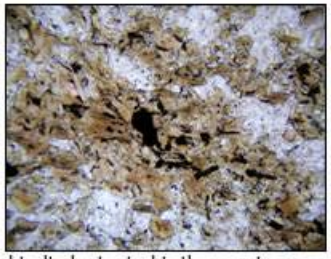

bt alt clast; qtz-bt-rtl-py-ap-tpz-mt?; trans; pln; 10x and digital zoom

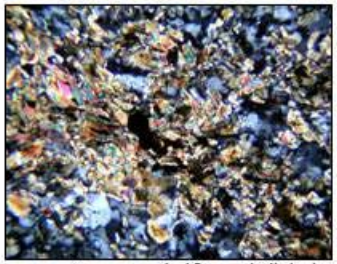

same; trans; xpol; 10x and digital zoom

Petrographic Section

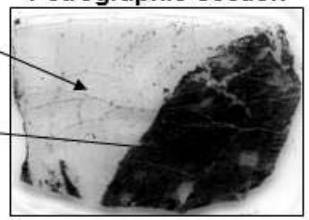

Sample: AR-13
Facies: B
Phase: Matrix
Borehole: 21.7-15.5
Elevation: 7429'

Macroscopic
Bt alt clasts with py; qtz-mo matrix; minor ca present.

Microscopic
• *Matrix:*
- ➢ no clast in thin or thick section
- ➢ few small grns of py in matrix; 10 to 50 microns
- ➢ mo occurring in matrix is variable size and shape; 20 to 500 microns; anhedral to euhedral (hexagons and blades); fl-mo assoc
- ➢ fl occurring along grn boundaries
- ➢ in general, mo assoc with finer grned qtz
- ➢ some very lg grns of qtz; > than field of view @ 5x (>2500 microns); no mo within these grns; some qtz grns have an "interlocking" texture (mostly smaller grns)
- ➢ fine-med grned bt with fl
- ➢ xcutting ca or ser vnlt

Paragenesis
Matrix:
qtz→qtz+mo+fl+/-bt→qtz+bt+fl+/-mo→qtz+ ser+py →ca/ser

Macroscopic

Petrographic Section

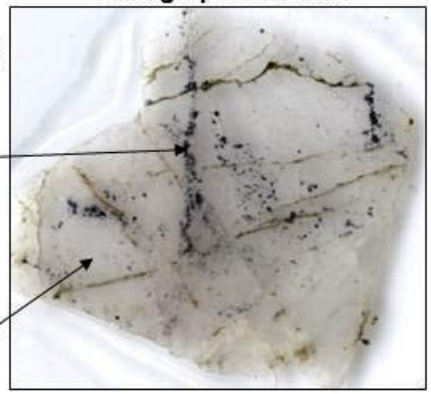

Microscopic

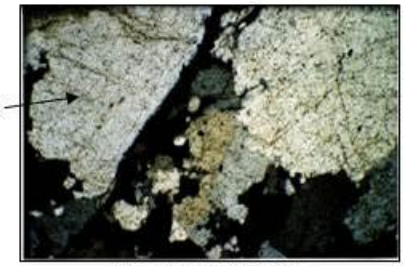

Qtz; trans; xpol; 10x.

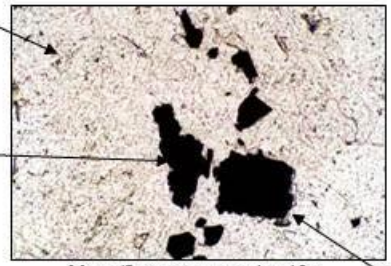

Mo w/fl, qtz; trans; pln; 10x.

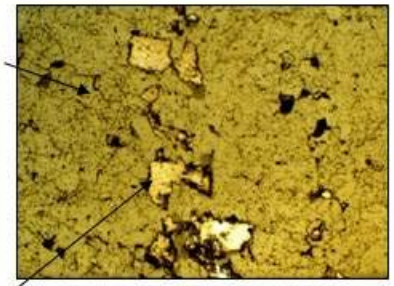

Mo and qtz; reflect; pln; 10x.

Sample: AR-147
Facies: B
Phase: Vein
Borehole: 21.7-15.5
Elevation: 7427.5'

Macroscopic

Microscopic

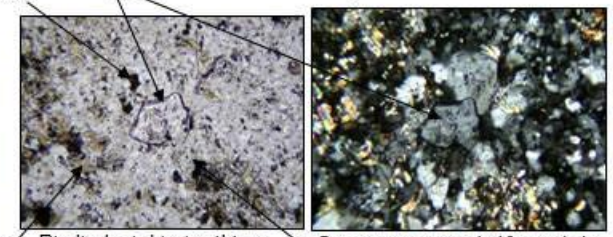

Bt alt clast; bt-qtz-rtl-tpz-kspar; trans; pln; 10x and d.z.

Same; trans; xpol; 10x and d.z.

Macroscopic
Qtz-mo vn; bt alt Tan xcut by minor ca vnlts

Microscopic

- *Vein:*
  - qtz-mo-fl-ca-tr py-[tr rtl-tr kspar-tr bt-tr tpz (from digested clast)]
  - partially "digested" clast
  - fl dissem throughout; also fl grns size of qtz
  - mo in euhedral blades or hexagons to anhedral
  - random variable grain size distribution of qtz
  - fairly random mo distribution with some ordered distribution
  - qtz grns in mo
  - ca as open-space filling
  - pretty well fractured and xcut by ca microvnlts

- *Clast:*
  - qtz-bt-kspar-rtl-py-par-tr mo-fl-tr tpz-leucoxene
  - typical bt alt clast
  - rtl inclusions in bt, both anhedral and euhedral; rtl-bt assoc; rtl-py assoc; rtl in py, py in rtl

Clast Cont'd
- some dissem fl
- most tpz alt to leucoxene
- tpz-bt assoc; tpz before bt; fl inclusions in tpz
- fine and crs grned bt
- py as microfracture fill with rtl and bt
- tr mo blades
- xcutting ca microvnlts

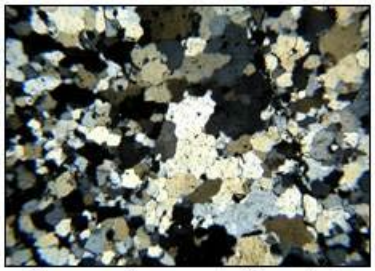

Qtz-mo vn; trans; xpol; 10x and d.z.

Paragenesis
Vein:
qtz→qtz+mo+fl→qtz+ca+/-mo+/-fl+/-py→ca

Vein Envelope:
qtz+bt+tpz+/-kspar+/-fl→qtz+fl+bt+tpz+rtl+/-kspar→qtz+ser+py+/-rtl+/-fl→qtz+fl+mo→ca

Petrographic Section

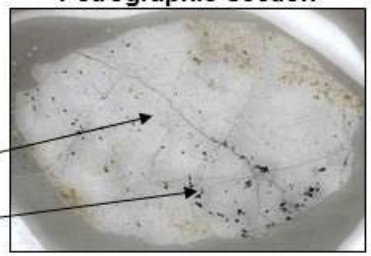

Sample: AR-167
Facies: B
Phase: Vein
Borehole: 19.9-12.1
Elevation: 7474.5'

Macroscopic

Qtz-mo vn in bt alt Tan.

Microscopic

• *Vein:*
- qtz-mo-fl-tr py-ca
- fl dissem throughout
- variable grn size for qtz
- mo assoc w/smaller grned qtz
- ca as open-space filling
- xcutting ca vnlts
- very fine xcutting ser vnlts

• *Clast:*
- bt-qtz-rtl-ser-tpz-py-leucoxene
- typical bt alt clast
- bt and qtz w/altered bt and leucoxene/rtl; ser center inside bt/rtl/leucoxene

Paragenesis

Vein:
qtz+mo+fl→qtz+mo+fl+py→qtz+ca→ca/ser

Clast:
qtz+bt→qtz+bt+tpz+/-rtl→qtz+rtl+/-bt+/-tpz→qtz+ser+py→ca/ser

Macroscopic

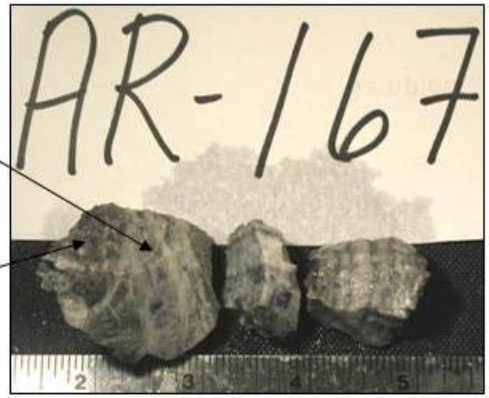

Microscopic

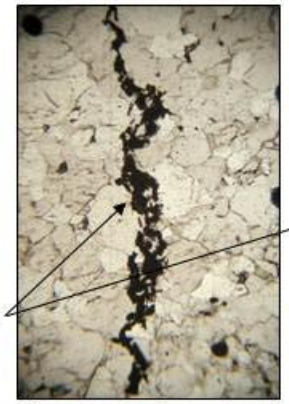

Qtz-mo vn and qtz grn size/mo relationship; trans; pln; 5x and d.z.

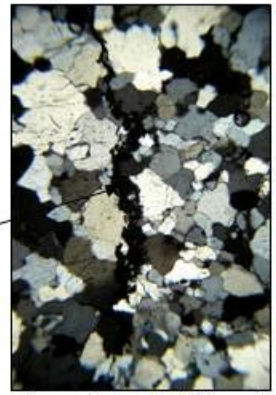

Same; trans; xpol; 5x and d.z.

Petrographic Section

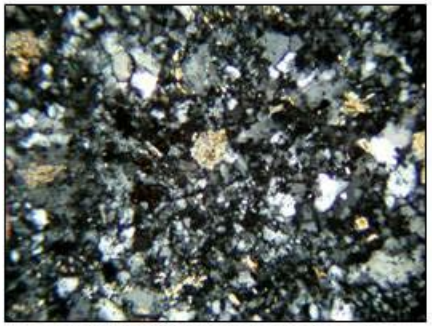

Bt alt clast; trans; xpol; 5x and d.z.

Sample: AR-131
Facies: C
Phase: Matrix
Borehole: 22.0-14.0
Elevation: 7505'

Macroscopic

Crs grn bt-kspar-mo-qtz-anhy-gypsum matrix; most anhy alt to gypsum.

Microscopic

• *Matrix:*

- qtz-mo-bt-kspar-rtl-gyp-py-fl-ap-ca-tr tpz
- qtz vn through large qtz grns, only 1 or 2 sm gns thick; lg matrix qtz grns are field of view at 5x; ca-gyp-fl with qtz vnlts xcutting lg qtz grns
- kspar alt to ser; rtl within kspar
- euhedral rtl in bt
- ap included in qtz
- rtl within bt within kspar with qtz vn adjacent; bt alt to rtl
- py grn within kspar; qtz and kspar within py
- fl slightly dissem throughout
- qtz and gyp grn within mo
- gyp occuring along grn boundaries; gyp in cleavage of bt; relict twinning of anhy in some gyp

Paragenesis

Matrix:

qtz+bt+/-kspar+/-mo+/-fl+/-rtl→qtz+kspar+mo+fl+/-bt+/-rtl→anhy+fl+mo→qtz+py+ser+/-rtl→qtz+ca+gyp+fl

Macroscopic

Microscopic

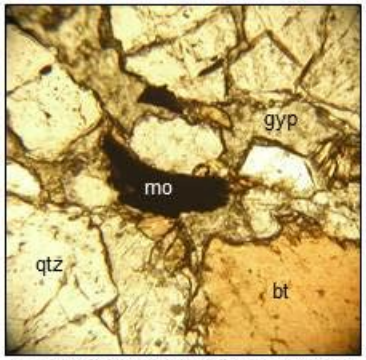

Qtz-mo-bt-gyp matrix; trans; pln; 10x and d.z.

Petrographic Section

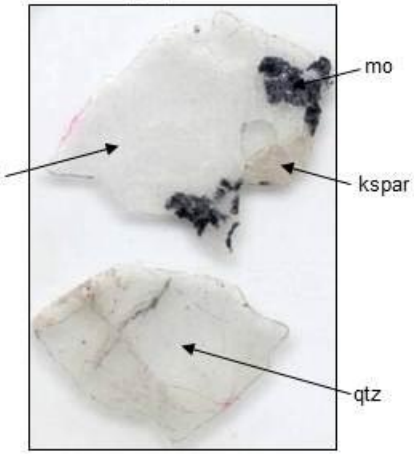

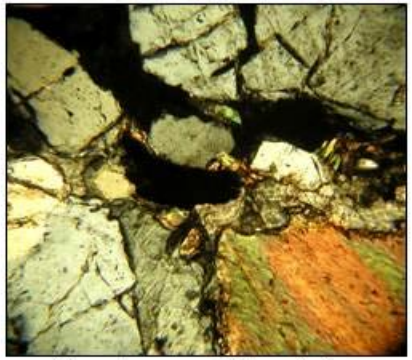

Same; trans; xpol; 10x and d.z.

Sample: AR-8
Facies: C
Phase: Matrix
Borehole: 21.7-15.5
Elevation: 7479.5'

Macroscopic
Predominantly bt alt clast with some kspar flooding, qtz-bt-ca-mo matrix.

Microscopic
• *Matrix:*
- qtz-mo-bt-ca-tr py-tr ser-tr hem-tr kaol
- subhedral to anhedral qtz grns; solid inclusions in qtz; larger qtz grns occurring with bt
- mo as euhedral to subhedral hexagons and blades
- interstitial ca
- fl dissem throughout and as vnlts

Paragenesis:
Matrix:
qtz→qtz+bt+mo+fl→qtz+ca+/-fl→qtz+ser+py→kaol

Macroscopic

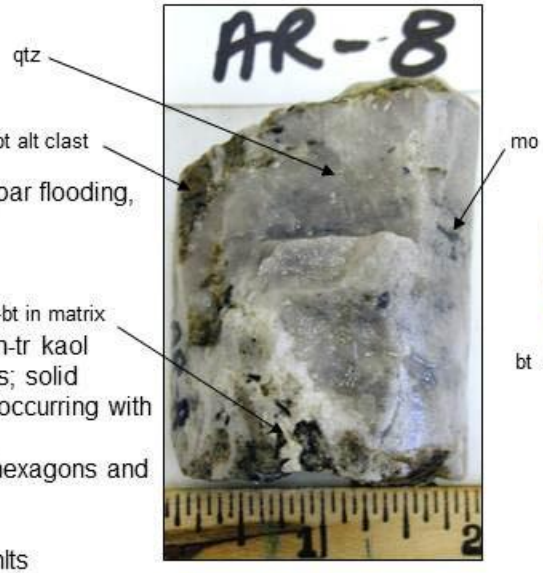

Microscopic

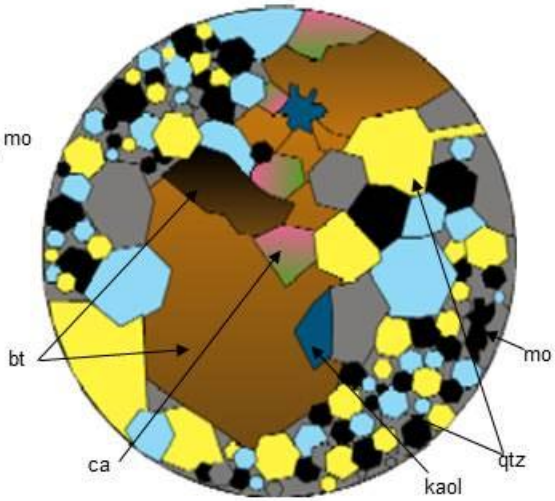

Field of view at 4x; qtz-mo-bt-ca matrix.

Petrographic Section

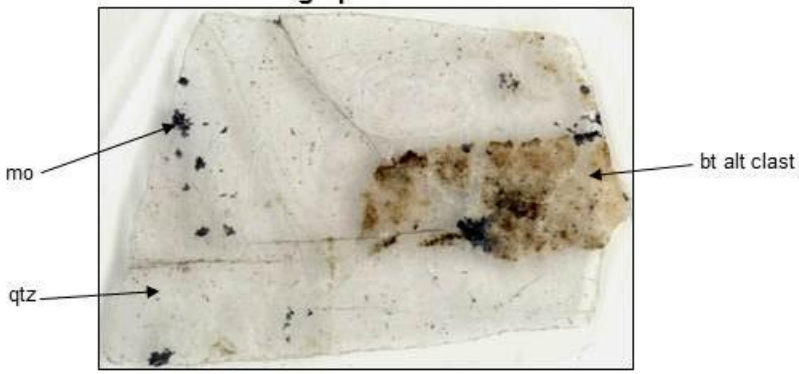

Sample: AR-166
Facies: C
Phase: Matrix
Borehole: 19.9-12.1
Elevation: 7539.5'

Macroscopic

Microscopic

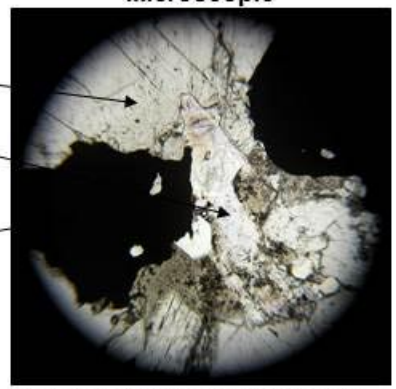

Fl-qtz-py matrix; trans; pln; 10x and d.z.

Petrographic Section

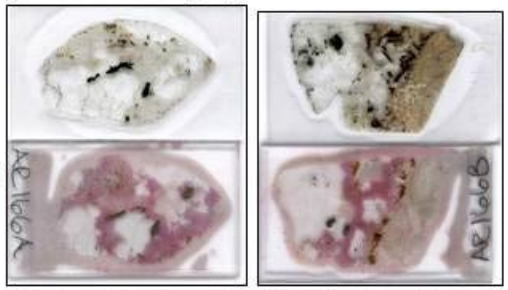

Thick sections and ca-stained thin sections; fl-ca-qtz-bt-py-bt alt clast.

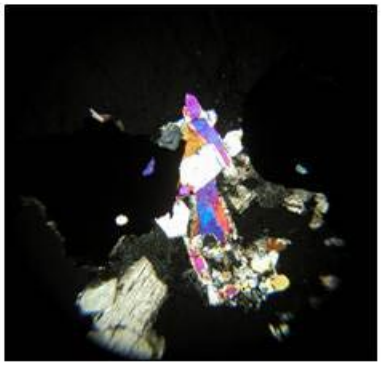

Same as above; trans; xpol; 10x and d.z.

Macroscopic
Blch clast; bt-qtz-fl-ca+/-kspar matrix; py in matrix and clast

Microscopic

- *Matrix:*
  - bt-qtz-kspar-rtl-tpz-fl-ca-py
  - crs grned ca, fl, and qtz with some crs grned py also
  - some rtl
  - fl has inclusions of qtz and ca
  - small subhedral to euhedral qtz crystals distributed throughout; within ca and bt; also xcutting bts
  - some concentric dogtoothspar patters in ca
  - bt growing along clast/matrix interface (outward into matrix); rtl inclusions in bt
  - some euhedral py, but mostly lg, anhedral grns
  - ca stain indicates all carbonate is ca
  - fairly lg kspar grain
  - fl has euhedral crystal faces against ca; fl first
  - ca may be open space filling
- *Clast:*
  - bt-ser-py-rtl-qtz-kspar-tpz-mo-leucoxene-some kaol
  - typical blch clast

Paragenesis

Matrix:
bt→bt+qtz→bt+qtz+kspar+/-rtl→fl+/-qtz+/-ca→ca+/-qtz+/-py

Clast:
qtz+bt+/-tpz→qtz+bt+/-tpz+/-kspar+/-rtl+/-mo→qtz+ser+py→kaol

Sample: AR-11
Facies: C
Phase: Vein
Borehole: 21.7-15.5
Elevation: 7465.5'

Macroscopic

Bt alt clasts, qtz-mo vnlt xcut by qtz-mo-ca matrix, py in qtz-mo vnlt.

Microscopic

- *Vein:*
  - qtz-mo-py-tr ca
  - mo occurs mostly with smaller qtz grns, but some in larger qtz, or along lg-sm qtz grn boundary; euhedral to subhedral hexagons and blades
  - qtz grn distribution is typical sm→lg←sm as seen before; ehuhedral to subhedral
  - py occurring in center of vn
  - tr ca in vn
  - fl dissem throughout
- *Clast:*
  - bt-qtz-rtl-fl-tpz-ap
  - fl dissem throughout
  - rtl dissem throughout clast

Paragenesis

Vein:

qtz→qtz+mo+fl→qtz+mo+fl+py+/-ca→qtz+ca

Vein Envelope:

qtz+bt+/-tpz+/-ap+/-rtl→qtz+fl

Macroscopic

Microscopic

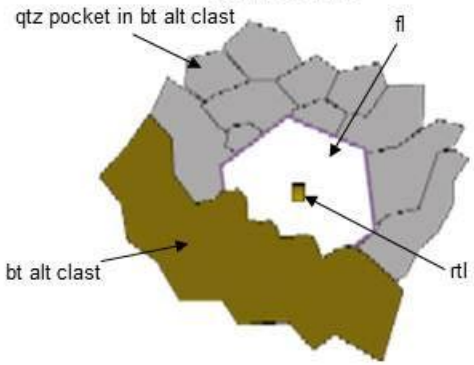

Field of view at 20x; fl in qtz pocket in bt alt clast; rtl inclusion in fl.

Petrographic Section

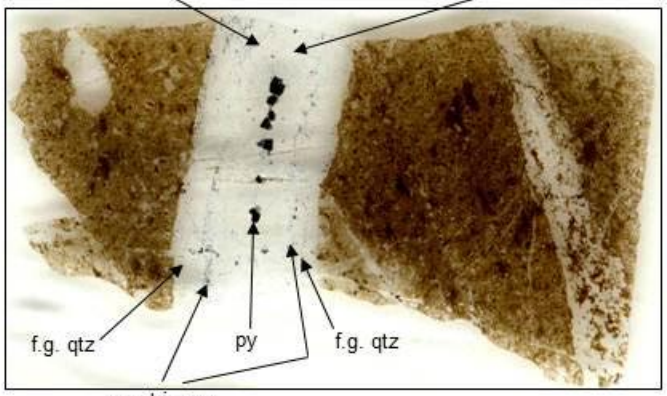

Sample: AR-81
Facies: C
Phase: Vein
Borehole: 22.0-14.0
Elevation: 7546'

Macroscopic
Blch ovrprnt bt alt Tan clasts, kspar-qtz-bt-mo matrix, qtz-mo vnlts, ca slick.

Microscopic
• *Vein:*
- qtz-mo-fl-ca-rtl
- med→small→large←small←med qtz grain size distribution within vnlt from outside vnlt to inside
- center of vnlt also contains ca as open space filling
- lots of fl; fl also occurring as open space filling in center of vn
- mo as euhedral blades and hexagons to anhedral; occurs along vnlt/clast interface and along interface of different qtz grn size
- some rtl in vnlt

• *Clast:*
- qtz-mo-rtl-bt-tpz-fl-py-ser
- tpz is euhedral to anhedral; fl included in tpz
- fl dissem throughout
- rtl dissem throughout; both fine grned and crs grned
- py with rtl; some py with fl
- py is subhedral to anhedral

Macroscopic

Microscopic

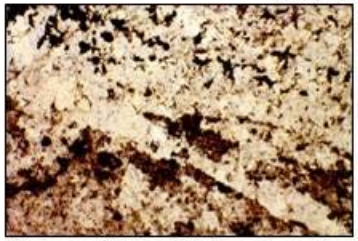
Qtz-mo vnlt/clast interface; trns; pln; 5x.

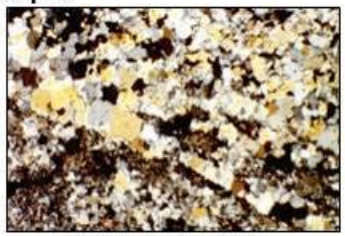
Same; trns; xpol; 5x.

Petrographic Section

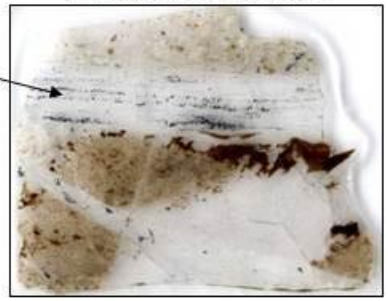

Paragenesis
Vein:
qtz→qtz+mo+fl+/-rtl→qtz+fl+ca

Vein Envelope:
qtz+bt+tpz+rtl→qtz+bt+/-tpz+/-rtl+/-mo+/-fl→qtz+fl+mo+/-rtl→qtz+ser+py+/rtl+/-fl

Sample: AR-6A
Facies: D
Phase: Matrix
Borehole: 21.7-15.5
Elevation: 7535'

Macroscopic

Microscopic

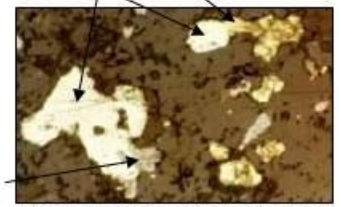

Rtl-py-cp-(mt?); reflect; pln; 40x.

Bt-gyp-anhy; trans; pln; 5x.

Macroscopic

Bt alt clasts, bt-qtz-anhy matrix, QSP, crs grned bt, grn and purple anhy.

Microscopic

- *Matrix:*
  - bt-anhy-mo-qtz-fl-gyp-ser-ca
  - crs grn bt; some ser selvages on edges and/or going through bt crystal; 20-2400 microns; euhedral to subhedral; bt growth from substrate of clast; bt containing euhedral inclusions of rtl
  - qtz, anhy, and fl growth from clast substrate also
  - most mo growth along matrix/clast interface, with most of the mo on the clast side; mo is anhedral to subhedral
  - anhy alt to gypsum
  - bt grn contained within lg anhy grn which is being altered to gyp along anhy/bt boundary
  - some py in matrix; occurs with fl or gyp or within lg anhy crystal
  - ca or ser vnlt xcutting matrix

- *Clast:*
  - bt-qtz-rtl-ser-py-cp-fl-anhy-tr tpz-tr ap-mt?
  - fl dissem throughout clast

Clast Cont'd

- rtl dissem throughout
- py-cp-rtl assoc; py is subhedral to euhedral; 20-100 microns; mt may be replacing py in some instances
- fl occurring in qtz pockets within clast
- fl vn xcuts clast
- bt alt to ser alt to kaol
- ser and/or ca stringers xcut clast and matrix

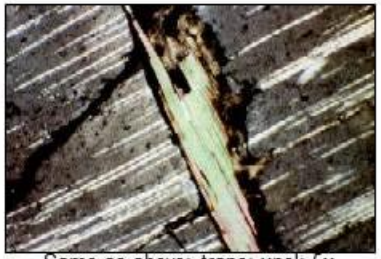

Same as above; trans; xpol; 5x.

Paragenesis

Matrix:

qtz→bt+/-rtl+/-fl→mo+fl→anhy(gyp)→ser +py+/-rtl+/-qtz+/-gyp→ca

Clast:

qtz+bt→qtz+bt+rtl+/-tpz+/-ap→qtz+fl+mo →ser+py+cp+/-mt→ca/kaol

Petrographic

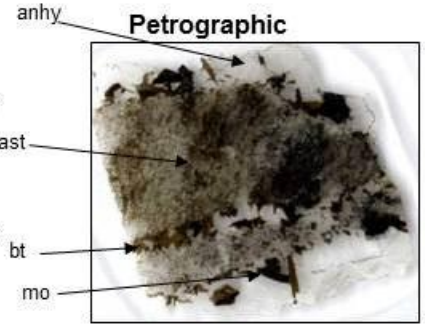

Sample: AR-164
Facies: D
Phase: Matrix
Borehole: 19.9-12.1
Elevation: 7588'

Macroscopic
Blch alt (with kspar+ and grn ser+) and bt alt Tan clasts; kf-bt-qtz-mo-fl-ca matrix; dissem mo in blch clasts

Microscopic
- *Matrix:*
  - bt-qtz-fl-ca-poss gyp-rtl-mo
  - lg euhedral to subhedral fl grns
  - lg euhedral to subhedral qtz;
  - ca as open space filling
  - fl after qtz, then ca
  - some gyp-ca vnlts xcutting everything
  - some qtz hydrothermally stressed by fl-ca vnlt fluids
  - inclusions of rtl in qtz adjacent to bt = qtz, bt and rtl cogenetic
  - some digested clast (qtz, ap, rtl, tpz?) in fl and qtz matrix
- *Clast:*
  - qtz-bt-tpz-rtl-ser-py-kspar
  - typical blch alt clast

Macroscopic

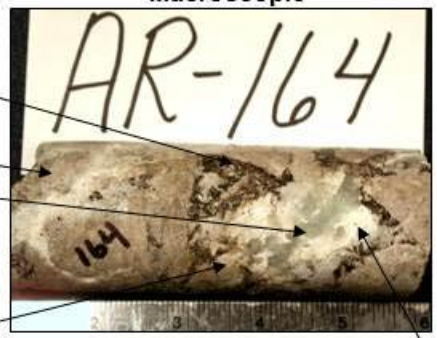

Petrographic Section

Ca-stained thin sxn. Thick sxn.

Paragenesis

Matrix:
kf→bt→bt+qtz+rtl→bt+qtz+mo+fl→fl +/-qtz→ca→ca+gyp

Clast:
qtz+bt+/-tpz→qtz+bt+rtl+/-tpz+/-kspar→qtz+ser+py

Microscopic

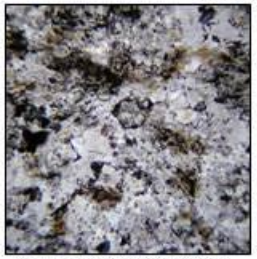

Clast: bt-tpz-qtz-rtl-ser-kspar; trans; pln; 10x and d.z.

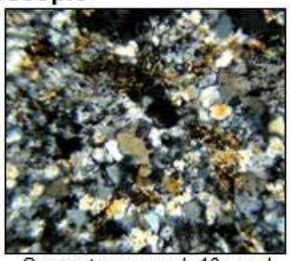

Same; trans; xpol; 10x and d.z.

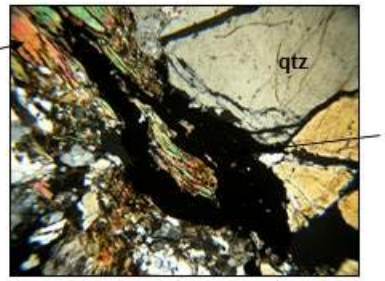

Bt-mo-qtz-ca matrix; trans; xpol; 10x and d.z.

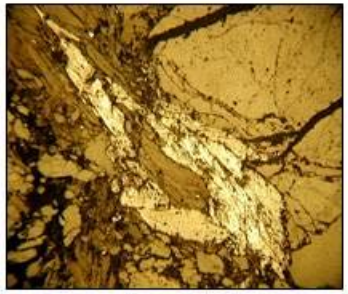

Same as above; reflect; pln; 10 x and d.z.

Sample: AR-78
Facies: D
Phase: Matrix
Borehole: 22.90-14.0
Elevation: 7576.5'

Macroscopic

Microscopic

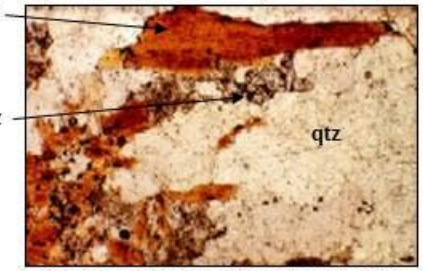

Qtz-kspar-bt-tpz matrix; trans; pln; 10x.

Macroscopic
Blch and blch ovrprnt bt alt Tan,
bt-qt-mo matrix; qtz-mo vnlt xcuts matrix.

Microscopic

- *Matrix:*
  - qtz-mo-bt-fl-tpz-py-rtl-kspar-ser-ca
  - moly is subhedral blades and hexagons to anhedral
  - closest to clast, smaller qtz grns; outer matrix contains very lg qtz grns
  - fl dissem throughout; not as much fl in very lg qtz grn; subhedral fl along matrix/clast interface containing inclusions of bt and qtz
  - tpz is euhedral to anhedral; some tpz alt to ser; tpz-bt assoc; fl inclusions in qtz
  - ser in matrix
  - kspar alt to ser
  - ser border on lg bt grns in matrix
  - ca vnlt xcuts matrix and vn

- *Clast:*
  - qtz-ser-bt-rtl-py-fl-topaz-mo-kaol
  - fl mostly w/mo; mo also assoc w/bt in clasts
  - rtl everywhere
  - fl w/tpz or included in tpz

Clast Cont'd
- bt along clast/matrix interface; inclusions of rtl in bt; tpz also along substrate
- ca vnlt xcuts matrix and vn

Same; trans; xpol; 10x.

Paragenesis

Matrix:
qtz+bt+kspar→qtz+bt+mo+fl+/-kspar→qtz +bt+fl+tpz+rt+/-mo→qtz+ser+py→ca

Clast:
bt+qtz→bt+qtz+tpz+rtl+fl+/-mo→qtz+rtl+ ser+py→kaol→ca

Petrographic Section

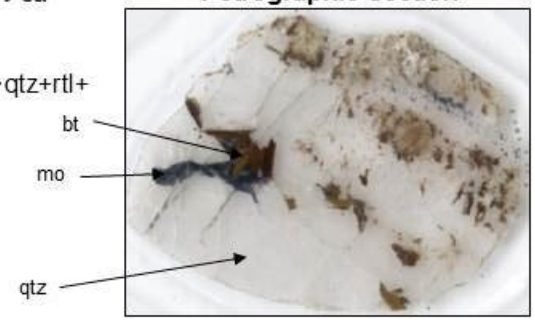

Sample: AR-143
Facies: D
Phase: Vein
Borehole: 21.7-15.5
Elevation: 7523.5'

Macroscopic

Macroscopic
Blch and blch ovrprnt bt Tan; qtz-mo-ca vn.

Microscopic

- *Vein:*
  - qtz-mo-ca-fl-py
  - ca as open sp filling in vn (euhedral qtz encapsulated by ca); ca also occurring as xcutting vnlts with very f.g. qtz causing stress features in preexisting vnlt qtz
  - mo is euhedral hexagons and blades to anhedral; fl-mo assoc; rtl-mo assoc; mo at clast/vn substrate or random stringer distributions throughout vn
  - qtz is euhedral to anhedral; 5-50 microns; no apparent grn size distribution pattern
  - py is subhedral to anhedral

Microscopic

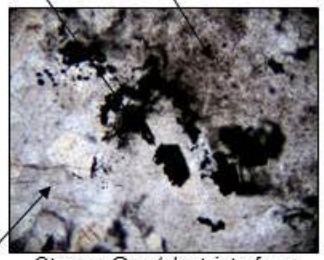

Qtz-mo @ vn/clast interface; trans; pln; 10x and d.z.

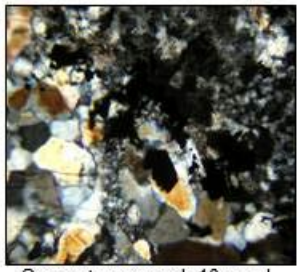

Same; trans; xpol; 10x and d.z.

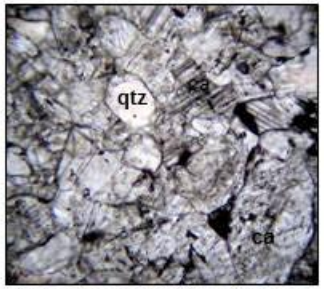

Qtz and ca in vn; trans; pln; 10x and d.z.

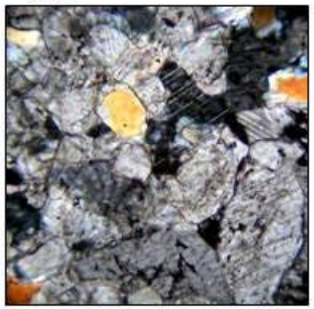

Same; trans; xpol; 10x and d.z.

- *Clast:*
  - qtz-ser-rtl-ca-par-leucoxene-kspar-kaol-tpz-ap
  - some kspars altered to ser and kaol
  - par present
  - leucoxene or "dirty" ser patches
  - lots of rtl
  - some tpz and/or ap
  - not a lot of qtz, but is there
  - ca vnlts xcutting clast

Paragenesis

Vein:
qtz→qtz+mo+fl→qtz+ca+/-mo+/-fl→qtz+py+/-mo+/-fl+/-ca→qtz+ca

Vein Envelope:
kspar+qtz→qtz+rtl+tpz+ap+/-kspar→qtz+ser+py→qtz+par→ca

Petrographic Section

Sample: AR-146
Facies: D
Phase: Vein
Borehole: 21.7-15.5
Elevation: 7509'

Macroscopic

Qtz-mo vn in blch Tan (with disseminated mo) a
blch ovrprnt bt Tan; qtz-ca-mo-bt matrix.

Microscopic

- *Vein:*
  - mo-qtz-ca-tr py-fl
  - minor rtl and tpz from "digested" Tan
  - mo with ca
  - fl dissem throughout; fl-mo assoc
  - variable qtz grain size, no distinct grain size affiliation with mo
  - py-mo assoc
  - ser vnlt xcuts qtz-mo vn

- *Clast:*
  - qtz-kspar-mo-rtl-py-poss cp-bt-ser-tpz-par-ca-ap-clay-ca-fl
  - mostly fine to crs grned bt, ser, par, and rtl with some kspar, qtz, ca, and tpz
  - bt altered to par
  - appears some kspars have been silicified
  - rtl everywhere
  - tpz alt to ser in some places

Macroscopic

Microscopic

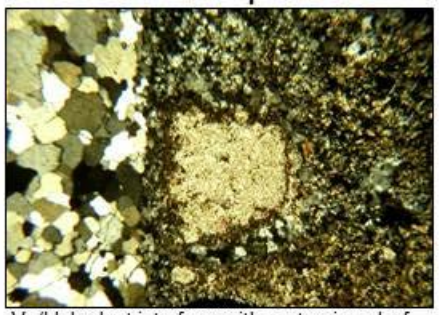

Vn/blch clast interface with protomineral of unknown origin alt to ser with bt/rtl rim; trans; xpol; 10x and d.z.

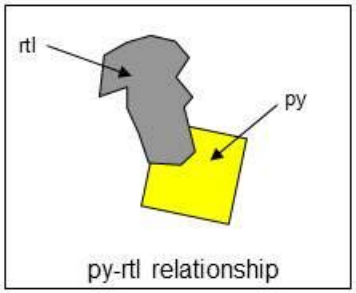

py-rtl relationship

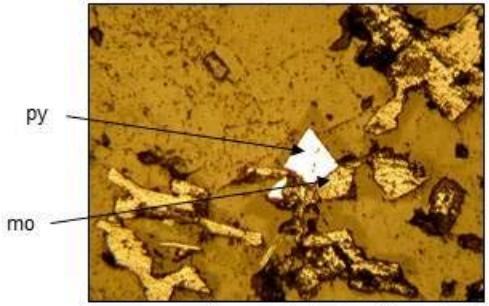

Py-mo assoc in vn; reflect; pln; 10x and d.z.

Paragenesis

Vein:
qtz→qtz+mo+fl+/-py→ca

Vein Envelope:
qtz+tpz+bt+rtl+/-kspar+/-fl→qtz+kspar+fl+/-rtl→qtz+mo+/-py→qtz+ser+py→qtz+par+/-kaol→ca+/-kaol

Petrographic Section

Sample: AR-5
Facies: E
Phase: Matrix
Borehole: 21.7-15.5
Elevation: 7578'

Macroscopic

Qtz-bt-mo-ca matrix, bt and blch alt tan clasts, QSP, dissem mo in clasts, grn ser, crs grned bt.

Microscopic

• *Matrix:*

- qtz-mo-bt-rtl-ca-fl-ser
- mo as euhedral blades and hexagons
- larger qtz frn on perimeter of sxn, smaller qtz grns in various areas in center of sxn; in some areas smaller grns occur in "pockets" where grns are failry uniform in size; in some areas, smaller grns occur intermixed with med to lg sized grns; smaller grns have dominant zoning within grns; smaller grns seem to be assoc with dissem f.g. ser and ser vns; lg qtz grns have some zoning but not as much as sm grns
- fl occurs with mo or as sm, high relief grns dissem within qtz; fl also occurs vnlts; anhedral to euhedral; 2 to 10 microns
- bt occurs as subhedral to euhedral grns; ser alt on bt rims and some centers; euhedral rtl inclusions in bt
- ca as matrix filling and as f.g. xcutting vnlts

Paragenesis

Matrix:

qtz→qtz+bt+rtl+/-fl→qtz+mo+fl→ser/ca

Macroscopic

Petrographic Section

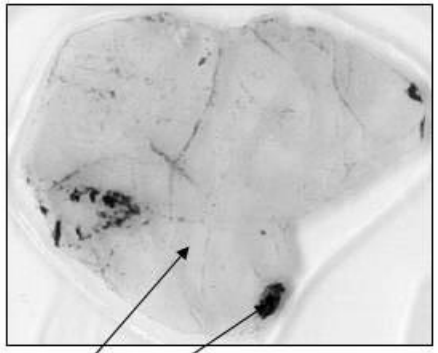

Microscopic

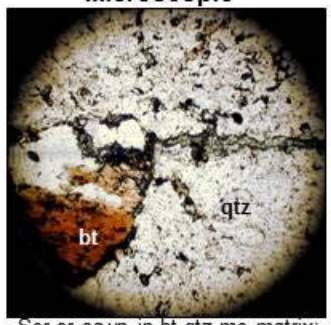

Ser or ca vn in bt-qtz-mo matrix; trans; pln; 10x and d.z.

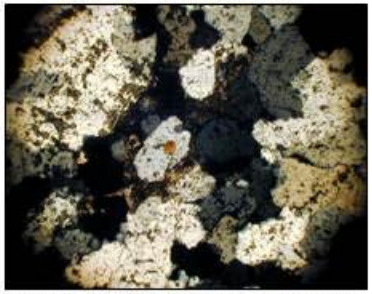

Qtz-bt-mo matrix; trans; xpol; 10x and d.z.

Rtl inclusions in bt; trans; pln; 10x and d.z.

Sample: AR-64
Facies: E
Phase: Matrix
Borehole: 22.0-14.0
Elevation: 7621'

Macroscopic
Blch Tan clasts with some dissem mo; qtz-bt-mo matrix and small qtz-mo vnlt; bt is crs grn; QSP.

Microscopic
• *Matrix:*
- qtz-bt-mo-fl-py-rtl-tpz
- very lg qtz grns 20 microns to 2000-2800 microns; some have serious zoning; subhedral to anhedral; inclusions of tpz in qtz
- tpz is abundant throughout matrix; occuring mostly adjacent to and in proximity to bt crystals; anhedral to euhedral; high relief; low birefringence; some relict tpz in matrix altered to ser; fl inclusions in tpz; 10 to 1000 microns in size
- anhedral to subhedral bt; 50 to 3000 microns in size; inclusion of euhedral qtz frn in bt; inclusions of rtl in bt (subhedral to euhedral); minor ser rims on bt
- mo occurring with bt and along bt grn boundaries; 2400 microns
- rtl and py dissem throughout; rtl-bt assoc; py in bt grn
- fl dissem throughout matrix; also fracture filling in lg qtz grns; also occurs as coarser euhedral to subhedral matrix filling

Macroscopic

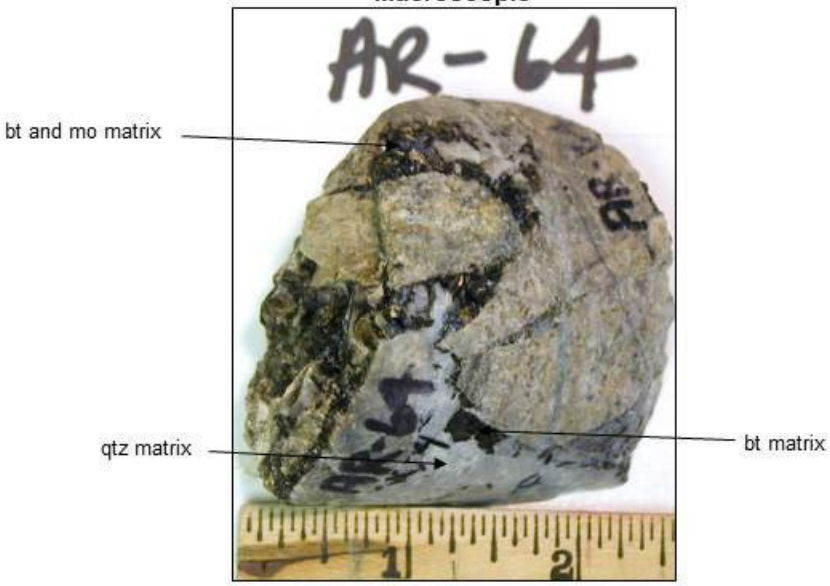

Microscopic

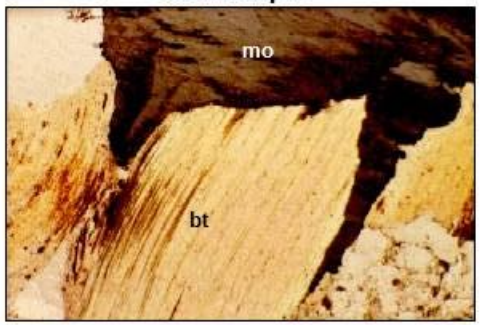

Mo filling bt grn boundaries in qtz-bt-mo matrix; trans and reflect; pln; 5x.

Sample: AR-64 cont'd

Matrix cont'd

- ➢ py is anhedral to euhedral; occurs with fl in some cases
- ➢ late stage ca vnlt xcuts matrix and clast
- ➢ bt, qtz, tpz, and fl growth from clast/matrix substrate

• *Clast:*

- ➢ qtz-bt-rtl-tpz-fl-ser-mo-py
- ➢ py as lg euhedral grns, 10-150 microns; some anhedral smaller grns
- ➢ fine grned qtz
- ➢ mo as subhedral blades; 550 microns; with tpz, rtl, and some bt
- ➢ rtl dissem throughout; 10-150 microns
- ➢ tpz-bt assoc
- ➢ bt mostly alt to ser, but some pristene bts remaining
- ➢ fl dissem throughout; some crser grns, but mostly f.g.
- ➢ lots of ser throughout; some tpz alt to ser
- ➢ no py-rtl assoc in this sample

Paragenesis

Matrix:

qtz+tpz+bt+rtl+fl+/-py→qtz+mo+fl+/-py→ser/ca

Clast:

qtz+bt+/-rtll+/-tpz→qtz+bt+fl+rtl+tpz→qtz+fl+mo+/-rtl+/-tpz→qtz+/-py+/-mo+/-fl→qtz+ser+py+/-fl→ca

Microscopic cont'd

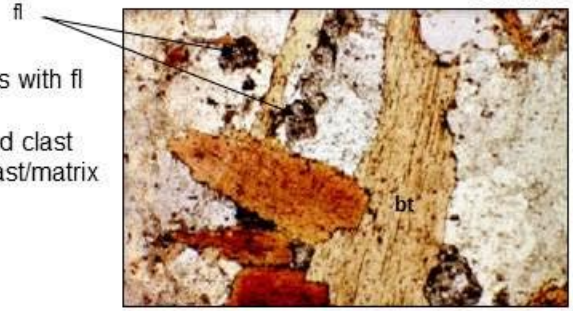

Bt-fl-tpz?-qtz matrix; trans; pln; 5x.

Same; pln; xpol; 5x.

Petrographic Section

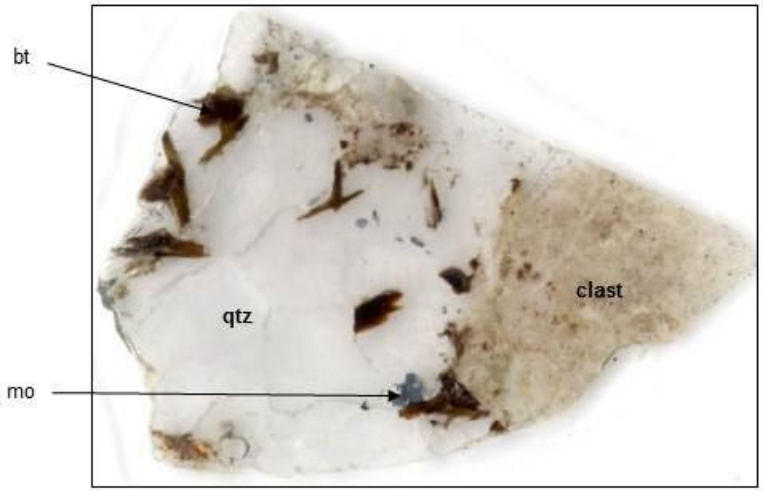

Sample: AR-3
Facies: E
Phase: Vein
Borehole: 21.7-15.5
Elevation: 7590'

Macroscopic

later qtz-mo vn

bt-ca matrix

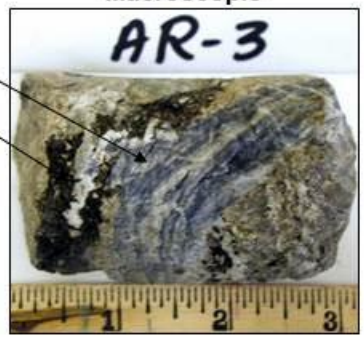

Macroscopic

Qtz-mo vnlt in Tan and xcutting some bt-qtz-ca matrix, some kspar flooding, QS(P), blched Tan, crs grned bt.

Microscopic

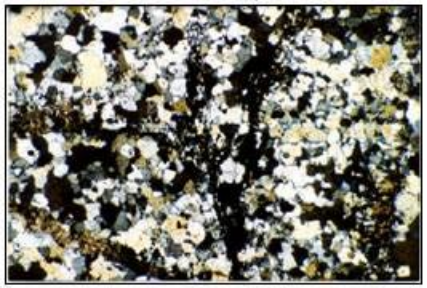

Qtz and mo in vn, and xcutting ca and/or ser vnlts; trans; xpol; 5x.

Microscopic

- *Vein:*
  - qtz-mo-ca-py
  - mo grns are euhedral blades and hexagons to anhedral
  - qtz is subhedral to anhedral; variable size; appears to have multiple generations; layers or bands in qtz subparallel to mo grns (see drawing); some structural distortion in qtz
  - some mo disseminated throughout vn rather than along boundary of varying qtz sizes, may be due to deformation or structural influence
  - some bt in vn; sm anhedral grns (may be from digestion of clast
  - fl dissem throughout; anhedral; 10-100 microns
  - py is euhedral to anhedral; very little py
  - minor ca occuring as open space filling in vn
  - ser or ca stringers xcut vn

- *Clast:*
  - bt-qtz-rtl-ser-kaol
  - bt is subhedral to anhedral

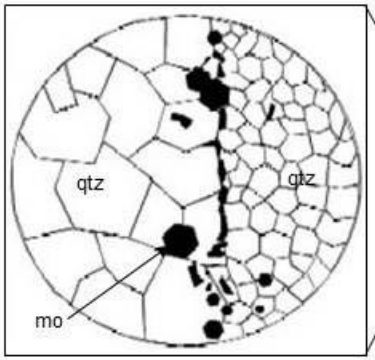

Mo relationship to qtz grn size distribution.

Petrographic Section

Paragenesis

Vein:
qtz+mo+fl→qtz+mo+fl+/-ca+/-py→ser/ca

Vein Envelope:
qtz+bt+rtl→qtz+ser→kaol

Sample: AR-138
Facies: E
Phase: Vein
Borehole: 21.7-15.5
Elevation: 7574'

Macroscopic

Possible qtz-mo vn; blch alt Tan; some bt+ and kspar+; dissem mo in clasts; py in vn.

Microscopic

- *Vein:*
  - qtz-mo-fl-ca-bt-tpz-tr kspar
  - mo typically occurring along vn/clast interface; crs grn; euhedral blades with a few euhedral hexagons to anhedral; mo assoc with med size qtz grns; mo-fl assoc; mo-bt-rtl assoc
  - py in vn
  - abundant rtl with py and mo; rtl is anhedral; py-rtl assoc
  - ca as open space filling
  - vn partially "digesting" clast; this is source of kspar, rtl, bt, tpz in vn
  - inclusions of rtl in bt

- *Clast:*
  - qtz-kspar-bt-ser-rtl-py-fl-tpz-mo
  - some tpz and kspar alt to ser
  - zircons in qtz and tpz
  - fl inclusions in tpz
  - mo assoc with bt, kspar, and rtl
  - lots of rtl, bt, qtz, and tpz; minor kspar

Macroscopic

Microscopic

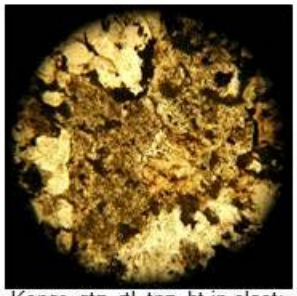

Kspar, qtz, rtl, tpz, bt in clast; trans; pln; 10x and d.z.

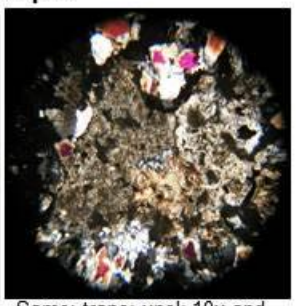

Same; trans; xpol; 10x and d.z.

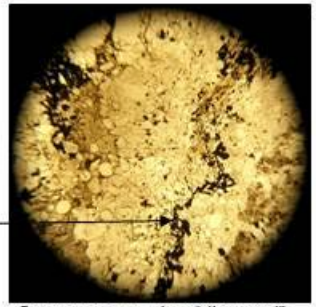

Qtz-mo-ca vn plus "digested" clast (kspar, bt, tpz); trans; pln; 10x and d.z.

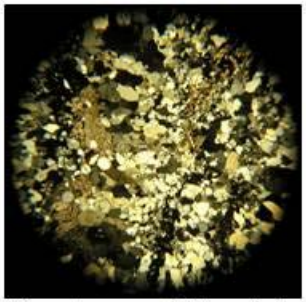

Same; trans; xpol; 10x and d.z.

Paragenesis

Vein:

qtz+mo+fl→qtz+ca+/-mo+/-fl

Vein Envelope:

qtz+tpz+zircon+fl+/-kspar+/-bt→qtz+kspar+/-bt+/-rtl+/-fl→qtz+bt+rtl+/-kspar+/-mo+/-fl→qtz+ser+py

Petrographic

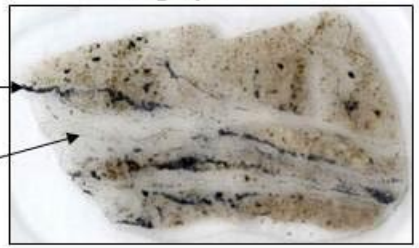

APPENDIX B – FLUID INCLUSION RAW DATA – MHBX

APPENDIX B and C ABBREVIATIONS

Abbreviation	Meaning
bt	biotite
cb	critical behavior
clath	clatherate
CO2d	CO2 disappearance
d	decripitation
decrep.	decripitation
hd	halite dissolution
hh	hydrohalite
hl	halite
hm	hematite
Incl.	inclusion
IND	indeterminate
l	liquid
ld	liquid disappearance
loc.	location
mo	molybdenite
op(s)	opaque(s)
ot(s)	other translucent daughter(s)
otd	other translucent daughter dissolution
P	primary
PS	pseudosecondary
rtl	rutile
S	secondary
s	solid
sylv	sylvite
Te	temperature of the eutectic
Th	temperature of homogenization
Tl-v	temperature of liquid/vapor homogenization
Tm	temperature of melting
v	vapor
vb	vapor bubble
vbd	vapor bubble disappearance

Sample Comments and Photographs	Sample	Facies	Inclusion	Paragenesis	Type	%L CO_2	%V CO_2	%L	%V	%S	Length in um	Width in um	Phase	Tm_{CO2}	Te	Tm_{hh}	Tm_{ice}	Tm_{clath}
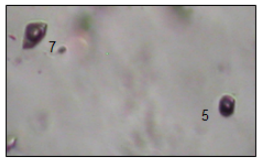	AR-173	SABQ	1	P	IIb.			0.75	0.1	0.15	6.25	9.38	l+v+s; l>v; s=hl, hm, op					
			2	PS	IIc.			0.75	0.15	0.1	6.25	6.25	l+v+s; l>v; s=hl, hm, op, ot					
			4	PS	Ic.			0.5	0.5		12.50	9.38	l+v; l>v				-16	
			5	IND	Ic.			0.5	0.5		6.25	3.13	l+v; l=v				-2	
			6	IND	Ic.			0.4	0.6		6.25	3.13	l+v+s; l>v; s=op				-1	
			6a	PS	IIb.			0.8	0.1	0.1	6.25	3.13	l+v+s; l>v; s=hl, hm					
			7	PS	Ic.			0.5	0.5		6.25	3.13	l+v; l>v				-3.5	
			10	PS	Ib.			0.8	0.2		6.25	12.50	l+v; l>v			-21		
			11	IND	Ic.			0.5	0.5		12.50	6.25	l+v; l>v			-21		
			12	IND	IIb.			0.8	0.1	0.1	6.25	3.13	l+v+s; l>v; s=hl, hm					
			13	PS	IIc.			0.75	0.15	0.15	6.25	6.25	l+v+s; l>v; s=hl, op, ot					
			14	PS	IIa.						3.13	1.56	l+v+s; l>v; s=hl					
AR-173 - Incl. 5, 7, and 13			17	PS	Ib.			0.95	0.05		6.25	15.63	l+v; l>v				-0.5	
			18	PS	IIb.			0.8	0.05	0.15	6.25	6.25	l+v+s; l>v; s=hl, op					
Evidence of boiling.			19	PS	IIa.			0.8	0.05	0.15	6.25	3.13	l+v+s; l>v, s=hl					
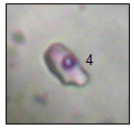	AR-97	SABQ	1	S	Ib.			0.9	0.1		9.38	3.13	l+v;l>v				-0.5	
			2	PS	IIc.			0.75	0.1	0.15	12.50	3.13	l+v+s; s=hm, op, hl, ot					
			3	IND	IIb.			0.88	0.05	0.07	6.25	6.25	l+v+s; s=hl, hm					
			4	S	Ib.			0.95	0.05		6.25	3.13	l+v; l>v				-0.7	
			7	IND	IIc.			0.8	0.1	0.1	6.25	9.38	l+v+s; l>v; s=hl, hm, ot					
			10	IND	Ic.			0.5	0.5		4.69	3.13	l+v; l=v				-1.8	
			11	IND	Ib.			0.8	0.2				l+v; l>v				-5.5	
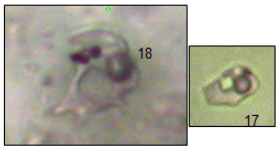			12	PS	IIc.			0.7	0.2	0.1	12.50	9.38	l+v+s; l>v; s=hl, ot, op					
			13	IND	Ic.			0.5	0.5		6.25	3.13	l+v; l=v				-1.5	
			14	IND	Ic.			0.5	0.5		6.25	3.13	l+v; l=v				-1.5	
			15	IND	IIc.			0.75	0.15	0.1			l+v+s; l>v; s=hl, ot					
			16	IND	IIc.			0.85	0.05	0.1	12.50	9.38	l+v+s; l>v;s=hl, ot, hm					
AR-97 - Incl. 4, 17, and 18			17	PS	IIb.			0.8	0.1	0.1	6.25	3.13	l+v+s; l>v; s=hl, op					
Evidence of boiling.			18	P	IIc.			0.7	0.1	0.2	12.50	12.50	l+v+s; s=hl, op, hm, ots					
	AR-105	A1	6	P	IIc.								l+v+s; l>v; s=hl, ops, ots					
			10	P	IIb.						13	13	l+v+s; l>v; s=hl, ops					
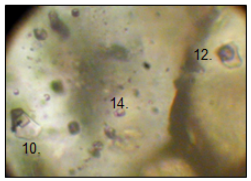			11	PS	IIa.						5	5	l+v+s; l>v; s=hl					
			12	IND	Ia.						9	9	l+v+s; l>v; s=ops		-24		-5.4	
			13	P	IIc.						13	13	l+v+s; l>v; s=hl, ops, ots					
			14	PS	IIa.						5	5	l+v+s; l>v; s=hl					
			15	P	Ic.								l+v; v>l					
			16	P	Ib.								l+v; l>v					
			17	P	Ic.								l+v; v>l					
			18	P	Ic.								l+v; v>l					
			19	P	IIa.								l+v+s; l>v; s=hl					
AR-105 - Inclusions 10, 12, 14			20	PS	IIb.								l+v+s; l>v; s=hl, op					
Solid inclusions of hl present; evidence of boiling.																		

Sample	Facies	Inclusion	Th_{CO2}	Ts_{sylv}	Ts_{ot1}	Ts_{ot2}	Ts_{hl}	Tl-v	Final Th	Final Th by vbd, ld cb, hd, CO2d, d, otd	% NaCl	% KCl	% $CaCl_2$	eq. wt. % NaCl+/- KCl+/-$CaCl_2$	KCl/NaCl	NaCl/CaCl2	comments
AR-173	SABQ	1					225	230	230	vbd	33.2			33.2			
		2					270	315	315	vbd	35.99			35.99			
		4						455	455	ld	19.51			19.51			
		5						375	375	ld	3.28			3.28			
		6						375	375	ld	1.65			1.65			
		6a					420	438	438	vbd	49.68			49.68			
		7						240	240	ld	5.62			5.62			
		10						380	380	vbd	23.35			23.35			
		11						335	335	ld	23.35			23.35			
		12					410	350	410	hd	48.54			48.54			
		13					360	375	375	vbd	43.35			43.35			
		14						230	230	vbd							
		17						235	235	vbd	0.83			0.83			
		18					450	450	450	vbd	53.26			53.26			
		19					400	240	400	hd	47.44			47.44			
AR-97	SABQ	1						234	234	vbd	0.83			0.83			
		2					220	359	359	vbd	32.92			32.92			
		3					408	375	408	hd	48.32			48.32			
		4						160	160	vbd	1.16			1.16			
		7					322				39.93			39.93			
		10						385	385	cb	2.96			2.96			
		11						306	306	vbd	8.51			8.51			
		12						252	252	vbd							Decrepitated at 385°C before Tshl.
		13						386	386	cb	2.47			2.47			
		14						385	385	cb	2.47			2.47			
		15					280	397	397	vbd	36.68			36.68			
		16					319	230	318.5	hd	39.64			39.64			
		17					340	353	353	vbd	41.49			41.49			
		18					438	394	438	hd	51.8			51.8			
AR-105	A1	6					366	400	400	vbd	43.93			43.93			
		10					402	374	402	hd	47.66			47.66			
		11					359			hd	43.25			43.25			Never saw vb disappear.
		12						360	359.8	vbd	8.38			8.38			No hh observed.
		13					413	374	413	hd	48.88			48.88			
		14					427	308	427	hd	50.49			50.49			
		15						386	386	cb							
		16						419	419	cb							
		17						443	443	ld							
		18						424	424	cb							
		19					404	334	404	hd	47.88			47.88			
		20					290	381	381	vbd	37.41			37.41			

Sample Comments and Photographs	Sample	Facies	Inclusion	Paragenesis	Type	%L CO_2	%V CO_2	%L	%V	%S	Length in um	Width in um	Phase	Tm_{CO2}	Te	Tm_{hh}	Tm_{ice}	Tm_{clath}
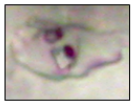 AR-112 - Incl. 12	AR-112	A1	1	IND	Ib.			0.85	0.15		6	9	l+v; l>v				0	
			2	IND	Ib.			0.95	0.05		25	13	l+v; l>v				10	
			3	IND	IIb.			0.7	0.1	0.2	5	5	l+v+s; l>v; s=hm, op, hl					
			4	IND	IIc.			0.65	0.15	0.2	6	3	l+v+s;l>v; s = ot, hl					
			5	IND	IIb.			0.75	0.05	0.2	6	6	l+v+s; l>v; s=hl, hm, op					
			6	PS	Ib.			0.9	0.1		9	3	l+v; l>v				-24	
			7	P	IIc.			0.78	0.1	0.12	9	9	l+v+s; l>v; s=hl, op, ots					
			9	IND	IIb.			0.8	0.1	0.1	13	6	l+v+s; l>v; s=hl, mo, op					
			11	IND	IIb.			0.85	0.07	0.08	6	5	l+v+s; l>v; s=hl, op					
			12	IND	IIb.			0.85	0.05	0.1	19	9	l+v+s; l>v; s=hl, hm, op					
			13	IND	Ib.			0.55	0.45		9	9	l+v; l>v				-10	
AR-112 - Inclusion 7			15	IND	Ib.			0.9	0.1		6	6	l+v; l>v		-18		-9.5	
 AR-106 - Inclusion 7	AR-106	A2	1	IND	IIc.			0.9	0.05	0.05	9	9	l+v+s; l>v; s=hl, ot					
			3	P	IIc.			0.85	0.05	0.1	13	6	l+v+s; l>v; s=hl, ot, hm					
			3a	IND	IIa.								l+v+s; l>v; s=hl					
			4	P	Ic.			0.45	0.55		11	11	l+v; v>l					
			6	IND	IIa.			0.5	0.25	0.25	16	16	l+v+s; l>v; s=hl					
			8	P	IIIa.			0.85	0.1	0.05	6.25	18.8	l+v+s; l>v; s=ops, hl, sylv		-42			
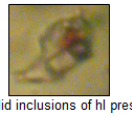 AR-106 - Inclusion 11			9	P	Ib.			0.75	0.25		34.38	34.4	l+v; l>v				-22	
			10	S	Ia.			0.85	0.05	0.1			l+v+s; l>v; s=ot					
			11	IND	IIc.			0.75	0.05	0.2	18.75	18.8	l+v+s; l>v; s=hm, hl, ots					
Solid inclusions of hl present; evidence of boiling.																		
Terrible polish; very hard to work with; evidence of boiling.	AR-118	A2	1	PS	IIc.			0.78	0.1	0.12	12.5	6.25	l+v+s; l>v; s=hl, ots					
			2	IND	Ib.			0.85	0.15		3.125	3.13	l+v; l>v				-3.2	
			4	IND	IIb.			0.7	0.15	0.15	6.25	3.13	l+v+s; l>v; s=hl, op					
			5	IND	IIc.			0.85	0.05	0.1			l+v+s; l>v; s=hl, hm, ots					
			6	IND	Ic.			0.65	0.45				l+v; v=l					
  AR-118 - Incl. 1 AR-118 - Incl. 6			7	IND	IIa.			0.7	0.15	0.15	6.25	3.13	l+v+s; l>v; s=hl					
			8	IND	IIa.			0.85	0.05	0.1	6.25	3.13	l+v+s; l>v; s=hl					
			9	PS	Ib.			0.85	0.15		6.25	6.25	l+v; l>v				0	
			10	PS	Ib.			0.95	0.05		3.125	3.13	l+v; l>v					
			11	PS	Ib.			0.9	0.1		16	16	l+v; l>v				0	
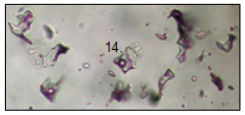			13	PS	Ib.			0.85	0.15		6.25	6.25	l+v; l>v				0	
			14	PS	Ib.			0.9	0.1		9	9	l+v; l>v				0	
			15	PS	Ib.			0.9	0.1		9	3.13	l+v; l>v				0	
AR-118 - Incl. 14																		
Solid inclusions of hl present; evidence of boiling.	AR-93	A3	1	IND	IIIa.			0.75	0.1	0.15	12.5	6.25	l+v+s; l>v; s=hl, hm, sylv, ot					
			2	IND	IIIa.			0.6	0.1	0.3	12.5	12.5	l+v+s; l>v; s=hl, sylv, ops, ot					
			3	IND	Ib.			0.55	0.45		9.375	6.25	l+v; l>v		-5		-3	
 			4	IND	Ib.			0.4	0.4	0.2	15.63	9.38	l+v+s; v>/=l; s=ot, hm					
			5	IND	Ib.			0.69	0.3		12.5	9.38	l+v; l>v					

Sample	Facies	Inclusion	Th_{CO2}	Ts_{sylv}	Ts_{ot1}	Ts_{ot2}	Ts_{hl}	Tl-v	Final Th	Final Th by vbd, ld cb, hd, CO2d, d, otd	% NaCl	% KCl	% $CaCl_2$	eq. wt. % NaCl+/-KCl+/-$CaCl_2$	KCl/NaCl	NaCl/CaCl2	comments
AR-112	A1	1						213	213	vbd	0			0			
		2						109	109	vbd	13.95			13.95			vb completed disappeared on freezing, snapped back at 10°C.
		3					375	189	375	hd	44.82			44.82			
		4					327	187	327	hd	40.35			40.35			
		5					383	192	383	hd	45.64			45.64			
		6						262	262	vbd							
		7					300	209	300	hd	38.16			38.16			Decrepitated at 281°C w/ hl almost gone, est. T of Ts hl is 300°C.
		9					175	193	193	vbd	30.7			30.7			
		11					204	150	204	hd	32.08			32.08			
		12					214	185	214	hd	32.6			32.6			
		13						475	475	ld	13.95			13.95			
		15						124	124	vbd	13.41			13.41			
AR-106	A2	1				180	245	218	245	hd	34.37			34.37			
		3					328	135	328	hd	40.44			40.44			
		3a					217	356	356	vbd	32.76			32.76			
		4						382	382	ld							
		6					315	472	472	d	39.35			39.35			Decrepitated at 472°C with quite a bit of vb left.
		8		66			291	254	291	hd	29	17		46	0.59		
		9						419	419	d							Decrepitated at 419°C w/ vb getting smaller.
		10						88	87.6	vbd							Daughters did not dissolve.
		11					350	231	350	hd	42.4			42.4			
AR-118	A2	1			295		376	278	376	hd	44.92			44.92			
		2						245	245	vbd	5.17			5.17			
		4					163	287	287	vbd	30.18			30.18			Not sure Ts hl is accurate.
		5					440		440	hd	52.04			52.04			No vb observed.
		6						465	465	cb							Estimate of final Th, could not see Tm ice.
		7					320	278	320	hd	39.76			39.76			
		8					272	290	290	vbd	36.12			36.12			
		9						218	218	vbd	0			0			
		10						173	173	vbd							
		11						230	230	vbd	0			0			
		13						280	280	vbd	0			0			
		14						219	219	vbd	0			0			
		15						224	224	vbd	0			0			
AR-93	A3	1		74			373	324	373	hd	37	16		53	0.47		
		2		63			359	225	359	hd	36	15		51	0.39		
		3						384	384	vbd	4.86			4.86			
		4							537	d							Decrepitated at 537°C; transluscent daughter did not dissolve completely.
		5						520	520	ld							Decrepitated at 520°C just before ld.

Sample Comments and Photographs	Sample	Facies	Inclusion	Paragenesis	Type	%L CO_2	%V CO_2	%L	%V	%S	Length in um	Width in um	Phase	Tm_{CO2}	Te	Tm_{hh}	Tm_{ice}	Tm_{clath}
AR-93 - Incl. 2 AR-93 - Incl. 4  AR-93 - Inclusions 8, 9, and 10  AR-93 - Incl. 12	AR-93	A3	6	PS	IIa.			0.68	0.3				l+v+s; l>v; s=hl					
			7	P	Ic.			0.5	0.5		9.375	6.25	l+v; l=v					
			8	S	Ib.			0.8	0.2		25	6.25	l+v; l>v				-0.1	
			9	S	Ib.			0.9	0.1		3.125	3.13	l+v; l>v				0	
			10	S	Ib.			0.9	0.1		9.375	9.38	l+v; l>v				-0.1	
			12	IND	IV.	0.075	0.075	0.85			18.75	9.38	$lH_2O+lCO_2+vCO_2$	-56.6			-0.1	4
			13	IND	IIc.			0.7	0.25	0.05	15.63	15.6	l+v+s; l>v; s=hl, op, ot					
			15	PS	IIc.			0.7	0.12	0.18	9.375	9.38	l+v+s; l>v; s=hl, ot					
Evidence of boiling. 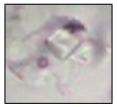 AR-91 - Inclusion 1 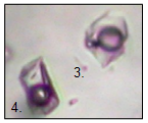 AR-91 - Inclusions 3 & 4	AR-91	A3	1	PS	IIc.			0.82	0.03	0.15	18.75	18.8	l+v+s; l>v; s=hl, hm, ot					
			3	IND	IIb.			0.75	0.2	0.05	9.375	6.25	l+v+s; l>v; s=hl, op					
			4	IND	Ia.			0.85	0.15		6.25	3.13	l+v+s; l>v; s=mo,bt, or rtl (op)				-16	
			5	IND	IIa.			0.8	0.15	0.05			l+v+s; l>v; s=hl					
			6	IND	Ib.			0.95	0.05		25	18.8	l+v; l>v				-3	
			7	IND	Ib.			0.85	0.15		6.25	6.25	l+v; l>v				-4	
			8	IND	IIa.			0.85	0.1	0.05	12.5	9.38	l+v+s; l>v; s=hl					
			9	PS	IIc.			0.85	0.1	0.05			l+v+s; l>v; s=hl, hm, ots					
			11	PS	IIc.			0.75	0.1	0.15	9.375	6.25	l+v+s; l>v; s=hl, ot, hm					
			12	IND	Ib.			0.75	0.25		12.5	9.38	l+v; l>v				-1.5	
			13	PS	Ia.			0.85	0.15	<0.01	6.25	6.25	l+v+s; l>v; s=op				-3	
			14	PS	IIb.			0.7	0.1	0.2	6.25	6.25	l+v+s; l>v; s=hl, hm					
			15	PS	IIc.			0.65	0.1	0.25	3.125	6.25	l+v+s; l>v; s=hl, op, poss ot					
			16	IND	IIa.			0.7	0.2	0.1	18.75	6.25	l+v+s; l>v; s=hl					
			17	IND	IIb.			0.85	0.1	0.05			l+v+s; l>v; s=hl, op, hm					
			18	IND	Ib.			0.85	0.15				l+v; l>v				-3.2	
Evidence of boiling. 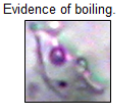 AR-13 - Incl. 8  AR-13 - Incl. 9  AR-13 - Incl. 12	AR-13	B	1	IND	Ib.			0.88	0.12		6.25	6.25	l+v; l>v				-5	
			2	IND	Ib.			0.7	0.3		6.25	3.13	l+v; l>v				-4.5	
			3	IND	Ib.			0.7	0.3		15.63	6.25	l+v; l>v		-46	-26	-19	
			4	IND	Ia.			0.87	0.1	0.03	9.375	6.25	l+v+s; l>v; s=ot		-50	-28	-22	
			6	P	IIb.			0.75	0.1	0.15	4.688	4.69	l+v+s; l>v; s=hl, op (mo, rtl or bt), hm					
			7	IND	Ia.			0.1	0.9	<0.01	6.25	3.13	l+v+s; l>v; s=op				-12	
			8	IND	Ia.			0.94	0.05	0.01	9.375	6.25	l+v+s; l>v; s=op				-18	
			9	IND	Ib.			0.55	0.45		6.25	3.13	l+v; l>v				-1.1	
			10	IND	IIc.			0.75	0.1	0.15	6.25	6.25	l+v+s; l>v; s=hm, hl, ot					
			12	IND	IIIa.			0.75	0.05	0.2	6.25	6.25	l+v+s; l>v; s=hl, sylv, op					
Evidence of boiling; No pictures available.	AR-169	B	1	PS	Ib.			0.8	0.2		7.813	6.25	l+v; l>v				-19	
			1a	PS	Ib.			0.8	0.2		12.5	6.25	l+v; l>v				-19	
			2	PS	IIb.			0.77	0.1	0.13	6.25	4.69	l+v+s; l>v; s=hl, mo or bt					
			3	S	Ib.			0.9	0.1		12.5	6.25	l+v; l>v				-1.3	
			4	PS	IIb.			0.73	0.12	0.15	12.5	12.5	l+v+s; s=hl, hm					
			5	IND	Ib.			0.55	0.45		12.5	9.38	l+v; l>v				-15	
			6	IND	Ib.			0.7	0.15	0.15	6.25	3.13	l+v; l>v				-1.5	
			7	PS	IIb.			0.75	0.12	0.13	6.25	3.13	l+v+s; l>v; s=hl, hm					
			8	S	Ib.			0.9	0.1		6.25	3.13	l+v; l>v				-2.5	

Sample	Facies	Inclusion	Th_{CO2}	Ts_{sylv}	Ts_{ot1}	Ts_{ot2}	Ts_{hl}	Tl-v	Final Th	Final Th by vbd, ld cb, hd, CO2d, d, otd	% NaCl	% KCl	% $CaCl_2$	eq. wt. % NaCl+/- KCl+/-$CaCl_2$	KCl/NaCl	NaCl/CaCl2	comments
AR-93	A3	6					357	475	475	d	43.06			43.06			Decrepitated at 475°C.
		7						386	386	vbd							
		8						253	253	vbd	0.17			0.17			
		9						171	171	vbd	0			0			
		10						252	252	vbd							
		12	30.6					260	260	d	0.17			0.17			Decrepitated at 260°C before final homogenization.
		13					246	475	475	d	34.43			34.43			Decrepitated at 475°C, bubble only shrunk slightly.
		15				370	388	297	388	hd	46.16			46.16			
AR-91	A3	1					420	81	420	hd	49.68			49.68			
		3					400	480	480	vbd	47.44			47.44			
		4						373	373	vbd	19.43			19.43			
		5					200	520	520	vbd	31.87			31.87			
		6						252	252	vbd	4.86			4.86			
		7						292	292	vbd	6.37			6.37			
		8					346	285	346	d	42.03			42.03			Decrepitated at 346°C before hl dissolution.
		9			157	203	365	327	365	d	43.83			43.83			Decrepitated at 365°C before hl dissolution.
		11			89		350	250	350	hd	42.4			42.4			
		12						385	385	vbd	2.47			2.47			
		13						266	266	vbd	4.86			4.86			
		14					448	278	278	hd	53.01			53.01			
		15					426	280	426	hd	50.37			50.37			
		16			135		209	479	479	vbd	32.33			32.33			
		17					170	390	390	vbd	30.48			30.48			
		18						232	232	vbd	5.17			5.17			
AR-13	B	1						308	308	vbd	7.82			7.82			
		2						389	389	cb	7.11			7.11			
		3						429	429	cb	21.66			21.66			
		4						351	351	vbd	6		19	25		0.41	
							530	260	530	hd							
		6									63.9			63.9			
		7						377	377	cb	15.96			15.96			
		8						195	195	vbd	20.65			20.65			
		9						371	371	vbd	2			2			
		10			434		532	313	532	hd	64.18			64.18			ot is most likely nahcolite ($NaHCO_3$).
		12					408	280	408	hd	48.32			48.32			no Ts for sylvite
AR-169	B	1						301	301	vbd	21.31			21.31			
		1a						322	322	vbd	21.66			21.66			
		2					430	286	430	hd	50.84			50.84			
		3						190	190	vbd	2.14			2.14			
		4					356	352	356	hd	42.96			42.96			
		5						382	382	cb	18.62			18.62			
		6						388	388	vbd	2.47			2.47			
		7					335	349	356	vbd	41.05			41.05			
		8						190	190	vbd	4.07			4.07			

Sample Comments and Photographs	Sample	Facies	Inclusion	Paragenesis	Type	%L CO_2	%V CO_2	%L	%V	%S	Length in um	Width in um	Phase	Tm_{CO2}	Te	Tm_{hh}	Tm_{ice}	Tm_{clath}
	AR-169	B	9	IND	IIIa.			0.75	0.1	0.15	18.75	12.5	l+v+s; l>v; s=hl, sylv, ot, op, hm					
			10	PS	IIc.			0.76	0.12	0.12	12.5	9.38	l+v+s; l>v; s=hl, ot, hm					
			11	S	IV.	0.075	0.025	0.9			7.813	12.5	$lCO_2+vCO_2+lH_2O$	unk			-2.5	6.5
Solid inclusions of hl present; evidence of boiling.	AR-8	C	1	P	IIb.						9.375	9.38	l+v+s; l>v; s=hl, op					
 AR-8 - Incl. 11			2	P	IIc.			0.6			6.25	6.25	l+v+s; l>v; s=hl, hm, ot, op					
			3	IND	Ia.			0.8	0.15	0.05			l+v+s, l>v; s=ot				-0.1	
			4	IND	Ib.			0.9	0.1		6.25	6.25	l+v+s; l>v		-24		-12	
			5	PS	IIb.			0.55	0.2	0.25	9.375	3.13	l+v+s; l>v; s=hl, op					
			6	IND	Ib.			0.87			18.75	18.8	l+v; l>v		-11		-1.3	
			7	P	IIa.							12.5	l+v+s; l>v; s=hl					
			8	P	IIc.			0.85	0.05	0.1	15.63	15.6	l+v+s; l>v; s=hl, ots, op					
			9	P	IIc.			0.78	0.12	0.1	9.375	9.38	l+v+s; v>v; s=hl, ot					
			11	P	IIIa.			0.5	0.1	0.4	15.63	15.6	l+v+s; l>v; s=hl, ops, sylv					
			12	P	IIIa.			0.8	0.15	0.05	6.25	6.25	l+v+s; l>v; s=hl, sylv, hm					
AR-8 - Incl. 12 and 16			13	P	IIc.			0.2	0.3	0.5	12.5	12.5	l+v+s; v>l; s=hl, op, ot					
			15	P	IIIa.						15.63	15.6	l+v+s; l>v; s= hl, sylv					
			16	P	Ic.						12.5	6.25	l+v; v>l					
			17	S	Ib.			0.9	0.1		6.25	6.25	l+v; l>v				-0.5	
			18	S	Ib.			0.95	0.05				l+v; l>v				-0.5	
			19	S	Ib.			0.95	0.05				l+v; l>v				-0.7	
AR-8 - Inclusions 17, 18, and 19			21	P	IIb.			0.5	0.25	0.25	6.25	6.25	l+v+s; l>v; s=hl, ops					
 AR-131 - Incl. 1	AR-131	C	1	S	IV.	0.15	0.1	0.75			9.375	6.25	$lCO_2+vCO_2+lH_2O$	-55.9			-5.5	8.5
			2	S	Ib.			0.9	0.1		2.083	3.13	l+v; l>v		-24		-2.2	
			3	IND	IIIa.			0.6	0.07	0.33			l+v+s; s=hl, sylv, op, hm					
 AR-131 - Incl. 3			4	IND	IIc.			0.78	0.05	0.07	12.5	12.5	l+v+s; l>v; s=hl, ots					
			5	IND	IIc.			0.85	0.08	0.08	6.25	6.25	l+v+s; l>v; s=hl, ot					
			6	IND	IIc.			0.77	0.1	0.13	12.5	3.13	l+v+s; l>v; s=hl, ot					
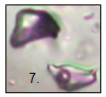 AR-131 - Incl. 7			7	IND	Ib.			0.85	0.15		9.375	3.13	l+v; l>v		-21		-13	
			8	IND	IIb.			0.7	0.05	0.25	6.25	3.13	l+v+s; l>v; s=hl, hm					
			9	PS	IIb.			0.68	0.1	0.22	12.5	6.25	l+v+s; l>v; s=hl, hm, op					
			10	IND	IIb.			0.85	0.05	0.1	6.25	6.25	l+v+s; l>v; s=hl, op					
			11	S	IV.	0.07	0.03	0.9			12.5	9.38	lCO2+vCO2+lH2O	-55.5			-4	9
			12	IND	IIIa.			0.7	0.1	0.2	10.8	15.6	l+v+s; l>v; s= hl, sylv, ot					
 AR-131 - Incl. 12			14	P	IIIa.			0.83	0.05	0.12	25	18.8	l+v+s; l>v; s=hl, ot, sylv					
			15	IND	IIIa.			0.83	0.05	0.12			l+v+s; l>v; s=hl, sylv, ot, op (mo)					
Solid inclusions of hl present; evidence of boiling.																		
 AR-6A - Inclusion 3	AR-6A	D	1	P	IIc.			0.55	0.2	0.25	18.75	9.38	l+v+s; l>v; s=hl, ot					
			3	IND	IIc.			0.82	0.03	0.15	15.63	6.25	l+v+s; l>v; s=hl, ot					
			6	IND	IIc.			0.7	0.15	0.15			l+v+s; l>v; s=hl, anhy?					
			7	S	Ib.			0.95	0.05				l+v; l>v				-0.4	
			8	IND	IIa.			0.85	0.1	0.05	6.25	6.25	l+v+s; l>v; s=hl					
			9		IIb.			0.7	0.1	0.2	6.25	6.25	l+v+s; l>v; s=hl, rtl, mo?, anhy?					
				IND														
			11	IND	Ib.			0.75	0.25		6.25	6.25	l+v; l>v				-5.6	

Sample	Facies	Inclusion	Th_{CO2}	Ts_{sylv}	Ts_{ot1}	Ts_{ot2}	Ts_{hl}	Tl-v	Final Th	Final Th by vbd, ld cb, hd, CO2d, d, otd	% NaCl	% KCl	% $CaCl_2$	eq. wt. % NaCl+/- KCl+/-$CaCl_2$	KCl/NaCl	NaCl/CaCl2	comments
AR-169	B	9			310		376	356	376	hd	44.92			44.92			
		10					260	415	415	vbd	35.32			35.32			
		11	31					188	188	CO2d	4.07			4.07			
AR-8	C	1					393	214	393	hd							
		2					378	180	378	hd	45.13			45.13			
		3						372	372	vbd	0.17			0.17			
		4						184	184	vbd	16.05			16.05			
		5					356	313	356	hd	42.96			42.96			
		6						358	358	vbd	2.14			2.14			
		7					247	302	302	vbd	34.49			34.49			
		8					357	168	357	hd	43.06			43.06			
		9					285	208	284.5	hd	37.01			37.01			
		11		92			470	305	470	hd	47	16		63	0.35		
		12		60			298	180	298	hd	31	14		45	0.49		
		13					387	345	386.5	hd	46.05			46.05			
		15		74			417	324	417	hd	40	14		54	0.37		
		16						360	360	ld							
		17						198	198.2	vbd	0.83			0.83			
		18						206	205.6	vbd	0.83			0.83			
		19						192	192	vbd	1.16			1.16			
		21					473	260	473	hd	56.17			56.17			
AR-131	C	1	22.9					130	130	d	8.51			8.51			Decrepitated at <130°C.
		2						241	241	vbd	3.6			3.6			
		3		94			457	218	457	hd	47	16		63	0.37		
		4			175		238	163	238	hd	33.95			33.95			
		5			105		270	206	270	hd	35.99			35.99			
		6					275	206	275	hd	36.33			36.33			
		7						288	288	vbd	17.25			17.25			
		8					470	218	470	hd	55.79			55.79			
		9					390	288	390	hd	46.37			46.37			
		10					280	189	280	hd	36.68			36.68			
		11	29.2					201	201	CO2d	6.37			6.37			
		12		75			258	226	258	hd	26	19		45	0.72		
		14			108		380	162	380	hd	45.33			45.33			
		15		89	432		286	180	432	otd	27	21		48	0.75		ot is most likely nahcolite ($NaHCO_3$).
AR-6A	D	1			414		390	331	414	otd	46.37			46.37			ot is most likely nahcolite ($NaHCO_3$).
		3					229	68	229	hd	33.42			33.42			
		6					250	280	280	vbd	34.68			34.68			
		7						186	186	vbd	0.66			0.66			
		8					224	386	386	vbd	33.14			33.14			
		9					300	365	364.5	vbd							
											38.16			38.16			
		11						388	388	vbd	8.65			8.65			

Sample Comments and Photographs	Sample	Facies	Inclusion	Paragenesis	Type	%L CO_2	%V CO_2	%L	%V	%S	Length in um	Width in um	Phase	Tm_{CO2}	Te	Tm_{hh}	Tm_{ice}	Tm_{clath}
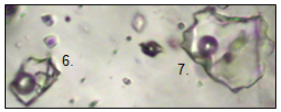 Evidence of boiling.	AR-6A	D	13	IND	Ia.			0.65	0.3	0.05	6.25	6.25	l+v+s; l>v; s=op				-6	
			14	IND	Ib.			0.5	0.5		9.375	3.13	l+v; l=v				-7	
			15	IND	IIb.			0.85	0.05	0.1	12.5	12.5	l+v+s; l>v; s=hl, op					
			16	IND	IIc.			0.8	0.12	0.08	12.5	12.5	l+v+s; l>v; s=hl, ot, op					
			17	IND	Ib.			0.6	0.4								-5.4	
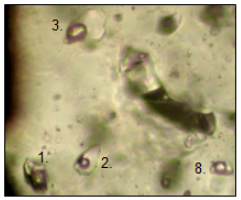 AR-78 - Inclusions 1, 2, 3, and 8 Possible solid inclusions of hl.	AR-78	D	1	IND	IIa.			0.65	0.25	0.1	12.5	12.5	l+v+s; l>v; s=hl					
			2	IND	Ia.			0.85	0.13	0.02	12.5	6.25	l+v+s; l>v; s=bt, mo, or rtl		37	-25	-24	
			3	P	Ib.			0.85	0.15		18.75	15.6	l+v; l>v			-24	-5.1	
			4	P	IIc.			0.7	0.1	0.2	18.75	9.38	l+v+s; l>v; s=hl, hm, ops, ot					
			5	IND	Ib.			0.8	0.2		18.75	15.6	l+v; l>v					
			6	P	IIb.			0.77	0.1	0.13	12.5	6.25	l+v+s; l>v; s=hl, op					
			7	IND	IIb.						6.25	6.25	l+v+s; l>v; s= hl, op					
			8	IND	Ia.			0.7	0.3				l+v+s; l>v; s= ot				-0.3	
			11	PS	IIb.			0.8	0.1	0.1	6.25	3.13	l+v+s; l>v; s= hl, op					
			13	IND	IIa.			0.9	0.05	0.05	6.25	6.25	l+v+s; l>v; s=hl					
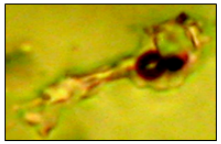 AR-5 - Inclusion 1 (not used in study) Evidence of boiling.	AR-5	E	2	P	IIc.			0.8	0.05	0.15	12.5	12.5	l+v+s; l>v; s=hl, op, ot					
			3	IND	Ia.			0.9	0.07	0.03	6.25	6.25	l+v+s; l>v; s= op		-31		-7.5	
			4	P	IIc.			0.8	0.05	0.15	15.63	15.6	l+v+s; l>v; s= hl, op, ot					
			5	IND	IIb.			0.85	0.05	0.1	18.75	18.8	l+v+s; l>v; s=hl, op					
			6	IND	IIa.			0.85	0.09	0.06	6.25	6.25	l+v+s; l>v; s=hl					
			6a	IND	Ic.			0.5	0.5		6.25	6.25	l+v; l=v					
			8	IND	IIb.			0.5	0.23	0.27			l+v+s; l>v; s=hl, op					
			9	IND	Ia.			0.8	0.18	0.02	6.25	6.25	l+v+s; l>v; s=ot				-23	
			10	IND	Ib.			0.85	0.15				l+v; l>v		21		-0.5	
			11	IND	Ib.			0.95	0.05				l+v; l>v		-37	-25	-24	
			12	IND	Ib.			0.6	0.4		12.5	12.5	l+v; l>v				-8	
			13	IND	IIb.			0.65	0.15	0.2	6.25	6.25	l+v+s; l>v; s=hl, ops					
			14	P	IIc.			0.75	0.15	0.1	9.375	6.25	l+v+s; l>v; s=hl, rtl, hm, ot					
			15	P	IIc.			0.85	0.05	0.1			l+v+s; l>v; s=hm, hl, op					
			17	IND	Ib.			0.9	0.1		6.25	6.25	l+v; l>v				-0.5	
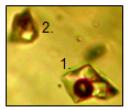 AR-64 - Incl. 1 & 2  AR-64 - Incl. 3  AR-64 - Incl. 10	AR-64	E	1	IND	IIc.			0.75	0.1	0.15	12.5	12.5	l+v+s; l>v; s=hl, ot					
			2	IND	IIa.			0.78	0.1	0.12	6.25	6.25	l+v+s; l>v; s=hl					
			3	IND	Ib.			0.85	0.15		12.5	6.25	l+v; l>v				0	
			5	IND	IIc.			0.5	0.15	0.35	6.25	4.69	l+v+s; l>v; s=hl, op, ot					
			6	IND	IIc.			0.7	0.1	0.2	12.5	12.5	l+v+s; l>v; s=hm, hl, ots					
			7	IND	Ib.			0.85	0.15		12.5	4.69	l+v; l>v		-36		0	
			8	IND	Ib.			0.7	0.3		18.75	4.69	l+v; l>v		-23	-23	-13	
			9	IND	IIc.			0.73	0.15	0.12	12.5	12.5	l+v+s; l>v; s=hl, op, ot					
			10	IND	IIc.			0.78	0.1	0.12	12.5	12.5	l+v+s; l>v; s=hm, hl, ot, op					
			12	IND	IIc.			0.75	0.1	0.15	9.375	9.38	l+v+s; l>v; s=hl, ots					

Sample	Facies	Inclusion	Th_{CO2}	Ts_{sylv}	Ts_{ot1}	Ts_{ot2}	Ts_{hl}	Tl-v	Final Th	Final Th by vbd, ld cb, hd, CO2d, d, otd	% NaCl	% KCl	% $CaCl_2$	eq. wt. % NaCl+/-KCl+/-$CaCl_2$	KCl/NaCl	NaCl/CaCl2	comments
AR-6A	D	13						410	410	vbd	9.19			9.19			
		14						390	390	cb	10.48			10.48			
		15					299	204	299	hd	38.09			38.09			
		16			400		201	298	400	otd	31.92			31.92			ot is most likely nahcolite ($NaHCO_3$).
		17						376	376	vbd	8.38			8.38			
AR-78	D	1					385	371	385	hd	45.85			45.85			
		2						383	383	vbd							
		3						467	466.5	vbd	7.96			7.96			
		4			290		370	220	370	hd	44.32			44.32			
		5						373	372.5	vbd							No change when frozen, did not see Tm ice.
		6					342	183	342	hd	41.67			41.67			
		7					407	183	407	hd	48.21			48.21			
		8						384	384	vbd	0.5			0.5			
		11					338	212	338	hd	41.31			41.31			
		13					190	300	300	vbd	31.39			31.39			
AR-5	E	2					403	120	403	hd	47.77			47.77			
		3						176	176	vbd	11.1			11.1			
		4					415	157	415	hd	49.11			49.11			
		5					286	117	286	hd	37.11			37.11			
		6					259	320	320	vbd	35.25			35.25			
		6a						485	485	ld							
		8					424	317	424	hd	50.14			50.14			
		9						488	488	vbd							
		10						290	290	vbd	0.83			0.83			
		11						220	220	vbd	12		13	25		0.79	
		12						408	408	cb	11.7			11.7			
		13					357	283	357	hd	43.06			43.06			
		14					403	297	402.5	hd	47.77			47.77			
		15					510	179	510	hd	61.12			61.12			
		17						252	252	vbd	0.83			0.83			
AR-64	E	1					346	343	346	hd	42.03			42.03			
		2					350	293	350	hd	42.4			42.4			
		3						240	240	vbd	0			0			
		5					370	310	370	hd	44.32			44.32			
		6					356	347	356	hd	42.96			42.96			
		7						239	239	vbd	0			0			
		8						490	490	vbd	16.89			16.89			
		9			186		220	348	348	vbd	32.92			32.92			
		10					365	340	365	hd	43.83			43.83			
		12					360	330	360	hd	43.35			43.35			

APPENDIX C – FLUID INCLUSION RAW DATA – VEINS

APPENDIX B and C ABBREVIATIONS

Abbreviation	Meaning
bt	biotite
cb	critical behavior
clath	clatherate
CO2d	CO2 disappearance
d	decripitation
decrep.	decripitation
hd	halite dissolution
hh	hydrohalite
hl	halite
hm	hematite
Incl.	inclusion
IND	indeterminate
l	liquid
ld	liquid disappearance
loc.	location
mo	molybdenite
op(s)	opaque(s)
ot(s)	other translucent daughter(s)
otd	other translucent daughter dissolution
P	primary
PS	pseudosecondary
rtl	rutile
S	secondary
s	solid
sylv	sylvite
Te	temperature of the eutectic
Th	temperature of homogenization
Tl-v	temperature of liquid/vapor homogenization
Tm	temperature of melting
v	vapor
vb	vapor bubble
vbd	vapor bubble disappearance

Sample Comments and Photographs	Sample	Facies Loc.	Incl.	Para-genesis	Type	%L	%V	%S	Length in um	Width in um	Phase	Te	Tm_{hh}	Tm_{ice}	Ts_{hl}	Tl-v	Final Th	Final Th by	eq. wt. % NaCl	comments
Evidence of boiling. 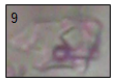 AR-174 - Incl. 9 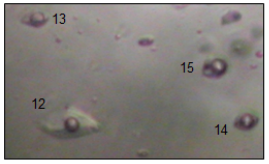 AR-174 - Incl. 12, 13, 14, and 15	AR-174	SA	1	IND	Ib.	0.9	0.1		6.25	3.13	l+v; l>v			-1.2		223	223	vbd	1.98	
			2	PS	IIa.	0.8	0.1	0.1	6.25	3.13	l+v+s; l>v; s=hl				285	173	285	hd	37.04	
			3	PS	IIb.	0.65	0.1	0.25	6.25	3.13	l+v+s; l>v; s=hl, hm, op				285	220	285	hd	37.04	
			4	PS	Ib.	0.9	0.1		9.38	9.38	l+v; l>v			-0.7		218	218	vbd	1.16	
			4a	PS	IIa.	0.8	0.1	0.2	6.25	6.25	l+v+s; l>v; s=hl				493	255	493	d	58.81	Decrepitated at 493°C before hl dissolved.
			5	P	Ic.	0.4	0.6				l+v; l>v					450	450	ld		
			6	PS	IIa.	0.8	0.1	0.1	18.75	9.38	l+v+s; l>v; s=hl				365	220	365	d	43.83	Decrepitated at 365°C before hl dissolved.
			7	PS	Ib.	0.9	0.1		9.38	3.13	l+v; l>v			-2		207	207	vbd	3.28	
			8	PS	Ib.	0.9	0.1		9.38	6.25	l+v; l>v			-1		216	216	vbd	1.65	
			9	PS	IIa.	0.85	0.05	0.1	6.25	12.50	l+v+s; l>v; s=hl				246	145	246	hd	34.43	
			10	PS	Ic.	0.5	0.5		6.25	3.13	l+v; l>v					400	400	ld		
			11	PS	Ib.	0.85	0.15		9.38	6.25	l+v; l>v			-3		290	290	vbd	4.86	
			12	PS	Ia.	0.9	0.1	<0.01	9.38	6.25	l+v+s; l>v; s=op			-0.2		237	237	vbd	0.33	
			13	PS	Ic.	0.5	0.5		4.69	4.69	l+v; l=v			-0.2		350	350	ld	0.33	
			14	PS	Ic.	0.4	0.6		3.13	4.69	l+v+s; l>v; s=op			-0.2		430	430	ld	0.33	
			15	PS	Ic.	0.4	0.6		6.25	6.25	l+v+s; l>v; s=op			-0.2		400	400	ld	0.33	
			16	PS	Ib.	0.85	0.15		6.25	9.38	l+v; l>v			-0.1		230	230	vbd	0.17	
Evidence of boiling. 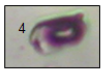 AR-102 - Incl. 4 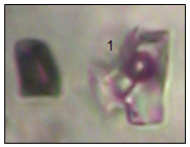 AR-102 - Incl. 1 (l+v+hl coexisting with v-rich)	AR-102	A1	1	P	IIa.	0.8	0.1	0.1	9.38	9.38	l+v+s; l>v; s=hl				255	310	310	vbd	35	
			2	IND	Ib.	0.6	0.4		6.25	3.13	l+v; l>v					470	470	vbd		
			4	IND	Ic.	0.4	0.6		6.25	4.69	l+v; l>v					390	390	ld		
			5	IND	IIb.	0.85	0.05	0.15	6.25	6.25	l+v+s; l>v; s=hl, hm				368	188	368	hd	44.12	
			7	PS	IIb.	0.8	0.1	0.1			l+v+s; l>v; s=hl, op				282	340	340	vbd	36.83	
			8	IND	IIa.	0.88	0.05	0.07			l+v+s; l>v; s=hl				314	164	314	hd	39.27	
			9	IND	IIa.	0.86	0.07	0.07	6.25	6.25	l+v+s; l>v; s=hl					175	175	vbd		
			10	PS	IIb.	0.8	0.1	0.1	6.25	6.25	l+v+s; l>v; s=hl, ot				280	178	280	hd	36.68	
			11	IND	IIb.	0.7	0.15	0.15	6.25	6.25	l+v+s; l>v; s=hl, hm				380	460	460	vbd	45.33	
			12	IND	Ib.	0.9	0.1		6.25	3.13	l+v; l>v			-6.3		220	220	vbd	9.58	
			13	IND	IIa.	0.6	0.2	0.2	6.25	3.13	l+v+s; l>v; s=hl					270	270	vbd		
			14	IND	IIa.	0.65	0.15	0.2	6.25	3.13	l+v+s; l>v; s=hl				395	178	395	hd	46.9	
			15	IND	IIc.	0.85	0.05	0.1	9.38	9.38	l+v+s; l>v; s=hl, ot, hm, op				290	115	290	d		
			16	IND	Ib.	0.85	0.15		9.38	3.13	l+v; l>v			-3.7			200	vbd	5.93	
			17	IND	IIc.	0.55	0.15	0.3	4.69	1.56	l+v+s; l>v; s=hl, op, hm, ot				400	220	400	hd	47.44	
Evidence of boiling.  AR-115 - Incl. 1  AR-115 - Incl. 10	AR-115	A1	1	PS	Ic	0.5	0.5		9.38	6.25	l+v; l>v			-6		475	475	ld	9.19	
			2	PS	Ib.	0.8	0.2		6.25	6.25	l+v; l>v			-3.2		210	210	vbd	5.17	
			2b	PS	Ic	0.5	0.5		7.81	4.69	l+v; l>v			-18		420	420	ld	20.95	
			3	S	Ib.	0.9	0.1		3.13	1.56	l+v; l>v			-3.2		193	193	vbd	5.17	
			4	PS	IIc.	0.75	0.1	0.15	9.38	9.38	l+v+s; l>v; s=hl, ot, op				360	315	360	hd	43.35	
			5	PS	IIc.	0.7	0.15	0.15	3.13	3.13	l+v+s; l>v; s=hl, ot				435	330	435	hd	51.44	
			6	PS	IIc.	0.75	0.1	0.15	6.25	3.13	l+v+s; l>v; s=hl, ot				300	560	560	vbd	38.16	
			7	PS	IIc.	0.8	0.07	0.13	6.25	6.25	l+v+s; l>v; s=hl, ot				350	250	350	hd	42.4	
			8	PS	Ib.	0.75	0.25		7.81	6.25	l+v; l>v			-2		420	420	d	3.28	Decrepitated at 420°C.
			9	PS	Ic	0.4	0.6		4.69	4.69	l+v; l>v			-1		418	418	ld	1.65	
			10	PS	Ic	0.5	0.5		6.25	3.13	l+v; l>v			-8		420	420	ld	11.7	
Evidence of boiling.	AR-110	A2	1	PS	Ia.	0.8	0.2	<0.01	3.13	3.13	l+v+s; l>v; s=op			-4		296	296	vbd	6.37	
			2	PS	Ic.	0.4	0.6		6.25	6.25	l+v; l>v			-6		290	290	ld	9.19	

Sample Comments and Photographs	Sample	Facies Loc.	Incl.	Para-genesis	Type	%L	%V	%S	Length in um	Width in um	Phase	Te	Tm_{hh}	Tm_{ice}	Ts_{hl}	Tl-v	Final Th	Final Th by	eq. wt. % NaCl	comments
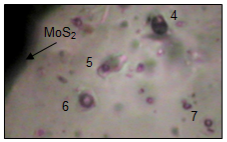 AR-110 - Incl. 4, 5, 6, and 7 and molybdenite grain	AR-110	A2	3	PS	Ic.	0.4	0.6	<0.01	4.69	4.69	l+v+s; l>v; s=op					395	395	ld		
			3a	PS	Ia.	0.6	0.4	<0.01	4.69	3.13	l+v+s; l>v; s=op					460	460	vbd		
			4	PS	Ic.	0.5	0.5	<0.01	6.25	6.25	l+v+s; l>v; s=op		-18			520	520	ld	23.66	
			5	PS	IIa.	0.78	0.1	0.12	6.25	3.13	l+v+s; l>v; s=hl				430	210	430	hd	50.84	
			6	PS	Ib.	0.6	0.4		4.69	6.25	l+v; l>v					540	540	vbd		
			7	PS	Ia.	0.87	0.1	0.03	3.13	3.13	l+v+s; l>v; s=op					348	348	vbd		
			8	PS	Ic.	0.4	0.6		4.69	3.13	l+v; l>v					450	450	ld		
			9	PS	Ic.	0.5	0.5		6.25	6.25	l+v; l>v			-4		380	380	ld	6.37	
			10	PS	Ib.	0.7	0.3		6.25	3.13	l+v; l>v			-0.5		328	328	vbd	0.83	
			11	PS	Ia.	0.85	0.15	<0.01	9.38	1.56	l+v+s; l>v; s=op			-6		358	358	vbd	9.19	
Evidence of boiling.  AR-119 - Incl. 1 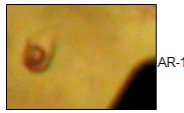 AR-119 - Incl. 5	AR-119	A2	1	PS	Ic.	0.5	0.5		6.25	3.13	l+v; l>v			-3.5		387	387	ld	5.62	
			2	IND	Ib.	0.8	0.2		6.25	3.13	l+v; l>v			-3		332	332	vbd	4.86	
			3	PS	Ia.	0.85	0.1	0.05	9.38	6.25	l+v+s; l>v; s=op			-2.5		266	266	vbd	4.07	
			4	PS	Ic.	0.5	0.5		12.50	12.50	l+v; l>v			-2		390	390	ld	3.28	
			5	PS	Ia.	0.8	0.2	<0.01	4.69	3.13	l+v+s; l>v; s=op			-4.7		342	342	vbd	7.39	
			6	PS	Ib.	0.85	0.15		6.25	6.25	l+v; l>v			-1		291	291	vbd	1.65	
			9	PS	IIb.	0.8	0.1	0.1	6.25	6.25	l+v+s; l>v; s=hl, op				135	320	320	vbd	29.1	
			11	PS	Ia.	0.9	0.1	<0.01	4.69	4.69	l+v+s; l>v; s=op			-1		200	200	vbd	1.65	
			12	IND	Ic.	0.4	0.6		6.25	3.13	l+v; l>v			-2.5		350	350	ld	4.07	
			13	IND	Ic.	0.5	0.5	<0.01	9.38	3.13	l+v+s; l>v; s=op					400	400	ld		
			14	PS	Ib.	0.8	0.2		12.50	4.69	l+v; l>v			-1.7		287	287	vbd	2.79	
			15	IND	Ib.	0.9	0.1		9.38	3.13	l+v; l>v			-3.5		245	245	vbd	5.62	
			16	IND	Ib.	0.75	0.25		4.69	1.56	l+v; l>v			-2		270	270	vbd	3.28	
Evidence of boiling. 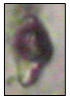 AR-14 - Incl. 3  AR 14 - Incl. 11	AR-14	A3	1	PS	IIb.	0.75	0.05	0.2	6.25	6.25	l+v+s; l>v; s=hl, op, hm				423	285	423	hd	50.03	
			2	PS	IIa.	0.7	0.15	0.15	6.25	6.25	l+v+s; l>v; s=hl				425	397	425	hd	50.26	
			3	PS	Ic.	0.5	0.5		6.25	12.50	l+v; l>v		-22	-12		560	560	cb	16.05	
			4	PS	Ic.	0.5	0.5		12.50	18.75	l+v; l>v					380	380	cb		
			6	PS	Ib.	0.85	0.15		6.25	3.13	l+v; l>v			-12		278	278	vbd	15.96	
			7	PS	Ic.	0.5	0.5		9.38	9.38	l+v;l>v					395	395	ld		
			8	PS	Ic.	0.45	0.55				l+v; v>l					408	408	ld		
			10	IND	IIc.	0.7	0.1	0.2	9.38	9.38	l+v+s; l>v; s=op, hl, hm, ot				432	300	432	hd	51.08	
			11	P	IIc.	0.7	0.12	0.18			l+v+s; l>v; s=hl, hm, ot				390	380	390	hd	46.37	
			12	PS	Ic.	0.5	0.5		18.75	12.50	l+v; l>v					475	475	cb		
			13	P	IIc.	0.85	0.05	0.1	9.38	9.38	l+v+s; l>v; s=hl, op, hm, ot				375	152	375	hd	44.82	
			14	PS	Ic.	0.5	0.5		6.25	3.13	l+v; l=v					480	480	ld		
			15	PS	Ic.	0.5	0.5				l+v; l=v			-6		520	520	ld	9.19	
			15a	PS	Ic.	0.5	0.5		9.38	3.13	l+v; l=v			-2		390	390	ld	3.28	
			16	PS	IIb.	0.4	0.1	0.5	12.50	3.13	l+v+s; l>v; s=hl, hm				520	365	520	hd	62.5	
			17	PS	IIa.	0.7	0.1	0.2	3.13	3.13	l+v+s; l>v; s=hl					253	253	vbd		
Evidence of boiling. 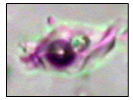 AR-90 - Incl. 4	AR-90	A3	1	PS	Ib.	0.9	0.1		6.25	3.13	l+v; l>v			-2		237	237	vbd	3.28	
			2	PS	IIa.	0.9	0.05	0.05	9.38	9.38	l+v+s; l>v; s=hl				364	343	364	hd	43.73	
			3	P	Ic.	0.5	0.5	<0.01	6.25	3.13	l+v+s; l>v; s=op			-4		380	380	ld	6.37	
			4	PS	IIa.	0.75	0.15	0.1	18.75	12.50	l+v+s; l>v; s=hl				364	375	375	vbd	43.73	
			5	PS	Ib.	0.85	0.15		18.75	28.13	l+v; l>v					385	385	vbd		
			6	PS	IIa.	0.9	0.05	0.05	9.38	9.38	l+v+s; l>v; s=hl				246	260	260	vbd	34.43	
			7	PS	IIa.	0.9	0.05	0.05	9.38	9.38	l+v+s; l>v; s=hl				350	400	400	vbd	42.4	
			8	PS	Ic.	0.5	0.5		6.25	6.25	l+v; l=v			-4		393	393	ld	6.37	
			9	P	IIb.	0.7	0.1	0.2	6.25	3.13	l+v+s; l>v; s=hl, hm				485	235	485	hd	57.75	

Sample Comments and Photographs	Sample	Facies Loc.	Incl.	Para-genesis	Type	%L	%V	%S	Length in um	Width in um	Phase	Te	Tm_{hh}	Tm_{ice}	Ts_{hl}	Tl-v	Final Th	Final Th by	eq. wt. % NaCl	comments
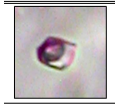 AR-90 - Incl. 8	AR-90	A3	10	PS	Ic.	0.4	0.6	<0.01	3.13	3.13	l+v+s; l>v; s=op					405	405	ld		
			11	PS	IIb.	0.75	0.05	0.2	3.13	3.13	l+v+s; l>v; s=hm, hl, op				400	200	400	hd	47.44	
			12	PS	Ia.	0.8	0.19	0.01	3.13	3.13	l+v+s; l>v; s=op					300	300	vbd		
			13	PS	Ic.	0.5	0.5	<0.01	6.25	4.69	l+v+s; l>v; s=op					420	420	ld		
Evidence of boiling.  AR-147 - Incl. 3 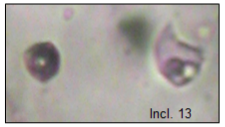 Incl. 13 (l+v+hl coexisting with v-rich)	AR-147	B	1	P	IIb.	0.85	0.03	0.12	9.38	9.38	l+v+s; l>v; s=hl, hm, op				320	62	320	hd	39.76	
			2	PS	Ia.	0.88	0.1	0.02	6.25	3.13	l+v; l>v; s=hm		-9			520	520	vbd	24.8	
			3	PS	Ia.	0.8	0.2	<0.01	9.38	6.25	l+v+s; l>v; s=hm		-9.5			415	415	vbd	24.73	
			4	IND	IIb.	0.7	0.15	0.15	6.25	3.13	l+v+s; l>v; s=hl, op				285	285	285	vbd	37.04	
			5	PS	IIb.	0.7	0.15	0.15	3.13	3.13	l+v+s; l>v; s=hl, hm				270	275	275	vbd	35.99	
			6	P	IIc.	0.8	0.1	0.1	9.38	9.38	l+v+s; l>v; s=hl, hm, ot					354	354	vbd		
			7	PS	IIb.	0.7	0.15	0.15			l+v+s; l>v; s=hl, hm				225	354	354	vbd	33.2	
			8	IND	IIb.	0.8	0.2	<0.01	12.50	9.38	l+v+s; l>v; s=hl, hm		-13					vbd	24.32	
			9	IND	IIb.	0.8	0.1	0.1	6.25	3.13	l+v+s; l>v; s=hl, hm				400	228	400	hd	47.44	
			10	IND	IIb.	0.8	0.1	0.1	9.38	3.13	l+v+s; l>v; s=hl, hm				270	300	300	vbd	35.99	
			11	PS	Ic.	0.45	0.55		6.25	6.25	l+v; l<v		-11			530	530	ld	24.52	
			12	PS	Ic.	0.5	0.5		6.25	3.13	l+v; l=v			-6				ld	9.19	
			13	P	IIc.	0.6	0.1	0.1	6.25	6.25	l+v+s; l>v; s=hl, ot				320	249	320	hd	39.76	
Evidence of boiling. 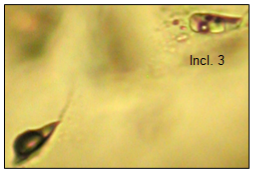 Incl. 3 (l+v+hl coexisting with v-rich)	AR-167	B	1	P	IIb.	0.7	0.1	0.2	6.25	6.25	l+v+s; l>v; s=hl, hm				448	220	448	hd	53.01	
			3	P	IIb.	0.7	0.1	0.2	6.25	12.50	l+v+s; l>v; s=hl, op, hm				290	215	290	d	37.41	Decrep. at 290°C with large hl remaining.
			4	P	IIb.	0.7	0.1	0.2	6.25	9.38	l+v+s; l>v; s=hl, op, hm				403	227	403	hd	47.77	
			5	S	Ib.	0.9	0.1		6.25	3.13	l+v; l>v			-0.4		183	183	vbd	0.66	
			6	S	Ib.	0.9	0.1		6.25	3.13	l+v; l>v			-0.4		193	193	vbd	0.66	
			7	P	IIb.	0.75	0.05	0.15	9.38	12.50	l+v+s; l>v; s=op, hl				390	225	390	hd	46.37	
			8	S	Ib.	0.9	0.1		12.50	6.25	l+v; l>v			-0.4		190	190	vbd	0.66	
			10	P	IIc.	0.8	0.05	0.15	6.25	6.25	l+v+s; l>v; s=hl, op, ot, hm				345		345		41.94	
			11	PS	Ia.	0.9	0.05	0.05	6.25	9.38	l+v+s; l>v; s=ot					184	184	vbd		
			12	PS	Ib.	0.8	0.2		3.13	6.25	l+v; l>v					359	359	vbd		
			13	P	Ic.	0.5	0.5		6.25	6.25	l+v; l>v			-0.3		409	409	ld	0.5	
Evidence of boiling. No pictures available.	AR-11	C	1	S	Ib.	0.95	0.05		6.00	6.00	l+v; l>v			-0.6		197	197	vbd	0.99	
			2	PS	Ib.	0.6	0.4		3.00	3.00	l+v; l>v			-5.5		379	379	vbd	8.51	
			3	S	Ib.	0.9	0.1		3.00	3.00	l+v; l>v			-0.4		199	199	vbd	0.66	
			4	PS	Ic.	0.5	0.5				l+v; l>v					387	387	cb		
			5	PS	Ic.	0.5	0.5				l+v; v>l			-2		380	380	cb	3.28	
			6	PS	Ic.	0.5	0.5				l+v; l>v					358	358	cb		
			8	P	Ib.	0.85	0.15				l+v; l>v			-4		392	392	vbd	6.37	
			9	PS	Ia.	0.55	0.45	<0.01			l+v+s; l>v; s=op					351	351	vbd		
			10	PS	Ib.	0.55	0.45				l+v; l>v	-47		-4.5		359	359	vbd	7.11	
			11	S	Ib.	0.8	0.2				l+v; l>v					227	227	vbd		
Evidence of boiling. 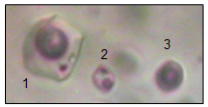 (l+v+hl coexisting with v-rich)	AR-81	C	1	PS	IIb.	0.78	0.2	0.02	9.38	9.38	l+v+s; l>v; s=hm, hl				335	445	445	vbd	41.05	
			2	PS	IIb.	0.8	0.1	0.1	3.13	3.13	l+v+s; l>v; s=hl, hm				400	215	400	hd	47.44	
			3	PS	Ic.	0.5	0.5		4.69	4.69	l+v: l>v			-5		412	412	cb	7.82	
			4	PS	Ic.	0.5	0.5		4.69	6.25	l+v; l>v			-1.6		403	403	ld	2.63	
			5	PS	Ib.	0.75	0.25		3.13	6.25	l+v; l>v		-21			387	387	vbd	23.35	
			6	PS	Ib.	0.9	0.1		3.13	3.13	l+v; l>v			-4.5		186	186	vbd	7.11	
			7	PS	IIb.	0.75	0.1	0.15	7.81	7.81	l+v+s; l>v; s=hm, hl, op				429	234	429	hd	50.73	
			8	PS	Ic.	0.5	0.5		4.69	3.13	l+v+s; l>v; s=op (mo)			-2		446	446	ld	3.28	

Sample Comments and Photographs	Sample	Facies Loc.	Incl.	Para-genesis	Type	%L	%V	%S	Length in um	Width in um	Phase	Te	Tm_{hh}	Tm_{ice}	Ts_{hl}	Tl-v	Final Th	Final Th by	eq. wt. % NaCl	comments
 AR-81 - Incl. 7	AR-81	C	9	PS	Ic.	0.5	0.5		6.25	7.81	l+v; l>v			-1.5		395	395	ld	2.47	
			10	PS	Ic.	0.4	0.6		7.81	7.81	l+v; l>v					420	420	ld		
			11	PS	Ib.	0.85	0.15		6.25	18.75	l+v; l>v		-19			310	310	vbd	23.55	
			12	PS	IIb.	0.75	0.1	0.15	7.81	7.81	l+v+s; l>v; s= hl, hm				423	198	423	hd	50.03	
			13	PS	IIb.	0.85	0.05	0.1	6.25	6.25	l+v+s; l>v; s=hl, op				410	247	410	hd	48.54	
Evidence of boiling. 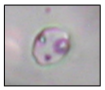 AR-143 - Incl. 11	AR-143	D	2	PS	Ia.	0.75	0.25	<0.01	6.25	3.13	l+v+s; l>v; s=op			-5		255	255	vbd	7.82	
			3	PS	IIa.	0.85	0.05	0.1	6.25	6.25	l+v+s; l>v; s=hl				311	182	311	d	39.03	Decrepitated at 311°C before hl dissolved.
			4	PS	Ib.	0.6	0.4		6.25	3.13	l+v; l>v			-8		367	367	vbd	11.7	
			5	PS	Ib.	0.75	0.25		3.13	1.56	l+v; l>v			-5		230	230	vbd	7.82	
			7	PS	IIb.	0.75	0.1	0.15	12.50	6.25	l+v+s; l>v; s=hl, op				360	200	360	hd	43.35	
			8	PS	IIb.	0.8	0.15	0.05	9.38	12.50	l+v+s; l>v; s=hl, op, hm					376	376	vbd		
			9	P	Ic.	0.5	0.5				l+v; l>v			-8		417	417	cb	11.7	
			10	PS	Ic.	0.5	0.5		6.25	3.13	l+v; l=v			-7		427	427	ld	10.48	
			11	PS	IIb.	0.85	0.1	0.05	6.25	6.25	l+v+s; l>v; s=hl, op				410	327	410	hd	48.54	
			12	PS	Ia.	0.85	0.1	0.05	6.25	6.25	l+v+s; l>v; s=op		-21			247	247	vbd	23.35	
			13	PS	IIb.	0.7	0.01	0.29			l+v+s; l>v; s=hl, hm				375		375	hd	44.82	
			14	PS	IIb.	0.8	0.05	0.15	6.25	6.25	l+v+s; l>v; s=hl, op, hm				397		397	hd	47.12	
			15	PS	IIb.	0.82	0.03	0.15			l+v+s; l>v; s=hl, hm				373		373	hd	44.62	
			16	PS	Ic.	0.5	0.5		3.13	3.13	l+v; l>v			-1.5		400	400	ld	2.47	
			17	PS	Ia.	0.9	0.05	0.05			l+v+s; l>v; s=op or hm			-0.5		320	320	vbd	0.83	
Evidence of boiling. 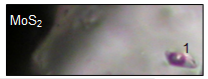  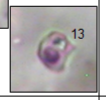	AR-146	D	1	P	Ic.	0.5	0.5		7.81	3.13	l+v; l>v		-21	-4		357	357	ld	6.37	
			2	PS	IIb.	0.75	0.05	0.25	6.25	6.25	l+v+s; l>v; s=hl, hm, op				451	225	451	hd	53.38	
			3	P	Ic.	0.5	0.5		4.69	1.56	l+v; l>v		-15	-8		464	464	ld	11.7	
			4	PS	IIb.	0.75	0.05	0.2	7.81	7.81	l+v+s; l>v; s=hl, ops				280	102	280	hd	36.68	
			5	PS	Ic.	0.5	0.5		6.25	4.69	l+v; l>v			-0.4		510	510	ld	0.66	
			6	PS	IIb.	0.75	0.05	0.2	3.13	3.13	l+v+s; l>v; s=hl, hm, op				422	122	422	hd	49.91	
			8	PS	Ic.	0.5	0.5		6.25	6.25	l+v+s; l>v; s=op			-4		378	378	ld	6.37	
			9	PS	Ic.	0.5	0.5		6.25	9.38	l+v; l>v			-3.5		405	405	ld	5.62	
			10	PS	IIb.	0.75	0.05	0.2	7.81	7.81	l+v+s; l>v; s=hl, op				373	70	373	hd	44.62	
			11	PS	IIb.	0.65	0.1	0.25	3.13	3.13	l+v+s; l>v; s=hl, op				380	213	380	hd	45.33	
			12	PS	IIa.	0.85	0.1	0.05	7.81	3.13	l+v+s; l>v; s=hl				280	280	280	vbd	36.68	
			13	PS	IIb.	0.7	0.15	0.15	6.25	6.25	l+v+s; l>v; s=hl, op				300	350	350	vbd	38.16	
Evidence of boiling. 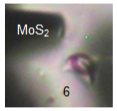 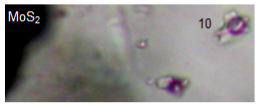	AR-138	E	1	P	Ia.	0.7	0.3	<0.01	12.50	6.25	l+v; l>v; s=op			-3		398	398	vbd	4.86	
			2	P	IIa	0.85	0.1	0.05	6.25	6.25	l+v+s; l>v; s=op				175	326	326	vbd	30.7	
			3	P	IIb.	0.85	0.05	0.1	9.38	12.50	l+v+s; l>v; s=hl, op, hm				169	88	169	hd	30.44	
			4	PS	Ic.	0.5	0.5		6.25	3.13	l+v+s; l>v; s=op			-4		385	385	ld	6.37	
			5	PS	Ic.	0.5	0.5		4.69	1.56	l+v+s; l>v; s=op			-6		450	450	ld	9.19	
			6	P	Ic.	0.5	0.5		6.25	3.13	l+v; l=v			-10		410	410	ld	13.95	
			7	P	Ic.	0.5	0.5		6.25	3.13	l+v; l>v			-5		380	380	ld	7.82	
			9	S	Ib.	0.85	0.15		6.25	3.13	l+v; l>v			-0.6		223	223	vbd	0.99	
			10	P	Ic.	0.5	0.5		6.25	7.81	l+v; l>v			-2		385	385	cb	3.28	
			11	P	Ic.	0.5	0.5		6.25	3.13	l+v; l>v			-6		370	370	ld	9.19	
Evidence of boiling.	AR-3	E	1	PS	IIc.	0.8	0.05	0.15	6.25	12.50	l+v+s; l>v; s=hl, ot				208	98	208	d	32.28	
			2	PS	Ic.	0.5	0.5	<0.01	6.25	3.13	l+v+s; l>v; s=op			-4		385	385	ld	6.37	
			3	PS	Ib.	0.75	0.25		3.13	3.13	l+v; l>v		-14			345	345	vbd	24.13	
			4	PS	IIb.	0.8	0.05	0.15	9.38	3.13	l+v+s; l>v; s=hl, hm				256	89	256	d	35.06	

Sample Comments and Photographs	Sample	Facies Loc.	Incl.	Para-genesis	Type	%L	%V	%S	Length in um	Width in um	Phase	Te	Tm_{hh}	Tm_{ice}	Ts_{hl}	Tl-v	Final Th	Final Th by	eq. wt. % NaCl	comments
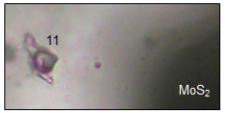	AR-3	E	5	IND	IIa.	0.7	0.15	0.15	6.25	6.25	l+v+s; l>v; s=hl				170	350	350	vbd	30.48	
			5a	IND	Ia.	0.75	0.25		3.13	4.69	l+v+s; l>v; s=op, hm			-1		378	378	vbd	1.65	
			6	PS	Ic.	0.5	0.5		6.25	3.13	l+v; l>v			-1		400	400	ld	1.65	
			7	PS	Ic.	0.5	0.5		6.25	3.13	l+v; l>v			-10		420	420	ld	13.95	
			10a	PS	Ic.	0.5	0.5		6.25	3.13	l+v; l>v			-1		378	378	ld	1.65	
			11	P	Ic.	0.5	0.5		12.50	9.38	l+v; l>v			-11		390	390	ld	14.98	
			12	PS	IIa.	0.75	0.15	0.2	6.25	6.25	l+v+s; l>v; s=hl					335	335	vbd		Halite not dissolving; may be an ot.
			13	PS	IIb.	0.75	0.05	0.2	4.69	1.56	l+v+s; l>v; s= hl, hm				370	135	370	hd	44.32	
			14	PS	IIb.		0.1		6.25	3.13	l+v+s; l>v; s=hl, op				360	100	360	hd	43.35	
			15	PS	IIc.	0.8	0.02	0.18	6.25	3.13	l+v+s; l>v; s=hl, ot, op				335	90	335	hd	41.05	

APPENDIX D – GAS ANALYSIS RAW DATA

All data in mol %. 0 means none detected. -- means not analyzed.

Sample #	Facies	Phase	Crush	H_2	He	CH_4	H_2O	N_2	H_2S	Ar	CO_2	SO_2	O_2
AR-173	SA	BQ	7277A	0.044289	0.00092787	0.017977	98.87262	0.305131	0	0.002424	0.601499	0	0.136709
AR-173	SA	BQ	7277B	0.078921	0.00056797	0.015336	98.02819	0.38309	0	0.003656	1.063166	0.00077	0.381343
AR-173	SA	BQ	7277C	0.071757	0.00028857	0.022569	98.56714	0.267812	0	0.00315	0.83391	0.000608	0.211621
AR-173	SA	BQ	7277D	0.044047	0.00018381	0.024471	98.189	0.511648	0.00163	0.00531	1.058822	0.000196	0.155599
AR-173	SA	BQ	7277E	0.045127	0.00057911	0.016604	97.99222	0.309022	0	0.003653	1.118874	0.000424	0.474801
AR-173	SA	BQ	7277F	0.047809	0.00021013	0.029623	97.7537	0.284964	0.00062	0.004412	1.229416	0.001019	0.602612
AR-173	SA	BQ	7277G	0.052100	0.00036599	0.017638	98.24617	0.387308	0.00031	0.005343	0.9618	0.001674	0.308241
AR-97	SA	BQ	7246A	0.003750	0.00021038	0.017554	98.73036	0.467839	0	0.012465	0.559763	0	0.192361
AR-97	SA	BQ	7246B	0.041131	0.00010098	0.022193	97.77618	0.917116	0.0025	0.013974	0.475013	0.000687	0.645701
AR-97	SA	BQ	7246C	0.044489	0.00038311	0.015475	98.59369	0.490465	0.00366	0.007447	0.606249	0.000181	0.227627
AR-97	SA	BQ	7246D	0.031706	0.00023366	0.017636	98.13042	0.577456	0.00123	0.010583	0.99155	0.000809	0.219762
AR-97	SA	BQ	7246E	0.052973	0.00014531	0.022966	97.70686	0.904134	0.00285	0.016534	0.839117	0.000948	0.420531
AR-97	SA	BQ	7246F	0.032035	0.00017642	0.009163	98.18441	0.500772	0.0019	0.009603	0.889373	0.000461	0.328361
AR-97	SA	BQ	7246G	0.019041	0.00001049	0.001543	99.00754	0.093217	0.00115	0.002301	0.203305	0.000766	0.55403
AR-97	SA	BQ	7246H	0.039853	0.00007927	0.003701	98.23022	0.286593	0.00226	0.007771	0.569472	0.000722	0.751204
AR-97	SA	BQ	7246I	0.033299	0.00026856	0.007627	98.96416	0.37319	0.00098	0.006208	0.449774	0.000293	0.148965
AR-97	SA	BQ	7246J	0.040640	0.00002453	0.00358	98.05976	0.235288	0.00216	0.005553	0.494117	0.000954	0.992727
AR-105	A1	M	7249A	0.021933	0.00074269	0.012639	96.57772	1.239473	0.00105	0.017709	1.872114	0.000945	0.223743
AR-105	A1	M	7249B	0.029079	0.00012330	0.011645	92.4607	0.248065	0.00165	0.010746	3.421386	0.004742	3.159436
AR-105	A1	M	7249C	0.035137	0.00064621	0.026925	97.52245	1.053322	0.0072	0.016004	1.249866	0.000496	0.078099
AR-105	A1	M	7249D	0.006742	0.00001577	0.003047	96.74905	0.418944	0.00218	0.008761	1.265579	0.002413	1.244011
AR-105	A1	M	7249E	0.026963	0.00005825	0.008345	88.67467	1.203134	0.00161	0.013422	4.554143	0.005807	4.648006
AR-105	A1	M	7249F	0.025105	0.00020724	0.00529	96.87923	0.234953	0.00076	0.010312	2.16285	0.002053	0.592472
AR-105	A1	M	7249G	0.036527	0.00009071	0.015409	97.43322	0.513361	0.00222	0.011289	1.868878	0.001471	0.093236
AR-112	A1	M	7253A	0.021403	0.00018525	0.004878	98.95262	0.367041	0	0.005773	0.380334	0.00017	0.254619
AR-112	A1	M	7253B	0.028548	0.00014241	0.010764	98.8936	0.402511	0.00023	0.003919	0.580227	0.000265	0.075913
AR-112	A1	M	7253C	0.001580	0.00011532	0.003432	99.13716	0.211187	0.00024	0.003821	0.46356	0.000307	0.162796
AR-112	A1	M	7253D	0.019451	0.00051056	0.005163	98.84525	0.373264	0.00563	0.004176	0.731825	0.000324	0.011211
AR-112	A1	M	7253E	0.029356	0.00034363	0.007053	98.90605	0.296986	0.00044	0.003894	0.669601	0.000191	0.082034
AR-112	A1	M	7253F	0.031998	0.00034423	0.012543	98.59725	0.494032	0	0.006218	0.724484	0.000232	0.123564
AR-112	A1	M	7253G	0.001625	0.00045314	0.071253	98.68329	0.460285	0.00206	0.005127	0.699767	9.1E-06	0.068135
AR-112	A1	M	7253H	0.127398	0.00317670	0.212214	97.48836	0.98863	0.00699	0.005975	1.151408	0.002698	0
AR-112	A1	M	7253I	0.032522	0.00004777	0.037014	97.91639	0.527995	0.00089	0.008632	1.224741	0.00036	0.225539
AR-106	A2	M	7252A	0.032831	0.00005529	0.012735	96.11548	0.488093	0.00238	0.006915	1.368935	0.003535	1.724109
AR-106	A2	M	7252B	0.044702	0.00027706	0.012862	94.20441	1.060931	0.00068	0.012438	3.159992	0.00346	1.342007
AR-106	A2	M	7252C	0.039009	0.00088817	0.013919	94.94617	0.611541	0	0.010719	3.671468	0.001626	0.630762
AR-106	A2	M	7252D	0.023419	0.00111427	0.013274	96.63847	0.814556	0.0013	0.007549	2.248051	0.000286	0.228409
AR-106	A2	M	7252E	0.052610	0.00034275	0.022973	90.92062	0.473809	0.00092	0.016234	5.637617	0.003078	2.557014
AR-106	A2	M	7252F	0.032176	0.00053262	0.019121	96.72137	0.955016	0.00183	0.009986	1.958718	0.001442	0.26814
AR-118	A2	M	7254A	0.035056	0.00024731	0.00626	98.07374	0.315923	0.00069	0.009464	0.884818	0.000265	0.597399

Sample #	Facies	Phase	Crush	C_2H_6	C_3H_6	C_3H_8	C_4H_8	C_4H_{10}	C_5H_{12}	C_6H_6	C_7H_{10}
AR-173	SA	BQ	7277A	28.48699	0	7.87362	0.505259	139.7643	3.290199	3.127794	1.209013
AR-173	SA	BQ	7277B	138.7219	0	0	1.764856	293.2106	9.132597	4.869301	2.009384
AR-173	SA	BQ	7277C	77.59536	0	0	2.701869	119.0073	6.988168	3.660866	1.534395
AR-173	SA	BQ	7277D	62.96814	14.03998	0.667058	0.063529	2.86E-11	10.54587	1.916468	0.741175
AR-173	SA	BQ	7277E	325.7266	29.18024	0	3.144036	2.91E-11	21.50476	5.236331	2.293692
AR-173	SA	BQ	7277F	385.0409	21.37955	0	2.176067	22.19097	18.90842	4.425899	2.12689
AR-173	SA	BQ	7277G	149.6369	0	0	3.847201	23.7757	8.656203	3.058525	1.461936
AR-97	SA	BQ	7246A	141.7823	4.57886	0	0	5.961474	2.474152	1.606519	0.694106
AR-97	SA	BQ	7246B	970.7168	35.82545	0	2.232559	24.83841	16.31193	2.954579	1.201782
AR-97	SA	BQ	7246C	79.39441	0	0	2.570497	16.23536	3.625371	1.236749	0.321312
AR-97	SA	BQ	7246D	155.7228	0	0	2.845747	15.66648	9.122255	1.764958	0.912226
AR-97	SA	BQ	7246E	254.6132	0	0	7.325489	35.92258	23.89804	5.496214	2.198485
AR-97	SA	BQ	7246F	392.8807	12.43344	0	1.387422	15.20828	12.27335	2.276796	0.996098
AR-97	SA	BQ	7246G	1082.909	27.83441	0	2.561636	28.88346	23.14215	3.655414	1.959855
AR-97	SA	BQ	7246H	995.7166	15.82563	0	3.684485	32.30616	26.90187	4.61842	2.249415
AR-97	SA	BQ	7246I	131.415	2.532229	0	0.751123	8.950507	7.31333	0.989503	0.485756
AR-97	SA	BQ	7246J	1520.36	44.41621	0	3.038822	37.75551	37.07857	6.092467	3.271057
AR-105	A1	M	7249A	268.274	22.63386	0	2.883056	15.10796	9.042312	1.179432	0.16849
AR-105	A1	M	7249B	6006.858	334.1326	0	9.956233	90.3246	66.51174	11.05108	5.40579
AR-105	A1	M	7249C	78.49156	3.887082	5.499409	1.649823	7.186728	1.412348	0.137485	0.262472
AR-105	A1	M	7249D	2747.281	165.2214	0	3.113326	38.84063	28.70334	6.327897	3.163949
AR-105	A1	M	7249E	7906.221	488.4774	0	9.791409	97.36758	104.3354	22.22422	10.01912
AR-105	A1	M	7249F	751.785	84.80533	0	2.033079	11.24682	13.79898	2.854961	1.211196
AR-105	A1	M	7249G	194.5315	26.6502	0	3.158404	13.81101	3.569557	0.897062	0.541975
AR-112	A1	M	7253A	114.5567	7.218747	0	0.281448	3.080709	3.4116	0.840539	0.311874
AR-112	A1	M	7253B	29.04618	0	1.346128	1.433161	4.398124	1.705868	0.516402	0.284311
AR-112	A1	M	7253C	137.7096	8.130833	0	0.658255	5.400468	4.950815	0.834407	0.366212
AR-112	A1	M	7253D	0.8342801	9.1844	0	0	0.87819	4.046991	0.892826	0.483004
AR-112	A1	M	7253E	25.04977	5.678215	3.589061	0	2.912764	2.336907	0.575857	0.254448
AR-112	A1	M	7253F	77.41109	5.107611	0	0.412956	5.462608	3.955682	0.695505	0.362242
AR-112	A1	M	7253G	66.35892	10.96535	0	0	1.14062	0.755749	0.643786	0.216928
AR-112	A1	M	7253H	1.255035	0	0	22.38337	86.88523	6.229117	2.68278	0
AR-112	A1	M	7253I	222.5109	21.64117	0	0	1.224741	9.846914	2.424986	1.187998
AR-106	A2	M	7252A	2172.5	139.6998	0	5.188263	64.12091	52.3207	10.59556	4.736515
AR-106	A2	M	7252B	1390.27	109.1777	0	3.697191	38.4571	31.34712	6.414784	3.096792
AR-106	A2	M	7252C	624.0027	90.5751	0	1.17487	7.710082	11.30812	3.157462	0.991296
AR-106	A2	M	7252D	171.7735	55.7067	0	0	5.84E-11	5.79997	1.641077	0.719376
AR-106	A2	M	7252E	2780.529	300.6541	0	0	1.35E-10	46.34121	14.09404	6.370507
AR-106	A2	M	7252F	241.7449	57.1358	0	0.90101	7.345191	7.599824	1.331928	0.548441
AR-118	A2	M	7254A	694.5026	32.22508	0	0.29199	11.90965	16.59919	3.8932	1.840422

Sample #	Facies	Phase	Crush	H_2	He	CH_4	H_2O	N_2	H_2S	Ar	CO_2	SO_2	O_2
AR-118	A2	M	7254B	0.041490	0.00008273	0.010457	98.10307	0.520294	0.00098	0.007431	0.692065	0.00034	0.557756
AR-118	A2	M	7254C	0.058787	0.00055105	0.007952	98.38948	0.357163	0.00502	0.011015	1.166999	0.000165	0
AR-118	A2	M	7254D	0.027363	0.00023143	0.013648	98.35352	0.668065	0.00248	0.011674	0.77734	0	0.137494
AR-118	A2	M	7254E	0.052070	0.00022159	0.023128	98.11446	0.498316	0	0.006512	0.921435	0.000567	0.350056
AR-118	A2	M	7254F	0.013363	0.00008550	0.025928	98.01463	0.638702	0.00211	0.006414	1.199981	0	0.090395
AR-118	A2	M	7254G	0.033750	0.00015840	0.003507	98.63291	0.156333	0.00016	0.003679	0.788018	0.000451	0.350203
AR-118	A2	M	7254H	0.176446	0.00023196	0.004594	99.09879	0.273609	0	0.003302	0.266738	0.000296	0.158477
AR-118	A2	M	7254I	0.025611	0.00002074	0.004553	98.41599	0.240264	0.00189	0.003407	0.396511	0.000644	0.794466
AR-118	A2	M	7254J	0.003418	0.00029576	0.005499	99.27827	0.229345	0.00061	0.0003	0.411889	0.000109	0.065142
AR-93	A3	M	7245A	0.000323	0.00021317	0.024715	92.08393	0.751699	0.00201	0.027216	6.235987	0.005045	0.719754
AR-93	A3	M	7245B	0.046216	0.00042557	0.009563	80.9598	3.412316	0.00278	0.033254	10.80606	0.01649	3.941795
AR-93	A3	M	7245C	0.042874	0.00056090	0.01816	93.67562	1.737169	0.00429	0.026875	4.036182	0.001627	0.392597
AR-93	A3	M	7246A	0.003750	0.00021038	0.017554	98.73036	0.467839	0	0.012465	0.559763	0	0.192361
AR-93	A3	M	7246B	0.041131	0.00010098	0.022193	97.77618	0.917116	0.0025	0.013974	0.475013	0.000687	0.645701
AR-93	A3	M	7246C	0.044489	0.00038311	0.015475	98.59369	0.490465	0.00366	0.007447	0.606249	0.000181	0.227627
AR-93	A3	M	7246D	0.031706	0.00023366	0.017636	98.13042	0.577456	0.00123	0.010583	0.99155	0.000809	0.219762
AR-93	A3	M	7246E	0.052973	0.00014531	0.022966	97.70686	0.904134	0.00285	0.016534	0.839117	0.000948	0.420531
AR-93	A3	M	7246F	0.032035	0.00017642	0.009163	98.18441	0.500772	0.0019	0.009603	0.889373	0.000461	0.328361
AR-93	A3	M	7246G	0.019041	0.00001049	0.001543	99.00754	0.093217	0.00115	0.002301	0.203305	0.000766	0.55403
AR-93	A3	M	7246H	0.039853	0.00007927	0.003701	98.23022	0.286593	0.00226	0.007771	0.569472	0.000722	0.751204
AR-93	A3	M	7246I	0.033299	0.00026856	0.007627	98.96416	0.37319	0.00098	0.006208	0.449774	0.000293	0.148965
AR-93	A3	M	7246J	0.040640	0.00002453	0.00358	98.05976	0.235288	0.00216	0.005553	0.494117	0.000954	0.992727
AR-91	A3	M	7263A	0.054201	0.00037409	0.02768	97.09684	0.273765	0	0.003399	1.626212	0.001402	0.860084
AR-91	A3	M	7263B	0.056334	0.00062481	0.030413	97.91481	0.402604	0	0.001484	1.391948	3.76E-10	0.189782
AR-91	A3	M	7263C	0.056022	0.00031833	0.019656	97.35162	0.423408	0	0.004317	1.671013	0.001115	0.444062
AR-91	A3	M	7263D	0.054811	0.00023850	0.01355	97.58632	0.243801	0.0002	0.00283	1.581434	0.001387	0.485059
AR-91	A3	M	7263E	0.052219	0.00042715	0.03242	98.26483	0.240605	0	0.003714	1.087602	0.000778	0.301173
AR-91	A3	M	7263F	0.045413	0.00006256	0.085841	98.64098	0.242325	0	0.002437	0.809126	0.000617	0.163722
AR-91	A3	M	7263G	0.133717	0.00049800	0.134232	98.16157	0.360078	0	0.004307	1.015387	0	0.179372
AR-91	A3	M	7263H	0.093838	0.00070847	0.10569	98.1938	0.373061	0	0.003785	1.082414	0.000445	0.13459
AR-91	A3	M	7263I	0.164674	0.00101826	0.185908	97.80251	0.507006	0	0.002464	1.157094	0	0.168391
AR-91	A3	M	7263J	0.066643	0.00107778	0.09661	98.03222	0.491505	0	0.002866	1.154709	0.000785	0.147764
AR-12	B	M	7237A	0.059412	0.00118636	0.027289	91.77087	1.323521	0.00259	0.028362	5.74132	0.001585	1.009909
AR-12	B	M	7237B	0.068121	0.00069189	0.010997	93.45786	0.412326	0.00102	0.018295	4.755166	0.001246	1.238467
AR-12	B	M	7237C	0.073443	0.00038316	0.018613	94.68614	1.100778	0	0.023514	3.645247	0	0.438144
AR-12	B	M	7237D	0.049285	0.00013935	0.012001	96.23711	0.955046	0.00035	0.011886	2.248371	0.000214	0.473887
AR-12	B	M	7237E	0.026215	0.00089010	0.013482	96.30472	1.134456	6E-05	0.01221	2.076535	0.00049	0.420708
AR-12	B	M	7237F	0.042254	0.00036788	0.023141	95.14874	2.594507	0	0.012491	1.934179	0	0.237533

Sample #	Facies	Phase	Crush	C_2H_6	C_3H_6	C_3H_8	C_4H_8	C_4H_{10}	C_5H_{12}	C_6H_6	C_7H_{10}
AR-118	A2	M	7254B	602.6154	13.02466	0	1.425653	20.81731	17.48848	3.294228	1.681717
AR-118	A2	M	7254C	1.085309	14.06234	0	0.968609	3.27E-11	0.82857	1.108649	0.28008
AR-118	A2	M	7254D	66.54027	0.04664	0	1.679054	6.125435	5.845594	1.119369	0.419763
AR-118	A2	M	7254E	301.1525	0	0	3.317165	15.86711	9.638207	1.640154	0.774005
AR-118	A2	M	7254F	57.91111	14.09978	0.287996	0.251996	2.555961	6.743896	1.511977	0.575991
AR-118	A2	M	7254G	277.6501	8.258424	0	0.094562	11.11105	8.05354	2.040966	1.103225
AR-118	A2	M	7254H	159.5282	4.63858	0	0.970928	4.846635	3.910384	0.797548	0.405442
AR-118	A2	M	7254I	1066.106	41.37984	0	1.87153	19.66296	29.71053	5.158602	2.426644
AR-118	A2	M	7254J	18.88924	0	19.01281	1.437493	9.094515	2.496049	0.247134	0.255371
AR-93	A3	M	7245A	1215.768	186.2065	0	3.928672	27.5007	48.20418	6.547786	2.993274
AR-93	A3	M	7245B	6784.693	539.0063	0	25.39425	200.0202	133.3468	20.96376	9.509334
AR-93	A3	M	7245C	509.8505	104.7793	0	0	7.709107	14.93387	2.179538	0.928322
AR-93	A3	M	7246A	141.7823	4.57886	0	0	5.961474	2.474152	1.606519	0.694106
AR-93	A3	M	7246B	970.7168	35.82545	0	2.232559	24.83841	16.31193	2.954579	1.201782
AR-93	A3	M	7246C	79.39441	0	0	2.570497	16.23536	3.625371	1.236749	0.321312
AR-93	A3	M	7246D	155.7228	0	0	2.845747	15.66648	9.122255	1.764958	0.912226
AR-93	A3	M	7246E	254.6132	0	0	7.325489	35.92258	23.89804	5.496214	2.198485
AR-93	A3	M	7246F	392.8807	12.43344	0	1.387422	15.20828	12.27335	2.276796	0.996098
AR-93	A3	M	7246G	1082.909	27.83441	0	2.561636	28.88346	23.14215	3.655414	1.959855
AR-93	A3	M	7246H	995.7166	15.82563	0	3.684485	32.30616	26.90187	4.61842	2.249415
AR-93	A3	M	7246I	131.415	2.532229	0	0.751123	8.950507	7.31333	0.989503	0.485756
AR-93	A3	M	7246J	1520.36	44.41621	0	3.038822	37.75551	37.07857	6.092467	3.271057
AR-91	A3	M	7263A	466.0888	30.1825	15.44902	1.691261	21.53105	20.09999	3.431309	1.935193
AR-91	A3	M	7263B	84.78356	24.6514	0	0	3.76E-11	8.351688	1.698177	0.54286
AR-91	A3	M	7263C	217.9335	33.68763	13.95296	1.019318	7.252197	7.369168	2.088767	1.25326
AR-91	A3	M	7263D	247.7159	0	0	6.784354	29.36724	14.51757	3.147054	2.134936
AR-91	A3	M	7263E	126.0965	14.55211	0	1.044098	8.24402	9.951555	1.729287	0.815701
AR-91	A3	M	7263F	57.51271	0	4.555382	3.212232	17.14539	10.47819	1.229872	0.598754
AR-91	A3	M	7263G	53.91703	0	28.68467	0	8.366786	15.02772	1.726157	0.649847
AR-91	A3	M	7263H	54.53204	0	21.55087	3.074057	23.59663	12.48024	0.909228	0.44379
AR-91	A3	M	7263I	62.34422	9.106328	30.60513	0	3.12E-11	5.600334	1.018243	0.543834
AR-91	A3	M	7263J	27.99014	0	3.337108	3.637332	15.68094	6.154596	0.969955	0.427242
AR-12	B	M	7237A	185.4446	65.39364	24.91733	0	1.44E-10	6.889584	43.63403	13.31986
AR-12	B	M	7237B	221.7809	38.42174	12.93405	0	12.22078	27.91282	34.57005	10.31871
AR-12	B	M	7237C	71.26458	58.06879	0	0	9.48E-11	0	6.452087	1.603909
AR-12	B	M	7237D	72.33009	33.79301	0	0	5.62E-11	0.359739	7.666945	3.012817
AR-12	B	M	7237E	53.67843	37.41917	0	0	5.4E-11	3.779294	5.502819	1.806586
AR-12	B	M	7237F	29.74767	25.64721	0	0	5.03E-11	4.119801	4.119801	1.257216

Sample #	Facies	Phase	Crush	H_2	He	CH_4	H_2O	N_2	H_2S	Ar	CO_2	SO_2	O_2
AR-12	B	M	7237G	0.055000	0.00035219	0.039176	96.68224	0.720665	5.1E-06	0.008429	1.958551	0.00162	0.514376
AR-12	B	M	7237H	0.082345	0.00088800	0.028495	95.14307	0.795908	0	0.009112	3.37943	0.001433	0.543831
AR-13	B	M	7238A	0.076249	0.00034109	0.055003	97.5836	0.60457	0.00025	0.006284	1.438101	0.000434	0.221688
AR-13	B	M	7238B	0.078331	0.00046736	0.033296	96.58109	0.700691	0	0.00682	2.331735	0.000732	0.257503
AR-13	B	M	7238C	0.058492	0.00101325	0.018592	97.51058	0.518539	0	0.005983	1.670076	0.00015	0.205604
AR-13	B	M	7238D	0.073539	0.00015039	0.023169	95.79883	1.47697	0.00048	0.008655	2.305059	0.000595	0.298999
AR-13	B	M	7238E	0.073294	0.00039303	0.041963	97.62355	0.595554	0.00337	0.007214	1.568077	0.000475	0.078893
AR-13	B	M	7238F	0.044644	0.00014621	0.017159	97.49465	0.376685	0.00217	0.005426	1.791299	0.001961	0.215134
AR-13	B	M	7238G	0.050980	0.00045828	0.014431	97.78645	0.183367	0.0009	0.004031	1.548356	0.000776	0.393298
AR-13	B	M	7238H	0.039092	0.00002692	0.010495	98.97208	0.138932	0.00209	0.003281	0.685424	0.001851	0.102342
AR-13	B	M	7238I	0.076238	0.00021669	0.017011	98.25951	0.330281	0	0.003831	1.149684	0.000394	0.156365
AR-169	B	M	7269A	0.018576	0.00033928	0.004896	99.20659	0.24895	0.00044	0.004692	0.410925	0.000432	0.097925
AR-169	B	M	7269B	0.021663	0.00043294	0.022045	99.4958	0.157614	0	0.002526	0.237982	0.000269	0.057848
AR-169	B	M	7269C	0.027204	0.00018560	0.014311	99.42061	0.170157	4.7E-05	0.003489	0.277604	0	0.083321
AR-169	B	M	7269D	0.009815	0.00001677	0.006449	99.56641	0.098086	0	0.001212	0.185699	0.000396	0.124493
AR-169	B	M	7269E	0.031185	0.00057646	0.007658	99.56901	0.117189	0	0.001329	0.200787	0.000242	0.067881
AR-169	B	M	7269F	0.053526	0.00039211	0.008197	99.22318	0.09166	0	0.002229	0.253969	0.000338	0.346532
AR-169	B	M	7269G	0.032310	0.00026860	0.009797	99.56258	0.090398	0	0.002278	0.201923	0.000308	0.095983
AR-169	B	M	7269H	0.035204	0.00005840	0.054547	99.56422	0.105383	0	0.000896	0.188699	0.000199	0.048287
AR-169	B	M	7269I	0.005803	0.00089854	0.007179	99.88881	0.034732	0.00353	0.001065	0.056812	4.66E-11	0.000485
AR-131	C	M	7274A	0.060643	0.00168912	0.021177	96.99199	0.46256	0.00293	0.008565	2.009681	0	0.412586
AR-131	C	M	7274B	0.033918	0.00014281	0.014819	97.927	0.391742	0.00184	0.00351	0.930406	0.001662	0.636871
AR-131	C	M	7274C	0.059482	0.00024254	0.034566	99.28057	0.238044	0.00074	0.002407	0.30119	0.000308	0.077058
AR-131	C	M	7274D	0.037483	0.00006146	0.031151	99.09508	0.283157	0.00217	0.001892	0.443125	0.000502	0.095862
AR-131	C	M	7274E	0.032267	0.00017829	0.015631	99.25567	0.125693	0.00249	0.001653	0.515721	0.000118	0.047012
AR-166 fl	C	M	7276A	0.018486	0.00030948	0.00523	99.71703	0.119865	0	0.002108	0.011041	7.27E-05	0.104703
AR-166 fl	C	M	7276B	0.043236	0.00015579	0.009798	99.61999	0.082932	0	0.001708	0.019846	0.000115	0.188473
AR-166 fl	C	M	7276C	0.035625	0.00011634	0.011344	99.6109	0.075697	0	0.001507	0.017057	0.000207	0.179933
AR-166 fl	C	M	7276D	0.071754	0.00015926	0.022448	99.05016	0.108306	0.00033	0.003035	0.044068	0.000229	0.440177
AR-166 fl	C	M	7276E	0.079678	0.00014832	0.025258	99.28827	0.092696	0	0.002028	0.03279	0.000308	0.292407
AR-166 fl	C	M	7276F	0.044455	0.00020995	0.015816	99.45471	0.061572	0	0.00154	0.021485	0	0.222072
AR-166 fl	C	M	7276G	0.007993	0.00009078	0.01109	99.48797	0.043702	0	0.001251	0.013001	0	0.204172
AR-8	C	M	6769A	0.056624	0.00007712	0.042518	97.03813	0.505119	0.00053	0.005321	2.351677	--	--
AR-8	C	M	6769B	0.062042	0.00069963	0.040204	96.96347	0.170543	0.00041	0.002567	2.760074	--	--
AR-8	C	M	6769C	0.029748	0.00006866	0.023609	97.46738	0.181038	0.0004	0.00299	2.29475	--	--
AR-8	C	M	6769D	0.032294	0.00003189	0.026796	96.98707	0.176194	0.00046	0.002931	2.774226	--	--
AR-8	C	M	6769	0.047695	0.00002638	0.032702	98.27916	0.158617	0.00039	0.001919	1.479491	--	--
AR-8	C	M	6769F	0.035878	0.00001954	0.026758	96.90057	0.147821	0.00042	0.002162	2.886377	--	--
AR-8	C	M	6769G	0.039812	0.00008658	0.04788	96.97694	0.162931	0.0005	0.002502	2.769355	--	--

Sample #	Facies	Phase	Crush	C_2H_6	C_3H_6	C_3H_8	C_4H_8	C_4H_{10}	C_5H_{12}	C_6H_6	C_7H_{10}
AR-12	B	M	7237G	113.6939	22.15121	19.38965	0	11.39877	15.78592	10.20405	3.153267
AR-12	B	M	7237H	98.84831	36.70061	5.102939	0.067589	2.500778	1.723509	6.860242	3.041487
AR-13	B	M	7238A	64.97339	0	11.1309	3.652776	29.62487	12.23824	10.12423	2.991249
AR-13	B	M	7238B	45.18902	10.98247	14.17695	1.025963	5.689433	6.062511	7.904581	2.401687
AR-13	B	M	7238C	55.16262	31.58114	0	0	4.34E-11	12.55897	7.999666	2.304705
AR-13	B	M	7238D	89.20576	13.46154	2.835222	0	7.191783	4.517915	13.78425	4.656218
AR-13	B	M	7238E	19.99298	0	11.07062	6.131182	22.31374	6.9309	4.531743	1.285823
AR-13	B	M	7238F	365.0309	0	39.91014	5.57094	40.26841	30.38043	19.88342	6.197895
AR-13	B	M	7238G	92.35943	0	16.75321	4.474748	24.71176	15.85516	11.53525	3.716054
AR-13	B	M	7238H	294.5954	0	39.38448	5.216078	47.04067	34.55909	16.40906	6.717158
AR-13	B	M	7238I	28.51216	7.852342	16.31402	1.276149	4.391793	1.609558	3.345581	1.391118
AR-169	B	M	7269A	31.55494	0	0	3.07372	19.86823	6.061147	1.240994	0.43969
AR-169	B	M	7269B	17.56783	0	0	2.696337	12.10853	4.488342	1.070919	0.376012
AR-169	B	M	7269C	12.42553	6.820718	0	0	7.22E-12	4.077996	1.371361	0.632936
AR-169	B	M	7269D	48.6959	0	0	2.183822	12.90238	8.612728	1.279467	0.651804
AR-169	B	M	7269E	22.24114	0	0	1.258933	9.822485	6.768519	0.821218	0.373463
AR-169	B	M	7269F	152.4193	0	0	2.582861	21.10733	18.53463	3.588577	1.594923
AR-169	B	M	7269G	23.30795	0	0	1.385191	9.221816	6.241435	0.949037	0.44625
AR-169	B	M	7269H	7.891394	0	4.675962	0.771779	5.71192	4.779746	0.83405	0.292484
AR-169	B	M	7269I	0	0	0.91354	0.049995	2.160568	1.394171	0.256223	0.094308
AR-131	C	M	7274A	198.6971	49.63911	0	0	5.23E-11	27.51252	4.119845	1.788616
AR-131	C	M	7274B	501.4515	0	15.06327	3.972833	30.16376	21.94827	5.22888	3.061035
AR-131	C	M	7274C	32.99229	0	0	0	9.830823	9.348921	1.099342	0.578284
AR-131	C	M	7274D	60.89867	0	0	1.577525	17.56548	12.89494	1.617406	0.762175
AR-131	C	M	7274E	21.21161	8.339212	0	0.232075	1.805024	2.289803	0.995342	0.773582
AR-166 fl	C	M	7276A	0	0	4.728139	0.040964	139.2403	38.76319	2.283247	0.639737
AR-166 fl	C	M	7276B	51.71915	0	0	1.051811	199.9247	80.42508	3.554726	0.894437
AR-166 fl	C	M	7276C	46.17085	0	0	0.855423	581.0684	4.917958	2.812065	1.024461
AR-166 fl	C	M	7276D	114.1908	0	0	3.339927	2262.979	10.96637	6.94779	2.519818
AR-166 fl	C	M	7276E	61.19175	0	0	3.116658	1632.919	9.764764	4.767946	1.732278
AR-166 fl	C	M	7276F	46.85284	0	0	1.88575	1565.387	9.229581	4.414119	1.616111
AR-166 fl	C	M	7276G	12.81984	0	0	2.89726	2045.904	6.915072	4.706602	1.718985
AR-8	C	M	6769A	--	--	--	--	--	--	--	--
AR-8	C	M	6769B	--	--	--	--	--	--	--	--
AR-8	C	M	6769C	--	--	--	--	--	--	--	--
AR-8	C	M	6769D	--	--	--	--	--	--	--	--
AR-8	C	M	6769	--	--	--	--	--	--	--	--
AR-8	C	M	6769F	--	--	--	--	--	--	--	--
AR-8	C	M	6769G	--	--	--	--	--	--	--	--

Sample #	Facies	Phase	Crush	H_2	He	CH_4	H_2O	N_2	H_2S	Ar	CO_2	SO_2	O_2
AR-8	C	M	6769H	0.048089	0.00000000	0.038803	96.66149	0.12856	0.0003	0.001836	3.120921	--	--
AR-8	C	M	6769I	0.039947	0.00000812	0.027581	96.4646	0.108111	0.00023	0.001778	3.357748	--	--
AR-8	C	M	6769J	0.044025	0.00001832	0.036833	96.98976	0.155079	0.00042	0.001805	2.772051	--	--
AR-8	C	M	6769K	0.048535	0.00006811	0.037216	97.84713	0.093463	0.00059	0.001653	1.971336	--	--
AR-10	D	M	7236A	0.000000	0.00052768	0.00517	99.35704	0.161001	0.00105	0.003638	0.417931	0	0.052202
AR-10	D	M	7236B	0.007809	0.00042208	0.007527	99.12111	0.175479	0.0004	0.003398	0.619327	5.95E-05	0.062357
AR-10	D	M	7236C	0.032836	0.00000812	0.006896	99.5155	0.083738	0.00167	0.001831	0.267535	0.000637	0.063528
AR-10	D	M	7236D	0.049426	0.00005967	0.018946	98.90327	0.25793	0	0.002125	0.562529	0.000447	0.195007
AR-10	D	M	7236E	0.056467	0.00041583	0.017818	98.77668	0.215644	0.00014	0.003883	0.759341	0	0.163547
AR-10	D	M	7236F	0.053478	0.00085687	0.023019	98.92396	0.469468	0.00093	0.004193	0.432303	0.000251	0.085897
AR-10	D	M	7236G	0.065870	0.00013123	0.007906	98.38786	0.428539	0.00199	0.006902	0.90301	0.000559	0.185627
AR-10	D	M	7236H	0.039572	0.00038682	0.041963	98.73001	0.3167	0.00132	0.00243	0.789271	0.000393	0.067207
AR-10	D	M	7236I	0.047943	0.00062047	0.072507	98.53065	0.311331	0	0.003023	0.932114	0.000172	0.08623
AR-10	D	M	7236J	0.100701	0.00026128	0.137625	97.59345	0.674913	0.00074	0.003196	1.024448	0.00026	0.429244
AR-10	D	M	7236K	0.064092	0.00018415	0.086584	98.83009	0.337245	0.00174	0.003557	0.562176	0.000336	0.107137
AR-10	D	M	7236L	0.118915	0.00010165	0.201669	98.43658	0.381883	0.00103	0.003393	0.792775	0	0.052374
AR-78	D	M	7243A	0.026805	0.00008970	0.008176	91.58312	1.553677	0.00125	0.017623	3.976954	0.003882	2.302632
AR-78	D	M	7243B	0.018180	0.00038107	0.036908	98.5557	0.683561	0.00222	0.011898	0.625612	0.00026	0.058618
AR-78	D	M	7243C	0.024453	0.00057807	0.021727	97.29128	1.275192	0.00827	0.032296	1.317032	0.001924	0.014909
AR-78	D	M	7243D	0.010368	0.00013546	0.01326	98.25403	0.445898	0.0013	0.008401	0.90205	0.000441	0.318095
AR-78	D	M	7243E	0.025862	0.00015956	0.015608	97.78312	0.977906	0.00141	0.008131	0.721579	0.00096	0.3899
AR-78	D	M	7243F	0.027867	0.00028475	0.03365	96.74103	2.109331	0.00178	0.013324	0.942159	0.000638	0.12461
AR-78	D	M	7243G	0.034293	0.00016540	0.059698	98.09083	0.626157	0	0.009401	0.992226	0.000271	0.166282
AR-78	D	M	7243H	0.030746	0.00008666	0.199428	97.985	0.765806	0.00294	0.011471	0.876187	0.000596	0.114516
AR-78	D	M	7243I	0.071621	0.00101875	0.136427	96.63441	1.02997	0.00744	0.019864	1.934438	0	0.152198
AR-78	D	M	7243J	0.044177	0.00010676	0.040386	89.26239	1.632064	0.00118	0.01455	4.256729	0.00484	3.88436
AR-78	D	M	7243K	0.035823	0.00029284	0.049707	97.93924	0.514327	0.00131	0.008005	1.173827	0.000579	0.23704
AR-78	D	M	7243L	0.060817	0.00038562	0.176143	94.73268	2.851436	0.00118	0.014308	1.943605	0.002047	0.188189
AR-6A	D	M	7247A	0.044967	0.00025910	0.010487	98.03019	0.944886	0.00296	0.015073	0.59555	0.000161	0.305783
AR-6A	D	M	7247B	0.054385	0.00017986	0.011925	94.77761	0.282053	0.00206	0.010813	2.504036	0.00133	1.987199
AR-6A	D	M	7247C	0.024092	0.00004939	0.007568	98.34425	0.580883	0.00254	0.008351	0.412234	0.000641	0.507371
AR-6A	D	M	7247D	0.041317	0.00016788	0.005699	98.02834	0.417309	0.00231	0.01484	1.105775	0.001034	0.322502
AR-164 fl	D	M	7267A	0.042227	0.00002219	0.014794	99.40316	0.136837	0.00169	0.003039	0.046728	0.000357	0.302813
AR-164 fl	D	M	7267B	0.069893	0.00013694	0.019727	99.27372	0.109477	0.00114	0.002758	0.05047	0.000506	0.378544
AR-164 fl	D	M	7267C	0.078135	0.00009993	0.014919	98.84596	0.110854	0.00138	0.003442	0.057311	0.000595	0.564686
AR-164 fl	D	M	7267D	0.077189	0.00009957	0.012756	99.05379	0.097735	0.00141	0.002949	0.064209	0.000553	0.482686
AR-164 fl	D	M	7267E	0.052901	0.00012320	0.008384	99.59476	0.102114	0	0.002022	0.019835	0.000103	0.155544
AR-164 fl	D	M	7267F	0.056893	0.00012735	0.008833	99.40855	0.087632	0.00057	0.002112	0.038871	0.00034	0.30644
AR-164 fl	D	M	7267G	0.038764	0.00007469	0.007141	99.42774	0.073545	0	0.00145	0.023526	0.00019	0.265746
AR-164 fl	D	M	7267H	0.064623	0.00015627	0.017507	99.12441	0.097142	0.00062	0.002517	0.041644	0.00046	0.383646

Sample #	Facies	Phase	Crush	C_2H_6	C_3H_6	C_3H_8	C_4H_8	C_4H_{10}	C_5H_{12}	C_6H_6	C_7H_{10}
AR-8	C	M	6769H	--	--	--	--	--	--	--	--
AR-8	C	M	6769I	--	--	--	--	--	--	--	--
AR-8	C	M	6769J	--	--	--	--	--	--	--	--
AR-8	C	M	6769K	--	--	--	--	--	--	--	--
AR-10	D	M	7236A	0	6.803916	2.436538	0	1.13E-11	0	0.860938	0.204786
AR-10	D	M	7236B	0	0.66268	12.12642	0	1.777468	3.338171	0.836091	0.210571
AR-10	D	M	7236C	180.7893	0	26.80164	2.514827	24.66136	17.5048	3.619746	2.175058
AR-10	D	M	7236D	47.27493	0	12.35876	1.400697	15.60455	21.31422	3.324546	1.215062
AR-10	D	M	7236E	34.86893	12.12668	0	0	1.97E-11	9.552509	2.604539	0.896022
AR-10	D	M	7236F	0	0	35.44456	0	9.68792	5.481607	3.544888	0.851638
AR-10	D	M	7236G	51.08326	0	9.003008	2.81739	27.31605	20.69698	3.621069	1.480936
AR-10	D	M	7236H	0	0	19.73178	10.64727	41.20786	15.20137	2.328351	0.615632
AR-10	D	M	7236I	21.59707	0	41.86122	11.89377	45.90659	26.63049	4.651247	1.537987
AR-10	D	M	7236J	136.774	0	50.31064	9.189298	71.84454	61.19028	17.30293	5.071017
AR-10	D	M	7236K	16.35369	0	24.21853	2.973909	7.988515	12.81198	3.187536	0.972564
AR-10	D	M	7236L	48.88252	12.05811	34.63635	0	2.06E-11	7.134977	7.666136	2.330759
AR-78	D	M	7243A	4793.542	328.8941	0	0	35.03696	58.81914	29.98623	11.65247
AR-78	D	M	7243B	47.75923	0.494234	15.37129	0	1.56E-11	0	2.28974	0.800784
AR-78	D	M	7243C	58.46304	0	24.64166	9.96993	25.66895	1.67263	2.515531	0.539983
AR-78	D	M	7243D	411.2896	21.15306	0	1.326013	12.58359	9.787239	2.958723	1.154624
AR-78	D	M	7243E	684.1146	29.94553	0	1.955479	19.12906	13.72443	3.485227	1.298842
AR-78	D	M	7243F	6.802386	0	13.21849	1.733572	8.95993	3.306978	2.345975	0.734884
AR-78	D	M	7243G	179.0372	16.5404	0	0	2.68E-11	9.207854	1.587561	0.406813
AR-78	D	M	7243H	109.5759	8.490248	8.034631	0	2.28E-11	4.196934	1.331804	0.709711
AR-78	D	M	7243I	85.32806	11.62597	22.5362	0	5.03E-11	2.727557	2.65018	1.121974
AR-78	D	M	7243J	7906.278	249.0186	0	21.32621	199.598	165.2462	36.30989	14.34518
AR-78	D	M	7243K	349.4131	27.23279	0	0.845156	6.972533	11.28048	1.866385	0.798203
AR-78	D	M	7243L	240.1518	0	24.72266	7.366263	17.60906	0	1.418832	0.699698
AR-6A	D	M	7247A	463.9569	10.91047	0	1.060078	9.951632	7.819565	2.018913	1.060078
AR-6A	D	M	7247B	3385.281	179.2639	0	1.802906	46.24954	49.80527	14.17284	7.562187
AR-6A	D	M	7247C	1037.684	45.16849	0	1.451064	17.84149	13.5996	2.996942	1.587101
AR-6A	D	M	7247D	539.6625	25.32225	0	1.42645	19.5501	17.21692	2.720207	1.127891
AR-164 fl	D	M	7267A	148.2668	0	34.35656	5.131709	133.7118	156.9003	3.825184	1.22475
AR-164 fl	D	M	7267B	170.9418	0	30.42331	5.064158	389.0645	333.5218	5.810609	1.407608
AR-164 fl	D	M	7267C	276.853	0	0	7.007435	2752.167	32.36074	5.469203	2.902237
AR-164 fl	D	M	7267D	245.2734	0	0	6.117788	1736.274	20.70597	4.00597	2.098977
AR-164 fl	D	M	7267E	49.15712	0	0	3.821095	542.2412	9.991298	1.445208	0.836658
AR-164 fl	D	M	7267F	145.1893	0	0	6.37401	722.4081	18.21479	2.713172	1.326656
AR-164 fl	D	M	7267G	105.0886	0	0	2.527142	1397.164	12.10661	2.621245	1.276745
AR-164 fl	D	M	7267H	165.9966	0	0	7.256843	2305.162	21.57855	3.475589	1.695734

Sample #	Facies	Phase	Crush	H_2	He	CH_4	H_2O	N_2	H_2S	Ar	CO_2	SO_2	O_2
AR-164 fl	D	M	7267I	0.051815	0.00005540	0.011002	99.31847	0.09969	0.00167	0.002298	0.046757	0.000371	0.353856
AR-164 fl	D	M	7267J	0.059134	0.00017345	0.008675	99.30885	0.138943	0.0008	0.003131	0.043611	0.00033	0.355645
AR-164 qtz	D	M	7268A	0.043550	0.00012210	0.008938	98.85699	0.174354	0	0.00168	0.738421	0	0.164319
AR-164 qtz	D	M	7268B	0.046914	0.00028522	0.010117	98.34935	0.330269	0	0.004195	0.958277	0.000262	0.273749
AR-164 qtz	D	M	7268C	0.055571	0.00021545	0.010724	98.48867	0.267373	0	0.002487	0.861438	0.000664	0.286819
AR-164 qtz	D	M	7268D	0.060385	0.00025208	0.018929	98.30334	0.460266	0	0.003473	0.967556	0.000283	0.172049
AR-164 qtz	D	M	7268E	0.077814	0.00029863	0.025896	98.4082	0.375535	0.00016	0.001232	1.058849	0.000427	0.038702
AR-5	E	M	7235A	0.068588	0.00072264	0.069041	97.9895	0.468762	0.00347	0.004259	1.319008	0	0.061506
AR-5	E	M	7235B	0.066754	0.00180657	0.068334	97.07475	0.959457	0.00014	0.004259	1.763283	0	0.053358
AR-5	E	M	7235C	0.034305	0.00011166	0.013211	98.10972	0.602501	0.00067	0.005052	0.933381	0.000491	0.286414
AR-5	E	M	7235D	0.050136	0.00009537	0.00454	98.17045	0.364959	0.0021	0.005905	1.00211	0.00114	0.371481
AR-5	E	M	7235E	0.035997	0.00010636	0.004601	98.20975	0.063169	0.00079	0.005101	1.176208	0.001124	0.476778
AR-5	E	M	7235F	0.021411	0.00015668	0.004308	98.84594	0.128549	0.00022	0.002582	0.747669	0.000302	0.237401
AR-5	E	M	7235G	0.040716	0.00028481	0.010177	98.55296	0.250569	0.00128	0.003173	0.969095	0	0.163541
AR-64	E	M	7251A	0.014622	0.00014995	0.008216	98.69043	0.470956	0.00093	0.010784	0.552467	0.00035	0.222072
AR-64	E	M	7251B	0.058928	0.00013308	0.012323	92.17375	0.221728	0.00232	0.011862	3.091696	0.004325	3.625754
AR-64	E	M	7251C	0.015199	0.00031310	0.019909	98.98652	0.363147	0.00038	0.005731	0.273507	0.00044	0.315195
AR-64	E	M	7251D	0.029447	0.00033313	0.03242	98.97104	0.397281	0.00181	0.005447	0.353171	0.000333	0.192551
AR-64	E	M	7251E	0.031112	0.00008974	0.01042	98.9637	0.244047	0.00186	0.006074	0.2878	0.00039	0.395955
AR-64	E	M	7251F	0.037536	0.00020337	0.020663	98.98491	0.205911	0.00091	0.005431	0.442341	0.000479	0.267976
AR-64	E	M	7251G	0.035048	0.00013085	0.006024	98.83811	0.215952	0.00099	0.006176	0.46607	0.000548	0.377556
AR-64	E	M	7251H	0.019028	0.00008867	0.011321	98.93369	0.26582	0.00064	0.00505	0.383133	0.000328	0.336272
AR-64	E	M	7251I	0.028858	0.00014387	0.018353	99.11776	0.229177	0.00056	0.003788	0.323502	0.000197	0.249234
AR-102	A1	V	7248A	0.022675	0.00010805	0.017175	99.03398	0.457674	0.00188	0.009561	0.352097	0.000107	0.094329
AR-102	A1	V	7248B	0.003460	0.00026264	0.010081	99.53632	0.250393	0	0.004669	0.138515	0	0.050944
AR-102	A1	V	7248C	0.016769	0.00010238	0.007123	99.40501	0.277429	0.00047	0.00596	0.135325	8.74E-05	0.129678
AR-102	A1	V	7248D	0.037110	0.00013576	0.088813	99.0702	0.433646	0.00046	0.007977	0.160879	0.000299	0.175868
AR-102	A1	V	7248E	0.063978	0.00030628	0.172172	98.07558	0.568806	0	0.010081	0.849409	0.000586	0.222941
AR-102	A1	V	7248F	0.079806	0.00040174	0.112488	98.12521	0.583685	0.00152	0.012251	0.733012	0	0.30587
AR-102	A1	V	7248G	0.103062	0.00033733	0.31497	98.18833	0.666525	0.00312	0.014095	0.622601	0.000257	0.063661
AR-110	A2	V	7250A	0.053843	0.00027515	0.026236	98.72955	0.803972	0.00262	0.011365	0.19977	0	0.154885
AR-110	A2	V	7250B	0.073304	0.00055166	0.02821	98.56582	0.919285	0.00581	0.01429	0.310536	5.31E-05	0.071801
AR-110	A2	V	7250C	0.053136	0.00039660	0.019044	98.48357	0.784223	0.00055	0.011833	0.371035	0.000459	0.242541
AR-110	A2	V	7250D	0.091571	0.00016597	0.114617	97.66303	1.309897	0.00207	0.017593	0.755351	0.000411	0.030823
AR-119	A2	V	7264A	0.035894	0.00024090	0.010949	98.83905	0.45997	0	0.005724	0.489865	0.000256	0.151868
AR-119	A2	V	7264B	0.026119	0.00027340	0.009064	98.98569	0.224636	0.00011	0.003731	0.549321	0.000396	0.19097
AR-119	A2	V	7264C	0.027358	0.00052342	0.01836	99.12349	0.264756	0.00063	0.003072	0.499449	0.000142	0.058856
AR-119	A2	V	7264D	0.030671	0.00024748	0.020618	99.2253	0.149435	0	0.001659	0.347374	9.55E-05	0.213604
AR-119	A2	V	7264E	0.021857	0.00029387	0.02454	99.15115	0.157354	0	0.002045	0.447482	0.000136	0.18476
AR-119	A2	V	7264F	0.022184	0.00022949	0.021573	99.30235	0.181892	0	0.001351	0.353667	8.56E-05	0.111479
AR-119	A2	V	7264G	0.068508	0.00112095	0.074017	98.88823	0.312672	0	0.00355	0.598517	0	0.046672
AR-119	A2	V	7264H	0.143286	0.00389425	0.187851	98.3053	0.435166	0.00414	0.003252	0.893267	0	0.005617
AR-119	A2	V	7264I	0.053553	0.00071471	0.096171	99.17867	0.369983	0.00124	0.00248	0.280689	0	0.014565

Sample #	Facies	Phase	Crush	C_2H_6	C_3H_6	C_3H_8	C_4H_8	C_4H_{10}	C_5H_{12}	C_6H_6	C_7H_{10}
AR-164 fl	D	M	7267I	199.2487	0	0	4.097742	913.8161	18.23084	3.106036	1.546238
AR-164 fl	D	M	7267J	217.9799	0	0	5.61582	563.442	15.62155	2.801587	1.485835
AR-164 qtz	D	M	7268A	37.43794	0	3.17521	3.662568	43.94343	23.26764	3.160441	1.425152
AR-164 qtz	D	M	7268B	99.50748	0	14.88204	3.967267	91.8317	49.00629	4.954292	1.69615
AR-164 qtz	D	M	7268C	131.3606	0	3.299306	6.219579	85.83364	30.30537	2.55847	0.887281
AR-164 qtz	D	M	7268D	59.03061	0	0	3.163909	50.2065	19.66075	1.877059	0.793396
AR-164 qtz	D	M	7268E	26.35476	0	0	9.243755	68.13696	22.53232	1.874163	0.582367
AR-5	E	M	7235A	75.8957	0	49.66064	0	6.92479	12.21401	5.513453	1.147537
AR-5	E	M	7235B	36.00624	30.71639	0	0	4.76E-11	9.90965	1.392994	0.546618
AR-5	E	M	7235C	85.115	0	17.6409	2.538796	15.7368	15.24211	3.724189	1.586747
AR-5	E	M	7235D	206.1441	0	10.56224	2.024263	21.52533	23.0786	5.351269	2.184601
AR-5	E	M	7235E	176.6193	0	30.91073	1.729025	29.32285	18.4547	4.434302	2.21127
AR-5	E	M	7235F	67.13322	0	13.55524	1.562629	13.92908	14.40759	2.82619	1.218701
AR-5	E	M	7235G	54.99614	16.11605	0	0.494238	2.52E-11	6.270044	3.052649	1.104768
AR-64	E	M	7251A	262.5378	12.26477	0	0.375678	5.60754	6.93346	1.839715	0.657436
AR-64	E	M	7251B	7409.094	315.1674	0	12.79962	117.4844	87.86599	19.3231	10.01709
AR-64	E	M	7251C	161.711	0	0	3.440717	15.3246	13.22132	1.930959	0.905308
AR-64	E	M	7251D	142.0664	0	0	0.88999	10.39028	5.905012	1.412682	0.826419
AR-64	E	M	7251E	539.2455	13.75973	0	0.972765	13.17261	13.71943	3.160046	1.585779
AR-64	E	M	7251F	300.4423	0	0	2.021498	18.81276	12.4519	1.835714	0.813907
AR-64	E	M	7251G	487.9711	12.48603	0	1.486765	15.74386	12.62119	2.428227	1.151194
AR-64	E	M	7251H	409.8257	13.28705	0	1.187712	9.739237	9.608972	1.927158	0.873543
AR-64	E	M	7251I	258.8724	5.496291	0	0.931684	8.708661	7.453475	1.827783	0.95433
AR-102	A1	V	7248A	91.3937	1.626686	0	1.13023	4.214596	4.41177	0.992912	0.369701
AR-102	A1	V	7248B	46.25838	0.199461	0	0.009696	2.8631	3.595843	0.493112	0.250712
AR-102	A1	V	7248C	203.0667	8.908419	0	0	3.398001	3.728193	0.843072	0.424919
AR-102	A1	V	7248D	224.3569	0	0	2.501667	10.90116	6.300019	1.481695	0.593643
AR-102	A1	V	7248E	316.7785	0	0	3.711916	23.71549	14.73724	1.749782	0.705009
AR-102	A1	V	7248F	354.5284	0	15.14402	7.791912	45.34409	25.97793	6.465162	2.492239
AR-102	A1	V	7248G	154.156	0	24.89159	2.017227	24.3437	22.18327	1.936289	1.027292
AR-110	A2	V	7250A	156.5295	8.206538	0	0	0.215751	8.314414	1.148676	0.605302
AR-110	A2	V	7250B	73.0628	0	0	4.977885	21.91449	2.170643	0.87571	0.425434
AR-110	A2	V	7250C	300.2823	0	0	4.704724	16.55929	8.385391	1.677078	0.701256
AR-110	A2	V	7250D	99.37397	0	0	7.440207	25.01722	10.40874	1.707093	0.717583
AR-119	A2	V	7264A	47.45324	0	0	1.087501	6.422132	5.946964	0.705406	0.347804
AR-119	A2	V	7264B	76.74569	0	0	1.647964	9.574672	6.443539	1.576552	0.697638
AR-119	A2	V	7264C	11.02783	11.42739	0	0.109879	1.748071	0.844069	0.48946	0.209769
AR-119	A2	V	7264D	91.23084	0	0	0.357795	7.482437	8.90667	1.386022	0.569693
AR-119	A2	V	7264E	88.9638	0.778618	0	0.174518	6.466107	5.68749	1.21715	0.501179
AR-119	A2	V	7264F	36.90511	0	0.11671	0.470377	7.239556	5.556103	1.075147	0.50928
AR-119	A2	V	7264G	49.29981	15.47764	0	0	1.56E-11	0.700264	1.197033	0.395021
AR-119	A2	V	7264H	65.5211	0	75.15051	0	2.23E-11	30.23707	9.638345	1.813331
AR-119	A2	V	7264I	0	1.24626	13.13064	0	7.02E-12	0.777509	0.673654	0.362089

Sample #	Facies	Phase	Crush	H_2	He	CH_4	H_2O	N_2	H_2S	Ar	CO_2	SO_2	O_2
AR-14	A3	V	7239A	0.000090	0.00175989	0.024296	96.59145	0.9435	0.00138	0.011383	2.231354	0.000676	0.18433
AR-14	A3	V	7239B	0.109097	0.00142277	0.026777	94.63767	1.09392	0	0.01696	3.968249	0.00021	0.130804
AR-14	A3	V	7239C	0.039438	0.00020238	0.021769	95.67883	1.228476	0.00051	0.011949	2.389806	0.001902	0.584372
AR-14	A3	V	7239D	0.083194	0.00072196	0.030687	93.88148	0.729512	8.9E-05	0.009555	4.310849	0.002276	0.900244
AR-14	A3	V	7239E	0.078755	0.00029668	0.022018	94.09553	0.578376	0	0.009608	4.474139	0.002465	0.703971
AR-14	A3	V	7239F	0.056847	0.00053991	0.021543	95.44643	1.232723	0.00027	0.01344	2.655247	0.001152	0.53428
AR-14	A3	V	7239G	0.042059	0.00072111	0.038479	96.4958	0.793198	0.00044	0.006179	2.284518	0.001526	0.320949
AR-14	A3	V	7239H	0.094807	0.00123995	0.055022	92.84933	1.26984	0.00034	0.011024	5.05035	0.003192	0.628734
AR-90	A3	V	7244A	0.062514	0.00173636	0.034695	95.47433	2.573232	0.00025	0.035422	1.343222	0.000144	0.458858
AR-90	A3	V	7244B	0.048272	0.00031427	0.01313	96.60479	1.114609	0.00175	0.016131	1.526228	0.000826	0.608734
AR-90	A3	V	7244C	0.101262	0.00049031	0.042877	95.5414	1.815618	0.00193	0.021779	2.087962	0.001875	0.347604
AR-90	A3	V	7244D	0.069940	0.00028220	0.025224	95.49876	1.935754	0.00384	0.033108	2.048594	0.002553	0.337885
AR-90	A3	V	7244E	0.101704	0.00027534	0.033001	95.99244	1.61933	0.0044	0.023472	1.830892	0	0.366635
AR-90	A3	V	7244F	0.077375	0.00095481	0.032956	95.01592	1.760928	0.00298	0.029293	2.602422	0.001567	0.416576
AR-90	A3	V	7244G	0.094691	0.00053048	0.019591	97.26973	1.348549	0.00186	0.023465	1.046621	0.000793	0.167719
AR-90	A3	V	7244H	0.075903	0.00035685	0.02453	93.46998	0.917525	0.00236	0.023747	3.972417	0.001021	1.305918
AR-90	A3	V	7244I	0.106997	0.00088593	0.041183	95.49753	1.383666	0.0057	0.020807	2.590101	0.001414	0.304888
AR-90	A3	V	7244J	0.120673	0.00033645	0.062829	94.35691	1.682573	0.00288	0.028489	3.616127	0.001096	0.113936
AR-147	B	V	7266A	0.005078	0.00147853	0.316579	97.2776	0.846354	0	0.014398	1.358559	0.00025	0.17233
AR-147	B	V	7266B	0.066257	0.00353684	0.168412	96.94962	0.746938	0.00295	0.018111	1.957353	0.001448	0.071193
AR-147	B	V	7266C	0.049724	0.00055390	0.076906	97.40533	0.43113	0.00033	0.006819	1.808908	0.001264	0.201236
AR-147	B	V	7266D	0.057071	0.00019463	0.047214	97.81421	0.474671	0.00049	0.005409	1.280676	0.000939	0.297587
AR-147	B	V	7266E	0.047252	0.00132527	0.04317	98.01741	0.46585	0	0.003978	1.206559	0.000835	0.203491
AR-147	B	V	7266F	0.050492	0.00021635	0.032718	97.72122	0.448874	0.00047	0.004547	1.52189	0.001169	0.204502
AR-147	B	V	7266G	0.037834	0.00020375	0.042022	97.95821	0.50931	0	0.004972	1.340288	0.000765	0.097751
AR-147	B	V	7266H	0.049337	0.00053497	0.052616	97.88437	0.381664	0	0.004633	1.541074	0.000589	0.079775
AR-147	B	V	7266I	0.031627	0.00026022	0.029634	98.55931	0.180532	0.00073	0.003188	1.054651	4.85E-05	0.13348
AR-147	B	V	7266J	0.027942	0.00038772	0.055456	98.3709	0.318347	5.7E-06	0.003467	1.101658	0.000576	0.112963
AR-167	B	V	7272A	0.031273	0.00020433	0.016057	97.82257	0.621081	0	0.00556	1.116287	0.000637	0.366642
AR-167	B	V	7272B	0.003484	0.00028806	0.004545	98.55524	0.294251	0	0.003425	0.784714	0.000583	0.334936
AR-167	B	V	7272C	0.046214	0.00078687	0.011539	97.44135	0.3263	0	0.003868	1.877838	0.001063	0.274386
AR-167	B	V	7272D	0.042927	0.00051318	0.021496	97.64154	0.573791	0	0.004432	1.478891	2.07E-05	0.222416
AR-167	B	V	7272E	0.030598	0.00076829	0.037396	96.83698	0.814011	0	0.007778	1.877324	0.000805	0.375429
AR-81	C	V	7262A	0.031732	0.00029255	0.006005	98.79975	0.461544	0.00057	0.008613	0.328179	0.000197	0.345342
AR-81	C	V	7262B	0.040504	0.00052862	0.010541	98.79618	0.614216	0.003	0.011664	0.45359	0	0.062427

Sample #	Facies	Phase	Crush	C_2H_6	C_3H_6	C_3H_8	C_4H_8	C_4H_{10}	C_5H_{12}	C_6H_6	C_7H_{10}
AR-14	A3	V	7239A	47.01463	23.63004	14.72694	0	6.02E-11	5.199055	5.199055	2.075159
AR-14	A3	V	7239B	85.1983	41.98407	14.40474	0	1.07E-10	1.785712	4.365074	1.190475
AR-14	A3	V	7239C	258.0513	0	122.7643	2.294214	6.428579	16.99152	15.39035	5.42486
AR-14	A3	V	7239D	313.2694	42.76362	119.4105	0	1.08E-10	15.51906	17.41583	5.776537
AR-14	A3	V	7239E	187.6007	63.53278	80.93719	0	1.12E-10	2.013363	10.29052	3.981984
AR-14	A3	V	7239F	186.2656	3.823556	156.4206	0	6.64E-11	14.84283	9.983728	3.929765
AR-14	A3	V	7239G	99.30801	30.06427	9.412216	0.845272	10.53163	5.482844	4.157824	1.507782
AR-14	A3	V	7239H	206.3068	71.05843	55.85687	0	1.26E-10	16.21162	8.38358	3.232224
AR-90	A3	V	7244A	126.3166	26.87788	0	0	3.09E-11	0.940256	1.316358	0.550721
AR-90	A3	V	7244B	577.6164	40.9945	0	1.358343	11.55355	15.32333	3.815571	1.541491
AR-90	A3	V	7244C	310.3129	0	0	11.92226	34.26346	10.46069	3.716573	1.315416
AR-90	A3	V	7244D	351.2111	0	0	16.77799	50.98952	17.18771	3.441639	1.024297
AR-90	A3	V	7244E	236.0935	38.61351	0	0	0.805592	0.183089	2.142143	0.787283
AR-90	A3	V	7244F	512.9113	0	0	10.98222	42.67971	17.20201	4.866529	1.691574
AR-90	A3	V	7244G	234.778	4.081821	0	2.616553	14.96668	5.955273	1.465269	0.575642
AR-90	A3	V	7244H	1813.686	199.3756	0	0	9.53E-11	30.70678	12.9898	5.640831
AR-90	A3	V	7244I	408.3294	0	0	10.85252	35.48438	8.521433	3.60024	1.346853
AR-90	A3	V	7244J	83.56868	44.26139	0	0	3.941578	5.641157	2.56745	1.554935
AR-147	B	V	7266A	10.7462	9.550668	26.65492	0	3.53E-11	16.72386	1.548757	0.80155
AR-147	B	V	7266B	89.31401	0	0	10.29567	41.37843	0	0.861235	0
AR-147	B	V	7266C	112.3151	0	13.04223	3.36457	21.81544	22.19531	3.455015	1.77273
AR-147	B	V	7266D	163.9649	14.47163	1.600844	0.781212	16.08529	15.13758	2.215569	1.126994
AR-147	B	V	7266E	69.7512	0	0.723936	2.823349	16.89183	8.988868	1.31515	0.844592
AR-147	B	V	7266F	75.77489	0	0	5.417928	29.67685	23.93933	2.800277	1.415357
AR-147	B	V	7266G	52.02998	0	0.281461	2.372309	16.11026	13.69774	1.353691	0.522712
AR-147	B	V	7266H	12.08202	0	0	2.511951	18.81651	10.87998	1.525663	0.662662
AR-147	B	V	7266I	24.32025	20.58679	0	0	2.837011	4.640464	2.615534	1.255035
AR-147	B	V	7266J	49.88305	3.21684	11.82078	1.101658	8.659027	6.698077	1.002508	0.561845
AR-167	B	V	7272A	145.575	10.28101	15.15918	1.20559	10.02426	7.892151	4.777709	2.009317
AR-167	B	V	7272B	146.9613	0.227567	7.509714	2.354143	15.81199	9.400875	2.016716	0.980893
AR-167	B	V	7272C	107.0931	0	11.2858	7.210896	28.82481	10.04643	1.464713	0.638465
AR-167	B	V	7272D	99.38146	28.54259	0	0	2.02608	6.625431	2.366225	0.754234
AR-167	B	V	7272E	126.6443	26.39518	9.818405	1.896097	14.32398	6.382902	2.384202	1.351674
AR-81	C	V	7262A	134.3957	0	10.52141	1.522749	13.82288	13.69161	2.73701	1.165034
AR-81	C	V	7262B	58.54938	11.55293	0	0	1.09E-11	1.882398	1.088616	0.294833

Sample #	Facies	Phase	Crush	H_2	He	CH_4	H_2O	N_2	H_2S	Ar	CO_2	SO_2	O_2
AR-81	C	V	7262C	0.013506	0.00030651	0.008541	98.89542	0.539634	0	0.008368	0.390101	0.000165	0.138129
AR-81	C	V	7262D	0.053470	0.00031885	0.006208	98.35034	0.722241	0	0.01147	0.462145	0.000296	0.373394
AR-81	C	V	7262E	0.026592	0.00019206	0.005133	99.09843	0.337675	0	0.006535	0.27941	0.000252	0.234166
AR-81	C	V	7262F	0.026504	0.00030262	0.010925	99.20634	0.329805	0	0.003823	0.300418	5.11E-05	0.116821
AR-81	C	V	7262G	0.047930	0.00072668	0.026657	98.19133	0.685754	0.00062	0.004905	0.819668	0.000283	0.21356
AR-81	C	V	7262H	0.030959	0.00048604	0.024882	98.54596	0.746098	0	0.009485	0.564081	0.000593	0.0719
AR-81	C	V	7262I	0.031616	0.00060250	0.047417	98.35115	0.804058	0	0.005774	0.598839	0	0.153139
AR-81	C	V	7262J	0.030043	0.00061043	0.016627	98.73916	0.532548	0	0.005687	0.467183	0.000303	0.199615
AR-11	C	V	6872A	0.024408	0.00003933	0.04316	98.91495	0.188309	0.00046	0.005243	0.81588	--	--
AR-11	C	V	6872B	0.013701	0.00001019	0.050034	99.10303	0.189937	0.00046	0.004077	0.632887	--	--
AR-11	C	V	6872C	0.052221	0.00002964	0.093026	98.69213	0.15879	0.00036	0.003774	0.990409	--	--
AR-11	C	V	6872D	0.045569	0.00001502	0.10052	98.3772	0.146753	0.00048	0.003569	1.313598	--	--
AR-11	C	V	6872E	0.045679	0.00002501	0.166642	98.44468	0.133527	0.00049	0.003234	1.194596	--	--
AR-11	C	V	6872F	0.037582	0.00005701	0.228027	97.82874	0.159844	0.00073	0.00416	1.724787	--	--
AR-11	C	V	6872G	0.005920	0.00012890	1.712793	96.56631	0.378065	0.0014	0.006112	1.317057	--	--
AR-143	D	V	7270A	0.030363	0.00014617	0.014152	99.4382	0.166029	0	0.002982	0.18116	4.96E-05	0.153835
AR-143	D	V	7270B	0.026160	0.00068637	0.017493	99.40255	0.169846	0.00223	0.002046	0.287781	0	0.084936
AR-143	D	V	7270C	0.008706	0.00007120	0.005311	99.71928	0.118352	0.00037	0.001464	0.079078	2.44E-05	0.064153
AR-143	D	V	7270D	0.005522	0.00005713	0.00329	99.77422	0.079438	0	0.001419	0.075845	4.01E-05	0.057702
AR-143	D	V	7270E	0.006087	0.00000000	0.002107	99.92245	0.021282	0	0.00025	0.03047	1.21E-05	0.016872
AR-143	D	V	7270F	0.018187	0.00002619	0.001847	99.61732	0.073944	0.00123	0.002238	0.085288	0.000171	0.184543
AR-143	D	V	7270G	0.022370	0.00008421	0.002286	99.74358	0.052416	0.00022	0.001394	0.06097	0.000107	0.110203
AR-143	D	V	7270H	0.005356	0.00000031	0.001815	99.89934	0.034952	0	0.000699	0.047261	8.42E-05	0.010038
AR-143	D	V	7270I	0.002689	0.00002478	0.001665	99.84987	0.038071	0	0.000834	0.049883	7.54E-05	0.054426
AR-143	D	V	7270J	0.010022	0.00012577	0.002805	99.82218	0.048561	0	0.000738	0.062279	0.000135	0.051173
AR-146	D	V	7271A	0.005780	0.00024937	0.00602	99.56433	0.109116	0	0.001153	0.258569	3.23E-05	0.05247
AR-146	D	V	7271B	0.061012	0.00027217	0.007804	99.1236	0.15416	0	0.002464	0.346725	0.000307	0.286827
AR-146	D	V	7271C	0.043282	0.00014327	0.017469	99.25992	0.132523	0	0.001802	0.380136	0.000335	0.156427
AR-146	D	V	7271D	0.006678	0.00037637	0.021448	99.44492	0.139559	0	0.000724	0.322497	9.42E-05	0.060265
AR-146	D	V	7271E	0.028285	0.00030078	0.019128	99.19176	0.163421	0.00013	0.002203	0.386217	0.000134	0.19775
AR-146	D	V	7271F	0.016845	0.00035768	0.058907	99.03511	0.218101	0	0.001078	0.567156	0.00015	0.098387
AR-146	D	V	7271G	0.066847	0.00038010	0.148258	98.92583	0.176876	0	0.004119	0.597478	0	0.072625
AR-146	D	V	7271H	0.057587	0.00014752	0.111852	99.16241	0.190357	0.0003	0.00219	0.361295	0.000279	0.105654
AR-146	D	V	7271I	0.062260	0.00019734	0.098035	99.135	0.193478	7E-06	0.002271	0.32897	9.15E-05	0.168948
AR-146	D	V	7271J	0.041697	0.00022163	0.047364	99.28825	0.183346	0.00109	0.00148	0.353289	0.000602	0.076755
AR-3	E	V	7234A	0.054086	0.00022353	0.08902	98.9539	0.577525	0.00018	0.005865	0.268542	0	0.041655
AR-3	E	V	7234B	0.031051	0.00017715	0.017345	99.37067	0.312335	0.00038	0.005149	0.166315	0.000161	0.092381
AR-3	E	V	7234C	0.085646	0.00092612	0.056951	98.95523	0.395048	0.00184	0.008086	0.47577	0.000468	0.008047
AR-3	E	V	7234D	0.111244	0.00005276	0.036399	99.11985	0.377692	0.00406	0.003946	0.340303	0	0
AR-3	E	V	7234E	0.080078	0.00018830	0.048183	99.23818	0.355367	0.00298	0.006012	0.23272	0.000169	0.03316
AR-3	E	V	7234F	0.046344	0.00018869	0.019785	99.06382	0.325341	0	0.00526	0.323139	0.000383	0.206682
AR-3	E	V	7234G	0.060785	0.00011058	0.023097	99.14191	0.255058	0.00096	0.004595	0.314106	0.000126	0.19008
AR-3	E	V	7234H	0.033024	0.00015579	0.028138	99.27567	0.343651	0.0003	0.003371	0.202495	0.000218	0.106959
AR-3	E	V	7234I	0.053954	0.00028306	0.022074	99.09872	0.239716	0	0.005594	0.358239	0.000132	0.212188

Sample #	Facies	Phase	Crush	C_2H_6	C_3H_6	C_3H_8	C_4H_8	C_4H_{10}	C_5H_{12}	C_6H_6	C_7H_{10}
AR-81	C	V	7262C	44.87725	4.806047	0	0.397903	2.223577	4.568086	1.045471	0.413507
AR-81	C	V	7262D	145.4231	0	29.94699	1.049069	11.48892	10.75411	1.663721	0.739432
AR-81	C	V	7262E	83.99908	0	13.18816	0.927642	7.999513	7.879367	1.341169	0.787937
AR-81	C	V	7262F	41.70404	1.234718	0	0.141197	2.631663	3.325629	0.645899	0.384535
AR-81	C	V	7262G	51.01611	0	0	8.6311	22.21299	2.426216	1.090158	0.29508
AR-81	C	V	7262H	25.0734	0	0	2.99527	18.25366	7.705346	0.885607	0.259477
AR-81	C	V	7262I	60.5426	9.180199	0	0.053896	0.736572	2.083959	0.658723	0.694653
AR-81	C	V	7262J	51.43219	0	2.307884	3.966384	14.2958	8.362576	1.247379	0.654056
AR-11	C	V	6872A	--	--	--	--	--	--	--	--
AR-11	C	V	6872B	--	--	--	--	--	--	--	--
AR-11	C	V	6872C	--	--	--	--	--	--	--	--
AR-11	C	V	6872D	--	--	--	--	--	--	--	--
AR-11	C	V	6872E	--	--	--	--	--	--	--	--
AR-11	C	V	6872F	--	--	--	--	--	--	--	--
AR-11	C	V	6872G	--	--	--	--	--	--	--	--
AR-143	D	V	7270A	102.5055	0	0	1.190219	11.72103	12.79712	1.576089	0.842392
AR-143	D	V	7270B	43.39442	9.545679	0	0	7.19E-12	8.052097	1.191411	0.584194
AR-143	D	V	7270C	22.61948	0	0	0.128106	3.412216	3.549812	1.462152	0.637369
AR-143	D	V	7270D	18.36351	0	0	0.24422	2.527903	2.787292	0.4983	0.23436
AR-143	D	V	7270E	1.801661	0	0	0.066728	0.883615	1.391846	0.217552	0.102987
AR-143	D	V	7270F	131.8803	0	0	1.107893	9.548863	7.527534	1.310879	0.688276
AR-143	D	V	7270G	51.91098	0	0	0.435325	5.125738	4.91844	0.859675	0.442032
AR-143	D	V	7270H	0	0	1.275098	0.648419	1.573787	0.090741	0.137057	0.071364
AR-143	D	V	7270I	18.85188	0	0	0.376619	2.558512	2.316079	0.377117	0.17509
AR-143	D	V	7270J	10.33897	0	1.228769	0.799042	4.310967	2.535387	0.425367	0.179364
AR-146	D	V	7271A	14.05837	3.26055	0	0	1.884965	2.704627	0.700721	0.261154
AR-146	D	V	7271B	144.4769	1.480516	0	0.381398	9.163944	10.03769	1.945128	0.814804
AR-146	D	V	7271C	63.97311	0	0	1.071984	6.401492	6.123992	1.440716	0.612019
AR-146	D	V	7271D	9.700721	0	3.476521	3.121775	11.14873	5.717879	1.025542	0.374097
AR-146	D	V	7271E	82.09042	0	0	0.718364	9.22286	10.94925	2.738278	1.035061
AR-146	D	V	7271F	10.84403	0	12.60788	0.192833	5.813352	7.673624	1.417891	0.550142
AR-146	D	V	7271G	2.246516	0	43.40676	3.997126	16.62183	3.387699	4.821645	1.631114
AR-146	D	V	7271H	45.25936	0	17.72149	1.54634	7.316214	4.436697	2.128025	0.881559
AR-146	D	V	7271I	80.00561	0	7.079443	0.240148	7.793309	8.704557	2.658081	0.967173
AR-146	D	V	7271J	9.771965	0	6.991582	6.574701	21.47995	9.136045	2.596672	0.886755
AR-3	E	V	7234A	0	0	31.696	6.093216	16.68988	1.130561	5.005621	1.388362
AR-3	E	V	7234B	2.374972	0	16.82105	1.377084	8.382253	3.916707	1.35879	0.503933
AR-3	E	V	7234C	55.58423	0	25.99132	5.756819	30.98691	0	1.631891	0
AR-3	E	V	7234D	0	0	29.65738	0	7.83E-12	0	3.287324	1.623244
AR-3	E	V	7234E	0	0	4.852221	0	9.25529	11.63369	1.105422	0.33279
AR-3	E	V	7234F	51.86378	0	8.013844	3.160298	15.50097	7.209229	3.418809	1.447662
AR-3	E	V	7234G	59.77428	0	15.24354	0.876354	4.695877	5.258126	4.095936	1.501424
AR-3	E	V	7234H	25.03854	0	5.983735	2.662813	13.88915	6.394801	2.265922	0.852505
AR-3	E	V	7234I	66.58946	0	5.230289	1.278913	6.064985	8.977468	1.923743	0.802455

Sample #	Facies	Phase	Crush	H_2	He	CH_4	H_2O	N_2	H_2S	Ar	CO_2	SO_2	O_2
AR-138	E	V	7265A	0.027716	0.00017533	0.00202	99.66494	0.075786	0	0.00164	0.068555	0.000135	0.149973
AR-138	E	V	7265B	0.004210	0.00030082	0.002267	99.55366	0.208494	0	0.002898	0.05617	4.9E-05	0.167216
AR-138	E	V	7265C	0.011592	0.00013772	0.001273	99.80001	0.060299	0	0.001038	0.048894	7.09E-06	0.074568
AR-138	E	V	7265D	0.008098	0.00008799	0.001866	99.76423	0.065016	0	0.000977	0.0583	0.00016	0.096976
AR-138	E	V	7265E	0.047295	0.00003635	0.002918	99.36824	0.114684	0.00174	0.002702	0.139906	0.000294	0.303235
AR-138	E	V	7265F	0.045937	0.00017028	0.003485	99.56528	0.070107	0	0.001568	0.089358	0.000184	0.212144
AR-138	E	V	7265G	0.041727	0.00013519	0.002855	99.67138	0.068532	0	0.001188	0.080785	6.57E-05	0.126793
AR-138	E	V	7265H	0.004114	0.00007903	0.001583	99.92802	0.026783	0.00036	0.001203	0.033953	0.000169	0.002755
AR-174	SA	V	7273A	0.069870	0.00035961	0.012601	98.86176	0.254365	0	0.002731	0.465776	0.000318	0.307848
AR-174	SA	V	7273B	0.029396	0.00036879	0.009874	99.05266	0.214328	0	0.001824	0.542366	8.08E-05	0.141163
AR-174	SA	V	7273C	0.047054	0.00018167	0.014168	99.09792	0.254218	0	0.001968	0.439268	9.66E-05	0.137467
AR-174	SA	V	7273D	0.040478	0.00008100	0.013758	98.66634	0.186709	0	0.00265	0.783764	0.00069	0.29067
AR-174	SA	V	7273E	0.082122	0.00041034	0.008686	98.16109	0.237869	0	0.002991	0.882244	0.000513	0.584333
AR-174	SA	V	7273F	0.070649	0.00041973	0.010033	98.25617	0.258663	0	0.002908	1.017094	0.000639	0.3568
AR-174	SA	V	7273G	0.052127	0.00078840	0.011671	98.50644	0.269035	0	0.002517	0.762279	0.001172	0.374232
AR-174	SA	V	7273H	0.085258	0.00032397	0.011539	98.33302	0.124476	0	0.002386	1.001378	0.000634	0.412305

Sample #	Facies	Phase	Crush	C_2H_6	C_3H_6	C_3H_8	C_4H_8	C_4H_{10}	C_5H_{12}	C_6H_6	C_7H_{10}
AR-138	E	V	7265A	74.55853	0	0	1.142804	7.346302	6.065704	1.011179	0.485366
AR-138	E	V	7265B	39.16083	0	0	0.465652	2.592822	4.085268	0.670112	0.288716
AR-138	E	V	7265C	15.44021	0	0.121257	0	1.98216	3.337499	0.503119	0.237136
AR-138	E	V	7265D	32.5605	0	0	1.132767	5.156044	3.18026	0.521784	0.32648
AR-138	E	V	7265E	159.8053	0	0	1.235374	13.87312	11.96899	1.76422	0.880011
AR-138	E	V	7265F	100.8097	0	0	0.94451	8.313831	5.755524	1.230454	0.590654
AR-138	E	V	7265G	54.03714	0	0	0.207618	4.813983	5.10077	0.792502	0.390192
AR-138	E	V	7265H	0.04108325	0	0	1.119094	4.345997	2.196766	0.232239	0.082846
AR-174	SA	V	7273A	216.1804	6.70251	0	1.015391	8.621505	8.551639	1.816525	1.001417
AR-174	SA	V	7273B	60.10501	10.92325	0	0.357962	2.917929	3.905035	1.025072	0.347114
AR-174	SA	V	7273C	62.92068	3.101229	0	0.276739	5.31953	3.812842	0.799467	0.386555
AR-174	SA	V	7273D	104.6717	0	0	6.458216	21.38892	12.51671	2.484532	1.12862
AR-174	SA	V	7273E	344.8425	1.73802	0	1.543926	21.0768	22.59426	3.599554	2.143852
AR-174	SA	V	7273F	221.4722	0	0	2.268119	19.3553	19.41632	2.552905	1.128974
AR-174	SA	V	7273G	130.8985	0	3.453122	3.750411	30.95613	23.10467	3.643692	1.646522
AR-174	SA	V	7273H	245.2775	0	0	2.573541	20.09765	14.89049	2.743775	1.381901